

# AN EXPERIMENTAL INVESTIGATION OF A LEAN BURN NATURAL GAS PRECHAMBER SPARK IGNITION ENGINE FOR COGENERATION

THÈSE N° 2346 (2001)

PRÉSENTÉE AU DÉPARTEMENT DE GÉNIE MÉCANIQUE

ÉCOLE POLYTECHNIQUE FÉDÉRALE DE LAUSANNE

POUR L'OBTENTION DU GRADE DE DOCTEUR ÈS SCIENCES TECHNIQUES

PAR

**Roger RÖTHLISBERGER**

Ingénieur mécanicien diplômé EPF  
de nationalité suisse et originaire de Langnau im Emmental (BE)

acceptée sur proposition du jury:

Prof. D. Favrat, directeur de thèse  
Prof. K. Boulouchos, rapporteur  
Prof. A. Bölcs, rapporteur  
Prof. R. Raine, rapporteur

Lausanne, EPFL  
2001



# Acknowledgements

This research work was carried out at the *Laboratory for Industrial Energy Systems (LENI)* of the *Swiss Federal Institute of Technology of Lausanne (EPFL)* under the direction of Prof. Daniel Favrat. It was financially supported by the *Swiss Federal Office of Energy (OFEN)*, under the grant no 69 801, the engine manufacturer *Liebherr Machines Bulle S.A.*, the cogeneration group manufacturer *Dimag S.A.*, the *Research Fund of the Gas Industry (FOGA)*, as well as by the *EPFL*, who are all gratefully acknowledged.

I would like to express my sincere gratitude to Prof. Daniel Favrat for giving me the opportunity to carry out this research work and for the total confidence he granted me throughout it. Further, I wish to thank him for his advice during the writing of this thesis report.

I am grateful to Prof. Robert Raine of the *Department of Mechanical Engineering of The University of Auckland, New Zealand* for the numerous fruitful discussions and his helpful suggestions for the writing of this thesis. Further, I wish to thank him very much for the English proof-reading and for accepting being co-examiner.

Prof. Albin Boelcs of the *Laboratory for Applied Thermodynamics and Turbomachinery (LTT)* of the *EPFL* and Prof. Konstantinos Boulouchos of the *Laboratory for Internal Combustion Engines and Combustion (LVV)* of the *Swiss Federal Institute of technology of Zürich (ETHZ)* are gratefully acknowledged for accepting being co-examiners of this thesis. Further, I thank Prof. Boulouchos for giving me the opportunity to test the gas engine piston developed at the *LVV*.

I would like to express my gratitude to Roger Mottier for his major contribution to the construction of the engine test bed and to the engine modifications, to Claude-Alain Paschoud for the engine instrumentation and the development of the testing facility control unit, to Geoff Leyland for the development of the program for experimental data processing, as well as to all my other colleagues from the *LENI* and the technical and electrical services of the *EPFL* who contributed to this research work.

I also thank the natural gas supplier *GAZNAT S.A.*, and particularly Raymond Miglioretti, for the numerous analyses of the natural gas composition.

Finally, I would like to thank all my family and my friends for their love, support and patience.



# Abstract

The operation of a cogeneration internal combustion engine with unscavenged prechamber ignition was investigated. The objective was to evaluate the potential to reduce the exhaust gas emissions, particularly the CO emissions, below the Swiss limits ( $\text{NO}_x$  and CO emissions:  $250$  and  $650 \text{ mg/m}_N^3$ ,  $5\% \text{ O}_2$ , respectively), without exhaust gas after treatment. The investigation was carried out on a small size gas engine (6 cylinders,  $122 \text{ mm}$  bore,  $142 \text{ mm}$  stroke) and required the development of cooled prechambers and the modification of the engine cylinder heads. The approach was essentially experimental, but included a numerical simulation based on the CFD-code *KIVA-3V* in order to assist and guide the experimentation.

The numerical simulation was carried out in order to evaluate the differences in flow characteristics at the location of the spark plug electrodes between direct and prechamber ignition. Further, the influence of the prechamber geometrical configuration was investigated through variations of the nozzle orifice diameter, number and orientation, as well as prechamber volume and internal shape. Based on the results of the numerical simulation, the most promising prechamber configuration parameters were selected for experimentation. Then, variations of the selected prechamber configuration parameters, as well as of the piston geometry, of the turbocharger characteristics and of the engine operating parameters, were carried out in order to determine their influence on the engine performance and emissions.

Through the generation of gas jets in the main chamber, the use of a prechamber strongly intensifies and accelerates the combustion process. However, this advantage is conditioned by a significant delay of the spark timing in order to generate substantial gas jets. This results in a large decrease in peak cylinder pressure and in an important reduction of  $\text{NO}_x$ , CO and THC emissions. Minimum emissions are achieved at a spark timing of about  $8^\circ \text{C}_{ABTDC}$ . The prechamber geometrical parametric study indicates that trends which increase the penetration of the gas jets and/or promote an early arrival of the flame front at the piston top land crevice entrance are beneficial to reduce the CO and THC emissions. In comparison with the direct ignition, the prechamber ignition yields approximately  $40\%$  and  $55\%$  less CO and THC emissions, respectively. However, this also leads to about  $2\%$ -point lower fuel conversion efficiency. The optimisation of the turbocharger results in a recovery of about  $1\%$ -point in fuel conversion efficiency, but a consequent change in the exhaust manifold gas dynamics causes an increase in THC emissions. At the rated power output ( $150 \text{ kW}$ ), the prechamber ignition operation fulfils the Swiss requirements for exhaust gas emissions and still achieves a fuel conversion efficiency higher than  $36.5\%$ .



# Résumé

Le fonctionnement d'un moteur à combustion interne de cogénération avec pré-chambre borgne a été investigué. L'objectif était d'évaluer le potentiel de réduction des émissions de polluants, particulièrement celles de CO, en dessous des valeurs limites prescrites en Suisse ( $\text{NO}_x$  et CO: 250 et 650  $\text{mg}/\text{m}_N^3$ , 5 %  $\text{O}_2$ , respectivement), sans traitement catalytique des gaz d'échappement. L'étude a été effectuée sur un moteur à gaz de faible taille (6 cylindres, 122 mm x 142 mm) et a nécessité le développement de préchambres refroidies, ainsi que la modification des culasses. L'approche était essentiellement expérimentale mais comprenait aussi une simulation numérique basée sur le code CFD *KIVA-3V*, dont le but était d'assister et de guider l'expérimentation.

La simulation numérique a été effectuée afin de comparer l'écoulement au niveau des électrodes de la bougie entre l'allumage direct et celui par préchambre. Par ailleurs, l'influence de la configuration géométrique de la préchambre a été étudiée au travers de variations du diamètre, du nombre et de l'orientation des orifices de transfert, ainsi que du volume et de la forme interne de la préchambre. Sur la base des résultats de la simulation numérique, les paramètres de configuration de la préchambre les plus prometteurs ont été sélectionnés pour être évalués expérimentalement. Une variation de ces paramètres, ainsi que de la géométrie du piston, des caractéristiques de la suralimentation et des conditions de fonctionnement, a ensuite été effectuée afin d'en déterminer l'influence sur les performances et émissions du moteur.

L'utilisation d'une préchambre intensifie et accélère fortement le processus de combustion par la génération de jets de gaz. Cependant, cet avantage requiert un important retard de l'allumage pour générer de substantiels jets de gaz. Ceci entraîne une large diminution de la pression maximale de combustion et une importante réduction des émissions de  $\text{NO}_x$ , CO et THC. Les plus faibles émissions sont atteintes pour un allumage de  $\approx 8^\circ \text{C}_{BTDC}$ . L'étude paramétrique de la géométrie de la préchambre indique que les tendances qui accroissent la pénétration des jets de gaz et/ou qui favorise une arrivée rapide du front de flamme à l'entrée de l'interstice de la couronne du piston réduisent les émissions de CO et THC. En comparaison de l'allumage direct, celui par préchambre réduit les émissions de CO et THC d'environ 40 % et 55 %, respectivement. Cependant, il conduit à une diminution de l'ordre de 2 %-point du rendement effectif. L'optimisation de la suralimentation permet de gagner environ 1 %-point sur le rendement effectif, mais un changement de la dynamique du collecteur d'échappement conduit à un accroissement des émissions de THC. A puissance nominale (150 kW), le fonctionnement avec préchambre satisfait les normes suisses en matière d'émissions de polluants et atteint toujours un rendement effectif supérieur à 36.5 %.





# Contents

<b>1</b>	<b>Introduction</b>	<b>1</b>
1.1	Background and motivation . . . . .	1
1.2	Literature review . . . . .	6
1.3	Aim . . . . .	13
1.4	Objectives . . . . .	13
1.5	Approach . . . . .	14
<b>2</b>	<b>Prechamber development</b>	<b>15</b>
2.1	Engine specifications . . . . .	15
2.2	Prechamber design and integration . . . . .	17
2.3	Instrumentation for pressure indication . . . . .	20
<b>3</b>	<b>Numerical simulation</b>	<b>25</b>
	Summary . . . . .	25
3.1	Simulation procedure . . . . .	26
3.1.1	CFD simulation code . . . . .	26
3.1.2	Mesh generation . . . . .	28
3.1.3	Calculation conditions . . . . .	29
3.1.4	Computation performance . . . . .	31
3.2	Results and comparison with the conventional combustion chamber . .	32
3.3	Parametric study . . . . .	38

3.3.1	Nozzle orifice cross sectional area . . . . .	38
3.3.2	Orientation of the nozzle orifices . . . . .	40
3.3.3	Prechamber swirl . . . . .	41
3.3.4	Number of nozzle orifices . . . . .	43
3.3.5	Addition of coaxial nozzle orifice . . . . .	45
3.3.6	Prechamber bottom geometry . . . . .	47
3.3.7	Prechamber internal volume . . . . .	50
3.3.8	Prechamber internal shape . . . . .	52
3.4	Conclusion . . . . .	55
<b>4</b>	<b>Experimental</b>	<b>57</b>
	Summary . . . . .	57
4.1	Testing facilities . . . . .	58
4.2	General experimental conditions . . . . .	58
4.2.1	Operating conditions . . . . .	58
4.2.2	Exhaust gas emission regulation . . . . .	60
4.2.3	Variable definition . . . . .	60
4.3	Direct ignition operation . . . . .	61
4.4	Prechamber ignition operation . . . . .	64
4.4.1	Effect of the prechamber on the combustion process . . . . .	65
4.4.2	Nozzle orifice cross sectional area . . . . .	75
4.4.3	Number of nozzle orifices . . . . .	79
4.4.4	Nozzle orifice distribution . . . . .	84
4.4.5	Nozzle orifice orientation . . . . .	89
4.4.6	Prechamber internal volume . . . . .	94
4.4.7	Prechamber internal shape . . . . .	99
4.4.8	Main combustion chamber geometry . . . . .	103

4.4.9 Spark timing . . . . .	109
4.4.10 Turbocharger turbine . . . . .	114
4.4.11 Engine load . . . . .	121
4.5 Conclusion . . . . .	129
<b>5 Conclusions</b>	<b>135</b>
<b>6 Further work</b>	<b>139</b>
<b>References</b>	<b>143</b>
<b>Notation</b>	<b>149</b>
<b>List of figures</b>	<b>153</b>
<b>List of tables</b>	<b>159</b>
<b>A Design</b>	<b>161</b>
A.1 Orientation of the nozzle orifices . . . . .	161
A.2 Prechamber and cylinder head drawings . . . . .	163
A.3 Drawings of the instrumentation holders . . . . .	176
<b>B Numerical simulation</b>	<b>185</b>
B.1 Sensitivity analysis . . . . .	185
B.1.1 Mesh resolution . . . . .	186
B.1.2 Turbulence model and initial turbulence intensity . . . . .	188
B.1.3 Initial prechamber temperature . . . . .	192
B.2 <i>KIVA-3V</i> input file (itape5) . . . . .	194
<b>C Experimentation</b>	<b>197</b>
C.1 Testing facilities . . . . .	197

C.1.1	Test bed . . . . .	197
C.1.2	Measurement instrumentation and acquisition systems . . . . .	199
C.1.3	Conditioning of the engine and dynamometer fluids . . . . .	204
C.2	Natural gas composition and properties . . . . .	214
C.3	Variable definition . . . . .	218
C.3.1	Steady state variables . . . . .	218
C.3.2	Dynamic variables . . . . .	227
C.4	Influence of specific engine parameters . . . . .	237
C.4.1	Introduction . . . . .	237
C.4.2	Volumetric compression ratio . . . . .	237
C.4.3	Valve overlap duration . . . . .	239
C.4.4	Location of the piston first compression ring . . . . .	242
C.4.5	Conclusion . . . . .	244
C.5	Tabulated experimental data . . . . .	246
<b>Curriculum vitae</b>		<b>251</b>

# Chapter 1

## Introduction

### 1.1 Background and motivation

The development of the human society is principally based on the consumption of fossil fuels which are converted into useful energy (heat, mechanical work or electricity) through the process of combustion. The combustion of fossil fuels, hydrocarbons or coal, essentially produces water and carbon dioxide ( $\text{CO}_2$ ), but also small amounts of nitrogen oxides ( $\text{NO}_x$ ). Further, depending on the combustion process, a small fraction of the fuel does not react or reacts only partially to form intermediate hydrocarbons and/or carbon monoxide ( $\text{CO}$ ) as well as particulates in some cases. In the 1960's, concern about the effect of these by-products and their derivatives, such as ozone ( $\text{O}_3$ ), on human health motivated the introduction of exhaust and flue emission regulations. Since then, continuous research has been carried out on the composition of combustion gases and the toxicity of the different components, and consequently on the reduction of the most toxic emissions. The increase in fossil fuel consumption and the requirements for better protecting human health and the environment has led to the introduction of a more and more stringent legislation.

In addition, the world wide increase in oil, coal and natural gas consumption has lead to an increase in  $\text{CO}_2$  production and a depletion of the fossil energy reserves. Since the beginning of the 1990's, concern about the global earth warming effect of  $\text{CO}_2$  developed in the industrialised countries and motivated the organisation of UN conferences on climate change. At the conference on environment and development of *Rio de Janeiro, Brazil* (Earth Summit) in 1992, the contribution of the increase in  $\text{CO}_2$  and other greenhouse gas emissions to the observed climate change was internationally acknowledged. In 1997, at the conference of *Kyoto, Japan*, the industrialised nations committed themselves to a specified reduction of their greenhouse gas emissions. This reinforces the common statement that at short to medium term, the main issue is probably no longer the depletion of fossil energy reserves, but the effect on the environment and on human health, of the emissions resulting from their consumption.

Therefore, sustainable development of human activities requires a more efficient and cleaner conversion of the primary energy, as well as a larger use of renewable fuels, such as biogas, and fuels characterised by a high hydrogen to carbon ratio, such as natural gas.

In practice, the electrical power generated from fossil fuels is mainly produced in large centralised power plants, which do not enable an economical heat recovery because of their remoteness from potential consumers. In parallel, fossil fuels are burnt in furnaces to produce heat for heating purposes (industrial processes or buildings). In comparison, the decentralised production of electrical power through smaller units enables a large heat recovery to cover part of the heating requirements. Therefore, the decentralised energy production, called cogeneration, appears as a particularly effective way of saving energy and preserving the global environment. Due to the relatively low local electrical power requirements, which ranges from a few *kW* to several *MW*, cogeneration units are mainly based on stationary internal combustion engines. In Europe, and particularly in Switzerland, these engines are usually operating on natural gas or biogas (sewage or landfill gas) on the *Otto* principle, mainly because of the stringent exhaust gas regulation in force. The spark ignition engine offers two cost effective alternatives to reduce the exhaust gas emissions, particularly the  $\text{NO}_x$  emissions; namely, lean burn operation, or the use of a three-way catalyst in association with a stoichiometric mixture. In comparison, diesel engines rely almost exclusively on the relatively expensive selective catalytic reactor (SCR) technology to reduce  $\text{NO}_x$  emissions and often require a particle filter to reduce soot. However, the diesel engine generates almost no CO and unburnt hydrocarbon (THC) emissions and is characterised by a significantly higher fuel conversion efficiency than the spark ignition engine.

With a limit of  $250 \text{ mg}/\text{m}_N^3$ , 5 %  $\text{O}_2$  [1], Switzerland has the most stringent requirement for  $\text{NO}_x$  emissions in Europe. In comparison, the German limit, which is often used as a reference, is  $500 \text{ mg}/\text{m}_N^3$ , 5 %  $\text{O}_2$  [2]. In addition, the CO emissions are limited to  $650 \text{ mg}/\text{m}_N^3$ , 5 %  $\text{O}_2$  in both countries.

There are several engine operating modes able to fulfil these requirements, but they almost all rely on a catalytic exhaust gas after treatment. The first of these operating modes is based on the use of a stoichiometric mixture and a three way catalyst and was investigated in an earlier phase of the present gas engine study [3, 4]. The three-way catalyst simultaneously reduces  $\text{NO}_x$ , CO and THC emissions to a very low level. However, the knocking tendency of the stoichiometric mixture does not allow engine supercharging and therefore limits the rated power output. Furthermore, the low power output combined with unfavourable combustion conditions results in a relatively low fuel conversion efficiency. Nevertheless, the combination of the stoichiometric operation with exhaust gas recirculation enables to overcome these limitations and to simultaneously achieve a high rated power output and a high fuel conversion efficiency [5].

Another approach is the lean burn operating mode, which enables the reduction of  $\text{NO}_x$  emissions by the decrease of the combustion temperature through a dilution of the fuel-air mixture with excess air. In comparison with the stoichiometric operation without exhaust gas recirculation, this mode enables engine supercharging and

is characterised by a higher fuel conversion efficiency and a better reliability. With a conventional combustion chamber, this operating mode is able to satisfy the German requirements without oxidation catalyst, but with a narrow margin [6, 7]. More elaborated combustion chambers [8, 9, 10] enable the engine operation at a higher relative air to fuel ratio and are thus able to reduce the  $\text{NO}_x$  emissions down to  $250 \text{ mg}/\text{m}_N^3$ , 5%  $\text{O}_2$ . However, this results in an increase in CO emissions beyond the legal limit and therefore requires the use of an oxidation catalyst. In an earlier phase of the present gas engine study [3, 4], the use of highly turbulent combustion chamber [11] further reduced the  $\text{NO}_x$  emissions to  $150 \text{ mg}/\text{m}_N^3$ , 5%  $\text{O}_2$ , but required also the use of an oxidation catalyst.

Cogeneration engines are typically operating up to 8 000 hours per year and have a lifetime of more than 100 000 hours. In comparison an automobile engine operated for up to 250 000  $\text{km}$  at an average speed of  $50 \text{ km}/\text{h}$ , corresponds to 5 000 hours. Because the engine is often the only installed heat supplier (in the case of failure, electrical power can be supplied by the network), these operating conditions require great engine robustness and very high reliability. In the case of natural gas operation, the use of an exhaust gas catalyst enables the reduction of the emissions far below the Swiss limits. However, this adds extra cost and increases the complexity of the cogeneration system, particularly in the case of the use of a three-way catalyst. This operating mode requires a precise control of the relative air to fuel ratio inside a narrow range by means of a lambda sensor. A deviation outside this range leads to a rapid increase in emissions far beyond the legal limits. Further, the aging of the exhaust gas after treatment system results in a progressive deactivation of the catalyst and a drift of the lambda sensor. Therefore, this requires frequent control of the exhaust emissions and the replacement of the catalyst and lambda sensor at regular intervals, which increases the maintenance costs. In addition, the greater complexity and the drift of the lambda sensor is likely to affect the cogeneration plant reliability. Moreover, when the engine is operating on biogas (sewage or landfill gas) or alternatively on biogas and natural gas, a catalyst cannot be used for exhaust gas after treatment. Sewage and landfill gases contain a certain amount of heavy metals, which rapidly deactivates the catalyst. In consequence, it appears that in order to achieve high reliability and to enable alternate operation on natural gas and biogas, it is necessary to reduce the exhaust emissions below the Swiss limits at the level of the combustion process.

Several different approaches enable the reduction of exhaust emissions at the level of the combustion process. However, only a few have a direct practical interest and the *two principal ones* are discussed here. The *first approach is the exhaust gas recirculation (EGR)*. Cooled exhaust gas is used to dilute the air-fuel mixture, instead of an excess of air as in the case of the lean burn operation, in order to decrease the combustion temperature and reduce the  $\text{NO}_x$  generation. Because of the higher heat capacity of the exhaust gases, a lower dilution is required to achieve the same  $\text{NO}_x$  emissions. Associated with a stoichiometric mixture, the use of EGR leads to a strong reduction of the  $\text{NO}_x$  emissions, but does not significantly decrease the high CO emissions characterising the stoichiometric operation [12]. However, the *combination of EGR with lean burn operation* strongly reduces the CO emissions and enables the Swiss requirements to be satisfied, but with only a narrow margin and a relatively low maximum fuel conversion efficiency of approximately 36% [5, 12]. Another aspect is

that the system required for EGR adds complexity to the cogeneration plant, which tends to reduce its reliability. No evidence has been found of commercial cogeneration gas engines operating with EGR. Therefore, due to the lack of experience, the long term effect of the highly corrosive exhaust gas on the engine intake system is unknown.

The *second principal approach is the lean burn operation with prechamber ignition*. As already mentioned, the lean burn operation with direct ignition (conventional combustion chamber) is able to fulfil the Swiss requirements for  $\text{NO}_x$  emissions, but generates too high CO emissions. The CO emissions result from the partial oxidation of fuel escaping the primary oxidation process (combustion through flame front propagation) [13]. During the compression stroke and part of the combustion process, a significant amount of the air-fuel mixture contained in the cylinder is compressed into the combustion chamber crevices. Because of the intense heat transfer to the combustion chamber walls, the flame front quenches at the entrance of the crevices, which leaves part of the air-fuel mixture unburnt. This unburnt mixture then emerges into the combustion chamber during the expansion stroke and mixes with the hot bulk gases. Through the secondary oxidation process, it reacts to form partially oxidised products, which then in part further react to  $\text{CO}_2$  and  $\text{H}_2\text{O}$ . This incomplete combustion results in significant concentrations of CO and THC in the exhaust gas. Therefore, a reduction of the CO and THC emissions requires a decrease in the amount of air-fuel mixture escaping the primary oxidation process. The amount of air-fuel mixture located in the crevices depends on their sizes, the pressure achieved during combustion and the time at which the flame front reaches their entrances. The two main combustion chamber crevices which account for most of the CO and THC emissions are the volume located between the piston, piston rings and cylinder liner and the volume located between the cylinder head, gasket and cylinder liner; the former contributing to the largest extent [13].

The reduction of the cylinder head gasket crevice strongly decreases the THC emissions [3, 4]. However, it does not significantly affect the CO emissions. This indicates that the main CO emissions source is the piston ring pack crevice, the size of which cannot easily be reduced without affecting the piston assembly friction and wear. Another way of decreasing the amount of unburnt mixture located in the piston ring pack crevice is the reduction of the combustion pressure. This can be achieved in two different ways. The first way consists of reducing the volumetric compression ratio. However, this leads to a rapid decrease in fuel conversion efficiency [13]. The second way consists of shifting the combustion process into the expansion phase through a delay of the spark timing. However, this also results in a decrease of the fuel conversion efficiency and is limited by the relatively slow burning velocity of lean air-fuel mixtures. The lean burn operating mode with direct ignition is mainly limited by the decrease of the burning velocity with the increase in relative air to fuel ratio. This results from the exponential decrease in chemical reaction kinetics with the reduction of combustion temperature. From a certain value called the lean operating limit, the flame front is no longer able to travel from a single ignition point (the spark plug location) through the whole combustion chamber before the temperature decrease during expansion quenches the flame. This leads to incomplete combustion, which results in high CO and THC emissions as well as a rapid decrease in the engine operating stability.



This problem has already been encountered in the case of large gas engines. For a cylinder bore over  $200\text{ mm}$ , the combustion process can no longer be sufficiently accelerated through an increase of the turbulence generated by the piston [14]. In order to overcome this problem, large gas engines operate with the spark plug located in a small prechamber of a volume between 1.5 and 4% of the compression volume [14, 15, 16, 17], which is connected to the main combustion chamber through nozzle orifices. After exhaust valve closure, the prechamber is fed with natural gas from a separate supply. During the compression stroke, the natural gas mixes with the lean air-fuel mixture flowing from the main combustion chamber through the nozzle orifices. At spark timing, the prechamber gas composition is close to stoichiometric. Just after spark timing, the easily ignitable prechamber mixture burns rapidly and produces strong jets of very hot combustion gases into the main chamber. The gas jets ignite the main cylinder charge at multiple locations and generate locally a high level of turbulence, which accelerates and intensifies the combustion process. However, the prechamber stoichiometric combustion generates a large quantity of  $\text{NO}_x$ , which has to be compensated by a large increase of the relative air to fuel ratio beyond 2.0 [16, 17, 18, 19] and sometimes up to 2.6 [14], in order to achieve low  $\text{NO}_x$  exhaust emissions. Consequently, the prechamber becomes the main source of  $\text{NO}_x$  emissions [20]. Further, due to engine supercharging, the prechamber fuel enrichment needs a natural gas supply at medium pressure. This usually requires the use of a separate compressor in order to operate the engine on the low pressure natural gas network or on biogas. The engine operation with enriched prechamber reduces the  $\text{NO}_x$  below  $250\text{ mg}/\text{m}_N^3$ , 5%  $\text{O}_2$ , but is characterised by CO emissions beyond the Swiss limits. The high CO emissions probably result from the extremely lean air-fuel mixture used. This increases the cylinder pressure during compression and combustion (higher cylinder load for the same engine power output) and the sensitivity to local flame quenching. Smaller gas engines operating with enriched prechamber [21, 22] are also characterised by high CO emissions.

Another way of taking advantage of the beneficial effect of the prechamber on the combustion process is to use an unscavenged prechamber. In this case, the prechamber is not separately fed with natural gas. At exhaust valve closure, the prechamber is filled with residual gas from the previous engine cycle. During compression, air-fuel mixture from the main chamber flows into the prechamber through the nozzle orifices and mixes with the residual gas. This operating mode relies exclusively on the prechamber configuration for the achievement of flammable conditions at the level of the spark plug electrodes. The principal interest of this approach is that it does not need a separate fuel supply to the prechamber. This operating mode was principally investigated in the case of automotive engines operating on gasoline [23, 24, 25, 26]. Due to the relatively small cylinder bore, the prechamber was in the form of a modified spark plug. The results indicate that the use of prechamber spark plug significantly accelerates the combustion process and improves the engine operating stability. In comparison to direct ignition, this enables an increase of the relative air to fuel ratio and yields higher fuel conversion efficiency. Finally, it achieves lower CO emissions at high values of relative air to fuel ratio. The use of prechamber spark plugs was also occasionally experimented on natural gas in the case of an automotive engine ( $86.5\text{ mm}$  bore) [23] and of a small size cogeneration engine ( $122\text{ mm}$  bore) [5]. In the latter case, the engine was operated in combined EGR-lean burn mode. Despite the relatively small

prechamber volume (less than 1 % of the compression volume [27]), the engine achieves a significantly higher fuel conversion efficiency and a lower cycle-by-cycle variability in comparison with the direct ignition operation at equal  $\text{NO}_x$  and CO emissions. Further, different studies on enriched [28, 29] as well as unscavenged [23, 26] prechambers have shown the determining influence of the prechamber configuration (volume, shape and features of the nozzle orifices) on the engine performance and emissions.

In summary, it seems that the use of an unscavenged prechamber may have two major effects on the mechanisms responsible for CO emissions:

- the simultaneous ignition of the main chamber charge at multiple locations inside the bulk gas generates a larger initial flame front surface; this promotes an early arrival of the flame front at the piston top land crevice entrance.
- the acceleration of the combustion process enables its shift into the expansion phase through a delay of the spark timing, which results in a reduction of the combustion pressure.

Both effects tend to decrease the amount of air-fuel mixture compressed into the piston ring pack crevice during the primary oxidation process and therefore are expected to reduce the CO emissions.

These findings motivated this investigation of the use of an unscavenged prechamber for application on a small size cogeneration gas engine in order to evaluate the potential of simultaneously reducing the  $\text{NO}_x$  and CO emissions below the Swiss limits. The installation of an unscavenged prechamber only requires a limited modification of the engine cylinder head and numerous large gas engines and indirect injection diesel engines are currently operating with prechambers. This emphasises the practical potential of this approach and indicates that this engine modification is not likely to significantly affect the engine reliability.

## 1.2 Literature review

The use of an unscavenged prechamber was mainly investigated in the case of automotive engines operating on gasoline. Only a few investigations were performed on larger engines operating on natural gas. This section presents the principal research works which were carried out during the past fifteen years and summarises the main results obtained.

In an extensive and detailed study, *Czerwinski* [23] (1985) compared the prechamber ignition with the conventional direct ignition on three different engines operating essentially on gasoline, but also, in few cases, on natural gas. The investigation was carried out on two one-cylinder (bore/stroke in *mm*: 82.6/114.3 and 101/130) and one four cylinder (86.5/84.4) four stroke engines. The prechamber were in the form of modified spark plugs with an internal volume corresponding to 0.4 to 6.3 % of the

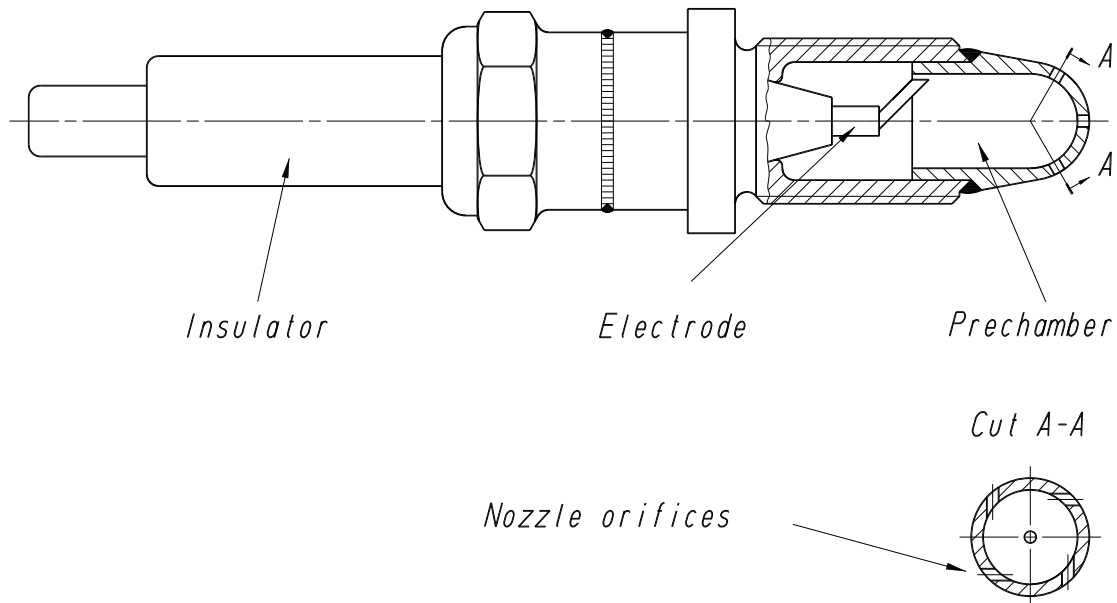


**Figure 1.1:** Schematic representation of a spark plug prechamber.

compression volume. A schematic representation is shown in **figure 1.1**. Variations of the prechamber internal volume, of the ratio between the total nozzle orifice cross sectional area and the prechamber internal volume, as well as of the ignition location in the prechamber were performed. The prechambers used were featured with four and five nozzle orifices with different orientations, including a central orifice, coaxial to the prechamber axis. Except in one particular case, the nozzle orifices were oriented in order to impart a swirl motion to the prechamber charge (see *Cut A-A* in **figure 1.1**). Further, a few prechambers were modified to enable pressure indication. In addition, variations of the spark timing, of the crankshaft rotational speed, of the volumetric compression ratio and of the rate of exhaust gas recirculation were carried out. The main results obtained are the following.

The prechamber ignition conditions depends on the concentration in residual gas, on the relative air to fuel ratio, on the internal flow characteristics (velocity and turbulence intensity), as well as on the pressure and temperature. The internal flow characteristics at ignition timing are determined by the prechamber geometrical configuration, which together with the ignition location and the ignition system used, have a major influence on the ignition process. The high flow velocity and turbulence intensity generated in the prechamber by the flow across the nozzle orifices during the compression stroke promotes a rapid prechamber combustion, but can also excessively perturb the spark discharge phase and the early stage of the flame kernel development. However, it is possible to reduce this detrimental effect by the use of an ignition system delivering more energy. The rapid prechamber combustion leads to a much shorter ignition delay in comparison with the direct ignition. The prechamber pressure increase resulting from combustion generates gas jets of unburnt, partially burnt and burnt mixture through the nozzle orifices, which penetrate into the main combustion chamber. This multiplies the number of main chamber ignition locations and dramatically increases the initial flame front surface. In turn, this strongly intensifies and accelerates the main chamber

combustion process. The rapid penetration of the gas jets also generates pressure pulsation in the main chamber, which then propagates back into the prechamber.

Depending on the prechamber configuration and engine operating conditions, the losses induced by the inflow and outflow through the nozzle orifices are partly or fully compensated by the acceleration of the combustion process. In comparison with the direct ignition, the engine operation with prechamber achieves a higher fuel conversion efficiency at idle and part load. When increasing the engine load, the pressure drop across the nozzle orifices increases and the fuel conversion efficiency decreases below the value achieved with direct ignition. However, it is possible to reduce this effect through an adjustment of the prechamber configuration, but this results in a decrease of the engine performance at idle and part load. Further, at full load, the use of a prechamber leads to a 1 to 3% reduction of the maximum engine power output. Regarding the  $\text{NO}_x$  and THC emissions, no clear trends were identified. Depending on the engine and operating conditions, these emissions were higher or lower than in the case of the direct ignition. However, prechamber ignition achieves lower CO emissions at high values of relative air to fuel ratio. In comparison to the direct ignition, the prechamber ignition requires a smaller spark advance in order to achieve maximum brake torque (MBT). Further, it leads to a much lower cycle-by-cycle variability, which consequently enables engine operation at a significantly higher relative air to fuel ratio or rate of exhaust gas recirculation.

An increase in engine load, in crankshaft rotational speed and in volumetric compression ratio increases the prechamber charge and turbulence intensity. This leads to stronger gas jets, which further accelerate and intensify the main chamber combustion process. A delay of the spark timing from MBT improves the ignition conditions but also causes a shift of the combustion process into the expansion phase, which results in a decrease in engine power output. When considering the same prechamber internal volume, the ratio between total nozzle orifice cross sectional area and prechamber internal volume ( $A_n/V_p$ ) influences the amount of mixture admitted in the prechamber during the compression stroke and determines the prechamber turbulence intensity. A decrease in the ratio  $A_n/V_p$  simultaneously reduces the spark timing advance for MBT and the cycle-by-cycle variability. For given engine operating conditions, main combustion chamber geometry and prechamber internal configuration, there is a optimum internal prechamber volume, which leads to the minimum spark advance for MBT and achieves the maximum fuel conversion efficiency, as well as results in the minimum cycle-by-cycle variability. The change from 4 to 5 nozzle orifices accelerates the main chamber combustion process, but also leads to a higher prechamber nose thermal load, which, in some cases, leads to auto-ignition at full load. The orientation of the nozzle orifices together with the ignition location in the prechamber have a significant influence on the ignition process and the early stage of the flame kernel development. This mainly results from the inhomogeneity of the flow and mixture conditions in the prechamber.

Only two series of experiments carried out on natural gas are presented, one with direct ignition and the other with prechamber ignition. The results indicates similar global trends as in the case of engine operation on gasoline.

In an other study, *Ohtsu et al.* [24] (1989) investigated the influence of the nozzle orifice cross sectional area of an unscavenged prechamber on the main chamber combustion process and compared the results to the ones obtained with conventional direct ignition. The experimentation was carried out on a small size single cylinder four stroke engine (bore/stroke in  $mm$ : 80/59) with side valves operating on gasoline. The engine was fitted with a relatively large horizontal prechamber (located on the side of the cylinder) with an internal volume corresponding to 25 % of the compression volume. The prechamber was connected to the main combustion chamber with a single nozzle orifice and equipped with a conventional spark plug. The pre- and main chambers were fitted with quartz windows in order to enable visualisation of the combustion process with a high speed camera and the main combustion chamber was instrumented for pressure indication. The nozzle orifice cross sectional areas investigated were 20, 35, 55 and 90  $mm^2$ . The engine was operated at a constant crankshaft rotational speed of 1000  $rpm$  and on a air-fuel mixture close to stoichiometric ( $A/F = 15$ ). The volumetric efficiency was kept as close as possible to 80 % and the spark timing was adjusted in order to achieved MBT for each configuration tested. Measurement of the engine operation without prechamber was also performed. No exhaust gas emissions were measured.

The ignition delay and combustion duration were evaluated from the heat-release rate computed from the main chamber pressure, as well as from the optical measurements. The results show a good agreement between the two methods. Further, they indicate that the flame front propagation in the prechamber is scarcely affected by the size of the total nozzle orifice cross sectional area. The smallest nozzle orifice cross sectional area achieves the deeper gas jet penetration and results in the higher main chamber flame propagation speed. An increase of this area leads to a decrease in the gas jet penetration and in the combustion velocity, with the latter gradually converging to the value characterising the direct ignition operation. Despite the very fast combustion promoted by the smallest nozzle orifice cross sectional area, it leads to relatively low brake mean effective pressure and fuel conversion efficiency in comparison with larger areas. This is thought to be due to the increase in heat and pressure losses induced by the more rapid flow through the smaller nozzle orifice. The best performance are achieved with the medium area (55  $mm^2$ ), thus indicating the existence of an optimum nozzle orifice cross sectional area.

*Mavinahally et al.* [25] (1994) studied the use of an unscavenged prechamber as a means for improving performance and reducing exhaust gas emissions of an engine with spark plug location at the edge of the combustion chamber. The investigation was performed on a single cylinder air-cooled compression-ignition four stroke engine (bore/stroke in  $mm$ : 87.5/110) converted for spark ignition operation on gasoline. For this purpose, the volumetric compression ratio was reduced from 17.5:1 to 8:1. The prechamber ( $\approx 1$  % of the compression volume) was mounted at the location of the diesel injector and fitted with a conventional spark plug. Four different prechamber configurations with variations of the number and diameter of the nozzle orifices as well as of the prechamber internal volume were selected for experimentation. In parallel to the conventional execution in stainless steel, one configuration was also manufactured in copper, in order to evaluate the influence of the material. In addition, the influence of the ignition location in the prechamber was investigated through the use of a modified

spark plug with an extended and bended electrode. In this case the spark plug gap was located close to the nozzle orifices and was formed by the bended electrode and the prechamber wall. Variations of the relative air to fuel ratio ( $20 \leq A/F \leq 26$ ) and of engine load were performed at a constant crankshaft rotational speed of 1500 *rpm*. The spark timing was adjusted to operate at MBT, as long as knock was not occurring. The main chamber was instrumented for pressure indication and the THC and CO emissions were measured. However, since the CO emissions were found to be very low (500 *ppm*!), they were not presented. The engine performance and emissions with direct ignition were also measured, in order to enable direct comparison.

The results indicate that the use of very large nozzle orifice diameters ( $\geq 6$  mm) yields lower fuel conversion efficiency than in the case of the direct ignition. This is explained by the fact that large orifices do not enable the generation of a sufficient pressure difference between prechamber and main chamber to produce substantial gas jets. The transfer of the ignition location from the closed end of the prechamber to a location close to the nozzle orifices leads to an increase in fuel conversion efficiency, which becomes significantly higher than in the case of the direct ignition when operating near the lean limit. This improvement is attributed to a faster and more repeatable ignition process, which is indicated by a shorter ignition delay. It enables a reduction of the spark advance required to achieve MBT. The longer ignition delay in the case of the spark plug location at the closed end of the prechamber is thought to be due to a poor local scavenging and an excessive mixture dilution. When considering an optimised configuration, the engine operation with prechamber ignition achieves a higher fuel conversion efficiency than with direct ignition. Further, it is characterised by a lower cycle-by-cycle variability, which extends the lean operating range and significantly reduces the THC emissions at high values of relative air to fuel ratio. Moreover, when operating on a relatively rich fuel-air mixture ( $A/F \approx 20$ ) the prechamber ignition enables engine operation at MBT spark timing instead of knock-limited spark timing in the case of direct ignition. This results in a significantly higher fuel conversion efficiency.

In comparison to the stainless steel version, the copper prechamber achieves somewhat lower fuel conversion efficiency and higher THC emissions when operating close to the lean limit. Consequently, it is characterised by a smaller lean operating range. The more stable combustion in the stainless steel prechamber is attributed to its approximately ten times lower thermal conductivity, which results in a higher overall prechamber wall temperature in comparison with the copper version. This reduces the heat transferred from the initial flame kernel located between the extended spark plug electrode and the prechamber wall and consequently leads to a lower cycle-by-cycle variability. In comparison with the direct ignition, the prechamber ignition enables engine part load operation at a higher relative air to fuel ratio. Further, the ability of the prechamber ignition to operate on a leaner air-fuel mixture and consequently with a wider throttle opening (lower pumping losses) results in significantly higher fuel conversion efficiency between 40 and 100 % of the full load.

In 1994, *Nakazono* [21] studied the effect of the main combustion chamber geometry on the performance and exhaust gas emissions of a prechamber gas engine operating without and with mixture enrichment. The investigation was performed on a single

cylinder four valve four stroke engine (bore/stroke in  $mm$ : 150/165, volumetric compression ratio 14:1) operating on locomotive gas 13A<sup>1</sup>. The engine was operated at a constant crankshaft rotational speed of 1500  $rpm$  and at a spark timing of  $10^\circ CA_{BTDC}$ . In the case of the unscavenged prechamber, the brake mean effective pressure was 9  $bar$ . Further, the engine was instrumented for main chamber pressure indication and exhaust gas emission measurement. The prechamber was located along the cylinder axis and featured with an internal volume of 4% of the compression volume, as well as with 4 orifices oriented at  $70^\circ$  from the prechamber axis.

Three piston bowl geometries generating different level of turbulence were investigated. In the case of the unscavenged prechamber, the results indicate that the piston producing the highest turbulence yields the shortest combustion duration, the highest maximum cylinder pressure and the lowest cycle-by-cycle variability. Consequently, it is characterised by the widest lean operating range. However, the piston generating the lowest turbulence achieves the highest fuel conversion efficiency. No results of measurement of exhaust gas emissions were presented. The gas jets issuing from the prechamber and the squish contribute to the generation of turbulence in the main combustion chamber. However, major changes in the rate of heat-release show that the combustion process is mainly governed by the main chamber geometry. In addition, a strong squish and a high swirl are suspected to perturb the development of the gas jets. Globally, the results of this study demonstrate the large influence of the piston bowl geometry.

In a recent study *Geiger et al.* [26] (1999) investigated different ignition systems in order to evaluate their ability to ignite lean air-gasoline mixture. Unscavenged and enriched prechambers were among the systems tested. The study was carried out on a water-cooled four valve four stroke single cylinder research engine (displacement volume:  $515\text{ cm}^3$ , volumetric compression ratio: 10.5:1). The engine cylinder head was derived from a modern production automotive engine with double spray gasoline injection in the intake port, directly before the intake valves. Further, the cylinder head was fitted with two quartz windows in order to enable 2D combustion process visualisation with a CCD camera, as well as Laser Doppler Anemometry (LDA) for measurement of local flow characteristics. The testing facilities were equipped for exhaust gas emission measurement and cylinder pressure indication. The engine was operated at a constant crankshaft rotational speed of 2000  $rpm$  and at a relatively low indicated mean effective pressure of 2.8  $bar$ .

In the case of the conventional direct ignition, results from variations of the intake port geometry in order to modify the cylinder flow indicate that an increase in cylinder charge motion (higher flow velocity and turbulence intensity) significantly extend the lean operating range. The unscavenged prechambers tested were in the form of modified spark plugs with an internal volume of approximately 2% of the compression volume (**figure 1.1**). Variations of the prechamber internal volume, of the number, total cross sectional area and orientation of the nozzle orifices, of the ignition location, as well as of the prechamber material were performed. Further, the prechamber was instrumented for pressure indication and wall temperature measurement. However, only very few

---

<sup>1</sup>gas of composition similar to natural gas, but not containing nitrogen and carbon dioxide: 88%  $CH_4$ , 6%  $C_2H_6$ , 4%  $C_3H_8$  and 2%  $C_4H_{10}$  [22]

results are presented in the publication. When operating with prechamber ignition, an increase in relative air to fuel ratio leads to a decrease of the prechamber combustion intensity. In comparison to the stoichiometric operation, the operation close to the lean limit results in no perceptible pressure difference between prechamber and main chamber ( $\Delta p \approx 1 \text{ bar}$  at  $\lambda = 1$ ). This results in a slower main chamber combustion process, which requires a larger spark advance in order to achieve the same indicated mean effective pressure.

In comparison with the operation with conventional direct ignition, the prechamber ignition leads to a shorter main chamber ignition delay. However, it yields a slightly lower fuel conversion efficiency and a higher cycle-by-cycle variability when increasing the relative air to fuel ratio. This results in a narrower lean operating range. The lower prechamber overall operating performance are attributed partly to the higher heat losses to the combustion chamber wall and to the pressure drop between chambers. Further, according to a numerical simulation of the engine cycle, the decrease in performance with the increase in relative air to fuel ratio is thought to be mainly due to the progressive increase in prechamber mixture residual gas concentration resulting from the increase in spark advance necessary to keep constant indicated mean effective pressure. This motivated the investigation of prechambers scavenged with methane.

More recently *Nellen et al.* [5] (2000) studied the combination of exhaust gas recirculation with the lean burn operating mode on a small size cogeneration natural gas engine, in order to evaluate the potential to reduce the exhaust gas emissions. This investigation was carried out at the *Laboratory for Internal Combustion Engines and Combustion (LVV) of the Swiss Federal Institute of Technology of Zürich* in the frame of a parallel project to the present study. The experimentation was performed on a six cylinder supercharged and intercooled four stroke diesel engine (bore/stroke in *mm*: 122/142) converted for gas operation with spark ignition. The engine was instrumented for pressure indication and measurement of exhaust gas emissions. In this study, ignition with a small unscavenged prechamber was compared with the conventional direct ignition. The prechamber tested was in form of a modified spark plug (**figure 1.1**) with an internal volume of less than 1% of the compression volume [27]. A variation of the spark timing was performed at a volumetric compression ratio of 10.5:1, as well as at a crankshaft rotational speed of 1500 *rpm* and a brake mean effective pressure of 14.4 *bar*. The unburnt mixture temperature was 90 °C.

The results indicate that the prechamber leads to a longer main chamber ignition delay in comparison with the direct ignition. However, it results in a shorter combustion duration and a lower cycle-by-cycle variability, particularly at the lean and EGR limits, respectively. Depending on the spark timing, prechamber operation yields lower or similar CO emissions. THC emissions are insensitive to spark timing variation. Further, the prechamber operation leads to higher fuel conversion efficiency and lower cycle-by-cycle variability at equal NO<sub>x</sub> and CO emissions.

---



The different research works reviewed in this section demonstrate the large influence of the prechamber and main chamber configuration on the engine performance and emissions. Some of them clearly indicate the existence of an optimum size of individual configuration parameters, which maximises fuel conversion efficiency at given engine operating conditions (load, spark timing, relative air to fuel ratio or EGR rate). In comparison to the conventional direct ignition, the engine performance and emissions can be lower or higher, depending on the combination between the combustion chamber geometry and the engine operating conditions. This stresses the importance of optimising the prechamber and main chamber configurations for given engine operating conditions. However, the use of an unscavenged prechamber generally leads to a lower cycle-by-cycle variability, which results in a wider lean or EGR operating range.

In addition, this literature review indicates that the majority of the investigation of unscavenged prechambers were performed on engine operating on gasoline and that no systematic study was carried out (at least published) in the case of natural gas operation. When considering the sensitivity to engine operating conditions, this emphasises the need of a detailed investigation dedicated to natural gas operation.

## 1.3 Aim

The overall aim is to demonstrate that the use of unscavenged prechambers (henceforth called *prechambers* for convenience) has the potential to reduce the exhaust emissions of a gas engine operating on the lean burn mode, while keeping performance at a high level. The demonstration is done on a *Liebherr* six cylinder turbocharged gas engine type *G 926 TI* intended for cogeneration.

## 1.4 Objectives

In order to achieve this aim, three successive objectives have been defined.

The first objective is the development and design of a modular cooled prechamber and its integration into the original engine cylinder head without casting modification. The purpose of the modularity is to ease the investigation of the influence of the prechamber configuration. In parallel, two cylinder heads are modified in order to enable pressure indication in the pre- and main chambers of one cylinder, as well as in the main chamber of another cylinder. The goal of instrumenting a second cylinder for pressure indication is to evaluate variations between cylinders.

The next objective is to measure the performance and emissions of the modified engine in order to establish the influence of the following parameters:

- engine operating parameters
  - relative air to fuel ratio

- spark timing
- load
- prechamber configuration
  - internal volume
  - internal shape
  - nozzle orifice features
- main combustion chamber geometry
- turbocharger characteristics.

The final objective is to combine all the features which reduce the CO emissions and compare the engine performance and emissions obtained with the resulting pre- and main chamber configuration with the one obtained in the case of the direct ignition operation.

## 1.5 Approach

The investigation approach is essentially experimental, but also includes a numerical study based on computational fluid dynamics (CFD). The objective of the numerical simulation is to evaluate the influence of the prechamber configuration on the internal flow characteristics, particularly at the location of the spark plug electrodes prior to ignition. The purpose is to:

- guide the selection of the more promising prechamber configurations for the experimental investigation, in order to reach an optimum more quickly and to reduce the cost of experimentation
- help the interpretation of the experimental results.

In addition, the experimental approach focuses on the fulfilment of the Swiss requirements for exhaust gas emissions. Therefore, for each geometrical configuration tested, mainly variations of the engine operating parameters close to the conditions which enable the achievement of the lowest NO<sub>x</sub> emissions are investigated.

# Chapter 2

## Prechamber development

### 2.1 Engine specifications

The engine used is derived from a *Liebherr* [30] heavy duty diesel engine type 926 converted for natural gas operation on the *Otto* principle and is intended for cogeneration applications. The main engine specifications are summarised in **table 2.1**.

**Table 2.1:** Main engine specifications

Manufacturer	<i>Liebherr Machines Bulle S.A., Switzerland</i>
Type	<i>G 926 TI (turbocharged, intercooled)</i>
Number of cylinders	6 in line
Bore	122 mm
Stroke	142 mm
Connecting rod length	228 mm
Total swept volume	9.96 l
Number of valves	2
Intake valve opening	15 °C $A_{BTDC}$
Intake valve closing	45 °C $A_{ABDC}$
Exhaust valve opening	54 °C $A_{BBDC}$
Exhaust valve closing	14 °C $A_{ATDC}$
Firing order	1-5-3-6-2-4
Swirl ratio	2.0 [13]
Volumetric compression ratio	12
Turbocharger	<i>KKK K27 3371 OLAKB</i>
Fuel and air mixer	<i>RMG 980 140/65-36-1.1</i>
Ignition system	<i>Fairbanks Morse IQ 250</i>
Spark plugs	<i>Bosch Super F6DC, electrode gap 0.4 mm</i>

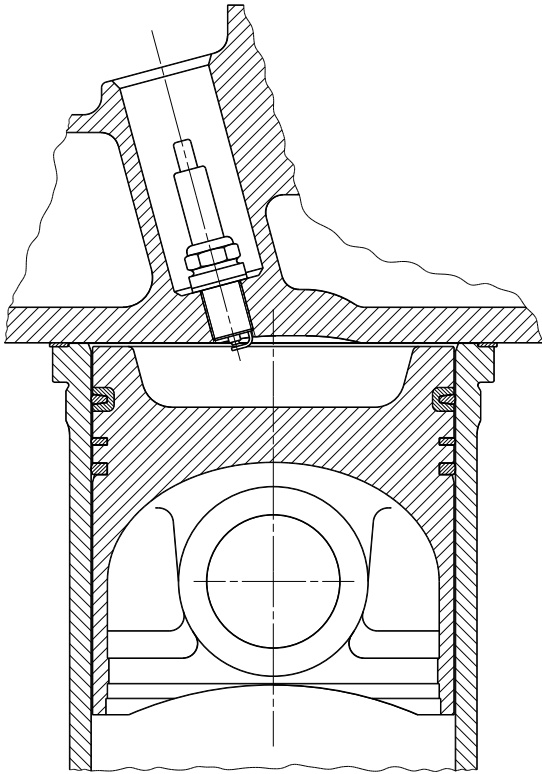


**Figure 2.1:** Schematic representation of the original combustion chamber with direct spark ignition and piston A,  $\epsilon = 12$ .

The engine is designed with one intake and one exhaust valve actuated by a side crankshaft via pushrods. Consequently, this gives an offset and tilted position of the spark plug well, which results in a non-axisymmetrical combustion chamber. In order to enable the fitting of ignition spark plugs at the location of the diesel injectors, the engine is equipped with new cylinder heads with a larger boss. The diesel injection pump was removed and an inductive ignition system *Fairbanks Morse IQ 250* [31] with one coil per cylinder installed. The preparation of the fuel and air mixture is achieved with a venturi type mixer *RMG 980 140/65-36-1.1* [32] located before the inlet of the turbocharger compressor, in order to achieve a good homogenisation. The fuel-air mixture composition is adjusted with a valve on the gas feed, which is actuated by a stepper motor. The engine load is controlled by a throttle valve situated between the mixer and the turbocharger. The combustion chamber was adapted to the spark ignition operation through a modification of the piston geometry and a reduction of the volumetric compression ratio. The original combustion chamber geometry developed by the engine manufacturer and formed by the piston called A is represented in **figure 2.1**. It is used here as reference geometry. Further, the engine is equipped with cylinder liners characterised by a reduced dead volume at the level of the cylinder head gasket to limit the carbon monoxide and hydrocarbons exhaust gas emissions [3, 4, 33]. The engine operates in lean burn mode and is supercharged with a turbocompressor *Kühnle, Kopp & Kausch (KKK) K27 3371 OLAKB* [34] and intercooled, in order to increase the power output and to limit the fuel-air mixture temperature, respectively. In order to preserve more energy for the turbocharger and maintain a higher temperature for possible exhaust gas after treatment, the engine is equipped with an insulated exhaust manifold. More detailed information on the engine conversion is given in [3].

## 2.2 Prechamber design and integration

The objective was to design a small water cooled prechamber, representing about 3 % of the main chamber compression volume, and to house it in the boss of the existing cylinder head used for the spark plug well. Further, this prechamber should allow the fitting of a conventional spark plug. The prechamber development and design was realised with the 3D-CAD program *I-DEAS 6* by *SDRC* [35]. In order to realise a compact prechamber volume located as close as possible to the main combustion chamber, and this without a significant reduction of the cylinder head mechanical strength, a simplified CAD model of the cylinder head was first realised (a complete designed would have been too arduous and superfluous). This model comprises the intake and exhaust port geometries, provided by the engine manufacturer in the form of *IGES* files, the valves, the valve-seat inserts and guides, as well as the relevant cooling water channels and fixing holes. It does not comprise the hollow volumes forming the cooling jacket and the one represented in figures are only approximate, but accurate enough for the purpose. The prechamber well was dimensioned to leave a minimum casting iron wall thickness of 4 mm at the level of the housing of the valve seat inserts. The prechamber integrated to the modified cylinder head is represented in **figure 2.2, a**.

The prechamber was designed on a modular basis formed by three parts, in order to limit the machining work for the experimental parametric study. The prechamber is composed of a first part, called the *nose*, which forms the main prechamber internal volume and supports the connecting orifices, called the *nozzle orifices*, to the main combustion chamber. The second part, called the *body*, holds the spark plug and forms the remaining internal volume, as well as leads the cooling water to the nose. These two parts are made out of heat resistant austenitic stainless steel *X15CrNiSi25-20* (*Böhler H525* [36]) to withstand the high combustion temperature and to slow down the erosion process of the nozzle orifices. However, because of the efficient prechamber cooling and the absence of erosion of the body, which have been demonstrated, its material could be replaced by a conventional stainless steel. The sealing between the nose and the body is realised with a tempered copper joint. Finally, a third part, called the *clamp*, made out of conventional stainless steel permits the prechamber to be fixed to the cylinder head with three studs. A picture of the whole prechamber is given in **figure 2.2, b** and a detail of the body with spark plug electrodes and positioning pin is showed in **figure 2.2, c**. In the case of an industrial application, the three different parts could be welded together.

The offset and inclined position of the prechamber well requires an accurate positioning of the prechamber nose, in order to permit a determined orientation of the nozzle orifices. This is accomplished by the alignment of the different parts with two pins and the global prechamber positioning by the fixing studs. The sealing of the prechamber well filled with cooling water is realised with a tempered copper joint on the side of the main combustion chamber, to withstand the high temperature, and with an O-ring joint on the other side. The prechamber is fixed with three studs, spring washers and nuts (**figure 2.6, a**). The studs are mounted in threaded holes machined in the cylinder head. Unlike the two gudgeons close to the clamp positioning pin, the

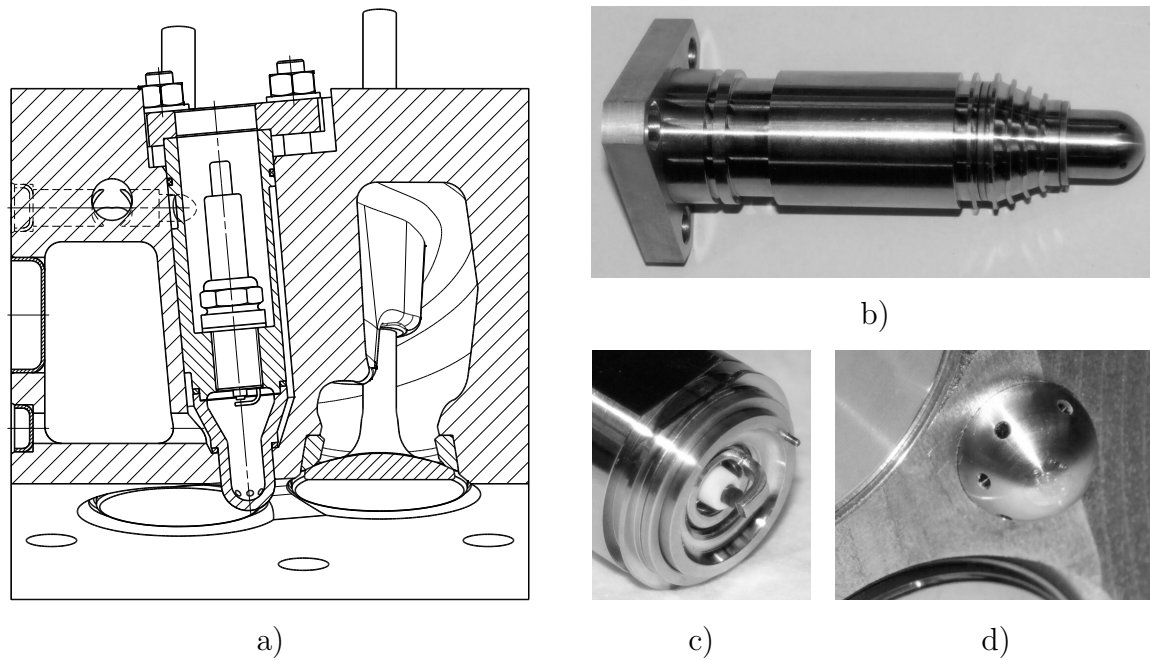


**Figure 2.2:** a) combustion prechamber integrated in the cylinder head, b) complete prechamber with fixing clamp and copper joints, c) detail of the prechamber body with spark plug electrodes and positioning pin, d) detail of the prechamber nose protruding into the main combustion chamber.

third one is fixed in a relatively thin cast iron wall ( $\approx 6 \text{ mm}$ ). A preliminary modification of the casting would therefore be required for an industrial application. All studs are blocked and sealed with *Loctite 262*. The limited space in the prechamber body required the use of small spark plugs (eg *Bosch Super F6DC*) with a tightening hexagon of 16 mm.

In order to limit the prechamber and spark plug operating temperature, part of the engine water flowing in the cylinder head is used to cool the nose and the bottom of the body. Through an additional hole in the cylinder head, cooling water is derived from the channel feeding the region between the valves and is conducted to an annular groove in the prechamber body (**figure 2.2, a**). The water flows along the body in a semi-circular channel milled on the outer surface. It is then distributed around the nose by several annular grooves (**figure 2.2, b**) to realise a more uniform cooling and avoid hot spots. Finally, the water exits the prechamber well through a second hole drilled in the cylinder head and connecting to the cooling jacket. The two complementary holes in the cylinder head face are sealed with steel obturation plugs. The channel feeding the prechamber well is threaded to allow the mounting of a calibrated restriction. A preliminary study consisting in a reduction by 50 % of the flow cross section in cylinder 1 head has not showed a perceptible effect on the combustion process. However, a more detailed study involving local temperature measurements is required to clarify the real influence of the water mass flow.

The orientation of the nozzle orifices was determined in order to achieve a relatively uniform distribution of the jets of combustion gas in the main combustion chamber, taking into account the offset position of the prechamber nose tip. Two different

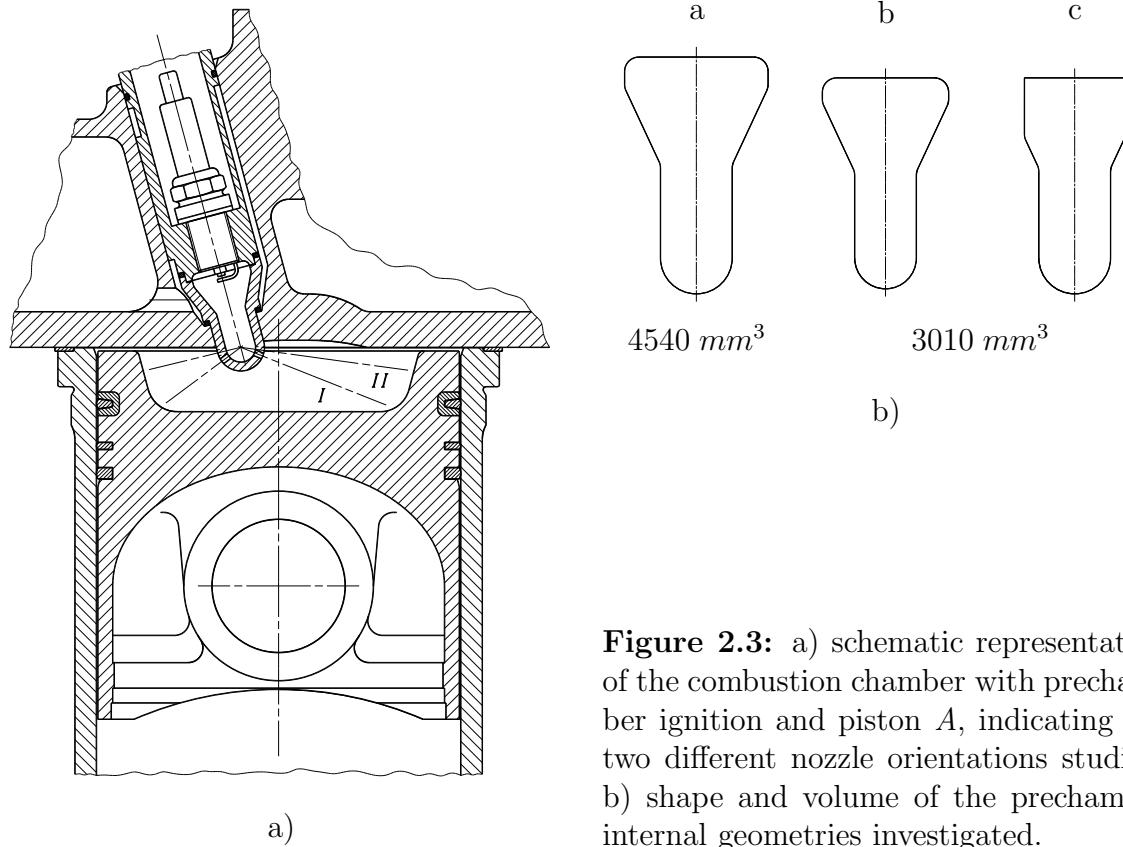


**Figure 2.3:** a) schematic representation of the combustion chamber with prechamber ignition and piston A, indicating the two different nozzle orientations studied, b) shape and volume of the prechamber internal geometries investigated.

orientations were studied and are represented together in **figure 2.3, a**. The chosen approach consists in pointing the orifices axes to equally distributed position on a curve located at the intersection between the surface of the piston bowl at TDC and a specific plane parallel to the cylinder head. In the first case (I), the plane is located in the bottom corner of the piston bowl and in the second case (II) tangent to the extremity of the prechamber nose. The first orientation yields a relatively uniform distribution of the jets of combustion gas in the main combustion chamber volume, while the second aims to promote an early arrival of the flame front in the squish region in order to limit the amount of unburnt mixture compressed in the piston top land crevice. The effective distribution of the nozzle orifices and the method to calculate their individual orientation is detailed in appendix A.1. The corresponding average angle from the prechamber axis is  $\approx 62^\circ$  (I) and  $\approx 78^\circ$  (II), respectively. Variations of the nozzle orifice diameter and number were also realised and their influence investigated. A picture of the prechamber nose tip protruding into the main chamber with 6 nozzle orifices of diameter  $2 \text{ mm}$  and oriented to  $\approx 62^\circ$  is showed in **figure 2.2, d**.

Two different prechamber internal volumes were evaluated while keeping a similar internal geometry. The first is of  $4540 \text{ mm}^3$  and the second of  $3010 \text{ mm}^3$ , which corresponds to 2.9% and 1.9% of the effective compression volume (including the prechamber volume), respectively. The internal dimensions of the smaller prechamber corresponds to a proportional reduction of the larger. Further, on the basis of the smallest volume, the influence of the internal prechamber shape was studied. The three different internal geometries are represented in **figure 2.3, b**.

**Table 2.2:** Summary of the prechamber configurations

$N_n$	$d_n$ in mm	$A_n$ in mm <sup>2</sup>	$\alpha_n$ in °	$V_p$ in mm <sup>3</sup>	Shape
4	2.12	14.10	$\approx 62$	4540	a
4	2.12	14.10	$\approx 78$	4540	a
4	2.50	18.85	$\approx 62$	4540	a
6	1.41	9.37	$\approx 62$	4540	a
6	1.73	14.10	$\approx 62$	4540	a
6	1.73	14.10	60, even	4540	a
6	1.73	14.10	$\approx 78$	4540	a
6	2.00	18.85	$\approx 62$	4540	a
6	2.00	18.85	$\approx 78$	4540	a
6	2.24	23.64	$\approx 62$	4540	a
6	1.63	12.52	$\approx 78$	3010	b
6	1.63	12.52	$\approx 78$	3010	c

All the combinations tested are summarised in **table 2.2**. They were selected on the basis of the numerical simulation results presented in chapter 3 and the motivation is discussed in chapter 4, where the experimental results are analysed and discussed. The drawings detailing the modification of the cylinder head and the geometry of the different prechamber configurations are given in appendix A.2.

## 2.3 Instrumentation for pressure indication

In order to evaluate the combustion process in the pre- and main chambers, the head of cylinder 1 and partly of cylinder 3 were instrumented for pressure indication. Cylinder 1 offers the best possible access to the prechamber and to the exhaust port to place the transducer membrane close to the variable to be measured. The head of cylinder 1 was further modified to enable pressure measurement in the pre- and main combustion chamber as well as in the intake and exhaust ports. Due to the lack of accessibility, the head of cylinder 3 was only modified to permit the main chamber pressure measurement. Cylinder 3 was selected because as cylinder 1 it was instrumented for pressure indication in the previous phases of the gas engine study [3, 4, 33], investigating the operation with direct ignition. Thus, it enables a direct comparison of the pressure cycle between direct and prechamber ignition in two different cylinders.

Due to their particular high sensitivity ( $\approx 80 pC/bar$ ) and accuracy, water cooled piezoelectric transducers of type *KISTLER 7061B* [37] were chosen for the measurement of the main chamber pressure. This required the machining of a hole in the cylinder head through the cooling jacket and the development of a specific transducer holder (**figure 2.4, a**). The holder is sealed with a tempered copper joint on the combustion chamber side and with an O-ring joint on the other side. The tilted holder



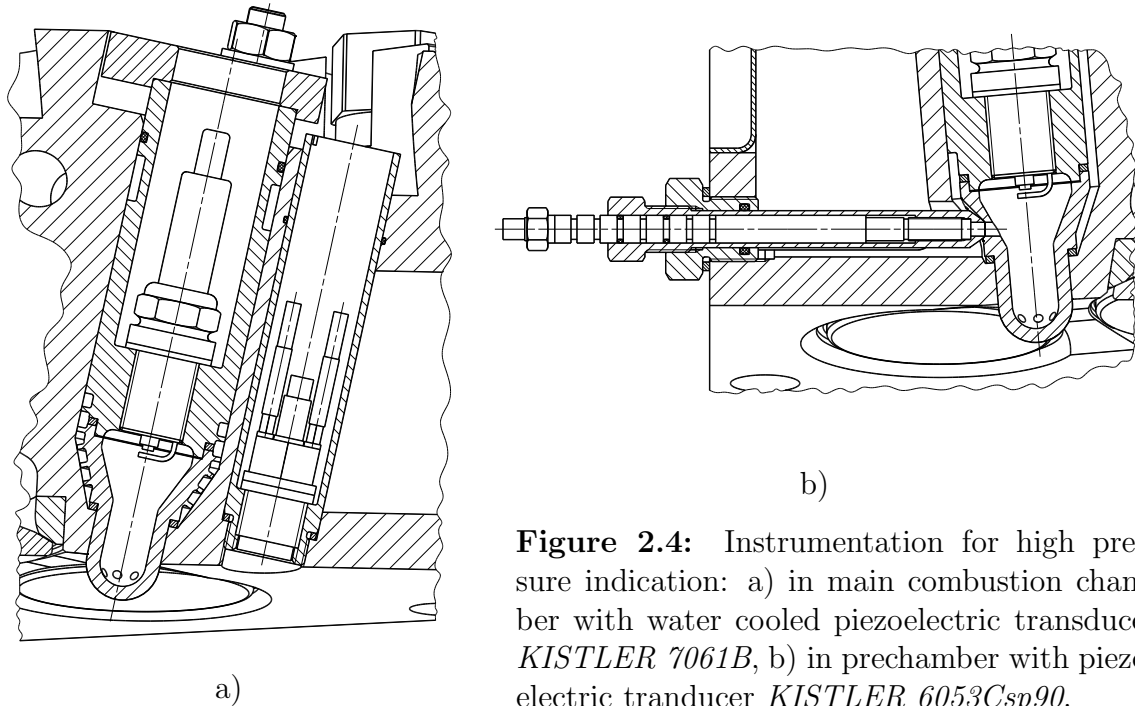


**Figure 2.4:** Instrumentation for high pressure indication: a) in main combustion chamber with water cooled piezoelectric transducer *KISTLER 7061B*, b) in prechamber with piezoelectric transducer *KISTLER 6053Csp90*.

position combined to the weak local casting iron wall thickness requires the milling of an elliptical O-ring groove. In the case of the prechamber, the small size of the volume to access and its location very close to the cylinder head face restrains the choice of applicable pressure transducers. A piezoelectric transducer of type *KISTLER 6053Csp90* was selected in order to minimise the length of the connecting duct between transducer membrane and prechamber volume, and therefore to limit the amplitude of parasitic pressure oscillations [38]. The fitting of the transducer required a modification of the prechamber well coolant exit and the development of a specific holder in two parts (**figure 2.4, b**). The coolant exit bore was increased from  $\phi 9 \text{ mm}$  to  $\phi 12 \text{ mm}$  to keep the same total flow cross section. The sealing between the prechamber and the cooling jacket is realised with the direct contact of the spherical surface of the transducer holder tip on a cone machined on the prechamber nose outer surface. The tightening torque is  $3 \text{ Nm}$ . On the other side, the sealing of the cylinder head is realised with a combination of an O-ring joint (between transducer holder and holder guide) and a tempered copper joint (between holder guide and cylinder head face). The sealing between transducer and holder is realised through a direct metal-metal contact, while two O-ring joints are used to damp out the lateral oscillation of the relatively long transducer body. Although the transducer is not externally cooled, the flow of water emerging from the prechamber well limits and stabilises its operating temperature, which reduces the sensitivity shift. Combined with the relatively high sensitivity ( $\approx 19 \text{ pC/bar}$ ) for this size of transducer, this measurement configuration is expected to yield an accurate prechamber pressure indication.

The intake and exhaust ports of cylinder 1 were instrumented with piezoresistive transducers of type *KISTLER 4045A5* to permit the evaluation of the breathing process. Special *KISTLER* cooling adapters with integrated damper were used to minimise the effect of engine vibrations and to withstand the high exhaust temperature. This required the development of specific holders, which are represented in **figure 2.5, a**

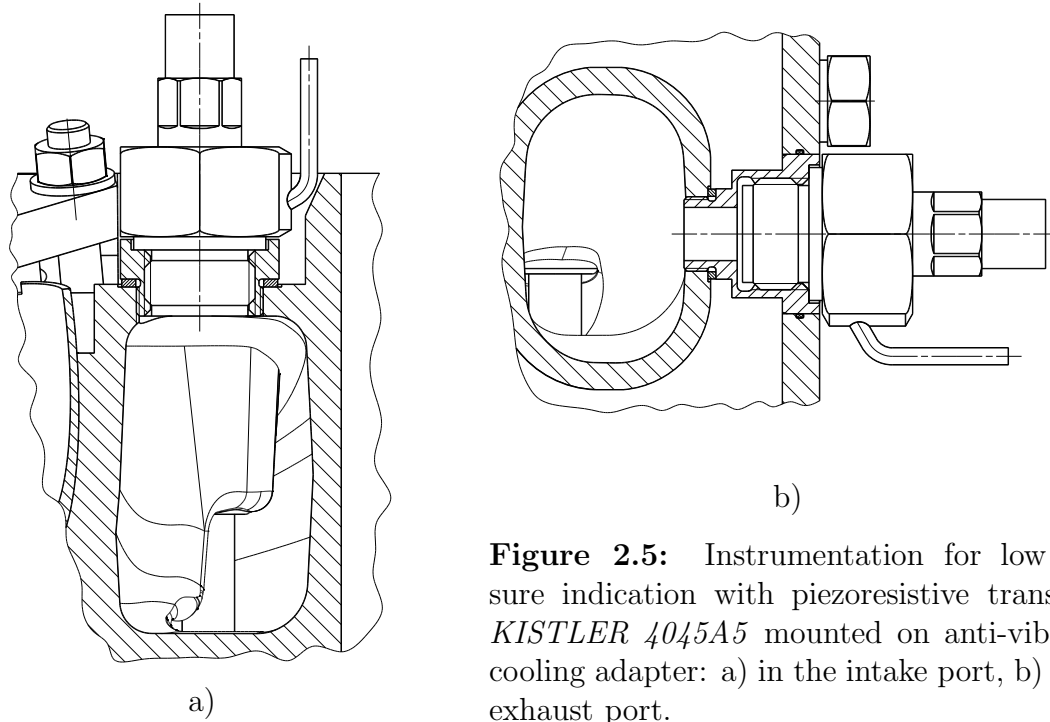


**Figure 2.5:** Instrumentation for low pressure indication with piezoresistive transducer *KISTLER 4045A5* mounted on anti-vibration cooling adapter: a) in the intake port, b) in the exhaust port.

for the intake port and **figure 2.5, b** for the exhaust port. Due to the presence of the cooling jacket around the exhaust port, the adapter could not be positioned as close to the gas flow as in the case of the intake port. However the pre-cooling realised with the engine water reduces the thermal shift (and increases the transducer lifetime) and therefore somewhat compensates the decrease of accuracy resulting from the parasitic pressure oscillations associated with the more remote location.

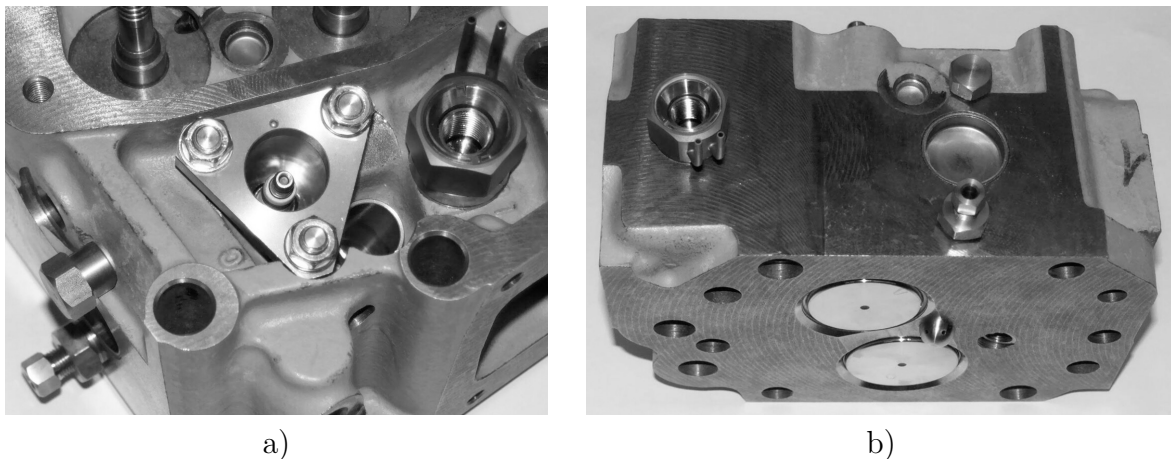


**Figure 2.6:** Instrumented cylinder 1 with prechamber: a) top view showing the prechamber fixing clamp and the anti-vibration cooling transducer adapter for intake port pressure measurement, b) side view showing the transducer adapter for prechamber pressure indication and the anti-vibration cooling transducer adapter for exhaust port pressure measurement.

**Table 2.3:** Main specifications of the pressure transducers [37]

Designation	7061B	6053Csp90	4045A5
Range in <i>bar</i>	0 ... 250	0 ... 250	0 ... 5
Sensitivity	$\approx 80 \text{ pC}/\text{bar}$	$\approx 19 \text{ pC}/\text{bar}$	$\approx 100 \text{ mV}/\text{bar}$
Natural frequency in <i>kHz</i>	$\approx 45$	$\approx 130$	$\approx 30$
Linearity in % <i>FSO</i>	$\leq \pm 0.5$	$\leq \pm 0.4$	$< \pm 0.3$
Hysteresis in % <i>FSO</i>	-	-	$< 0.1$
Repeatability in % <i>FSO</i>	-	-	$< 0.1$
Acceleration error in <i>bar/g</i> *	$< 0.004$	$\leq 0.001$	$< 3 \cdot 10^{-4}$
Temp. operat. range in $^{\circ}\text{C}$	-50 ... 350	-50 ... 350	20 ... 120
Thermal shift in %	$\approx 1 @ 200 \pm 50 ^{\circ}\text{C}$	$\leq \pm 1 @ 200 \pm 50 ^{\circ}\text{C}$	$\leq \pm 1$
Tightening torque in <i>Nm</i>	25	1.5	12 ... 20

\* gravitational acceleration  $g = 9.80665 \text{ m/s}^2$

The instrumented cylinder 1 is shown in **figure 2.6** and the main specifications of the pressure transducers are summarised in **table 2.3**. The detailed drawings of the different transducers and adapters holders are given in appendix A.3.



# Chapter 3

## Numerical simulation

### Summary

In order to evaluate the effects and consequences of transferring the ignition point of the conventional combustion chamber into a small prechamber connected to the main combustion chamber through small orifices, the respective flows during the compression stroke were simulated using the CFD-code *KIVA-3V*. The prechamber flow characteristics at the location of the gap between the spark plug electrodes and in the crank angle period where the ignition is expected to occur (between  $30^\circ CA_{BTDC}$  and TDC) were compared to the corresponding conditions in the conventional combustion chamber at the experimental spark timing for minimum  $NO_x$  exhaust emissions ( $26.7^\circ CA_{BTDC}$ ). The influence of the prechamber geometrical configuration was evaluated through variations of the nozzle orifice diameter, number and orientation, as well as prechamber volume and internal shape. The results show that the velocity magnitude is mainly dependent on the prechamber shape, and that it is generally of the same order as with direct ignition. Further, the turbulence intensity varies strongly with the geometrical configuration and reaches, in most cases, a much higher value in the prechamber. High turbulence intensity promotes rapid prechamber combustion, but also perturbs the ignition process and the early stage of the flame kernel growth, which is expected to increase the probability of ignition failure. The partial dilution of the unburnt mixture with unscavenged prechamber residual gas generally leads to a slightly lower fuel to air equivalence ratio. However, nozzle orifices imparting a swirl motion or a prechamber shape with an almost uniform cross section can result in fuel concentration very close to or beyond the flammability limit. In most cases, the mixture temperature is not significantly affected by changes in the prechamber geometrical configuration. However, depending on the prechamber spark timing, the mixture temperature can be similar or much higher ( $\approx 100 K$ ) than in the case of direct ignition. The prechamber charge and thereby the amount of energy available for the main chamber ignition depends on the prechamber volume and on the pressure drop across the nozzle orifices. Finally, the strong turbulence generated in the main chamber by the flow towards the nozzle orifices should promote a rapid propagation of the flame front in the early stage of the main chamber combustion process.

## 3.1 Simulation procedure

The simulation procedure is based on the use of the CFD-code *KIVA*, version *3V* [39]. The *KIVA-3V* package includes two separate programs for mesh generation (*K3PREP*) and results visualisation (*K3POST*) in addition to the CFD-code. However, these pre- and post-processors have not been elaborated to treat complex geometries and therefore were replaced by commercial programs. The mesh generation was realised with the software *HEXA* by *ICEMCFD* [40] and the results visualisation was done with the program *EnSight 6* by *CEI* [41]. The use of these two softwares required the implementation of different interfaces to link them to the CFD-code and to link the mesh generator to the 3D-CAD program *I-DEAS 6* by *SDRC* [35] for the geometry transfer. The complete simulation procedure is summarised in **figure 3.1**.

A simplified geometry, not including the combustion chamber crevices and the spark plug electrodes, is first designed with the CAD-program. The geometrical model is limited to include only the curves and surfaces necessary for the block-structure mesh generation. The selection of the corresponding geometry and the production of the input file for the mesh generation software is realised by the *SDRC Mesher Interface* by *ICEMCFD* [42]. The semi-automated hexahedral mesh generation program *HEXA* is used to realise the discretisation of the computational domain. *KIVA-3V* requires a mesh input file containing the vertices coordinates and a certain number of flags which identify the type of element the vertices or cells belong to (surface or volume; piston face or bowl, liner wall, cylinder head, . . . ; on moving or non-moving surface; attached to an active or an non-active cell; corresponding fluid region; . . .), which are called here boundary conditions. The corresponding file is generated by the *KIVA-3V* output interface of the *Mesh Editor* by *ICEMCFD* [43], after introduction of the boundary conditions characterising each element describing the geometry (i.e. curves, surfaces and volumes). The *KIVA-3V* own mesh generation program was used in the case of the conventional combustion chamber (without prechamber) to control and validate the mesh generation procedure with *HEXA*. Several anomalies were identified in the output interface, that required modifications by the *ICEMCFD* software developers. In addition to the grid description file, *KIVA-3V* needs the calculation conditions (engine parameters, sub-models used, initial conditions, time step, . . .) in the form of another input file. The visualisation of the simulation results requires a preliminary conversion of the *KIVA-3V* output file to a suitable format for *EnSight 6*. This is realised with the help of an interface written by N. Nordin [44], freely available on the World Wide Web. The control and validation of the visualisation procedure was realised through comparing the results of given *KIVA-3V* examples included in the package with the values published in the program manuals.

### 3.1.1 CFD simulation code

The purpose of this section is to give a general insight into the *KIVA*-code capabilities and specifications. The *KIVA* software having been used as a development tool, a detailed description is beyond the scope of this study. A thorough description is given in the code manuals [39, 45, 46, 47].

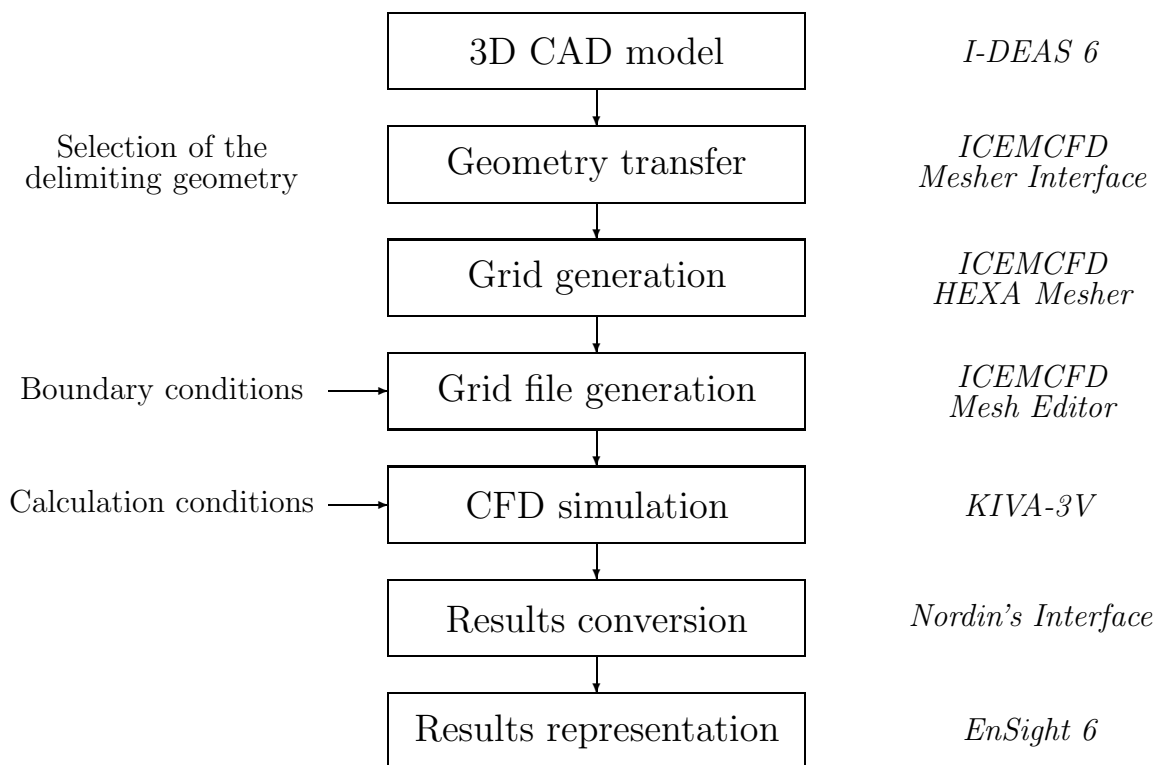


**Figure 3.1:** CFD simulation procedure.

*KIVA* is a computer program for numerical simulation of transient two- and three-dimensional chemically reactive fluid flows with sprays. The code is applicable to laminar and turbulent, subsonic and supersonic, single-phase or dispersed two phase flows. *KIVA* has been developed since the end of the seventies at the *Los Alamos National laboratory*, in the U.S.A., especially for the simulation of internal combustion engines. *KIVA* is a research program written in Fortran with access to the source code and available for a moderate fee. Since its first public release in 1985, new versions of the code have been made available: *KIVA-II* [45] in 1989, *KIVA-3* [46] in 1993, *KIVA-3V* [39] in 1997 and *KIVA-3V, release 2* [47] in 1999.

*KIVA-3V* solves through a time marching method the unsteady differential equations of motion of a turbulent chemically reactive mixture of ideal gases, coupled to a single-component vaporising fuel spray. The code allows the consideration of an arbitrary number of species and chemical reactions, only limited by the computer performance and its memory capacity. A stochastic particle method is used to calculate evaporating liquid sprays, including the effect of droplet collisions and aerodynamics breakup. A particle-based liquid wall film model is also implemented. The temporal difference scheme considered is mainly implicit, with explicit methods used only for resolving convection. The coupled implicit equations are solved by a method similar to the *SIMPLE* algorithm and the program uses either the partial-donor-cell differencing (faster) or the quasi-second-order upwind scheme (more accurate) for convection. *KIVA-3V* uses a block structure mesh with connectivity defined by indirect addressing, that allows the modelling of complex geometries without generating a large number of unactivated cells. The code permits also to model vertical and canted valves. The standard  $k-\epsilon$  and the renormalised group (RNG) theory  $k-\epsilon$  turbulence models are available

in addition to the modified KIVA sub-grid scale (SGS) model. Further, the program incorporates a mixing controlled turbulence combustion model.

Except the correction of the bugs reported by the *Los Alamos National Laboratory*, the source code was not modified for the present study. Most of the simulation was performed after the last correction and the modifications made have had no significant influence on the results presented here.

### 3.1.2 Mesh generation

For constructive reasons mentioned previously, the designed combustion prechamber is tilted and its nose is set off the main combustion chamber axis, thus forming a non-axisymmetrical whole (**figure 2.1**). A numerical simulation based on the real geometry would lead to a prohibitive computation time, mainly because of numerous small cells required for an adequate mesh resolution in the prechamber and in the nozzle orifices. The way to overcome the actual computer limits is to consider an axisymmetrical geometry and to simulate only a periodic sector including a single nozzle orifice. The principal drawback of this simplification is to neglect the influence of the asymmetry on the prechamber flow pattern. The change in numerical solution resulting from variations of the nozzle parameters should give some indication on the influence of the asymmetry.

The mesh generation is performed on the geometry of the combustion chamber when the piston is positioned at bottom dead centre. This operation requires the fulfilment of certain *KIVA* specific rules for the part of the mesh located in the squish region and undergoing an adjustment procedure (snapping) during the simulation. These rules specify that all the grid lines in the squish region must be vertical in the z-direction [45, page 94] and horizontal in the y-direction, around the periphery of the cylinder [46, page 32]. On the other hand, the radial grid lines do not need to be horizontal (x-direction). To satisfy these rules, the fixed cells commonly located in the piston bowl in conventional combustion chamber mesh have to be attached to the cylinder head, around the prechamber nose. According to the *KIVA* denomination, these cells as well as the one located in the prechamber and in the nozzle orifice must be defined as belonging to the dome in cylinder head.

The first operation of the *HEXA* mesh generation procedure consists of splitting the computational domain into distinct blocks. This important process is essential for the final mesh configuration. Apart from one particular case where an extra central orifice was added to the prechamber, the computational domain has been split into 14 individual blocks: 7 in the main combustion chamber, one in the nozzle orifice and 6 in the combustion prechamber (**figure 3.2**). The main objective of the numerical simulation was to study the flow in the prechamber during the compression stroke. This required a particular refinement of the corresponding part of the mesh to achieve an adequate resolution. On the other hand, the mesh in the main combustion chamber was kept relatively coarse to reduce the computing time. The final mesh resolution was chosen on the basis of a sensitivity analysis detailed in appendix B.1. This analysis shows that the mesh heterogeneity has no adverse consequence on the numerical solu-



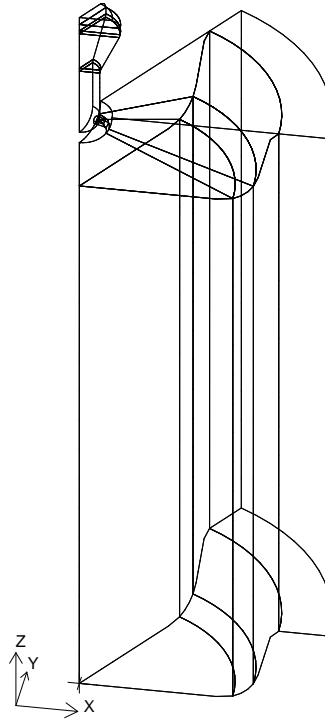


**Figure 3.2:** Blocking of the computational domain.

tion in the prechamber because of the strong filtering effect of the small nozzle orifice. The most frequently used mesh for a  $60^\circ$  sector is given in **figure 3.3** at two different crank angles. The total number of cells is 8'714, with 1'499 cells in the prechamber (including the nozzle orifice) and 7'215 cells in the main chamber. The mesh for a  $45^\circ$  (8 nozzle orifices) and for a  $90^\circ$  (4 nozzle orifices) were realised through a proportional decrease and respectively increase of the number of azimuthal cells. The prechamber volume representing only about 3 % of the compression volume, the cell density in the prechamber is far higher than in the main chamber. To enable different initial conditions in the main- and prechamber, two distinct fluid regions have been defined. The first encompass the main combustion chamber and the second the nozzle orifice and the prechamber.

### 3.1.3 Calculation conditions

The present section describes the general calculation conditions considered in the numerical simulation. These have been kept constant during the geometrical parametric study. The principal calculation and initial conditions are summarised in **table 3.1** and the corresponding *KIVA-3V* input file is given in appendix B.2.

The purpose of the numerical simulation is to study the influence of geometrical parameters on the flow field inside the prechamber during the compression stroke and particularly in the ignition window. Therefore, the simulation was limited to a non-reacting mixture of fuel, air and residual gas from the previous cycle. To reduce the number of species involved, the practical fuel, natural gas, was substituted by methane,

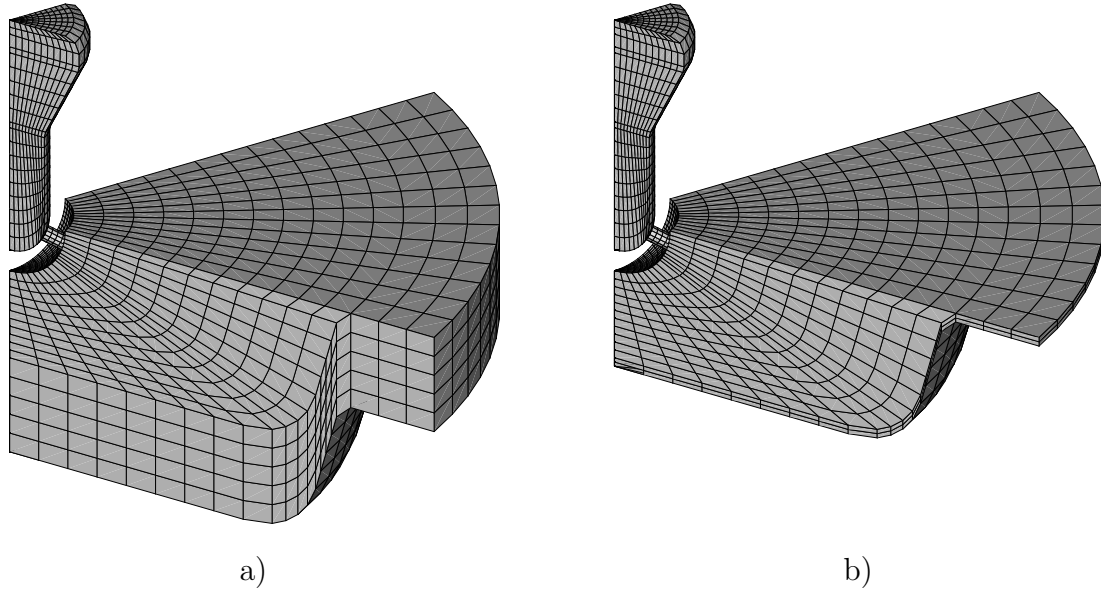


**Figure 3.3:** Mesh of the computational domain: a) at  $30\text{ }^{\circ}\text{C}_{ABTDC}$ , b) at TDC.

**Table 3.1:** Main calculation and initial conditions

	Main chamber	Prechamber
Region	1	2
$n$		1500 rpm
$T_{cyl. wall}$	180 °C	-
$T_{cyl. head}$	180 °C	180 °C
$T_{piston}$	280 °C	-
$p$		2.63 bar
$T$	105 °C	205 °C
$k$		12.6 m <sup>2</sup> /s <sup>2</sup>
$\phi$	0.565	0.000
$c_{CH_4}$	0.0287	0.0000
$c_{O_2}$	0.2123	0.0979
$c_{N_2}$	0.7431	0.7431
$c_{CO_2}$	0.0087	0.0874
$c_{H_2O}$	0.0072	0.0716

its main component. The residual gas was assumed to consist of the reaction products of the methane-air mixture after complete combustion. In consequence, the gas mixture considered in the simulation included five species which are  $\text{CH}_4$ ,  $\text{O}_2$ ,  $\text{N}_2$ ,  $\text{CO}_2$  and  $\text{H}_2\text{O}$ . The necessary thermo-chemical data was provided by the *JANAF* tables [48]. The main combustion chamber, forming the first fluid region, was filled with an unburnt mixture of methane and air, containing 10 % residual gas (typical value for a spark ignition engine with a relative large valve overlap, operating at full load [13]). The combustion prechamber and the nozzle orifice, forming the second fluid region, were filled exclusively with residual gas. The fuel to air equivalence ratio, the initial pressure and the initial temperature were derived from experimental results of the engine equipped with the conventional combustion chamber (same piston, direct ignition), operating at a power output of 150 kW and crankshaft rotational speed of 1500 rpm (requirement for power generation). These results correspond to the operating point characterised by the lowest  $\text{NO}_x$  emissions achieved. The pressure distribution at the beginning of the simulation (shortly after inlet valve closure) was considered uniform throughout the whole combustion chamber. The prechamber temperature was assumed 100 °C above the calculated main chamber value. This value was chosen on the basis of a sensitivity analysis presented in appendix B.1.

*KIVA-3V* does not allow the definition of different swirl conditions in the distinct fluid regions. On the other hand, due to the limited interface between the two chambers, the flow through the inlet port during the intake stroke does not generate a significant swirl motion in the prechamber. Further, the filtering effect of the small prechamber nozzle orifices strongly reduces the influence of the main chamber large scale flow on the overall prechamber flow. In consequence, the simulation was performed without initial swirl motion. The cylinder wall, cylinder head and piston temperatures were evaluated on the basis of experimental results in conventional lean burn operating mode. As a result of a sensitivity analysis detailed in appendix B.1, the renormalised group (RNG) theory  $k - \epsilon$  model was selected to simulate the flow turbulence. The initial turbulence kinetic energy was chosen equal to 50% of the value based on the mean piston speed ( $k_{S_p} = 0.5 S_p^2$ ). The boundary layer drag and the wall heat transfer were simulated by the *Law-of-the-wall* model. Finally, the numerical resolution was performed using the *Quasi-Second-Order-Upwind* scheme.

The simulated angular domain extends from  $130^\circ\text{CA}_{BTDC}$  to  $30^\circ\text{CA}_{ATDC}$  and the results were stored from  $90^\circ\text{CA}_{BTDC}$  to  $30^\circ\text{CA}_{ATDC}$ , every  $10^\circ\text{CA}$ . The maximum resolution time step was limited to 1 to  $2 \cdot 10^{-7}$  s. This relatively short time step is a result of the presence of some very small cells located in the prechamber, close to the nozzle orifice.

### 3.1.4 Computation performance

*KIVA-3V* has been implemented on a *Silicon Graphics (SGI) Origin 2000*, equipped with eighty 195 MHz *MIPS R10000* processors. The computation was performed sequentially on a single processor. The resolution rate was about 55 MFlops, leading to a total execution time of less than 30 CPU hours in most of the cases, but sometimes up to 80 CPU hours. This large execution time is due to the time step restriction imposed by the presence of some very small cells in the prechamber mesh.

*KIVA-3V* has been originally developed on *Cray* computers. In order to evaluate the performance on this type of vectorial platform, the code was implemented on a *Cray J90* and achieved a resolution rate of 46 MFlops, less than on the *SGI Origin 2000*. An attempt to utilise the automatic parallelisation option of the *SGI Fortran* compiler was made to speed up the program execution. The computation on two processors led to an increase of the resolution rate of about 30% ( $\approx 72$  MFlops). Further attempts to operate on 4 or more processors led to premature program interruption. The reason is associated with the indirect addressing used in the code, which is not suitable for parallel implementation based on loop decomposition. The execution on multiple processors requires a preliminary adaptation of the code. A way would be to solve every mesh block on a separate processor and to establish a communication procedure between the processors of neighbour blocks [49].

Due to the relatively low performance achieved with the original code in the simulation of a non-reacting flow, the modelling of the combustion process would require a preliminary modification of the code to benefit from the large capacity (up to GFlops) of recent supercomputers and avoid taking a prohibitive execution time. This was beyond the scope of the present study.

## 3.2 Results and comparison with the conventional combustion chamber

In order to enable the analysis and interpretation of the numerical simulation results, the flow field characteristics were represented in a cutting plane along the prechamber axis and through the centre of the nozzle orifice. The numerical flow field, originally established on the basis of a  $60^\circ$  sector mesh, is represented reflected about the prechamber axis to match the physical configuration and thus ease the comprehension. The flow field evolution is represented through successive frames at discrete crank angle values during the compression stroke. The global evolution of the first prechamber flow pattern, velocity magnitude, turbulence kinetic energy and fuel to air equivalence ratio during the second half of the compression stroke is represented in **figure 3.4** to **figure 3.6**. The lower scale limit of the fuel to air equivalence ratio was set to a value close to the practical flammability limit encountered in natural gas engine applications [16, 17, 19].

Shortly after inlet valve closure (simulation conditions), the unburnt fuel and air mixture contained in the main combustion chamber starts to flow into the prechamber filled with residual combustion gas from the previous engine cycle. The flow through the nozzle orifices accelerates and reaches a maximum velocity magnitude of about  $100\text{ m/s}$ , corresponding to a Reynolds number ( $Re$ ) of order  $10^5$ , between  $20$  and  $30^\circ CA_{BTDC}$  and then decelerates because of the piston motion slowing down (**figure 3.4**). The jets issuing from the nozzles converge to a single point where the flow is reoriented and guided along the prechamber axis by the lower prechamber part. The nozzle jets generate several annular recirculation zones (one per nozzle orifice), which perturb the flow along the lower part of the wall. The recirculation zones are only partly represented

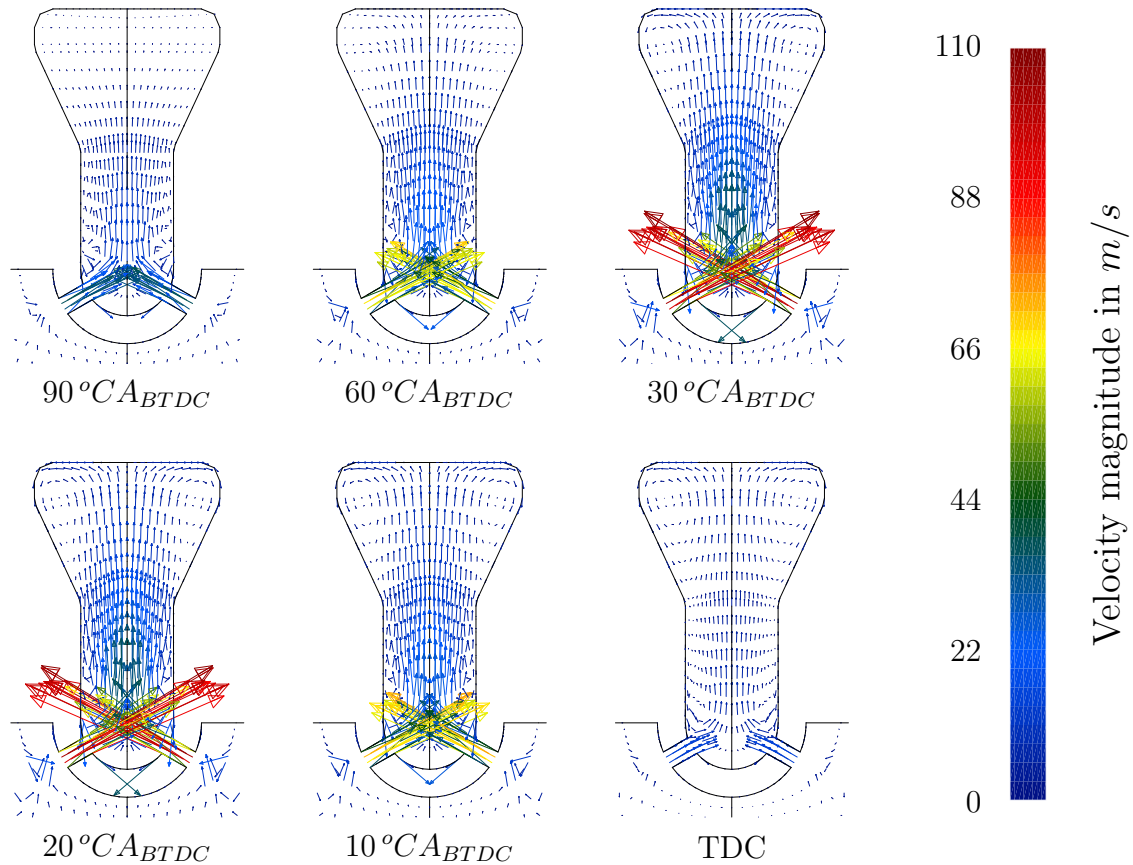


**Figure 3.4:** Evolution of the prechamber flow pattern and velocity magnitude during compression ( $V_p = 4540 \text{ mm}^3$ ,  $d_n = 2 \text{ mm}$ ,  $N_n = 6$ ,  $A_n = 18.85 \text{ mm}^2$ ,  $\alpha_n = 60^\circ$ ).

here because of the limited local mesh resolution. A further mesh refinement would be required to enable an adequate description of this kind of flow details but was out of the scope of this study. In the upper prechamber part, delimited by the location where the cross section starts to increase, the flow decelerates due to expansion. Because of the high cone angle and also of local instabilities, the flow detaches from the wall at the level of the cross section change and forms a large annular recirculation zone located at the outer skirt of the upper prechamber part. Due to the inertia forces, the flow inversion occurs only after the piston has reached TDC. The flow acceleration through the nozzle orifices generates locally a very strong turbulence which is entrained downstream (**figure 3.5**). An important turbulence is also generated upstream close to the nozzle inlet, on the main chamber side. Most of the turbulence dissipates through flow expansion in the upper prechamber part, as well as during deceleration after 30 to  $20^\circ\text{CA}_{BTDC}$ .

The unburnt fuel and air mixture flowing into the prechamber progressively replaces the residual gas which is compressed in the upper prechamber part (**figure 3.6**). The residual gas located at the bottom of the prechamber is very rapidly mixed with the jets of unburnt mixture by the local recirculation zones. Due to the high turbulence intensity, part of the unburnt mixture front diffuses into the residual gas, forming a thin flammable transitional region. The prechamber shape forces the residual gas into

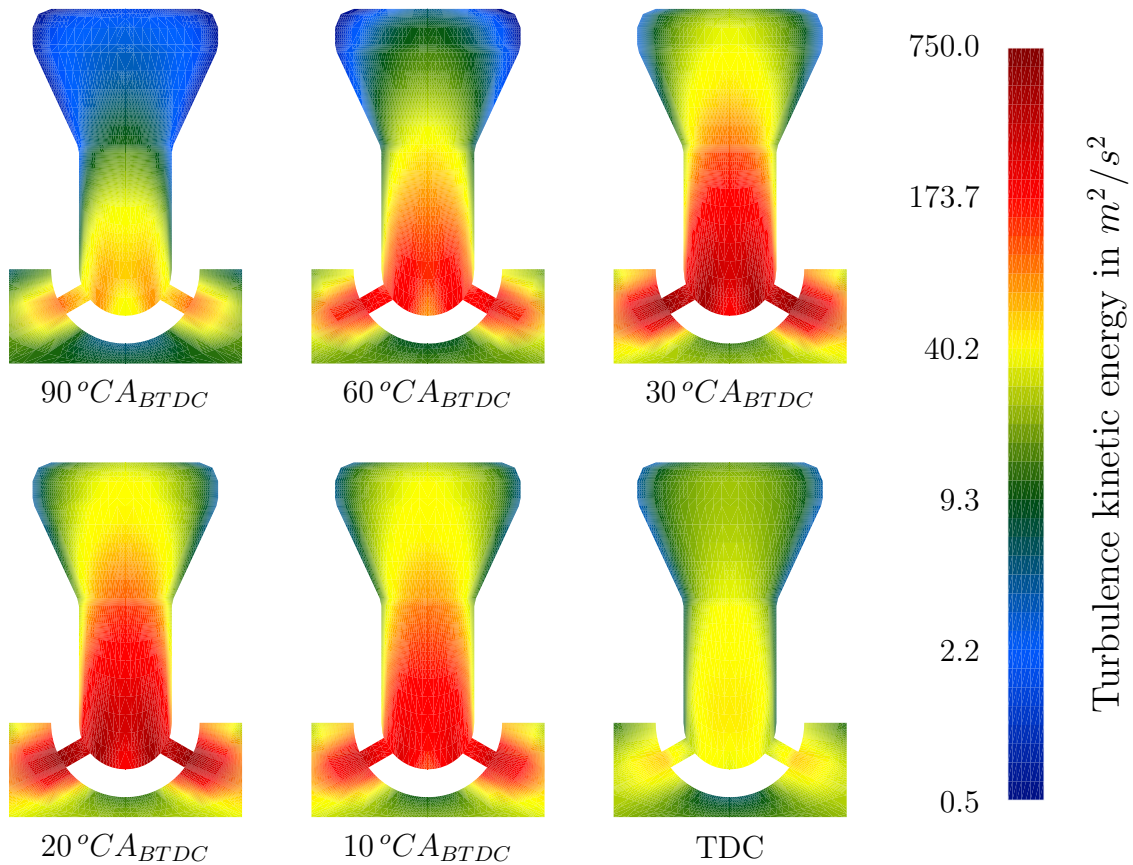


**Figure 3.5:** Evolution of the prechamber turbulence kinetic energy during compression ( $V_p = 4540 \text{ mm}^3$ ,  $d_n = 2 \text{ mm}$ ,  $N_n = 6$ ,  $A_n = 18.85 \text{ mm}^2$ ,  $\alpha_n = 60^\circ$ ).

the outer skirt of the upper part. When the head of the transitional region reaches the prechamber top, the unburnt mixture is entrained by the main recirculation zone and mixes with the residual gas. Simultaneously, part of the residual gas diffuses towards the prechamber axis into the incoming unburnt mixture. From this crank angle (about  $30^\circ CA_{BTDC}$ ), the fuel to air equivalence ratio in the vicinity of the spark plug location remains approximately constant, but is slightly lower than in the main combustion chamber. The recirculation zone progressively homogenises the mixture of residual gas, fuel and air, which reaches an overall practical flammability shortly before TDC. At this stage, the numerical simulation indicates that practical ignition conditions are achieved well before TDC, thus offering a large spark timing window. On the other hand, a late spark timing will increase the amount of energy available for main chamber ignition and promote a more complete combustion of the prechamber mixture. Moreover, a late spark timing will benefit from a higher mixture temperature, which will ease prechamber ignition and accelerate combustion.

In order to evaluate the effect of transferring the ignition location into a prechamber, the flow in the conventional combustion chamber equipped with the original piston with bathtub bowl (A) (**figure 2.3**) and alternatively with a high turbulence generating piston with re-entrant bowl (B) (**figure 4.3**) was simulated and compared to the numerical results of the first prechamber design. The simulation was based on  $60^\circ$

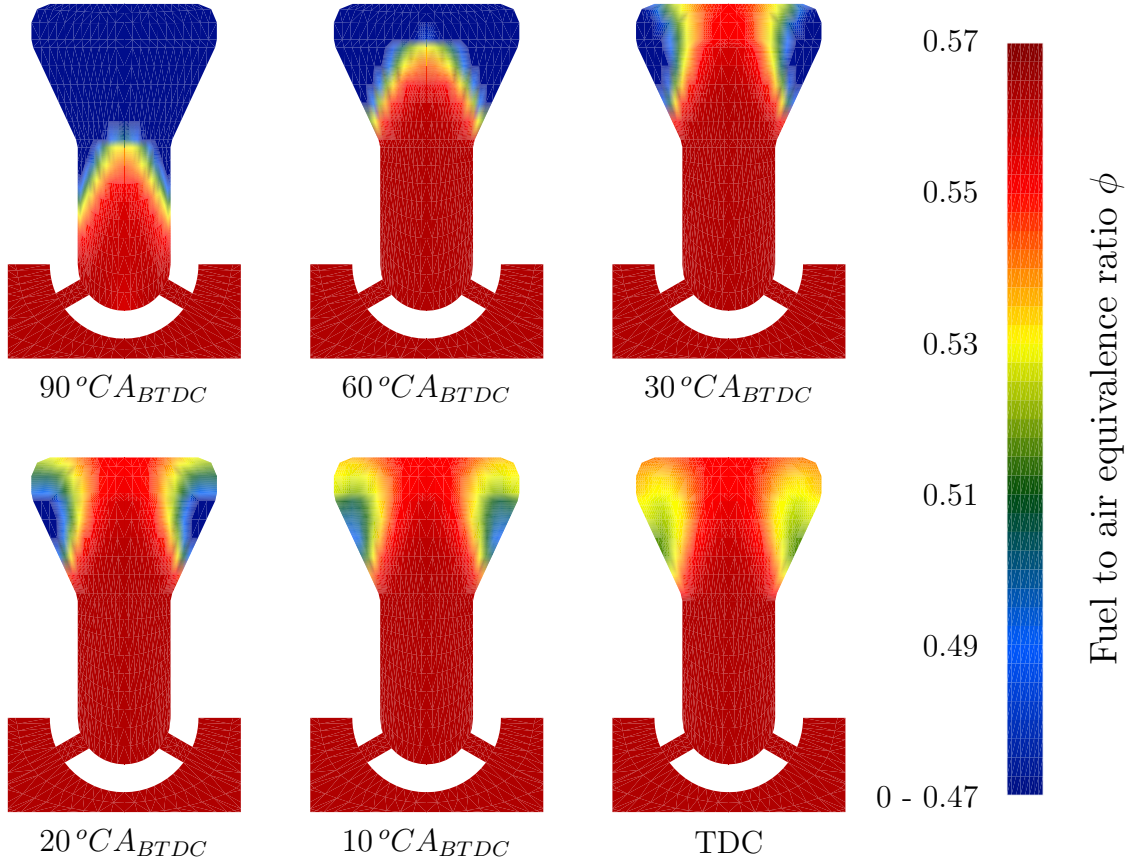


**Figure 3.6:** Evolution of the prechamber fuel to air equivalence ratio during compression ( $V_p = 4540 \text{ mm}^3$ ,  $d_n = 2 \text{ mm}$ ,  $N_n = 6$ ,  $A_n = 18.85 \text{ mm}^2$ ,  $\alpha_n = 60^\circ$ ).

sector mesh comprising 8164 cells in the case of piston *A* and 8736 cells in the case of piston *B*. The initial calculation conditions were identical to the prechamber case (table 3.1), except for the swirl ratio which was fixed at 2.0 (table 2.1). The computation time was less than one CPU hour in both cases. The flow characteristics at the location of the spark are represented for the different cases together in **figure 3.7**. The ignition window represents the angular domain in which prechamber spark timing is likely to occur. The actual optimal spark timing in the conventional combustion chamber is  $26.7^\circ \text{CA}_{BTDC}$ . This value represents the latest spark advance which achieves the lowest  $\text{NO}_x$  exhaust emissions while keeping a satisfactory engine cycle by cycle variability.

The flow velocity at the prechamber spark location increases during the compression stroke to reach its maximum value in the ignition window (**figure 3.7, a**). However, the velocity remains lower than in the conventional combustion chamber at the optimal spark timing (close to the left limit of the ignition window), independently of the piston used. The lower flow velocity prevents an excessive stretching of spark and of the initial flame kernel, thus reducing the probability of ignition failure. The high turbulence generated by the nozzle jets and diffusing in the prechamber reaches an intensity up to twice the value characterising the conventional combustion chamber at optimal spark timing (**figure 3.7, b**). The higher turbulence intensity promotes the combustion

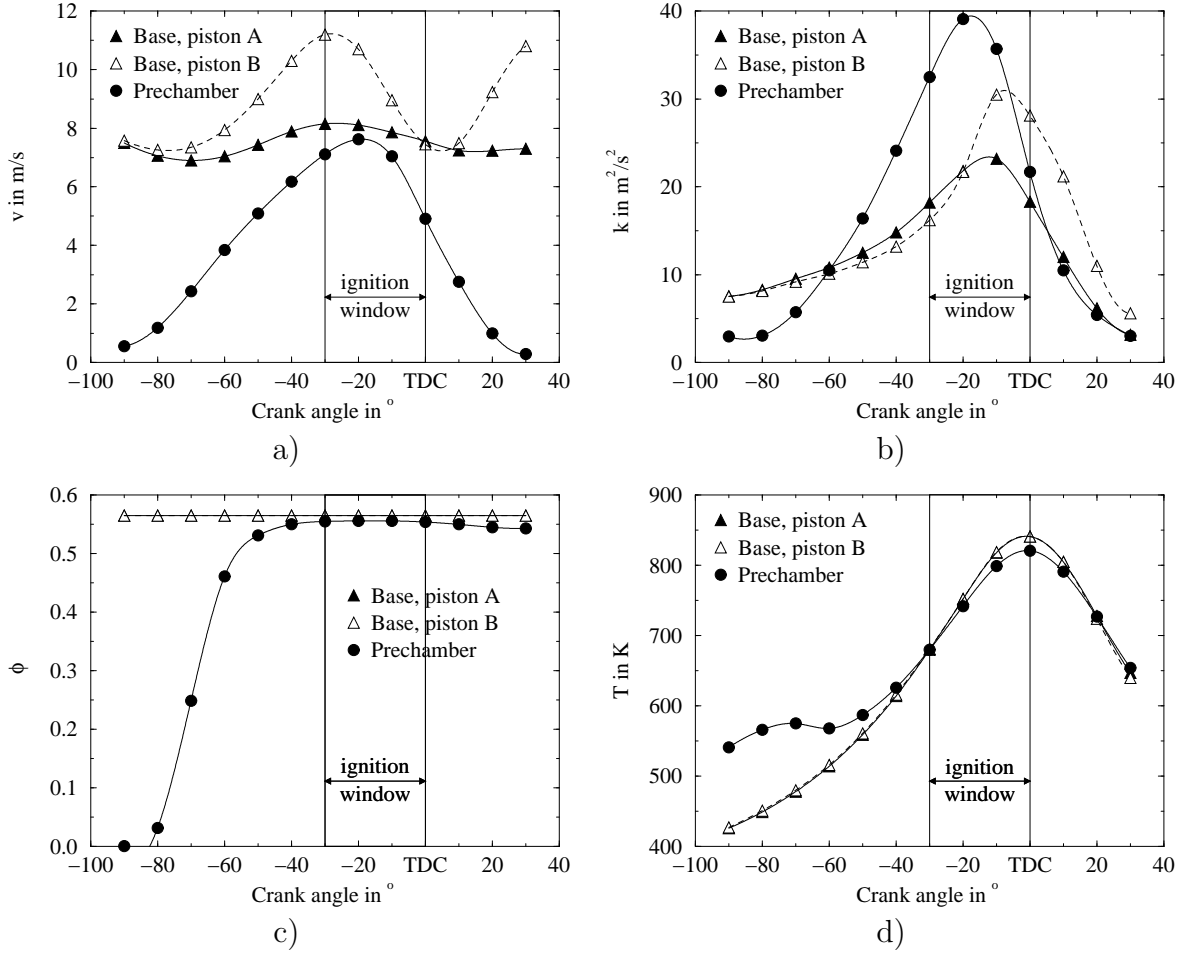


**Figure 3.7:** Comparison of the flow conditions at the location of the spark plug gap between conventional combustion chamber (base, pistons A and B) and prechamber ( $V_p = 4540 \text{ mm}^3$ ,  $d_n = 2 \text{ mm}$ ,  $N_n = 6$ ,  $A_n = 18.85 \text{ mm}^2$ ,  $\alpha_n = 60^\circ$ ): a) velocity magnitude, b) turbulence kinetic energy, c) fuel to air equivalence ratio, d) temperature.

process but also perturbs the ignition arc discharge phase and the initial flame kernel generation [50]. Through the progressive replacement of the residual gas by the fresh incoming mixture, the fuel to air equivalence ratio increases rapidly to reach an almost constant value in the ignition window (figure 3.7, c). Because of complementary dilution with residual gas, the maximum value is slightly lower than in the case of the conventional combustion chamber, thus closer to the lean flammability limit. The prechamber temperature remains at first relatively constant because of the mixing with cooler fresh incoming mixture and then increases due to compression. In comparison to the conventional combustion chamber, it reaches a somewhat lower maximum value at TDC. The difference in peak temperature originates in the stronger heat transfer to the prechamber resulting from the larger surface area and the higher turbulence intensity in comparison to the conventional combustion chamber. Depending on the complementary spark timing delay allowed by the use of a prechamber, the temperature at the time of ignition will be similar or higher than the one in the conventional combustion chamber. A higher temperature will promote ignition and accelerate the initial flame kernel growth.



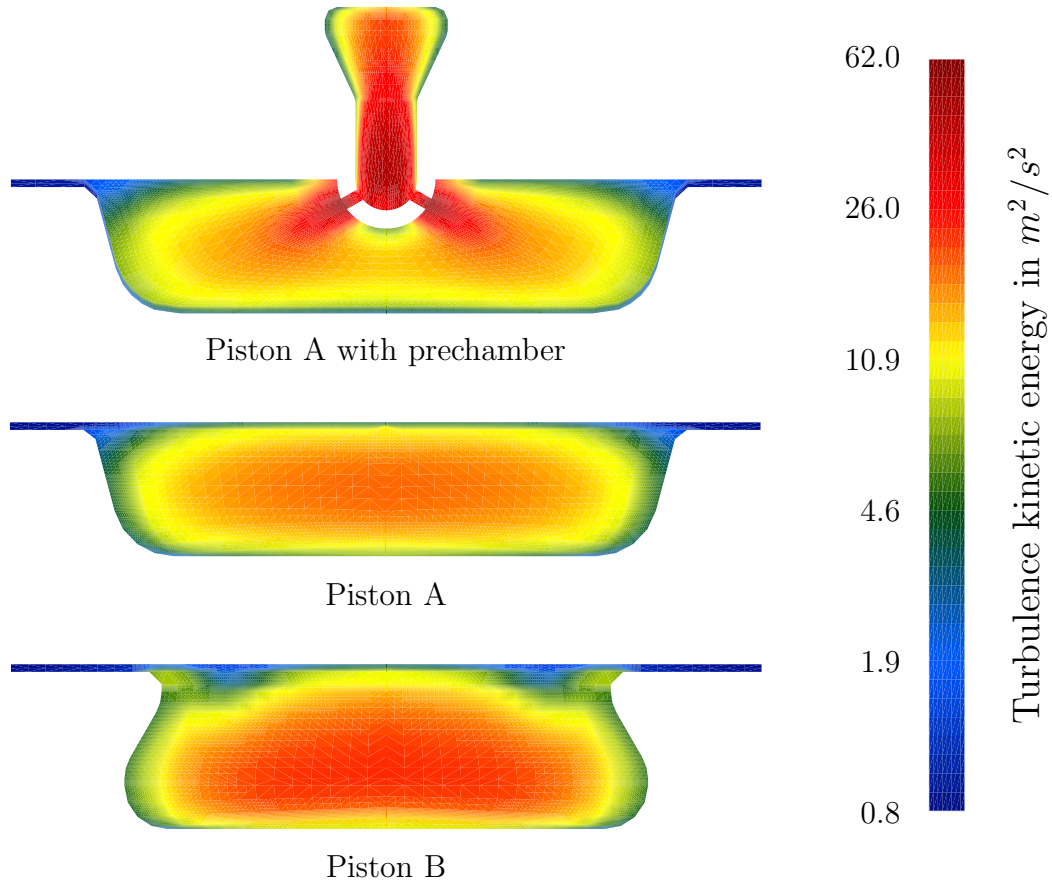


**Figure 3.8:** Distribution of the turbulence kinetic energy in the main combustion chamber at TDC; comparison with the conventional combustion chamber equipped with piston A and B and simulated without swirl.

In order to evaluate the influence of the prechamber on the main chamber flow during the compression stroke, the conventional combustion chamber equipped alternatively with the two different pistons (*A* and *B*) was simulated again, but this time without swirl to allow an objective comparison (the main chamber could not be simulated with swirl). The results are presented together at TDC in **figure 3.8**. During the compression stroke, the main chamber flow towards the nozzle orifices produces locally a very high turbulence, which decreases when the piston approaches TDC (**figures 3.5**). However, the residual level largely exceeds the overall turbulence intensity in the conventional combustion chamber and the difference is even more pronounced at an earlier crank angle. This additional turbulence should accelerate the early stage of the flame front propagation. However, the swirl motion raises the global level of turbulence in the conventional combustion chamber. Therefore, taking into account this parameter should somewhat reduce the gain in turbulence associated with the presence of the prechamber. The prechamber has only a weak influence on the main chamber flow pattern and velocity magnitude. Further, due to the somewhat lower volumetric compression ratio resulting from the slight increase in compression volume ( $\approx 3\%$ , corresponding to the prechamber volume), the presence of the prechamber also has a moderate effect on the main chamber temperature. Finally, the fuel to air equivalence ratio remains unchanged.

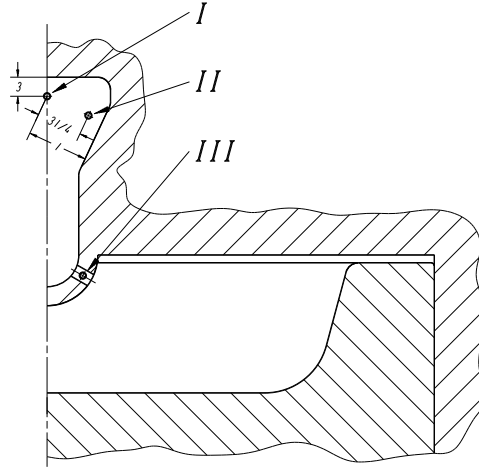


**Figure 3.9:** Reference locations in the combustion prechamber.

### 3.3 Parametric study

The objective of the parametric study was to evaluate the influence of geometrical changes on the prechamber flow during the compression stroke, and particularly on the ignition conditions. In order to analyse and interpret the influence of parametric variations, the numerical results at particular prechamber locations were plotted together. Three different positions in the plane of symmetry going through the centre of the nozzle orifice were taken into account (**figure 3.9**). The first location (I) corresponds to the position between the spark plug electrodes (*Bosch Super F6DC*). Even though the spark plug electrodes are not modelled, the flow characteristics at this particular location give an indication of the conditions that prevail during the ignition process and the early stage of the flame kernel growth. The second position (II) has been chosen at three quarter of the distance separating the ignition point (I) and the nearest lateral wall. This point is located close to the middle of the main prechamber recirculation zone and is consequently a sensitive indicator of changes in the main flow pattern. The third point (III) is located in the middle of the nozzle orifice and gives information on the flow conditions at this particular position. The calculation conditions were unchanged during all the parametric study. Only the geometrical parameter indicated in each section was changed, and the simulation results are compared with the base prechamber one.

#### 3.3.1 Nozzle orifice cross sectional area

The total nozzle orifice cross sectional area of the base prechamber design ( $18.85 \text{ mm}^2$ ) was decreased and then increased by 50 %, alternatively. The orifice diameter was consequently reduced to  $1.41 \text{ mm}$  ( $A_n = 9.42 \text{ mm}^2$ ) and increased to  $2.45 \text{ mm}$  ( $A_n = 28.27 \text{ mm}^2$ ), respectively. The mesh was adjusted to accommodate the variation of orifice diameter, without change in the number of cells.

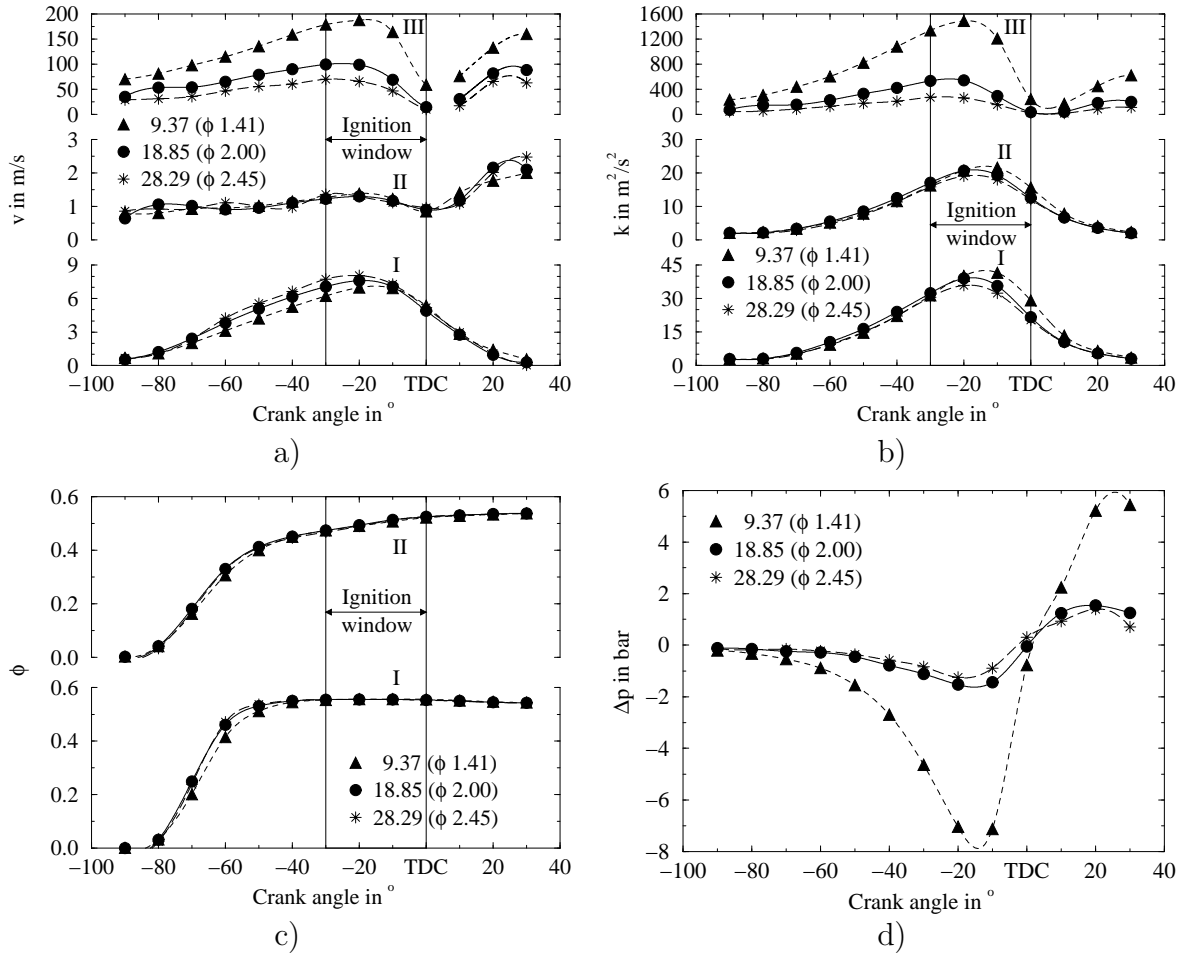


**Figure 3.10:** Influence of the total cross sectional area of the nozzle orifices on the flow at different locations in the prechamber ( $V_p = 4540 \text{ mm}^3$ ,  $N_n = 6$ ,  $\alpha_n = 60^\circ$ ): a) velocity magnitude, b) turbulence kinetic energy, c) fuel to air equivalence ratio, d) pressure difference between pre- and main chamber.

The increase of total cross sectional area yields a strong reduction of nozzle flow velocity (**figure 3.10, a**) and consequently leads to a drastic decrease of turbulence generation (**figure 3.10, b**). This causes a significant reduction of turbulence intensity in the upper prechamber part (I and II). The increase of total cross sectional area strongly reduces the pressure drop between main- and prechamber (**figure 3.10, d**). This yields an increase of incoming mass flow, which results in a somewhat higher velocity at the ignition location (I). The relative stability of the velocity in the main recirculation zone (II) indicates no significant variation of the main flow pattern. The increase of axial velocity accelerates the transfer of unburnt mixture at the prechamber top, but has no noticeable effect on the fuel to air equivalence ratio in the ignition window (**figure 3.10, c**). Finally, due to the reduction of pressure drop, the increase of total cross sectional area enables a more extensive prechamber filling. However, a larger amount of unburnt mixture will also be expelled again in the main chamber prior to completion of the prechamber combustion. Thus, the eventual benefit of larger orifices in this regard will essentially depend on the prechamber combustion characteristics and therefore cannot be evaluated here.

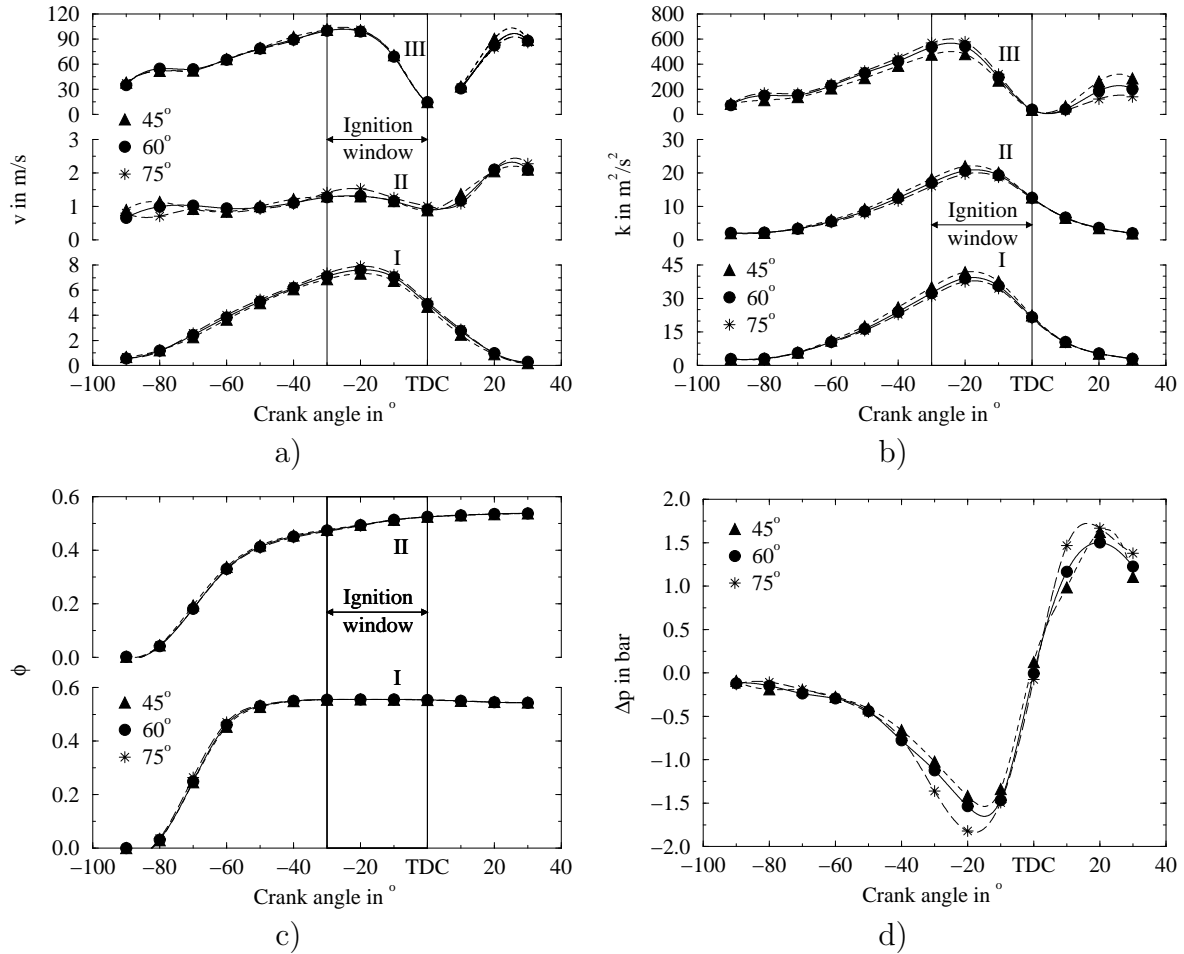


**Figure 3.11:** Influence of the nozzle orifice orientation on the flow at different locations in the prechamber ( $V_p = 4540 \text{ mm}^3$ ,  $d_n = 2 \text{ mm}$ ,  $N_n = 6$ ,  $A_n = 18.85 \text{ mm}^2$ ): a) velocity magnitude, b) turbulence kinetic energy, c) fuel to air equivalence ratio, d) pressure difference between pre- and main chamber.

### 3.3.2 Orientation of the nozzle orifices

In the base prechamber design (**figure 2.3**), the orientation of each nozzle orifice from the prechamber axis (smallest angle between the orifice and prechamber axes, when both are in the same plane) was determined in order to point towards the bottom corner of the piston bowl, when the piston is located at TDC. The objective was to achieve a relatively uniform distribution of the jets of combustion products issuing from the prechamber into the clearance volume. The angle is different for each orifice and the average value is about  $60^\circ$ . This value was considered for the simulation of the base prechamber. Due to its significant influence on the main chamber combustion process and therefore on the engine performance and exhaust emissions [15, 22], the nozzle orifice orientation was varied by  $\pm 15^\circ$  from the base value of  $60^\circ$ . The mesh was adjusted consequently, while keeping the number of cells constant.

A larger orientation angle causes a greater local reorientation of the main chamber flow towards the nozzle orifices, which produces more turbulence (**figure 3.11, b**).

This does not affect the velocity magnitude in the nozzle orifices (III) (**figure 3.11, a**), but significantly increases the pressure drop between main chamber and prechamber (**figure 3.11, d**). On the one hand, the increase of the orientation angle increases the proportion of turbulence dissipated in the recirculation volume located at the prechamber bottom and consequently reduces the turbulence intensity in the upper part. This effect is more pronounced for the transition from  $45^\circ$  to  $60^\circ$  than further to  $75^\circ$ . On the other hand, it increases the size of the annular recirculation zone at the nozzle exits and thereby reduces the effective flow cross section in the prechamber lower part. This causes an increase in axial velocity that is partly compensated by the mass flow reduction associated with the increase in pressure drop. This finally results in a slight velocity increase at the ignition point (I), but does not significantly affect the main flow pattern (II). A somewhat higher prechamber axial velocity compensates the reduction in mass flow and enables a similar transfer of unburnt mixture to the ignition region (**figure 3.11, c**).

### 3.3.3 Prechamber swirl

Imparting a swirling motion to the combustion chamber charge accelerates considerably the combustion process through an extension of the flame surface [13]. The swirl motion is commonly generated by the flow through the intake port(s) and valve(s). In the case of an engine with prechambers, part of the swirl motion can also be produced by the jet of combustion products emerging from suitably oriented nozzle orifices. During the compression stroke, this particular nozzle configuration also produces a swirl motion in the prechamber. In order to evaluate its effect on the flow characteristics, the nozzle orifices were rotated by an angle of  $15^\circ$  about an axis parallel to the prechamber one and passing through the orifice centre of gravity; this corresponds to an azimuthal inclination. Consequently, the nozzle orifices are no longer converging to a single point in the prechamber bottom. The mesh was adjusted to the new configuration, while the number of cells was kept constant.

The comparison with the base prechamber shows a fundamental change in the flow pattern (**figure 3.12**). The inclination of the orifices induces a strong swirling motion in the prechamber characterised by a high radial velocity, particularly in the lower part. The centrifugal forces generated entrains a shift of the main prechamber axial flow component from the axis to the wall. This results in a flow inversion of the principal recirculation zone located at the prechamber top skirt and its extension down into the lower part, while leaving an almost stagnant zone along the axis of the upper part. This change in flow pattern consequently reduces the quantity of turbulence transferred to the prechamber top centre (**figure 3.13**). The residual gas are compressed in the centre of the upper part and progressively incorporated into the unburnt mixture (**figure 3.14**). This results in a very low fuel concentration in the region where ignition should occur. The flow characteristics in the nozzle orifices (III) are not significantly affected by their inclination (**figure 3.15, a and b**). Due to its position on the prechamber axis, the flow at the ignition point becomes almost stagnant when approaching TDC. The corresponding turbulence kinetic energy increases progressively towards the end of the compression stroke. However, the level reached in the major part of the ignition

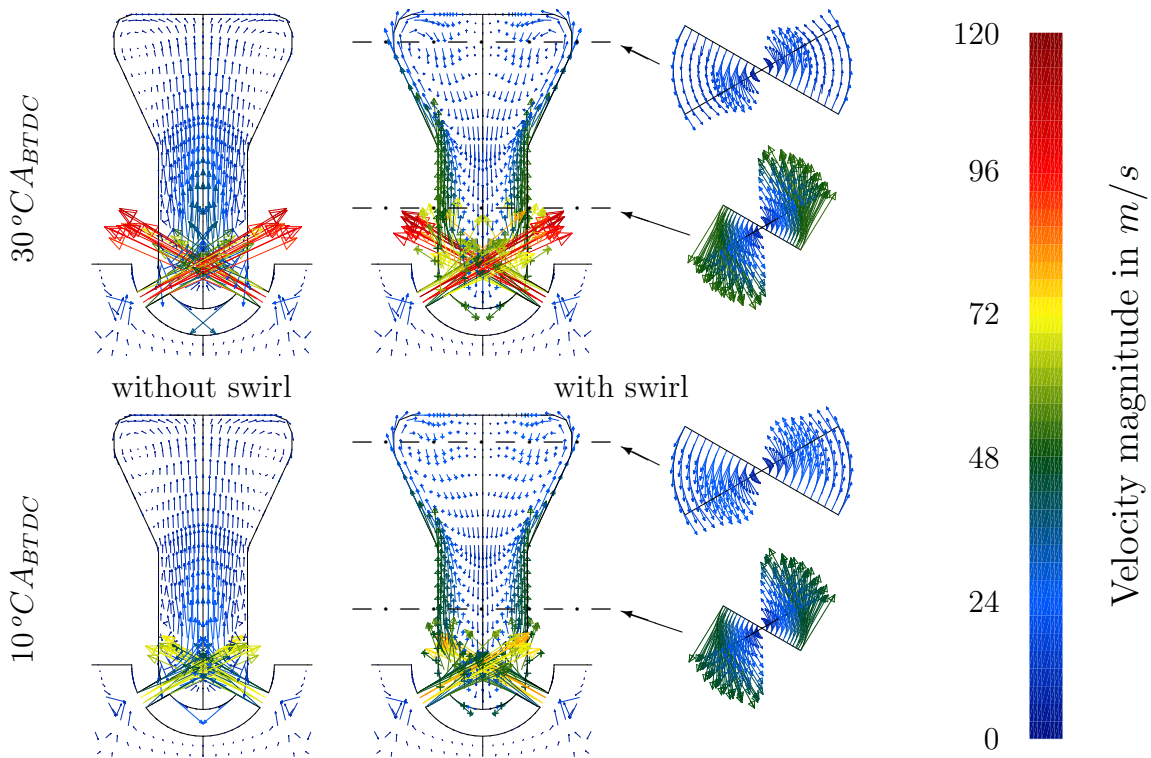


**Figure 3.12:** Effect of a prechamber swirl motion generated by a  $15^\circ$  azimuthal inclination of the nozzle orifices on the flow pattern and velocity magnitude in the prechamber ( $V_p = 4540 \text{ mm}^3$ ,  $d_n = 2 \text{ mm}$ ,  $N_n = 6$ ,  $A_n = 18.85 \text{ mm}^2$ ,  $\alpha_n = 60^\circ$ ).

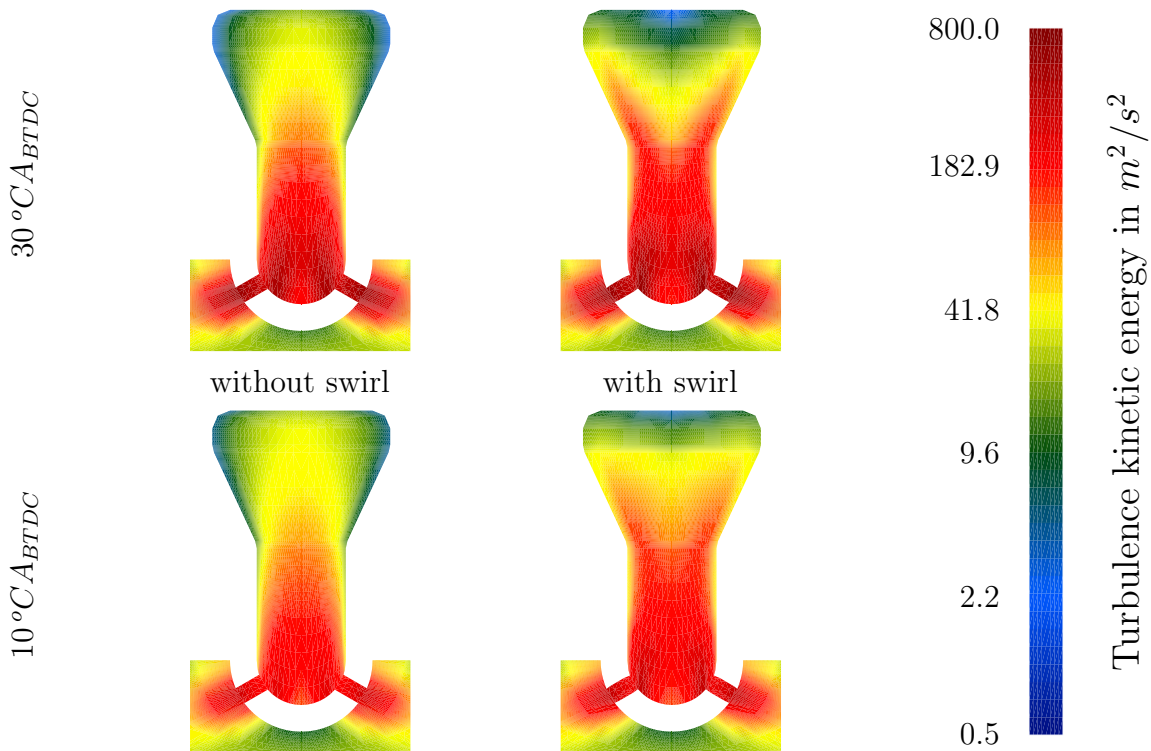


**Figure 3.13:** Effect of a prechamber swirl motion generated by a  $15^\circ$  azimuthal inclination of the nozzle orifices on the distribution of turbulence kinetic energy in the prechamber ( $V_p = 4540 \text{ mm}^3$ ,  $d_n = 2 \text{ mm}$ ,  $N_n = 6$ ,  $A_n = 18.85 \text{ mm}^2$ ,  $\alpha_n = 60^\circ$ ).

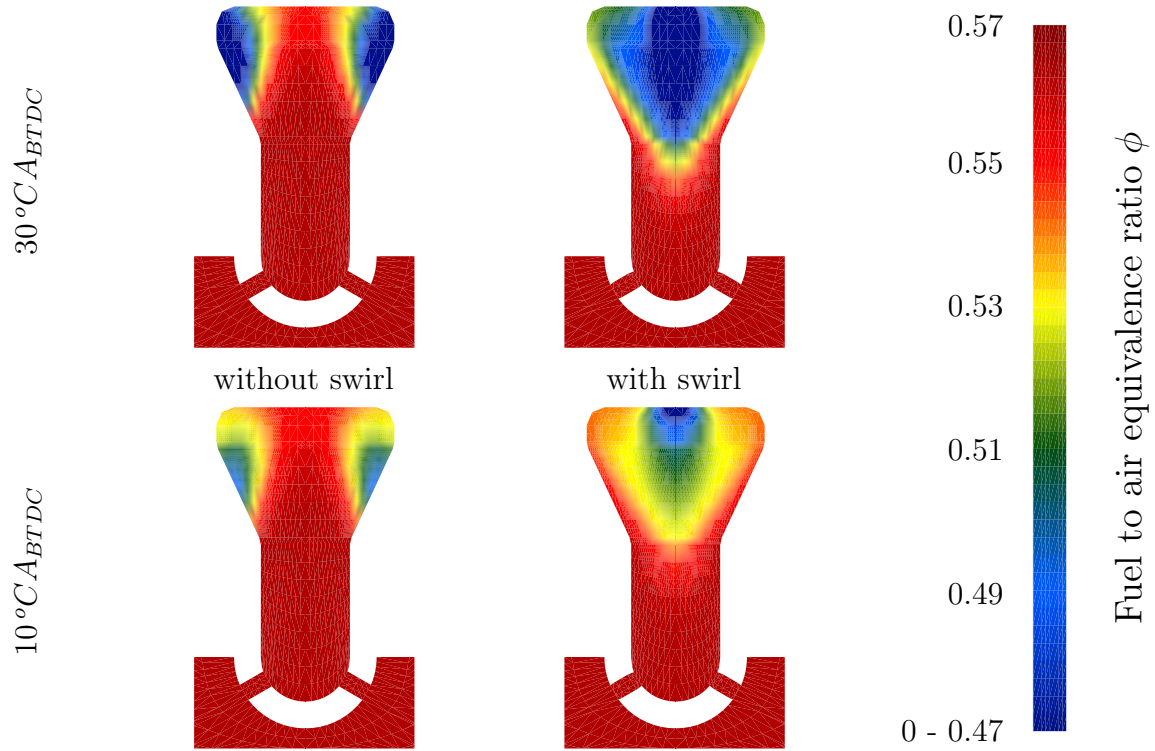


**Figure 3.14:** Effect of a prechamber swirl motion generated by a  $15^\circ$  azimuthal inclination of the nozzle orifices on the distribution of fuel to air equivalence ratio in the prechamber ( $V_p = 4540 \text{ mm}^3$ ,  $d_n = 2 \text{ mm}$ ,  $N_n = 6$ ,  $A_n = 18.85 \text{ mm}^2$ ,  $\alpha_n = 60^\circ$ ).

window is much lower than in the case of the base prechamber. The compression and stagnation of the residual gas at the prechamber top centre results in a much lower fuel to air equivalence ratio at the ignition point (**figure 3.15, c**), which may be beyond the lean flammability limit. The generation of the swirl motion causes an increase in main flow kinetic energy which is compensated by a decrease of prechamber pressure (energy conservation). This is illustrated by the increase of the pressure drop between main- and prechamber (**figure 3.15, d**).

### 3.3.4 Number of nozzle orifices

Starting from the base prechamber design, the number of nozzle orifices was reduced from 6 to 4 and increased to 8, respectively. In order to maintain similar flow conditions between main- and prechamber, the total nozzle orifice cross sectional area was kept constant ( $18.85 \text{ mm}^2$ ) through adaptation of the orifice diameter. This resulted in 4 orifices of  $\phi 2.45 \text{ mm}$  and in 8 orifices of  $\phi 1.73 \text{ mm}$ . The angle of the sector mesh was increased to  $90^\circ$  in the case of 4 orifices and reduced to  $45^\circ$  in the case of 8 orifices. The mesh resolution was kept approximately constant through a proportional adjustment of the number of azimuthal cells; 7604 and 11352 cells for  $45^\circ$  and  $90^\circ$ , respectively.

An increase in the number of nozzle orifices multiplies the sources of turbulence generation. This results in a higher turbulence intensity in the upper prechamber part

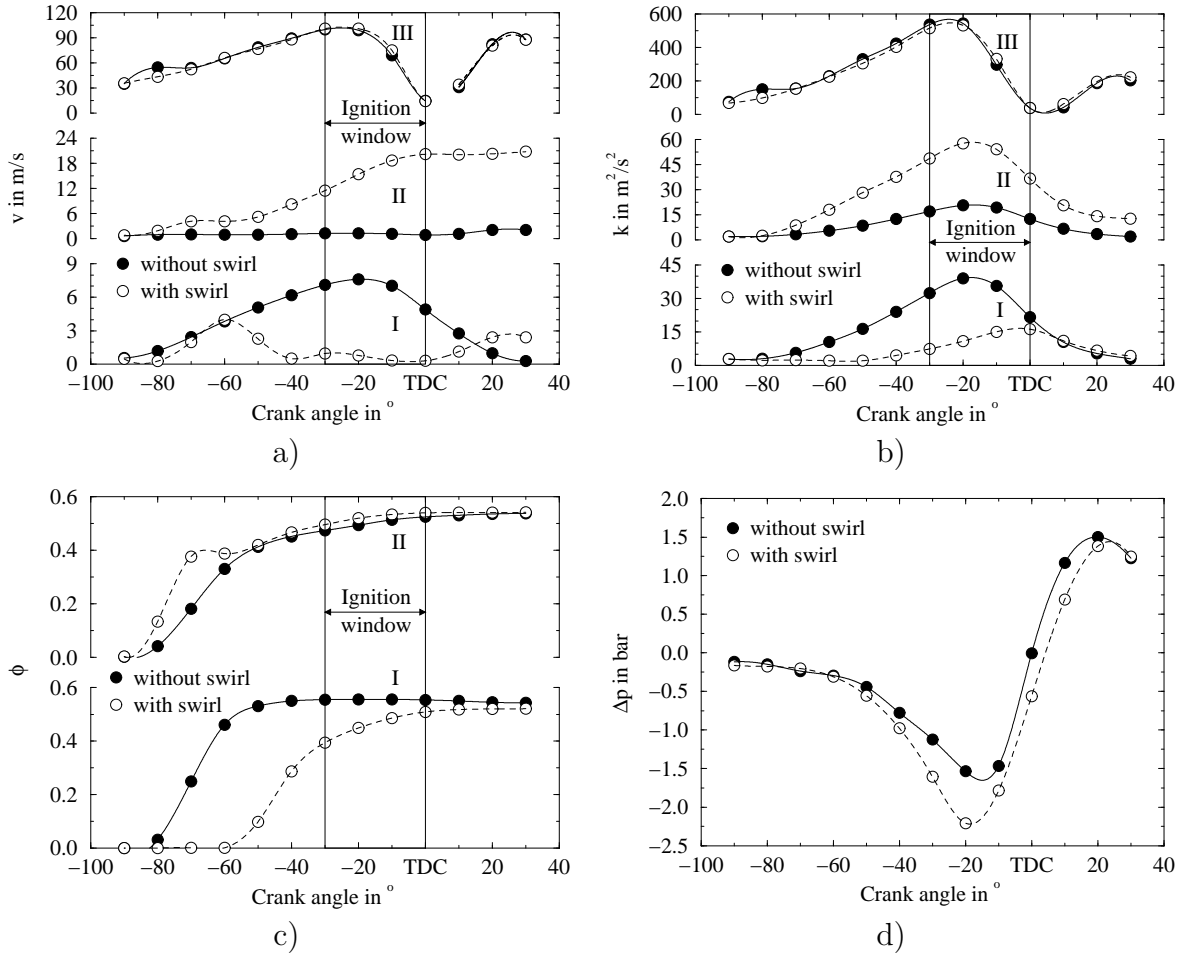


**Figure 3.15:** Effect of a prechamber swirl motion generated by a  $15^\circ$  azimuthal inclination of the nozzle orifices on the flow at different locations in the prechamber ( $V_p = 4540 \text{ mm}^3$ ,  $d_n = 2 \text{ mm}$ ,  $N_n = 6$ ,  $A_n = 18.85 \text{ mm}^2$ ,  $\alpha_n = 60^\circ$ ): a) velocity magnitude, b) turbulence kinetic energy, c) fuel to air equivalence ratio, d) pressure difference between pre- and main chamber.

and particularly in the vicinity of the ignition point (I) (**figure 3.16, a**). The effect is more pronounced in the case of a transition from 4 to 6 orifices than further to 8. The multiplication of the orifices also increases the proportion of the flow in the lower prechamber part that is perturbed by the annular recirculation zones at the nozzle exits. This consequently reduces the effective local flow cross section and results in an increase in axial velocity, which affects the conditions at the ignition point (**figure 3.16, b**). However, the weak velocity variation in the main recirculation zone (II) indicates no significant change in the flow pattern. Due to the higher axial velocity, the unburnt mixture reaches the prechamber top earlier (**figure 3.16, c**). Nevertheless, this has no perceptible influence on the fuel to air equivalence ratio in the ignition window. The adjustment of the orifice diameter in order to keep the total cross sectional area constant results in the same nozzle flow characteristics (III) and almost identical pressure drop between main- and prechamber (**figure 3.16, d**). This last point corroborates that the established influence principally originates in the variation of the number of orifices.



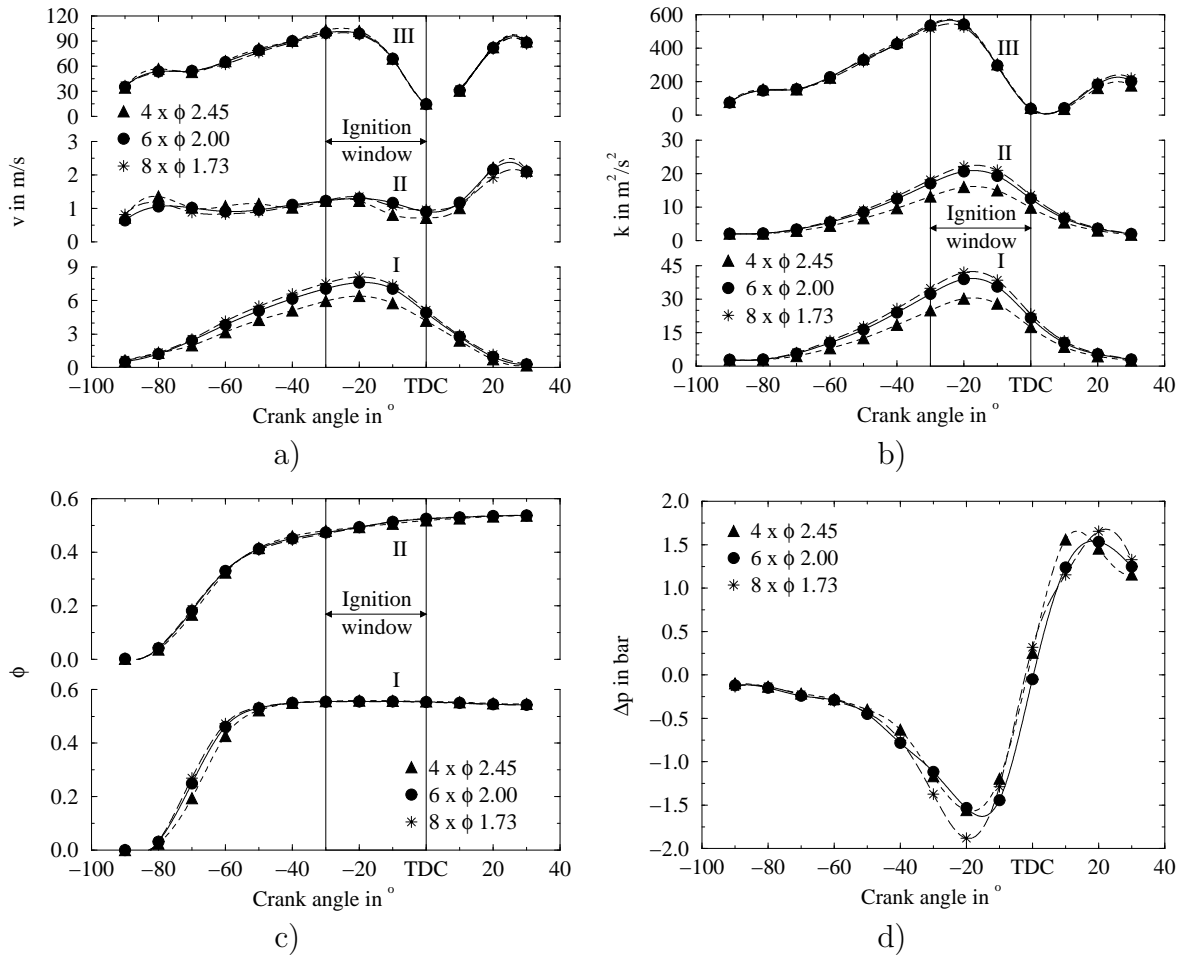


**Figure 3.16:** Influence of the number of nozzle orifices at different locations in the prechamber ( $V_p = 4540 \text{ mm}^3$ ,  $A_n = 18.85 \text{ mm}^2$ ,  $\alpha_n = 60^\circ$ ): a) velocity magnitude, b) turbulence kinetic energy, c) fuel to air equivalence ratio, d) pressure difference between pre- and main chamber.

### 3.3.5 Addition of coaxial nozzle orifice

A more uniform distribution of the jets of combustion products issuing from the prechamber into the main chamber can be realised through the addition of a complementary nozzle orifice located coaxially at the prechamber bottom. In order to maintain the total nozzle orifice cross sectional area constant and equal to the value of the base prechamber ( $18.85 \text{ mm}^2$ ), the orifice diameter was reduced from 2 to 1.85 mm. The mesh was modified to integrate the complementary orifice. The presence of the coaxial nozzle creates a direct connectivity between the main- and prechamber mesh blocks in such a way that their respective number of azimuthal cells can no longer be set independently. In order to keep the prechamber mesh resolution as close as possible to the base case, its azimuthal cells distribution was also applied to the main chamber. This results in a reduction of the total number of cells from 8714 to 5769.

In comparison to the base configuration, the presence of a coaxial orifice adds a new annular recirculation zone to the flow. However, this reduces strongly the size

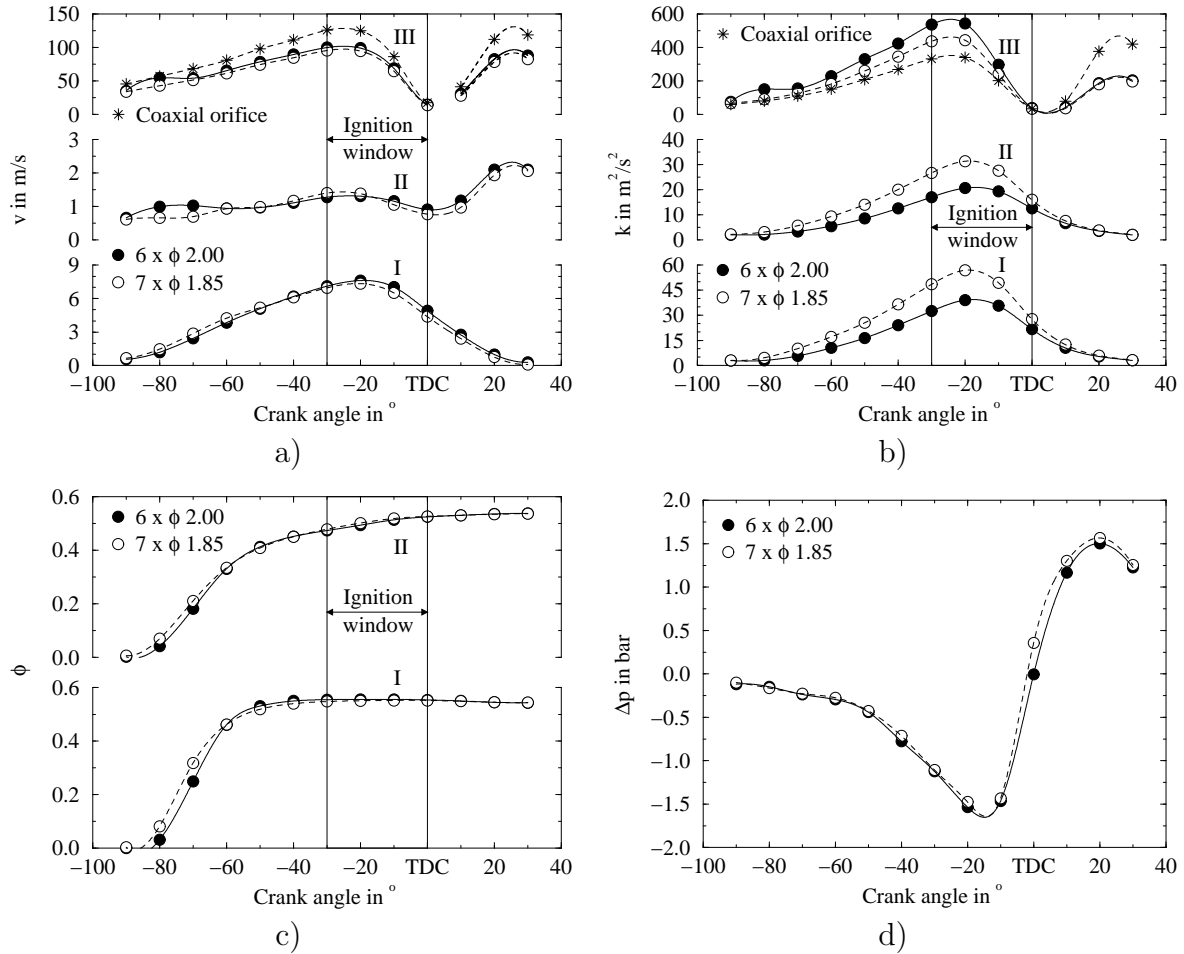


**Figure 3.17:** Effect of a coaxial nozzle orifice on the flow at different locations in the prechamber ( $V_p = 4540 \text{ mm}^3$ ,  $A_n = 18.85 \text{ mm}^2$ ,  $\alpha_n = 60^\circ$ ): a) velocity magnitude, b) turbulence kinetic energy, c) fuel to air equivalence ratio, d) pressure difference between pre- and main chamber.

of the bottom recirculation volume and consequently the local dissipation of turbulence. The better coaxial orifice alignment to the main chamber flow results in a higher nozzle velocity (**figure 3.17, a**), but also strongly reduces the turbulence generated upstream of the orifice inlet (**figure 3.18**). Despite a higher nozzle velocity, the much lower turbulence kinetic energy in the coaxial orifice compared to the tilted one (**figure 3.17, b**) indicates that the major part of the turbulence is generated upstream in the main chamber region close to the orifice inlet. Compared to the base case, the decrease of turbulence kinetic energy in the tilted orifices originates partly in the somewhat lower local velocity and mainly in the consequent reduction of turbulence generation upstream of the orifice inlet. The overall lower turbulence generation is largely over-compensated by the reduction of dissipation in the prechamber bottom and leads to a much higher turbulence intensity in the upper prechamber part. On the other hand, the global prechamber flow pattern and velocity magnitude in the upper prechamber part are only slightly affected. A somewhat higher axial velocity in the lower prechamber part accelerates the transfer of unburnt mixture towards the ignition region (**figure 3.17, c**). The more intense local turbulence also enhances

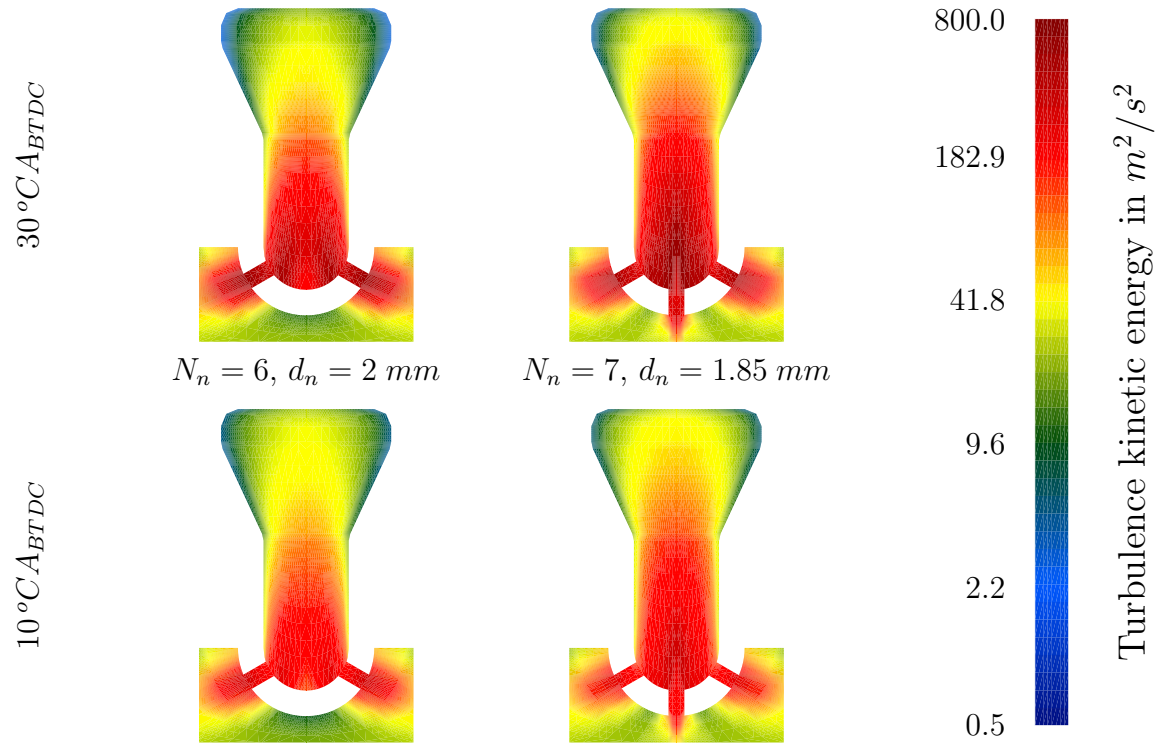


**Figure 3.18:** Effect of a coaxial orifice on the distribution of turbulence kinetic energy in the prechamber ( $V_p = 4540\text{ mm}^3$ ,  $A_n = 18.85\text{ mm}^2$ ,  $\alpha_n = 60^\circ$ ).

the incorporation of residual gas into the unburnt mixture, which results in a slightly lower maximum fuel to air equivalence ratio in the ignition window. The very similar global pressure drop between main- and prechamber during compression indicates an approximately similar prechamber filling (**figure 3.17, d**).

### 3.3.6 Prechamber bottom geometry

During the compression stroke, the jets emerging into the base prechamber interact with the bottom geometry (geometry of the lowest part of the prechamber internal volume) to form annular recirculation zones. This type of flow induces losses which are detrimental to a rapid transfer of the fresh mixture to the ignition location and an efficient filling of the prechamber. In consequence, the base prechamber geometry ( $\alpha$ ) was modified in a first stage to suppress the bottom recirculation volume (**figure 3.20,  $\beta$** ). In a second stage, the bottom geometry was further modified to better lead the flow towards the prechamber top ( $\gamma$ ). The mesh was adjusted to the geometry variations, without change in the number of cells. The only secondary consequence is a small reduction in prechamber volume, which is however limited to less than 2 %.

A better leading of the incoming flow increases strongly the axial velocity in the lower prechamber part, but does not affect significantly the global flow pattern (**figure 3.19**). The higher axial velocity originates in larger nozzle outlet recirculation zones, which consequently reduces the effective flow cross section. The suppression

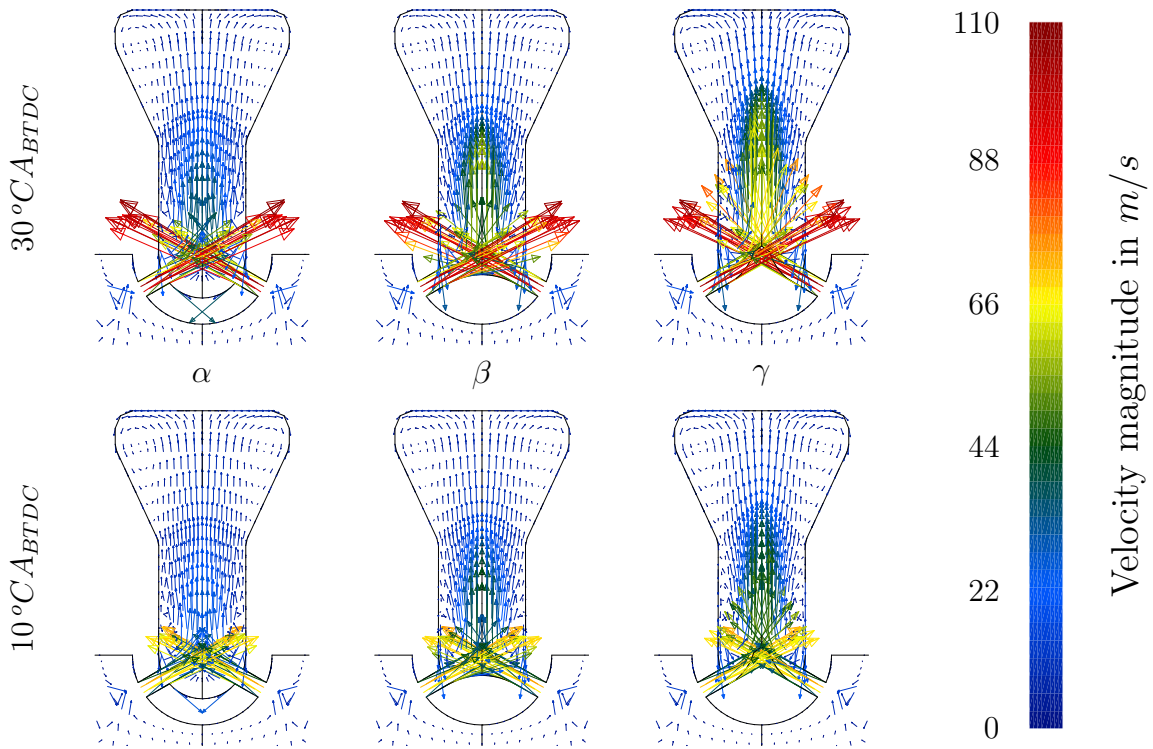


**Figure 3.19:** Influence of the prechamber bottom geometry on the flow pattern and velocity magnitude in the prechamber ( $V_p = 4540 \text{ mm}^3$ ,  $d_n = 2 \text{ mm}$ ,  $N_n = 6$ ,  $A_n = 18.85 \text{ mm}^2$ ,  $\alpha_n = 60^\circ$ ).

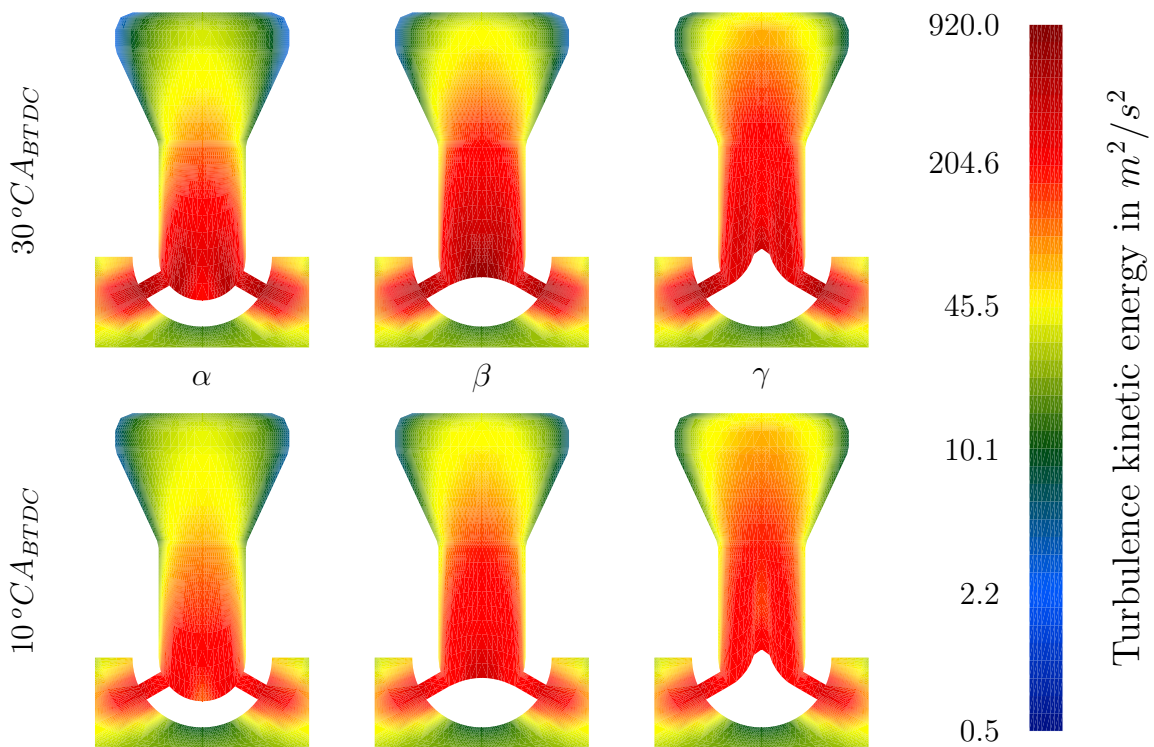


**Figure 3.20:** Influence of the prechamber bottom geometry on the distribution of turbulence kinetic energy in the prechamber ( $V_p = 4540 \text{ mm}^3$ ,  $d_n = 2 \text{ mm}$ ,  $N_n = 6$ ,  $A_n = 18.85 \text{ mm}^2$ ,  $\alpha_n = 60^\circ$ ).

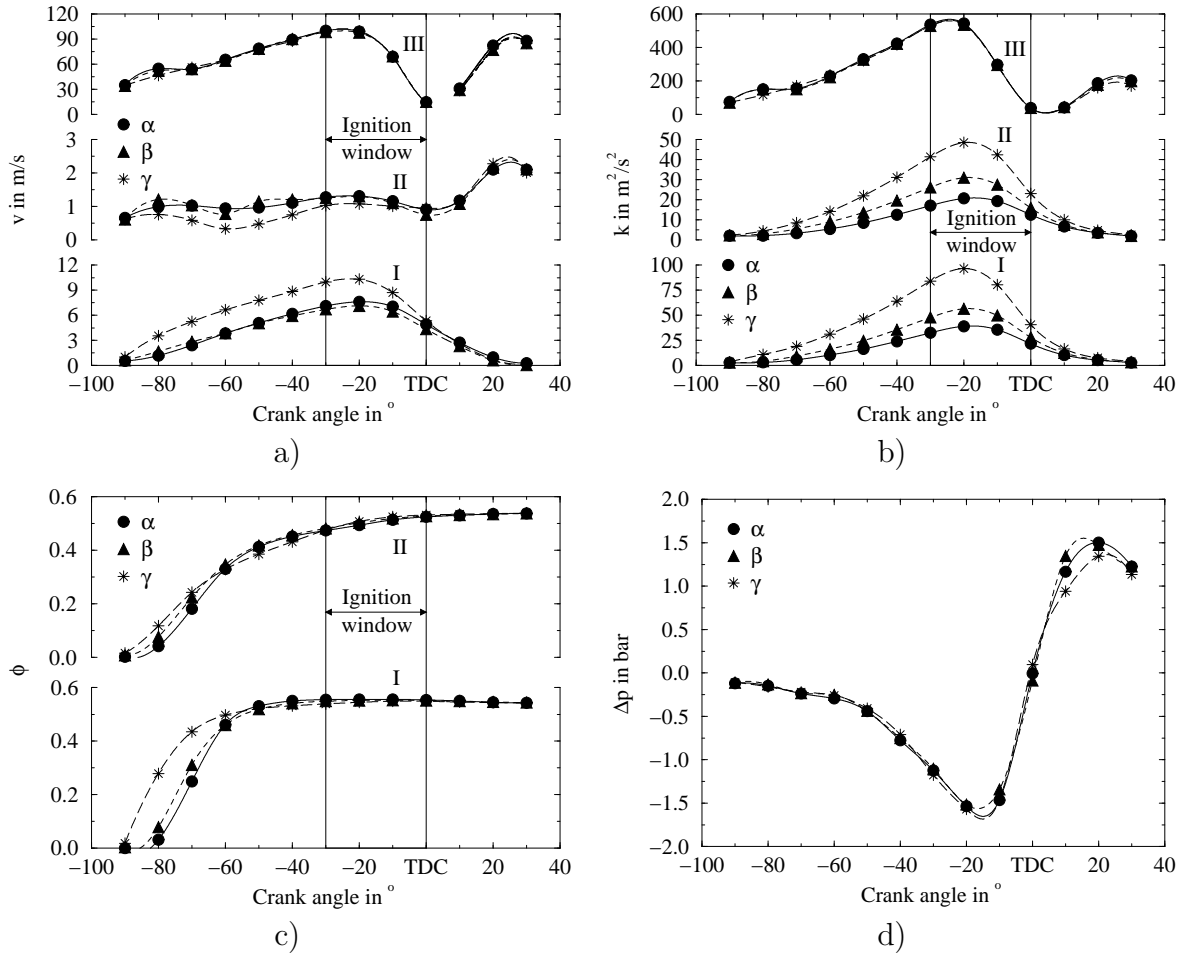


**Figure 3.21:** Influence of the prechamber bottom geometry on the flow at different locations in the prechamber ( $V_p = 4540 \text{ mm}^3$ ,  $d_n = 2 \text{ mm}$ ,  $N_n = 6$ ,  $A_n = 18.85 \text{ mm}^2$ ,  $\alpha_n = 60^\circ$ ): a) velocity magnitude, b) turbulence kinetic energy, c) fuel to air equivalence ratio, d) pressure difference between pre- and main chamber.

of the recirculation zone in the prechamber bottom reduces strongly the local dissipation of turbulence and therefore results in a more efficient transfer in the upper part (**figure 3.20**). The creation of a dome in the prechamber bottom ( $\beta$ ) has little influence on the flow velocity in the vicinity of the ignition point (**figure 3.21, a**), but increases significantly the level of turbulence in this region (**figure 3.21, b**). The higher flow velocity in the lower prechamber part accelerates the transfer of unburnt mixture to the upper part, which results in a faster rise in fuel to air equivalence ratio at the ignition point (**figure 3.21, c**). The creation of a protuberance to even better lead the incoming flow ( $\gamma$ ) increases further the velocity and turbulence kinetic energy at the ignition location. The much higher axial velocity in the lower part contributes to an even more rapid transfer of unburnt mixture in this region. In both cases, the higher turbulence intensity in the upper part accelerates the incorporation of the residual gas into the unburnt mixture, which reduces somewhat the maximum fuel to air equivalence ratio in the ignition window. Finally, the change in prechamber bottom geometry has no perceptible effect on the pressure drop across the nozzle orifices during

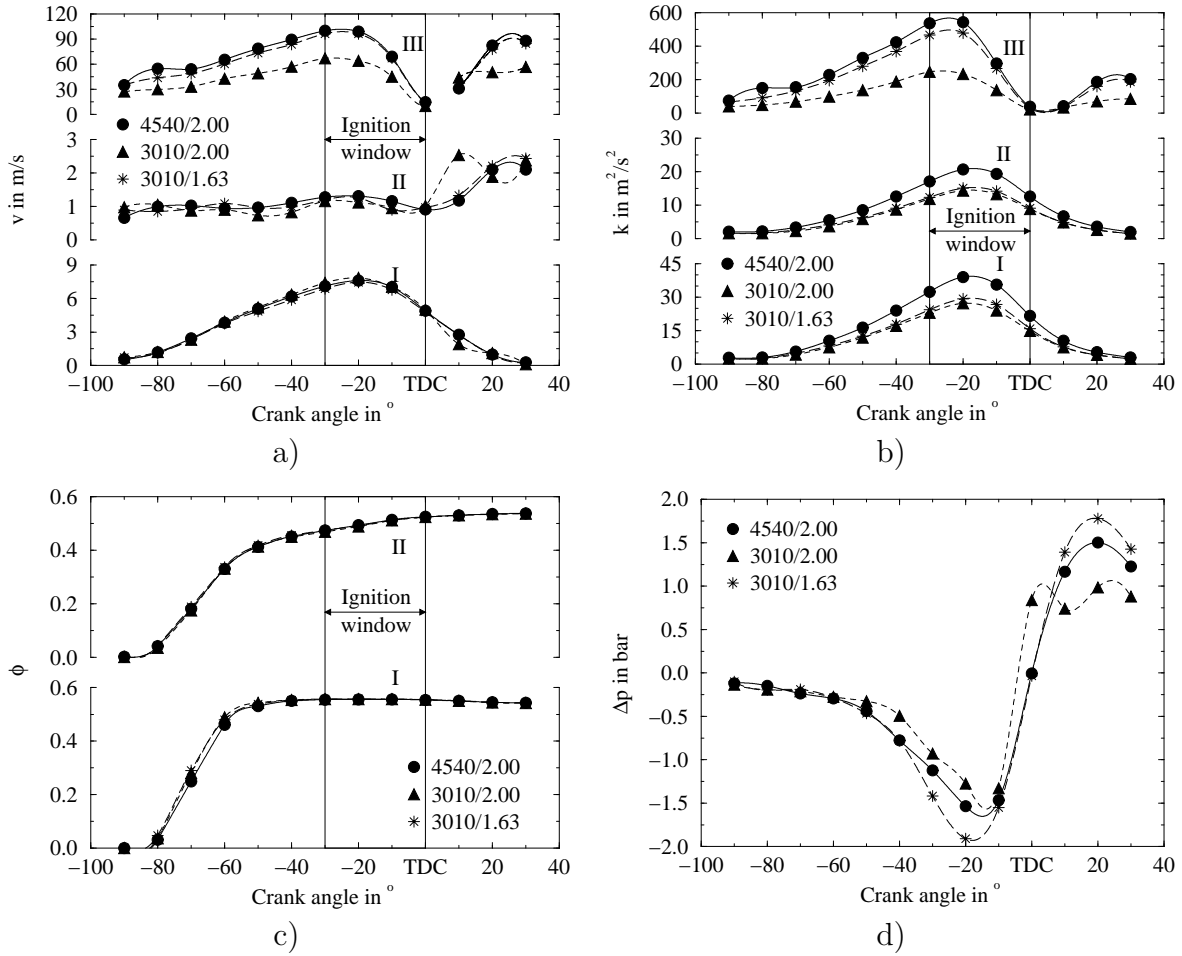


**Figure 3.22:** Influence of the prechamber volume on the flow at different locations in the prechamber ( $N_n = 6$ ,  $\alpha_n = 60^\circ$ ): a) velocity magnitude, b) turbulence kinetic energy, c) fuel to air equivalence ratio, d) pressure difference between pre- and main chamber.

compression (**figure 3.21, d**), which indicates a similar filling. On the other hand, an improvement of the flow leading ( $\gamma$ ) will significantly reduce the pressure drop during expansion.

### 3.3.7 Prechamber internal volume

The internal volume of the base prechamber ( $4540 \text{ mm}^3$ ) corresponds to 2.9 % of the total compression volume (clearance and prechamber volumes). This represents the maximum volume which can be fitted into the original cylinder head without prejudice to its mechanical stability, while keeping a compact geometry. A further volume increase can only be realised through an increase of prechamber length. Typical prechamber volumes used in heavy duty gas engine operating with stratified charge ranges from 1.5 to 5 % of the clearance volume [15, 16, 21, 28, 29]. In order to evaluate the influence of this parameter, the prechamber internal dimensions were proportionally reduced to obtain a volume of  $3010 \text{ mm}^3$ , corresponding to 1.9 % of the compression

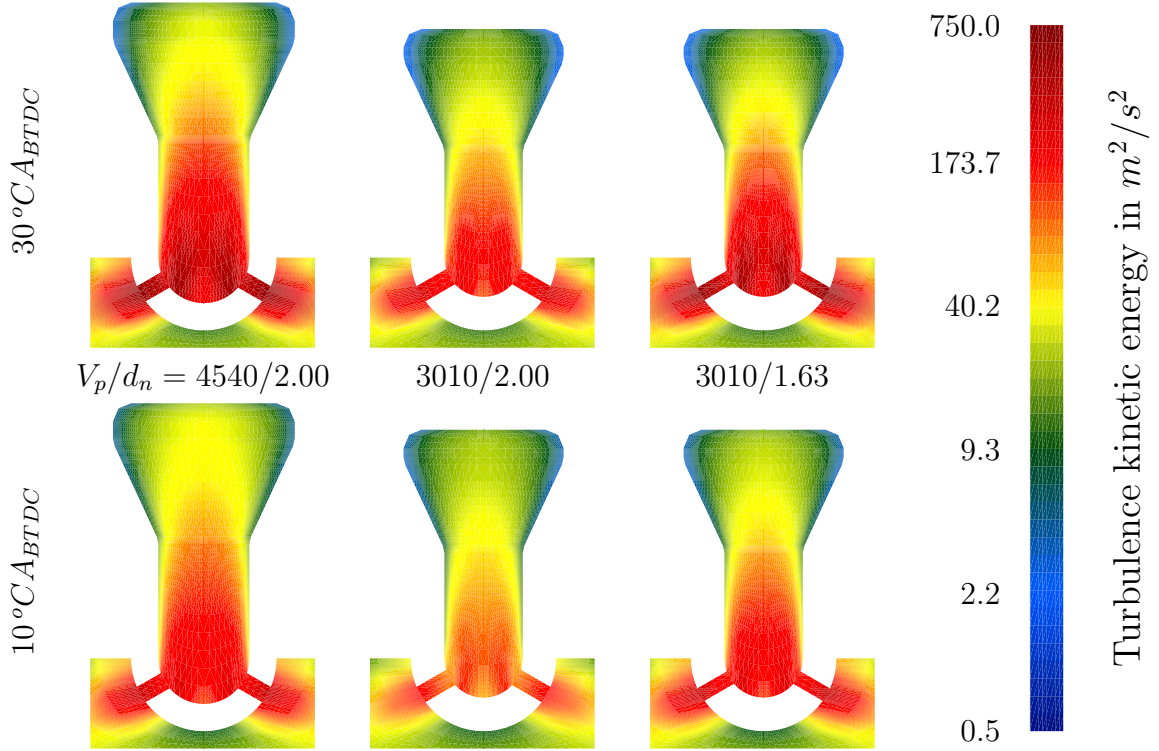


**Figure 3.23:** Influence of prechamber volume on the distribution of turbulence kinetic energy in the prechamber ( $N_n = 6$ ,  $\alpha_n = 60^\circ$ ).

volume. Two different cases were studied. In the first case, the nozzle orifice diameter remained unchanged. In the second case, the ratio between the total nozzle orifice cross sectional area and the prechamber internal volume ( $A_n/V_p$ ) was kept constant, what theoretically leads to a constant pressure drop between pre- and main chamber [23]. In the later case, this leads to a reduction of the orifice diameter from 2.00 to 1.63 mm. The mesh was adjusted to the new geometry, while the total number of cells was not changed. According to the sensitivity analysis (Appendix B.1), an increase of mesh resolution has no significant effect on the numerical solution.

The proportional reduction of the prechamber dimensions in order to obtain a smaller internal volume results in a similar flow pattern and velocity magnitude in the upper prechamber part (**figure 3.22, a**). In the case of the small prechamber, the reduction of the nozzle orifice diameter leads to a strong increase of the orifice flow velocity, which reaches values very close to the large prechamber one. In turn, this causes an important increase in turbulence generated (**figure 3.23**). However, the level achieved remains significantly lower than in the case of the large prechamber (**figure 3.22, b**). The decrease of the internal diameter of the lower prechamber part causes a significant increase in turbulence dissipation at the prechamber bottom. In the case of the large nozzle orifices, the decrease in the turbulence generated combined to the higher turbulence dissipation leads to a drastic reduction of the turbulence intensity in the upper prechamber part. Further, the higher turbulence generated through the reduction of the nozzle orifice diameter is largely dissipated in the lower prechamber part. However, it enables a further diffusion towards the prechamber top, which results in a somewhat higher turbulence intensity in the upper prechamber

part. In the case of the reduced internal volume, the unburnt mixture reaches the prechamber top somewhat earlier, but without affecting the fuel to air equivalence ratio in the ignition window (**figure 3.22, c**). In the case of a constant nozzle orifice diameter, the decrease of prechamber volume reduces significantly the pressure drop across the nozzle orifices (**figure 3.22, c**). The evolution of the pressure drop after TDC results from the interaction between the prechamber flow inertia and the piston motion. This behaviour is not studied in detail because this part of the cycle is strongly affected by the combustion process, not simulated here. On the other hand, when the ratio  $A_n/V_p$  is kept constant, the pressure drop across the orifices remains the same up to  $40^\circ C A_{BTDC}$  and then increases significantly. Although a fixed ratio  $A_n/V_p$  does not enable the achievement of a similar pressure drop across the orifices during the whole compression phase, it enables to obtain reasonably similar nozzle orifice flow conditions. Therefore, keeping a constant ratio  $A_n/V_p$  is expected to better isolate the effect of the reduction of the internal volume.

### 3.3.8 Prechamber internal shape

An insight into the influence of the prechamber internal shape on the flow characteristics was established on the basis of three distinct cases (**figure 3.24**). In order to allow a significant geometrical variation in the available space of the cylinder head, a reduced prechamber volume of  $3000 \text{ mm}^3$  was considered. The first case ( $\alpha$ ) corresponds to a uniform radial reduction of the base prechamber. The proportion of volume located in the upper part was then reduced ( $\beta$ ) and increased ( $\gamma$ ), respectively. The largest diameter of the upper prechamber part of case  $\beta$  is  $14 \text{ mm}$ , which corresponds to the thread dimension of a standard spark plug. In the case  $\gamma$ , this diameter is very close to the maximum value that can be fitted into the cylinder head. With a value of  $19.64 \text{ mm}^2$ , the cross sectional area of the lower prechamber part of case  $\gamma$  approaches the total area of the nozzle orifices. Therefore, this part acts almost like a prolongation of the orifices up to the main prechamber volume. The mesh used was adapted to each case, but the total number of cells remained the same as for the base case (8714). This insured a sufficient mesh resolution, even in the upper part of the case  $\gamma$ . Nevertheless, in this latter case, the presence of numerous very small cells in the lower part led to a drastic increase of the computation time (total of  $\approx 80$  CPU hours).

The volume distribution between lower and upper prechamber parts governs the internal flow pattern and thereby the velocity distribution and intensity (**figure 3.24**) that determines the transfer of turbulence and unburnt mixture. An increase of the lower part volume in order to achieve a more uniform distribution ( $\beta$ ) causes a reduction of the velocity in the upper part and the quasi suppression of the main recirculation zone. In consequence, far less turbulence is transferred to this part (**figure 3.25**) and the unburnt mixture reaches the prechamber top later in the compression stroke (**figure 3.26**). The residual gas is compressed in the upper prechamber skirt and is incorporated to a more limited extent into the incoming unburnt mixture. On the other hand, a reduction of the lower part volume in order to form a more compact cavity ( $\gamma$ ) causes a very strong increase of velocity in this region and along the axis of the upper



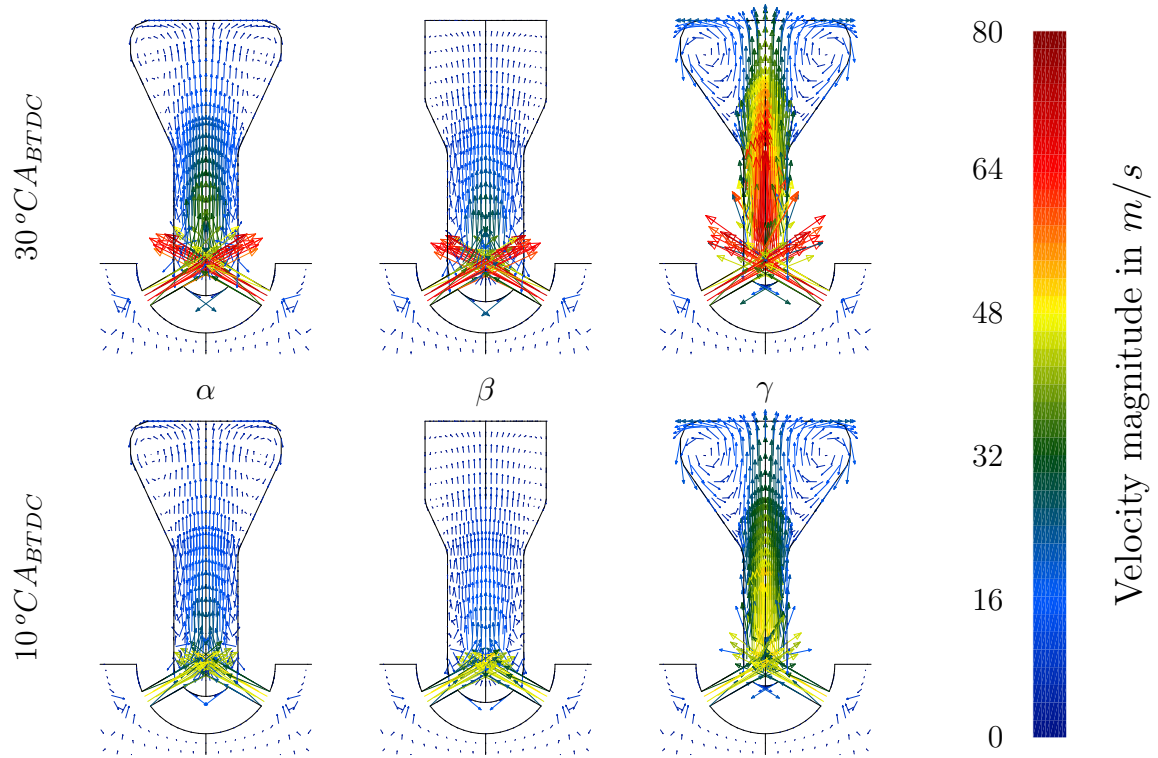


**Figure 3.24:** Influence of the prechamber shape on the flow pattern and the velocity magnitude in the prechamber ( $V_p = 3000 \text{ mm}^3$ ,  $d_n = 2 \text{ mm}$ ,  $N_n = 6$ ,  $A_n = 18.85 \text{ mm}^2$ ,  $\alpha_n = 60^\circ$ ).

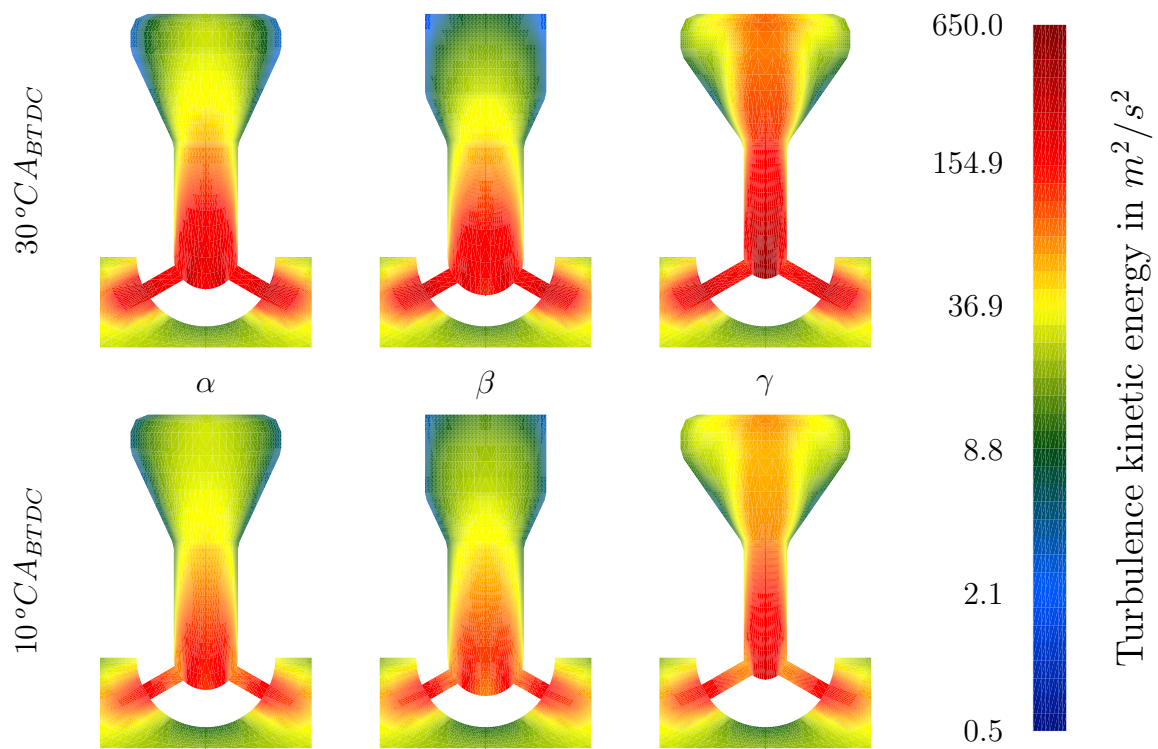


**Figure 3.25:** Influence of the prechamber shape on the distribution of turbulence kinetic energy in the prechamber ( $V_p = 3000 \text{ mm}^3$ ,  $d_n = 2 \text{ mm}$ ,  $N_n = 6$ ,  $A_n = 18.85 \text{ mm}^2$ ,  $\alpha_n = 60^\circ$ ).

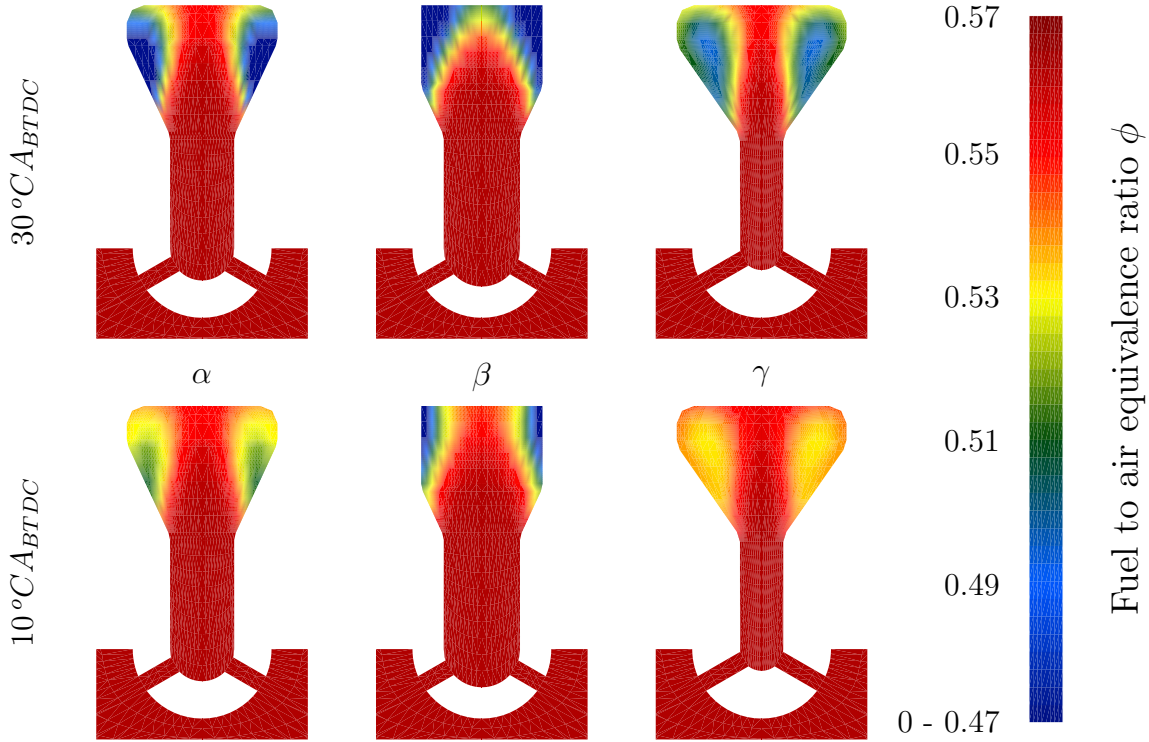
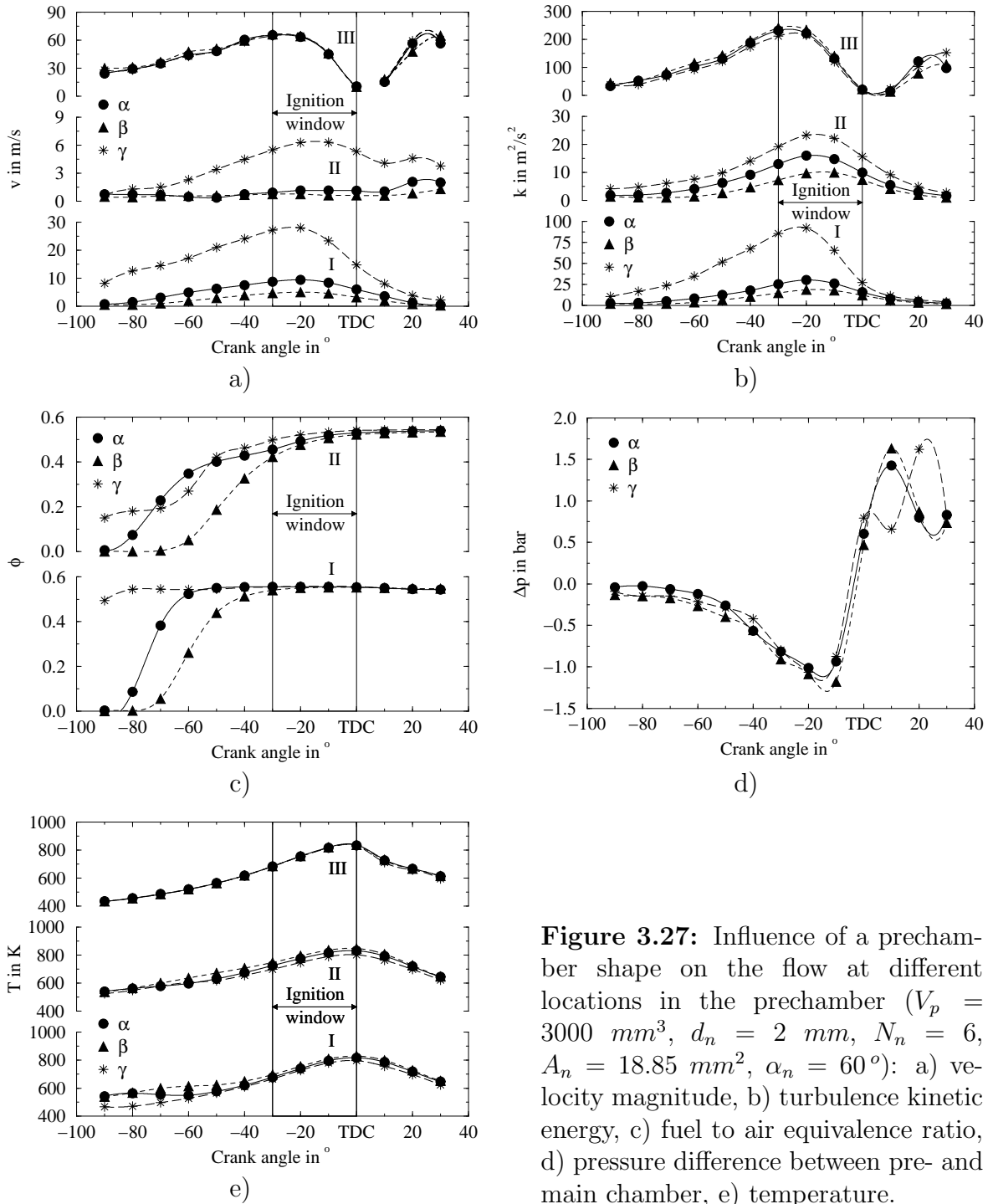


**Figure 3.26:** Influence of the prechamber shape on the distribution of fuel to air equivalence ratio in the prechamber ( $V_p = 3000 \text{ mm}^3$ ,  $d_n = 2 \text{ mm}$ ,  $N_n = 6$ ,  $A_n = 18.85 \text{ mm}^2$ ,  $\alpha_n = 60^\circ$ ).

part. This accelerates the transfer of turbulence and unburnt mixture into the upper part and increases the velocity of the main recirculation flow, which promotes rapid diffusion throughout the volume.

The geometry variation has only a very weak effect on the nozzle flow (**figure 3.27, a**) and the corresponding turbulence generation (**figure 3.27, b**). However, the flow characteristics at the ignition point are strongly dependent on the prechamber configuration. A more uniform distribution of the volume along the axis ( $\beta$ ) reduces to a large extent the velocity magnitude and the turbulence kinetic energy. This consequently delays the arrival of unburnt mixture, and thus leads to a slightly lower fuel to air equivalence ratio at the beginning of the ignition window (**figure 3.27, c**). The lower flow velocity reduces the heat transfer to the prechamber wall, which results in a somewhat higher mixture temperature (**figure 3.27, e**). A concentration of the volume in the upper part ( $\gamma$ ) generates very high velocity and turbulence kinetic energy in the vicinity of the ignition location, which creates flammable conditions much more rapidly. However, the velocity and turbulence intensity reached in this case are much higher than those characterising the conventional combustion chamber (**figure 3.7**). These conditions could excessively perturb the ignition process and therefore not be practical. The very high velocity also increases the heat transfer to the wall, which slightly reduces the mixture temperature (**figure 3.27, e**). An almost equal pressure drop across the nozzle orifices for all the three cases (**figure 3.27, d**) indicates a similar prechamber charge.



### 3.4 Conclusion

The effects and consequences of transferring the ignition point of the conventional combustion chamber into a small prechamber attached to the main combustion chamber is evaluated through a comparison of the respective flows at the location of the gap between the spark plug electrodes. The prechamber flow characteristics in the crank angle period where the ignition is expected to occur (between  $30^\circ CA_{BTDC}$  and TDC) are compared to the one in the conventional combustion chamber at the latest possible spark timing ( $26^\circ CA_{BTDC}$ ).

The velocity magnitude essentially depends on the internal prechamber shape. An important reduction of the lower part cross section results in an increase in flow velocity which can exceed the value of the conventional combustion chamber. However, the velocity magnitude is in most cases of the same order and therefore not critical. The flow through the nozzle orifices produces a very high turbulence which is then partially transferred to the prechamber top. The turbulence generation is governed by the number of nozzle orifices and their size and distribution. The diffusion of turbulence towards the spark plug depends primarily on the amount generated and on the proportion of it that is dissipated in the recirculation zones located at the prechamber bottom, but also on the prechamber internal shape. The turbulence intensity at the ignition location varies strongly with the geometrical configuration and reaches in most cases a much higher value than in the conventional combustion chamber. A high turbulence intensity is expected to promote a rapid prechamber combustion. However, it also perturbs the ignition process and the early stage of the flame kernel growth, which increases the probability of ignition failure. The partial dilution of the unburnt mixture with unscavenged prechamber residual gas leads to a slightly lower fuel to air equivalence ratio. In the particular case of nozzle orifices imparting a swirl motion, the residual gas only partly mixes with the unburnt mixture and mainly remains located along the axis of the upper prechamber part. This results in a fuel concentration at the ignition point very close to or beyond the flammability limit. A uniform prechamber cross section results in the compression of the residual gas at the top (stratification) and can therefore also lead to a critical fuel to air equivalence ratio at the spark plug location. In general, the mixture temperature is not significantly affected by the prechamber geometrical changes. However, an important variation in flow velocity resulting from an alteration of the prechamber internal shape modifies the heat transfer to the wall and causes a moderate change in mixture temperature. Depending on the possible delay of the prechamber spark timing, the mixture temperature relevant to ignition is similar or higher than in the conventional combustion chamber. An excessive reduction of the nozzle orifice diameter leads to a strong increase of pressure drop between main- and prechamber and consequently to a decrease of prechamber filling. The reduction of prechamber filling, which can also be achieved through a smaller prechamber volume, results in a decrease of the energy available for the main chamber ignition.

The converging flow to the nozzle orifices during compression produces a strong turbulence in the main combustion chamber. Therefore, the residual level of turbulence at TDC is much higher than in the vicinity of the spark plug in the conventional combustion chamber. This is expected to promote a rapid propagation of the flame front in the early stage of the main chamber combustion process.

# Chapter 4

## Experimental

### Summary

The engine operation with prechamber ignition was experimentally investigated in order to evaluate the potential to reduce the exhaust gas emissions, particularly the CO emissions, below the Swiss limits, without exhaust gas after treatment. Variations of the prechamber configuration, as well as the piston geometry, the turbocharger characteristics and the engine operating parameters, were carried out to determine their influence on the engine performance and emissions. In comparison with the direct ignition, the prechamber ignition strongly intensifies and accelerates the combustion process. This results from the distribution of ignition sources in the main combustion chamber by means of jets of combustion products issuing from the prechamber. The penetration of the gas jets into the main chamber dramatically increases the initial flame front surface. When comparing with the direct ignition, the prechamber ignition required a significant delay of the spark timing in order to generate substantial gas jets. In turn, this strongly reduces the maximum cylinder pressure and results in an important decrease in  $\text{NO}_x$ , CO and THC emissions. Minimum emissions are achieved at a spark timing of about  $8^\circ\text{C}_{ABTDC}$ . The prechamber geometrical parametric study indicates that trends which increase the penetration of the gas jets and/or promote an early arrival of the flame front at the piston top land and cylinder head gasket crevice entrances are beneficial to reduce the CO and THC emissions. In comparison to the original piston, the use of a piston generating significantly more turbulence leads to an approximately 0.5 %-point higher fuel conversion efficiency. However, it induces no significant change in the CO and THC emissions at low  $\text{NO}_x$  emissions. In comparison with the direct ignition, the prechamber ignition yields approximately 40 % and 55 % less CO and THC emissions, respectively. However, this also leads to a reduction of about 2 %-point in fuel conversion efficiency. The adjustment of the turbocharger characteristics in order to operate the engine at wide open throttle results in an increase of about 1 %-point in fuel conversion efficiency. Nevertheless, a consequent change in the exhaust manifold gas dynamics causes an increase of approximately 40 % in THC emissions. At nominal load, the prechamber ignition operation fulfils the Swiss requirements for emissions and achieves a fuel conversion efficiency higher than 36.5 %.

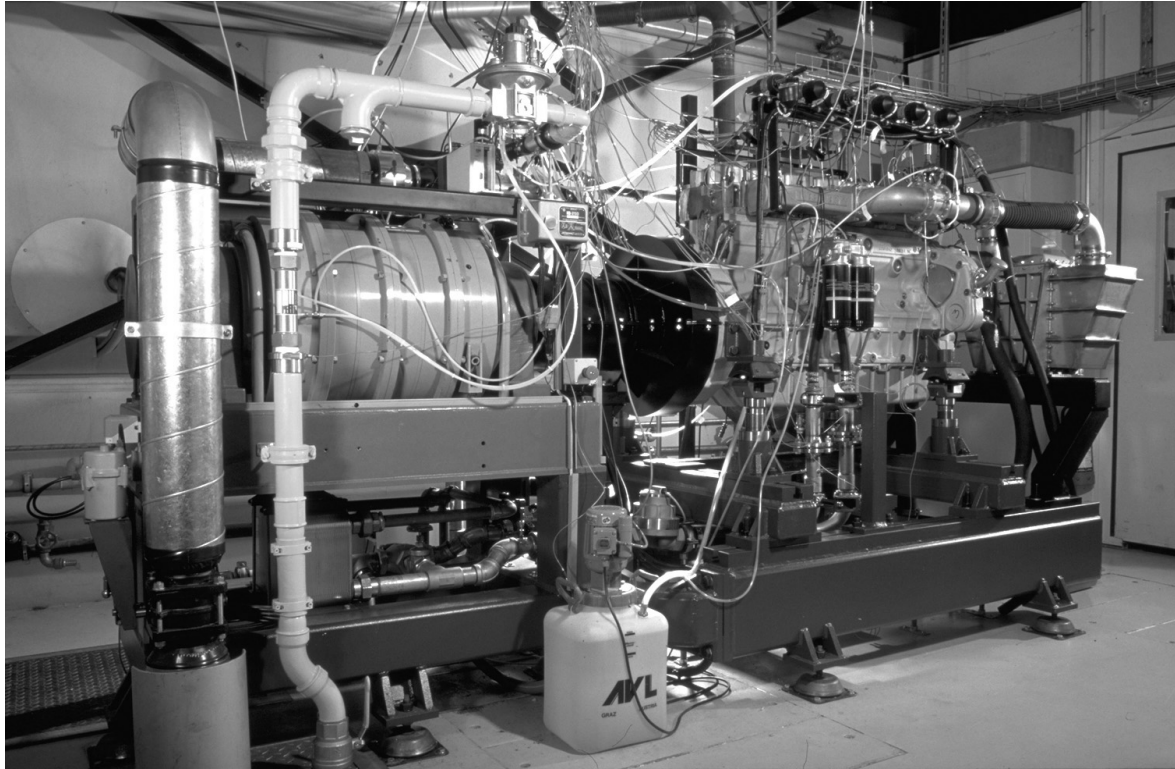


Figure 4.1: Test bed with gas engine *Liebherr G 926 TI*.

## 4.1 Testing facilities

The experimental investigation was carried out on a test bed especially developed for the study of gas engines (**figure 4.1**) during the early stage of the gas engine project. The test bed is equipped with a direct natural gas supply from the network as well as from an intermediate storage tank at high pressure. The storage tank is used to keep the natural gas composition constant over several series of experiments. The testing facilities and the instrumentation used are described in appendix C.1.

## 4.2 General experimental conditions

### 4.2.1 Operating conditions

The experimental conditions are summarised in **Table 4.1**. The engine being dedicated to cogeneration, the crankshaft rotational speed was kept constant at  $1500 \pm 5$  rpm. The engine room temperature was maintained between  $29$  and  $36$  °C through an unregulated ventilation and cooling system. The combustion air temperature was regulated to  $25 \pm 0.5$  °C and its relative humidity (RH) kept as close as possible to  $50 \pm 0.5$  %. The value of  $30$  % RH imposed by the standard *ISO 3046/1* [51] could not be respected because of the high air moisture during experiments and the limited drying capacity of the combustion air conditioning system. The air pressure before fuel

**Table 4.1:** General experimental conditions

Crankshaft rotational speed	$1500 \pm 5 \text{ rpm}$
Maximum brake mean effective pressure	$12 \pm 0.1 \text{ bar}$
Maximum brake power output	$150 \pm 1.3 \text{ kW}$
Engine room temperature	$29\text{-}36 \text{ }^\circ\text{C}$
Intake air pressure	$980 \pm 5 \text{ mbar}$
Intake air temperature	$25 \pm 0.5 \text{ }^\circ\text{C}$
Intake air relative humidity*	$50 \pm 0.5 \%$
Natural gas pressure†	$980 \pm 5 \text{ mbar}$
Natural gas temperature	$14\text{-}27 \text{ }^\circ\text{C}$
Fuel-air mixture temperature after intercooler	$90 \pm 1 \text{ }^\circ\text{C}$
Exhaust gas pressure after turbocharger	$1050 \pm 5 \text{ mbar}$
Cooling water inlet temperature	$80 \pm 0.5 \text{ }^\circ\text{C}$
Cooling water mass flow	$2.45 \pm 0.03 \text{ kg/s}$
Lubricating oil inlet temperature	$90 \pm 0.5 \text{ }^\circ\text{C}$
Lubricating oil mass flow	$1.21 \pm 0.01 \text{ kg/s}$

\* when not otherwise specified

† through zero pressure regulator controlled by intake air pressure

and air mixer was maintained at  $960 \pm 5 \text{ mbar}$ . This value corresponds to an atmospheric pressure of  $980 \text{ mbar}$  reduced by the pressure drop of a lightly loaded standard air filter for stationary engine [52]. Due to the relatively low local atmospheric pressure ( $970$  to  $980 \text{ mbar}$ ) and the limited boosting capacity of the air conditioner, this pressure is somewhat lower than *ISO 3046/1* standard of  $1000 \text{ mbar}$ .

The natural gas was supplied from storage and the exact composition was determined by gas chromatography to enable an accurate calculation of the engine fuel conversion efficiency. The composition and properties of the different natural gas blends used are given in appendix C.2. The natural gas temperature before the fuel-air mixer is not regulated and depends on the atmospheric conditions (outside storage) as well as on the engine load (gas mass flow and room temperature). The values measured are between  $14$  and  $27 \text{ }^\circ\text{C}$ . Although the variation is relatively important, it has only a weak influence on the mixture temperature because of the high air-fuel ratio ( $\approx 27 \text{ kg}_{dry \text{ air}}/\text{kg}_{ng}$  for  $\lambda = 1.7$ ). The natural gas pressure is equalised to the air pressure through a zero pressure regulator.

The exhaust pressure after turbocharger was adjusted at full load to a constant value of  $1050 \pm 5 \text{ mbar}$ . This value corresponds to the fixed atmospheric pressure of  $980 \text{ mbar}$  increased by the exhaust system pressure drop of  $70 \text{ mbar}$  prescribed by the engine manufacturer. The inlet engine cooling water and lubricating oil temperatures were regulated to  $80 \pm 0.5 \text{ }^\circ\text{C}$  and  $90 \pm 0.5 \text{ }^\circ\text{C}$ , respectively. The lubricating oil flow is generated by the engine gear-type pump, while the cooling water flow is produced by an external centrifugal pump as in most cogeneration engines. The cooling water and

lubricating oil mass flow rates were  $2.45 \pm 0.03 \text{ kg/s}$  and  $1.21 \pm 0.01 \text{ kg/s}$ . The fuel-air mixture temperature after turbocharger compressor was regulated to  $90 \pm 1 \text{ }^\circ\text{C}$ . This cooling water temperature level enables, in practice, direct lubricating oil and fuel-air mixture cooling with engine water, though the test bed is equipped with three independent cooling circuits.

## 4.2.2 Exhaust gas emission regulation

The regulation for the emission of pollutant substances contained in combustion exhaust gases in force in Switzerland is prescribed by the Swiss Clean Air Act (*OPair*) [1]. For stationary combustion engines, the Act limits the emissions of solid particles, of nitrogen monoxide (NO) and dioxide (NO<sub>2</sub>), regrouped under the generic NO<sub>x</sub>, and of carbon monoxide (CO). The emission of unburned hydrocarbon THC is unlimited. The limits are expressed in mass of pollutant emitted per unit of exhaust gas volume at normal conditions (1013 mbar, 0 °C). They apply for dry exhaust gas (0% RH) and an oxygen (O<sub>2</sub>) residual concentration of 5%. Pollutant concentrations measured on moist exhaust gas and/or containing a different oxygen residual concentration have to be corrected to the reference values. The method of correction is detailed in appendix C.3. For natural gas and biogas<sup>1</sup> operation, the solid particles and the CO emissions are limited to 50 and 650 mg/m<sup>3</sup>, respectively. The NO<sub>x</sub> emissions are limited to 250 mg/m<sup>3</sup> for natural gas operation and to 400 mg/m<sup>3</sup> for biogas operation; they are expressed in equivalent NO<sub>2</sub>. In the case of natural gas operation, the limit corresponds to half of the value prescribed in Germany<sup>2</sup>, one of the most severe in Europe.

The emissions of NO<sub>x</sub>, CO, THC, O<sub>2</sub> and CO<sub>2</sub> were measured in this project. The maximum concentration for solid particles has been essentially prescribed to limit the soot emission of diesel engines. Due to the very small quantity of solid particles emitted by spark ignition engine operating on gaseous fuels (typically two to three orders of magnitude less than a diesel engine [53]), their concentration in the exhaust gas was not measured. According to the *OPair* standard, the emission values given in the following sections are expressed in mg/m<sub>N</sub><sup>3</sup>, 5% O<sub>2</sub>. However, they are also expressed in mass of pollutant emitted per unit of net mechanical work delivered at the crankshaft in the tabulated data given in appendix C.5. Henceforth, the emission limits prescribed by the *OPair* are called *Swiss limits* for convenience.

## 4.2.3 Variable definition

All the variables used to represent the experimental results are described in detail in appendix C.3.

---

<sup>1</sup>gas produced by biomass or sewage digestion as well as landfill decomposition if the concentration in inorganic and organic, chlorinated and fluorinated components, expressed in equivalent hydrochloric or hydrofluoric acid, is not exceeding 50 mg/m<sup>3</sup>

<sup>2</sup>[2] NO<sub>x</sub>, CO and solid particles: 500, 650 and 50 mg/m<sub>N</sub><sup>3</sup>, 5% O<sub>2</sub>, respectively; NMHC: 150 mg/m<sub>N</sub><sup>3</sup>, when the NMHC mass flow rate exceeds 3 kg/h.



### 4.3 Direct ignition operation

This section summarises the principal results obtained with direct spark ignition in early phases of the gas engine study [3, 4] and illustrates the influence of the main engine parameters affecting the principal exhaust gas emissions.

The experimental investigations carried out on the basis of the original combustion chamber geometry developed by the engine manufacturer (**figure 2.1**, piston *A*) have shown that the combustion chamber crevice volume located between the cylinder liner, the cylinder head and the cylinder gasket represents a major source of CO and THC emissions. This finding led to a modification of the cylinder liner and gasket to reduce as much as possible this crevice volume. The emissions and performance after modification are represented in **figure 4.2**. The results are generally represented as function of NO<sub>X</sub> emissions in order to clearly illustrate the effect of the different combustion chamber configurations on this determining pollutant; this study aims at reducing the NO<sub>X</sub> emissions exclusively by the control of the combustion process, without exhaust gas after treatment. The references given in brackets in the figure legends correspond to the series of tabulated data given in appendix C.5.

A piston generating a higher turbulence through an important increase of the piston front surface and developed in a parallel project at the *Swiss Federal Institute of Technology of Zürich (ETHZ)* [11] (**figure 4.3, a**, piston *B*) was then evaluated. The higher turbulence level generated by piston *B* leads to a shortening of the combustion process (**figure 4.2, a**) and an improvement of the combustion stability, expressed by the coefficient of variance of the indicated mean effective pressure ( $COV_{p_{mi}}$ ), (**figure 4.2, b**), which results in an important reduction of the THC emissions (**figure 4.2, c**). However, the CO emissions are not significantly affected. The faster combustion process yields, at constant NO<sub>X</sub> emissions, higher fuel conversion efficiency (**figure 4.2, b**). The lower methane concentration of the natural gas blend used for the test of piston *B* (NG1: 92.2%) compared to the blend used for piston *A* (NG2: 95.9%) account for a part of the combustion acceleration [54]. The effect of fuel composition is somewhat attenuated by the lower fuel-air mixture temperature used with piston *B*. The much better combustion stability enables a further increase in relative air to fuel, which results in a further reduction of NO<sub>X</sub> emissions, far below the Swiss limit. However, the satisfaction of the Swiss limit for CO requires the use of an oxidation catalyst.

A complementary study of the influence of specific engine parameters was undertaken in order to evaluate the potential to reduce the relatively high CO emissions. The main objective was to reduce the CO emissions under the Swiss limit without catalytic exhaust gas after treatment, to enable the operation on biogas produced by sewage digestion or landfill decomposition. This biogas contains heavy metals, which contaminate the catalyst and rapidly deactivate it. The parameters investigated were the volumetric compression ratio, the intake and exhaust valve overlap duration and the location of the first piston compression ring. For practical and financial reasons, the experiments were carried out with natural gas. The results are presented and discussed in detail in appendix C.4. This complementary study indicates that the volumetric compression ratio represents the major parameter influencing the engine exhaust emissions. Further, its reduction results in a decrease of the CO emissions under the Swiss

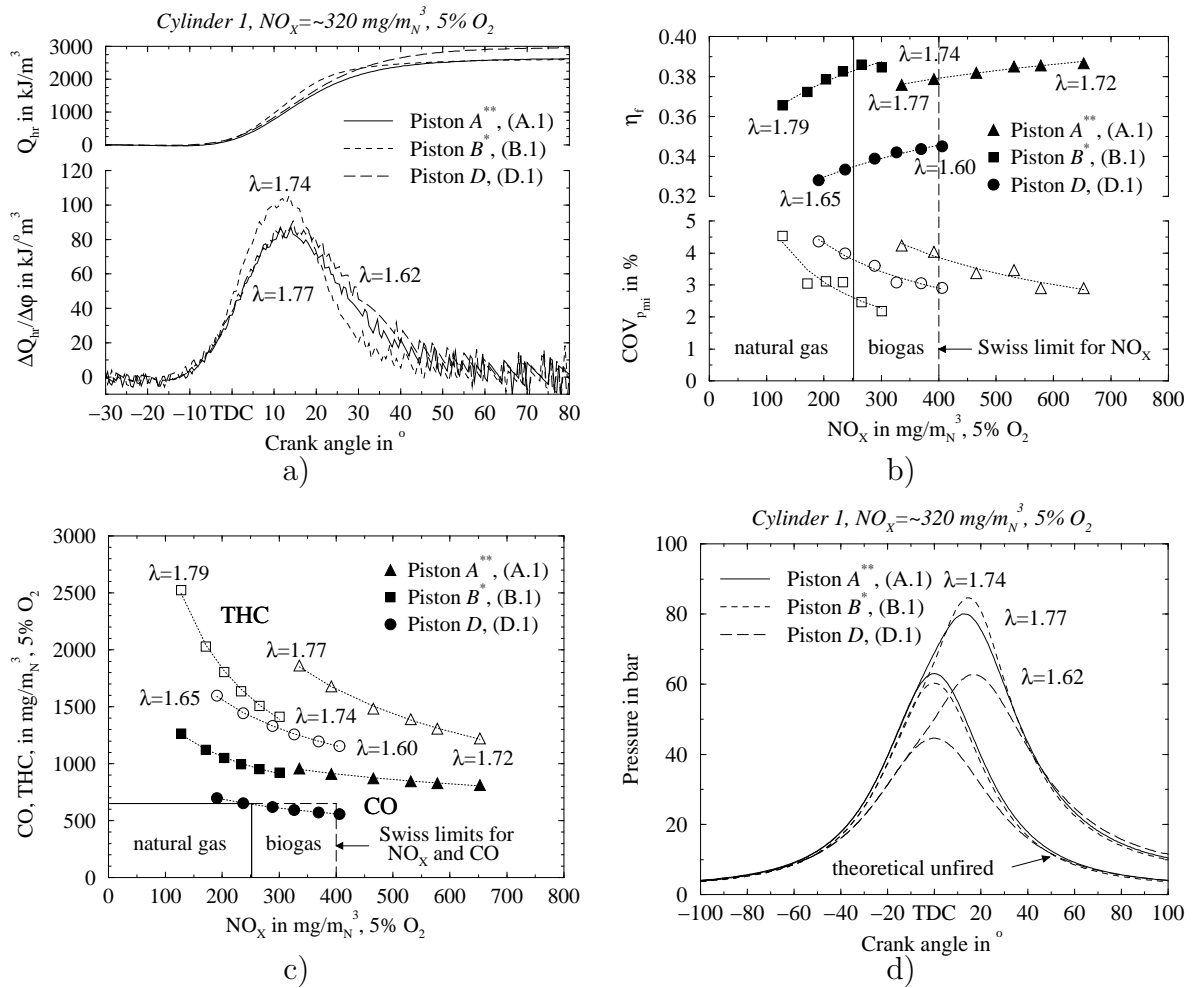


**Figure 4.2:** Performance and emissions of the combustion chambers *A* and *B*,  $\epsilon = 12.0$ , and *D*,  $\epsilon = 9.0$ , as function of  $\text{NO}_x$  emissions; a) mean heat-release rate and integral, b) fuel conversion efficiency and coefficient of variance of  $p_{mi}$ , c)  $\text{CO}$  and  $\text{THC}$  emissions, d) mean pressure cycle;  $ST = 26.7^\circ\text{C A}_{BTDC}$ ,  $T_{mixt} = 90$  (\*50)  $^\circ\text{C}$ ,  $RH = 30$  (\*\*45) %.

limit in the case of biogas operation. This is illustrated by the experimental results obtained with a new piston designed to reduce the compression ratio to 9.0 and to increase as much as possible the squish surface in order to promote the generation of turbulence (**figure 4.3, b**, piston *D*). The decrease of cylinder pressure resulting from the reduction of volumetric compression ratio from 12.0 to 9.0 (**figure 4.2, d**) leads to a slowing down of the combustion process (**figure 4.2, a**), which yields an important decrease of fuel conversion efficiency (**figure 4.2, b**). In comparison to piston *A*, the decrease in peak combustion temperature resulting from the reduction of peak cylinder pressure enables a further reduction of the  $\text{NO}_x$  emissions and a decrease in relative air to fuel ratio, which improves the combustion stability. The much lower cylinder pressure reduces the amount of unburned mixture stored in the combustion chamber crevices at the end of the primary combustion process and therefore the quantity of  $\text{CO}$  emissions generated through hydrocarbon partial secondary oxidation. On the other hand, the slower combustion process results in an increase of the average temperature

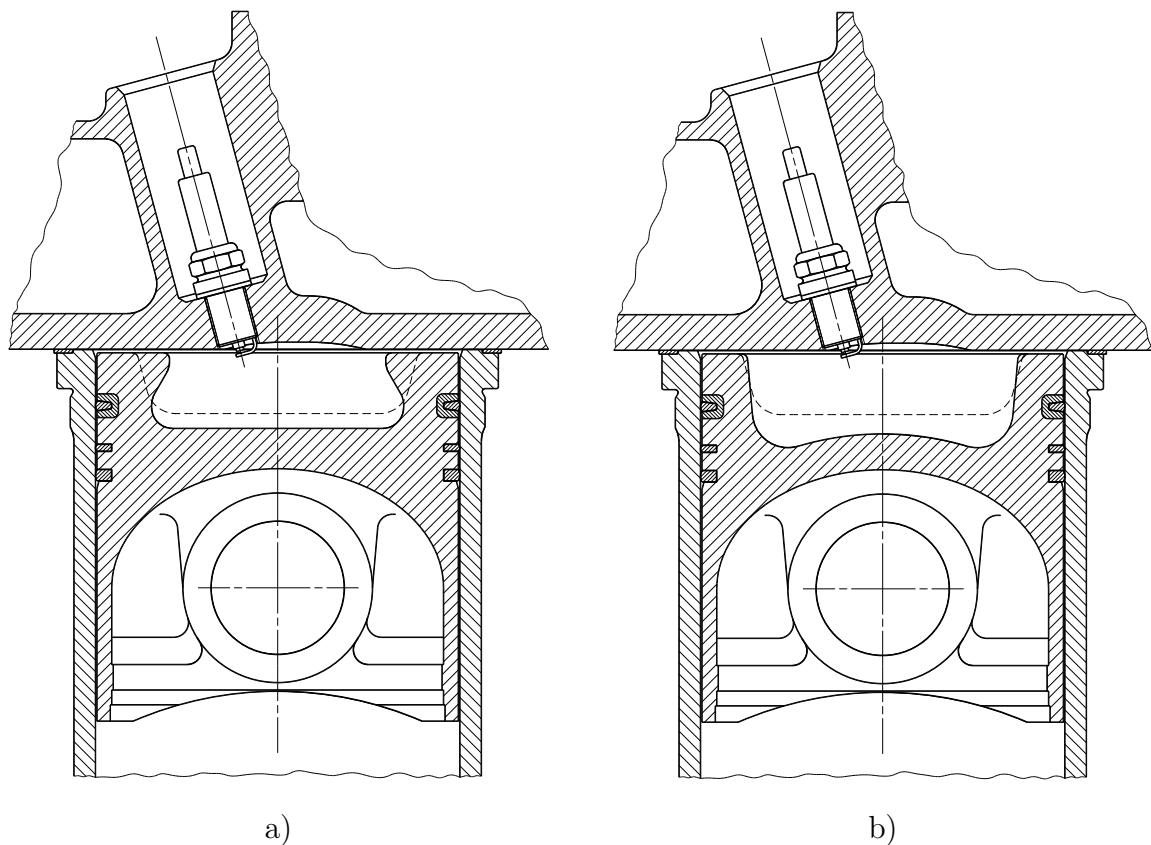


**Figure 4.3:** Combustion chamber: a) with piston *B*,  $\epsilon = 12.0$  [11], b) with piston *D*,  $\epsilon = 9.0$ ; with the dashed outline of piston *A*,  $\epsilon = 12.0$ .

during expansion, which promotes a more complete oxidation of the unburnt hydrocarbons emerging from the crevices. In comparison to piston *A*, both of these effects result in a simultaneous and important reduction of CO and THC emissions (**figure 4.2, c**).

From the results presented, two distinct methods to satisfy the requirements of the Swiss Clean Air Act are emerging. The first method, only applicable to natural gas, consists in using a high turbulence combustion chamber to maximise the fuel conversion efficiency and reduce the  $\text{NO}_x$  emissions, while abating the CO emissions by exhaust gas after treatment with an oxidation catalyst. The second method, destined to biogas, is based on the reduction of the volumetric compression ratio to decrease the raw exhaust emissions under the Swiss limit. This approach, however, leads also to an important reduction of the fuel conversion efficiency. These two methods clearly illustrate the actual limits of the lean burn operation with direct spark ignition. The reduction of the CO emissions without catalytic treatment, in order to decrease the investment and maintenance cost and to improve the engine reliability to satisfy the emissions regulation, leads to an increase of the operating cost through an augmentation of the specific fuel consumption. The simultaneous requirement of low exhaust gas emissions, high primary energy conversion efficiency and reliable engine operation (therefore without exhaust gas after treatment) motivated the search for a new degree of freedom related to the combustion chamber configuration. This was realised through

the addition of a small combustion prechamber and the transfer of the ignition location into this prechamber.

## 4.4 Prechamber ignition operation

This section presents and discusses the experimental results of the engine operation with prechamber ignition. On the basis of the numerical simulation results presented in chapter 3, several prechamber geometrical parameters were selected to determine experimentally their influence on the combustion process. They are the

- orifice
  - total cross sectional area
  - number
  - distribution
  - orientation
- prechamber
  - internal volume
  - internal shape

The influence of the following parameters was also investigated:

- relative air to fuel ratio
- spark timing
- engine load
- main combustion chamber geometry
- turbocharger characteristics

The experimental results are generally presented in two different ways. In the first way, the results are presented at a constant value or as a function of the relative air to fuel ratio, while maintaining all the other operating parameters constant. This is mainly used to analyse and discuss the influence of geometrical variations on the combustion process. In the second way of representation, the results are presented as a function of  $\text{NO}_x$  emissions. This enables the direct evaluation of the effect of a geometrical variation on the tradeoffs between  $\text{NO}_x$  emissions and, respectively, CO emissions, THC emissions and fuel conversion efficiency.

Although the pressure cycle was measured simultaneously in the main combustion chamber of cylinder 1 and 3, the following discussion is principally supported by the results from cylinder 1, essentially because the prechamber pressure cycle was only measured in this particular cylinder. The results of cylinder 3 are simultaneously presented in the particular cases where they are leading to an interpretation which is inconsistent with the one based on the results of cylinder 1. The references given in brackets in the figure legends correspond to the series of tabulated data given in appendix C.5.

#### 4.4.1 Effect of the prechamber on the combustion process

In order to enable an objective comparison between direct and prechamber ignition operation, reference measurements were first performed on the engine operating with the original combustion chamber (piston *A*) and direct ignition on a natural gas of known composition. In this case, the engine was operated at a spark timing of  $26.7^\circ CA_{BTDC}$ , which enables to achieve the lowest  $NO_x$  emissions. After replacement of the conventional cylinder heads by the modified version equipped with prechamber, measurements were performed on the engine operating on the same natural gas blend. In this case, the investigation was performed with the base prechamber featured with an internal volume of  $4540\text{ mm}^3$  and 6 nozzle orifices of diameter  $2.00\text{ mm}$  ( $A_n = 18.85\text{ mm}^2$ ), non-evenly distributed and oriented at an angle of  $\approx 62^\circ$  from the prechamber axis. The engine was operated at a spark timing of  $16.8$  and  $10.8^\circ CA_{BTDC}$ .

#### Results summary

When considering the same  $NO_x$  emissions, the transition from direct ignition to prechamber ignition results in:

- a very strong intensification and acceleration of the combustion process (**figure 4.5, b** and **figure 4.6, c**)
- an important reduction of  $\approx 26\%$  and  $\approx 50\%$  of the CO and THC emissions, respectively (**figure 4.6, a**)
- a slight decrease of the fuel conversion efficiency of less than  $0.5\%$ -point (**figure 4.6, b**)
- a significant decrease of the cycle-by-cycle variability (**figure 4.6, b**)

In comparison to the direct ignition, the prechamber ignition enables a significant reduction of  $NO_x$  emissions.

## Analysis and discussion

The analysis and discussion of the first experimental results is divided into four different sections. The first section is an attempt to describe the flow dynamics between prechamber and main chamber as well as its influence on the combustion process. Based on the considerations established in the first section, the three following sections compare the direct and prechamber ignition operation. They discuss the influence on the combustion process and the engine performance, the effect on the CO and THC emissions and finally the influence on the turbocharger operation, respectively.

### a) Prechamber flow dynamics and combustion

Based on the experimental results obtained with prechamber ignition at two different spark timings, this section is an attempt to analyse and discuss the prechamber flow dynamics and its effect on the combustion process in the prechamber as well as in the main chamber. The results of the numerical simulation presented in chapter 3 are used here to support the discussion. Due to the absence of direct optical access into the engine combustion chambers, the analysis of the prechamber flow dynamics and combustion is essentially based on the behaviour of the difference of pressure between the prechamber and the main chamber; an example is given in **figure 4.4, c**. In most experiments, the maximum pressure difference does not exceed approximately 8 bar. This relatively moderate pressure difference generates a nozzle orifice velocity of about  $200\text{ m/s}$  (**figure 3.10, a**) which remains much lower than the speed of sound at the temperature reached at the end of the compression stroke (approximately  $580\text{ m/s}$  at  $900\text{ K}$ ). This indicates that the flow in the nozzle orifices does not choke [55] and consequently a higher pressure difference between pre- and main chamber should result in an increase of the gas jet intensity and penetration. This assumption is used throughout this study to support the discussion on the effect of changes in the prechamber configuration or in engine operating parameters. The analysis of the main chamber combustion process is based on the pressure cycle measured in the main combustion chamber, which is used to calculate the heat release rate and integral. The results analysed are represented in **figure 4.4** and **figure 4.5**.

During the compression stroke fresh mixture flows from the main chamber into the prechamber, creating a pressure drop across the nozzle orifices (**figure 4.4, c**). Shortly after spark discharge, the initial flame kernel grows rapidly due to the high level of turbulence (**figure 3.7, b**). The flame expansion yields a pressure increase above the main chamber pressure which reverses the flow (**figure 4.4, a**). In a first stage, part of the fresh mixture located close to the nozzle orifices (most remote place from the spark plug electrodes) is expelled again into the main chamber, forming gas jets which enhance the turbulence in the vicinity of the nozzle orifice outlets.

When the flame front reaches the prechamber bottom, it may travel through the orifices or quench, depending on the relative fuel to air ratio and the heat transfer to the prechamber nose. In a second stage, the flame front and/or hot combustion products containing substantial concentrations of highly reactive free radicals are expelled into the main chamber in the wake of the unburned mixture jets characterised by a very

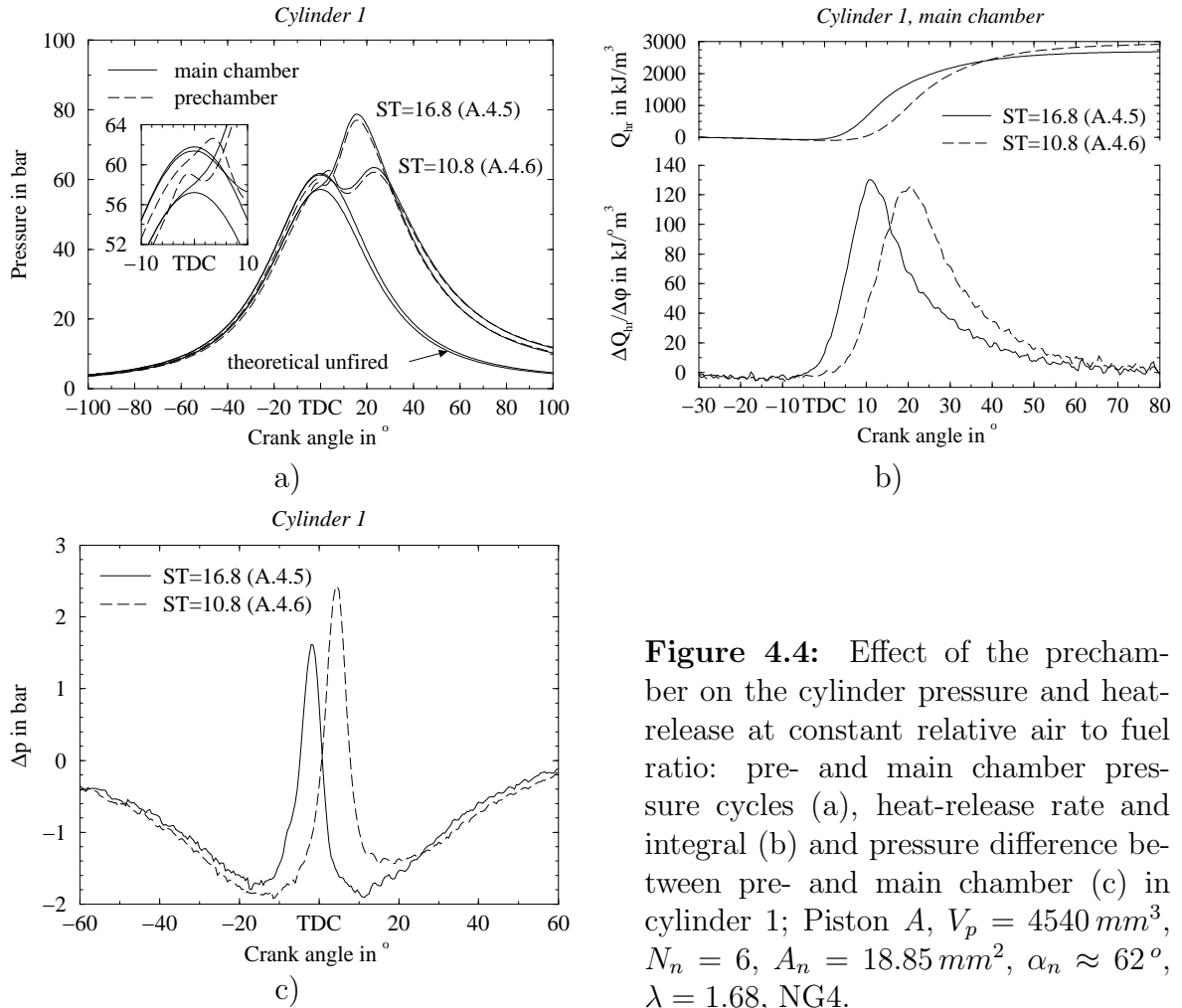


**Figure 4.4:** Effect of the prechamber on the cylinder pressure and heat-release at constant relative air to fuel ratio: pre- and main chamber pressure cycles (a), heat-release rate and integral (b) and pressure difference between pre- and main chamber (c) in cylinder 1; Piston A,  $V_p = 4540 \text{ mm}^3$ ,  $N_n = 6$ ,  $A_n = 18.85 \text{ mm}^2$ ,  $\alpha_n \approx 62^\circ$ ,  $\lambda = 1.68$ , NG4.

high turbulence level. The hot combustion products are spread out and mixed with unburnt mixture entrained in the jet wakes. If the flame quenches before reaching the nozzle orifice outlets, the dispersed free radicals re-initiate locally the oxidation reactions to form multiple flame kernels. The individual flames generated propagate towards each other to eventually coalesce in a large flame front encompassing the jet wake. If the flame front survives the travel through the nozzle orifices, its interaction with the jet is extremely difficult to evaluate without optical visualisation. However, two different situations could at least arise.

In the first situation, the local turbulent mixing occurring in the jet wake is so strong that the flame quenches, as in the previous case. In the second situation, the flame propagates extremely rapidly in the jet wake due to the very high turbulence level, increasing dramatically the flame front surface. The main difference between the two situations resides in the time required to obtain a flame front encompassing the jet wakes. In the first situation, the re-ignition in the main chamber results in a delay, while not in the second situation because of the very fast first stage of the flame front propagation. This delay is essential for the penetration of the jets into the main chamber; the longer the delay, the deeper the penetration. Once the flame front has settled in the main chamber, the pressure rises rapidly and overshoots the value in the prechamber, thus reversing again the flow. The multiple flame fronts (one per gas jet issuing from a nozzle orifice) propagate throughout the main chamber.

Up to shortly before peak pressure, the pressure drop across the orifices increases strongly. Following peak pressure, it decreases continuously until approximately the end of the main chamber primary oxidation process. Only later in the expansion stroke the prechamber pressure becomes higher than the main chamber one and the flow reverses again. The flow does not reverse shortly after peak pressure because of the strong heat transfer from the hot combustion gases to the prechamber wall. Due to the small combustion gas volume contained in the prechamber, the relatively large wall surface and the high turbulence level, the hot gases cool fast enough to maintain the prechamber pressure below the main chamber one. However, the heat transfer decreases with the reduction of temperature during expansion, thus progressively reducing the pressure difference between both chambers.

The combination of a relatively high residual turbulence in the main chamber generated by the converging flow to the nozzle orifices during the compression stroke (**figure 3.8**) and the intense turbulence generated by the gas jets issuing from the multiple orifices enhances strongly the first stage of the combustion process. This results in a very steep increase of the heat-release rate (**figure 4.4, b**). At constant relative air to fuel ratio, a shift of the spark timing towards TDC leads to an increase of the maximum pressure difference between pre- and main chamber (**figure 4.4, c**). This originates mainly in the larger mass of unburnt mixture located in the prechamber at combustion start (**figure 3.6**), which increases the amount of chemical energy available to generate the gas jets. Further, the better homogenisation of the unburnt mixture with the residual gas by the main annular recirculation zone at the top of the prechamber should enable a more complete fuel conversion. Finally, a later start of the prechamber combustion process reduces the fraction of the pressure increase required to overcome the pressure drop across the orifices (**figure 3.10, d**). The consequent increase in the jet intensity and penetration compensate to a large extent for the reduction of chemical reaction kinetics resulting from the decrease of peak combustion temperature (**figure 4.4, b**). The slight decrease of the air to fuel ratio required to achieve approximately the same  $\text{NO}_x$  emissions yields a further intensification of the combustion process which over-compensates the detrimental effect of the spark timing delay (**figure 4.5, b**). The shift of the combustion process into the expansion phase leads to a reduction of the maximum cylinder pressure and the appearance of a second peak of pressure corresponding to the maximum value reached at the end of compression (**figure 4.5, a**). An increase of the spark advance leads to a decrease of the maximum pressure difference between pre- and main chamber and therefore reduces the intensity of the gas jets. This originates in the decrease of the mass of unburnt mixture located in the prechamber when combustion starts and in the higher pressure drop to overcome. From a spark timing of about  $30^\circ\text{CA}_{BTDC}$  (measured with natural gas of unknown composition), the pressure difference between pre- and main chamber remains negative. No flow reversion occurs and consequently no jets develop in the main chamber. In this case, the flame front propagates through the nozzle orifices and then in the main combustion chamber, similarly to the direct ignition operation. However, the high residual turbulence in the main chamber generated by the converging flow to the nozzle orifices during the compression stroke significantly accelerates the first part of the combustion process. The engine was able to operate up to a spark advance of about  $35^\circ\text{CA}_{BTDC}$  (maximum value which can be realised with the actual configuration of the ignition system).



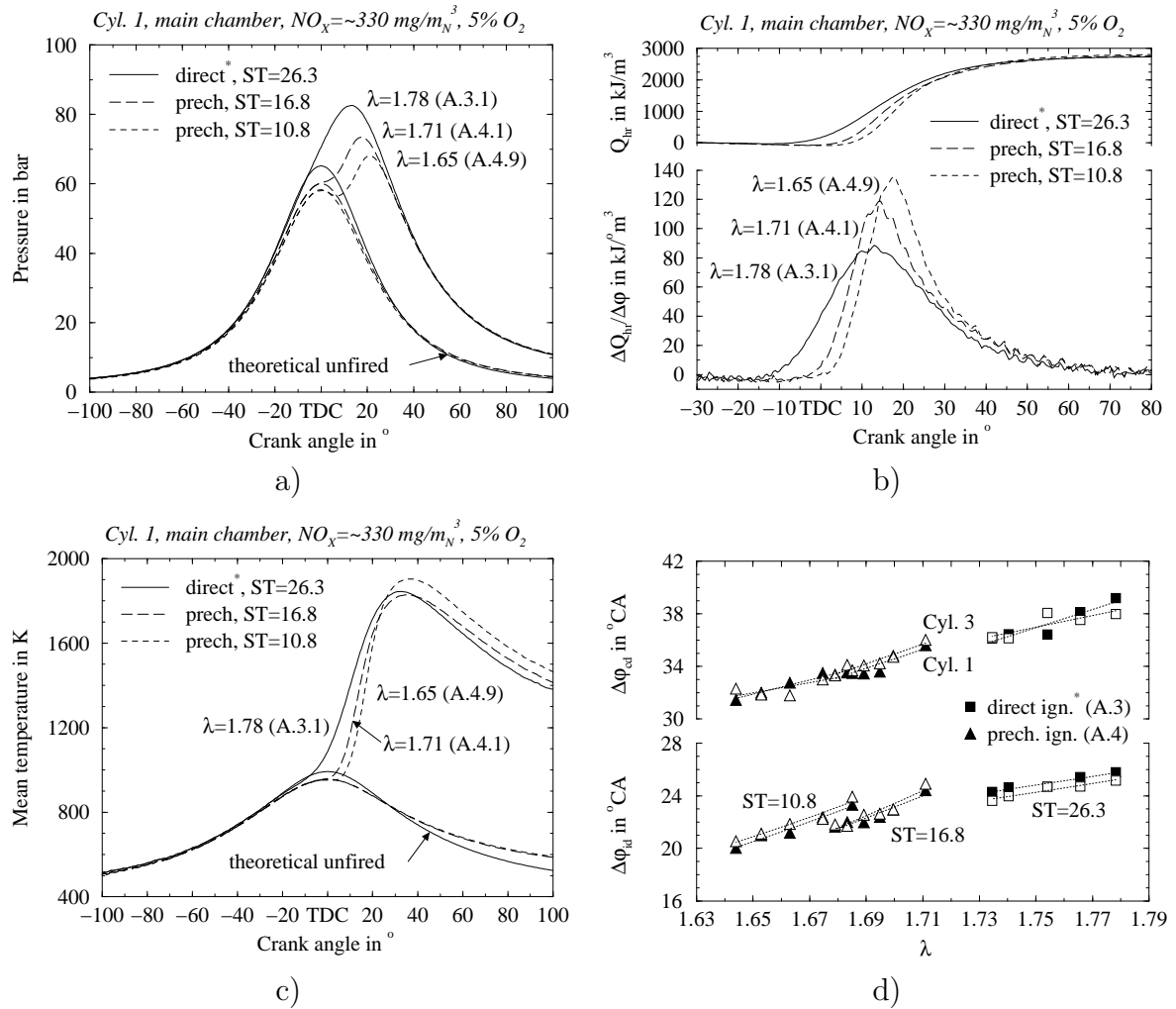


**Figure 4.5:** Effect of the prechamber on the cylinder pressure, heat-release and mean temperature: main chamber pressure cycle (a), heat-release rate and integral (b) and mean combustion temperature (c) in cylinder 1 at  $NO_x \approx 330 \text{ mg/m}_N^3$ ,  $5\% O_2$ ; d) ignition delay and combustion duration as function of relative air to fuel ratio; Piston  $A$ ,  $V_p = 4540 \text{ mm}^3$ ,  $N_n = 6$ ,  $A_n = 18.85 \text{ mm}^2$ ,  $\alpha_n \approx 62^\circ$ ,  $RH = 50$  (\*35)%, NG4.

## b) Combustion process and engine performance

The analysis and discussion of the effect of the transition from direct to prechamber ignition on the combustion process and the engine performance are based on the results presented in **figure 4.5** and **figure 4.6**. The transition from direct to prechamber ignition significantly accelerates the combustion process (**figure 4.5, b**), which results in an important decrease in the ignition delay and combustion duration (**figure 4.6, c**). The prechamber operation enables a delay of the spark timing, which further enhances the combustion process. The more rapid combustion process compensates to a large extent for the detrimental effect of the late combustion and results in only a moderate decrease of less than 0.5 %-point in fuel conversion efficiency (**figure 4.6, b**). Finally, the acceleration of the combustion process yields a reduction of the cycle-by-cycle variability, which allows a decrease in  $NO_x$  emissions.

In comparison to the operation with direct ignition and for approximately the same  $\text{NO}_x$  emissions, the use of a prechamber strongly intensifies the combustion process and increases dramatically the maximum heat-release rate (**figure 4.5, b**). The later part of the combustion process with prechamber ignition differs only moderately from the combustion process with direct ignition. This seems to indicate that the gas jets only affect the first part ( $\approx 75\%$ ) of the combustion process and that the second part ( $\approx 25\%$ ) essentially depends on the main chamber turbulence intensity. In the case of the prechamber ignition, the slightly higher heat-release rate towards the end of the combustion process yields a moderate increase of the mean combustion temperature (**figure 4.5, c**). The delay of the prechamber spark timing shifts the combustion process in the expansion phase, which results in a further increase of the mean combustion temperature. The shift of the combustion process into the expansion phase yields an important decrease of maximum cylinder pressure (**figure 4.5, a**). At the later prechamber ignition timing, the pressure increase due to combustion occurs entirely during the expansion phase and therefore generates only positive mechanical work (usually at conventional spark timings, part of the combustion heat is already released before the end of the compression stroke, not producing positive mechanical work).

For each combustion chamber configuration (direct or prechamber ignition) and spark timing, the ignition delay in the main chamber decreases with the reduction of the relative air to fuel ratio, with a more pronounced effect in the case of the prechamber ignition (**figure 4.5, d**). However, the general trend is independent of the combustion chamber configuration and ignition timing. At this stage it is important to emphasise that the main chamber ignition delay does not account for the energy released during the prechamber combustion process, because the prechamber pressure increase does not directly affect the main chamber pressure (**figure 4.4, a**). This means that in reality more fuel is burnt during the ignition delay in the case of prechamber ignition. Therefore, a similar general trend between main chamber ignition delay and relative air to fuel ratio (**figure 4.5, d**) indicates a very fast prechamber combustion process and a sufficiently intense promotion of the main chamber flame development process by the gas jets to compensate the prechamber ignition delay and combustion duration. In the case of the prechamber ignition, a delay of the spark timing yields a decrease of the prechamber turbulence intensity (**figure 3.5**), which should result in a lower prechamber combustion speed. This is thought to be at the origin of the higher ignition delay observed at constant relative air to fuel ratio (**figure 4.5, d**). However, the results show that the main chamber combustion duration depends only on the relative air to fuel ratio. This tends to support the conclusion that the intensification of the main chamber combustion process by the prechamber ignition compensates for the detrimental effect of the later spark timing on the ignition delay.

At constant relative air to fuel ratio, the delay of the spark timing strongly reduces the  $\text{NO}_x$  emissions (**figure 4.6, a**). In turn, the possible decrease of the relative air to fuel ratio to achieve the same  $\text{NO}_x$  emissions results in a simultaneous reduction of the ignition delay and of the combustion duration (**figure 4.6, c**). This almost fully compensates the detrimental effect of the spark timing delay and results in only a weak decrease of less than 0.5 %-point in fuel conversion efficiency between direct and prechamber ignition (**figure 4.6, b**). In the case of prechamber ignition, the spark timing has no perceptible effect on the fuel conversion efficiency.

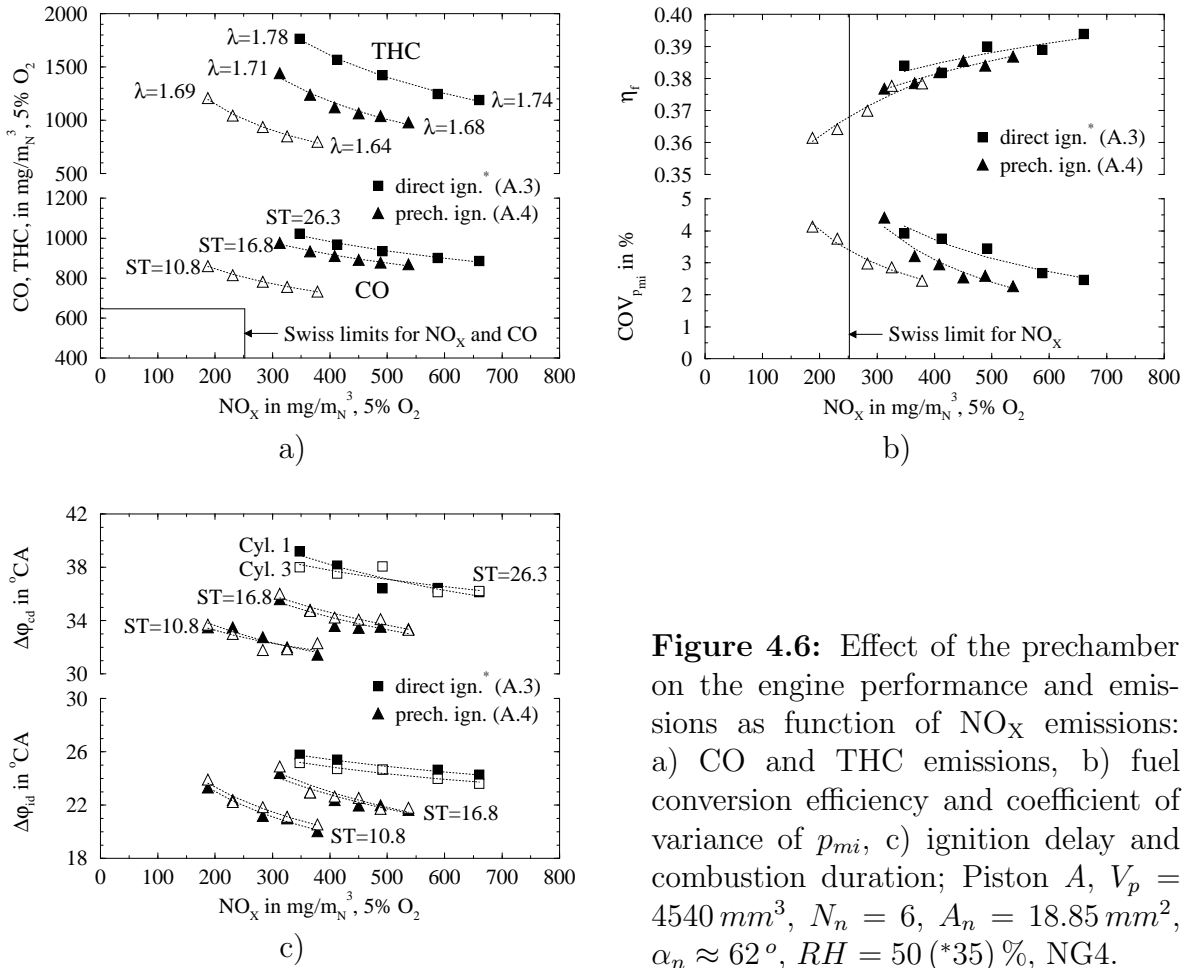


**Figure 4.6:** Effect of the prechamber on the engine performance and emissions as function of  $\text{NO}_x$  emissions: a) CO and THC emissions, b) fuel conversion efficiency and coefficient of variance of  $p_{mi}$ , c) ignition delay and combustion duration; Piston A,  $V_p = 4540 \text{ mm}^3$ ,  $N_n = 6$ ,  $A_n = 18.85 \text{ mm}^2$ ,  $\alpha_n \approx 62^\circ$ ,  $RH = 50$  (\*35)%, NG4.

The cycle-by-cycle variability influences the engine operating stability. It depends on stochastic changes in the cylinder flow field, which affect the ignition conditions and consequently the combustion process. Further, the effect of the flow field stochastic variations on the combustion process is more pronounced in the case of a long combustion duration (the tendency to bulk gas quenching increases when the combustion extends into the expansion phase). An increase of the ignition delay due to local variation of the flow field shifts the combustion into the expansion phase. The exponential reduction of the chemical reaction kinetics with the decrease of temperature during expansion increases the combustion duration and thus amplifies the effect of the change in ignition delay. When considering the same  $\text{NO}_x$  emissions, the improvement of the engine operating stability through the transition from direct to prechamber ignition (**figure 4.6, b**) results from different effects. First, the lower relative air to fuel ratio results in a shorter prechamber ignition delay (**figure 4.5, d**). This reduces the minimum flame kernel volume required to enable flame self propagation and thus the time available to the local flow field to interact with the ignition volume by increasing the mixing with cold unburnt mixture and/or stretching the initial flame kernel. Further, the gas jets should be significantly less sensitive to variation of the main chamber flow field. In addition, the reduction of the ignition delay and combustion duration compensates the effect of the delay of the spark timing and leads to a similar angular position of the end of the combustion process (**figure 4.5, b**). This means that the combustion process does not extend further into the expansion phase and consequently

a more frequent occurrence of bulk gas quenching is not to be expected. Finally, the slightly higher mean combustion temperature during expansion (**figure 4.5, c**) should even reduce the tendency to bulk gas quenching at the end of the combustion process. In the case of the later prechamber ignition timing, the engine operating stability is further improved by a lower relative air to fuel ratio and probably also by stronger gas jets and a higher mean combustion temperature at the end of combustion. Moreover, the lower cycle-by-cycle variability at the later spark timing enables further reduction of the  $\text{NO}_x$  emissions by an increase of the relative air to fuel ratio.

### c) CO and THC emissions

The effect of the transition from direct to prechamber ignition on the CO and THC emissions is presented in **figure 4.6, a**. The delay of the spark timing, enabled by the transition from direct to prechamber ignition, results in an important decrease in CO and THC emissions of  $\approx 26\%$  and  $\approx 50\%$ , respectively.

Several mechanisms are responsible for the presence of unburnt and partially burnt hydrocarbons in the exhaust gas [13, 56, 57]. A certain proportion of the unburnt fuel-air mixture escapes the primary oxidation process (propagation of the flame front). During the compression stroke and the first stage of the combustion process until cylinder peak pressure is reached, unburnt mixture is compressed into the combustion chamber crevices. This unburnt mixture then emerges into the combustion chamber during the expansion stroke. Further, the deterioration of the combustion stability increases the frequency of premature flame front extinction (bulk gas quenching) resulting from a stochastic shift of the combustion process into the expansion phase. Other effects such as lubricating oil and deposit absorption and desorption as well as wall flame quenching are also contributing, but to a more limited extent. Hydrocarbons escaping the primary oxidation process mix with the hot bulk gases and react to form intermediate combustion products like CO and fully oxidised components like  $\text{H}_2\text{O}$  and  $\text{CO}_2$ . The proportion of the different products depends on the local temperature and pressure of the bulk gases when the mixing process occurs and the evolution of the temperature during the expansion and exhaust strokes. This temperature evolution in turn depends on the location of the mixing region relative to the exhaust valve; secondary oxidation reactions occurring close to the exhaust valve freeze earlier because of the strong temperature drop during the exhaust blow down. Below a temperature of about  $850^\circ\text{C}$ , the kinetics of CO oxidation into  $\text{CO}_2$  becomes slower than the kinetics of THC oxidation into  $\text{H}_2\text{O}$  and CO [13]. This seems to indicate that the temperature evolution is even more important for the CO oxidation. Thus, the amount of THC and CO in the exhaust gas mainly depends on the engine operating stability, on the amount of unburnt mixture compressed into the combustion chamber crevices and on the local bulk gas temperature during expansion and exhaust. In turn, the quantity of the unburnt mixture stored in the combustion chamber crevices prior to arrival of the flame front at the crevices entrance principally depends on the crevice volume and on the cylinder pressure. Thus, for a given combustion chamber configuration (ie fixed crevices volume and distribution), a reduction of the cylinder pressure and an early arrival of the flame front at the crevice entrances decrease the amount of hydrocarbons escaping the primary oxidation process. Further, an increase of the bulk gas temper-

ature during expansion and exhaust promotes a more complete chemical reaction into fully oxidised products.

When considering equal  $\text{NO}_x$  emissions, the transition from direct to prechamber ignition (early spark timing) leads to an important decrease of  $\approx 25\%$  in THC emissions and a moderate reduction of  $\approx 7\%$  of the CO emissions (**figure 4.6, a**). Several effects contribute to this result. First, the improvement of the combustion stability (**figure 4.6, b**) tends to reduce the amount of fuel escaping the flame front combustion through bulk gas quenching. Further, the important decrease in cylinder pressure during combustion (**figure 4.5, a**) and the more rapid arrival of the flame front at the crevices entrance resulting from the penetration of the gas jets into the main combustion chamber should reduce the amount of hydrocarbon escaping the primary oxidation process. Finally, the slightly higher mean combustion temperature during expansion (**figure 4.5, c**) promotes a more complete secondary oxidation. The delay of the prechamber ignition timing results in a further large decrease of  $\approx 35\%$  and  $\approx 20\%$  in THC and CO emissions, respectively. This is thought to be due to a further improvement of engine operating stability, to a complementary decrease of the cylinder pressure, as well as a deeper penetration of the gas jet into the combustion chamber. The expected earlier arrival of the flame front at the crevice entrance should reduce the amount of hydrocarbon located in the combustion chamber dead volume during the primary oxidation process. This effect is particularly important in the case of the piston top land crevice and may partly explain the more pronounced reduction of CO emissions. Due to its remote location from the exhaust valve, the unburnt hydrocarbon emerging from this particular crevice has more time to react to generate CO, which is then partially oxidised into  $\text{CO}_2$ . The chemical reactions of hydrocarbons emerging from other crevices located closer to the exhaust valve are more likely to rapidly freeze during the exhaust blow down, thus leaving proportionally more unburnt hydrocarbon than carbon monoxide in the exhaust gas. This assumption is supported by the results of a previous study [3, 4, 33] which show that the reduction of the combustion chamber dead volume located between the cylinder liner, the cylinder head and the gasket results in a strong reduction of the THC emissions, but only in a slight decrease in CO emissions. The larger reduction of the CO emissions may also partly originate in the significantly higher mean combustion temperature during expansion. An increase of the bulk gases temperature during the expansion and the exhaust stroke delays the instant where the THC oxidation kinetics start to differ significantly from the CO oxidation kinetics and progressively more CO is generated than can be oxidised into  $\text{CO}_2$ . This increases the proportion of hydrocarbon fully oxidised before both reaction kinetics are simultaneously quenched during exhaust blow down.

#### d) Turbocharger operation

This section aims to briefly analyse and discuss the influence of the transition from direct to prechamber ignition on the turbocharger operation. In order to support the discussion, the total pressure and temperature at the inlet and outlet of the compressor and turbine are presented as functions of  $\text{NO}_x$  emissions in **figure 4.7**.

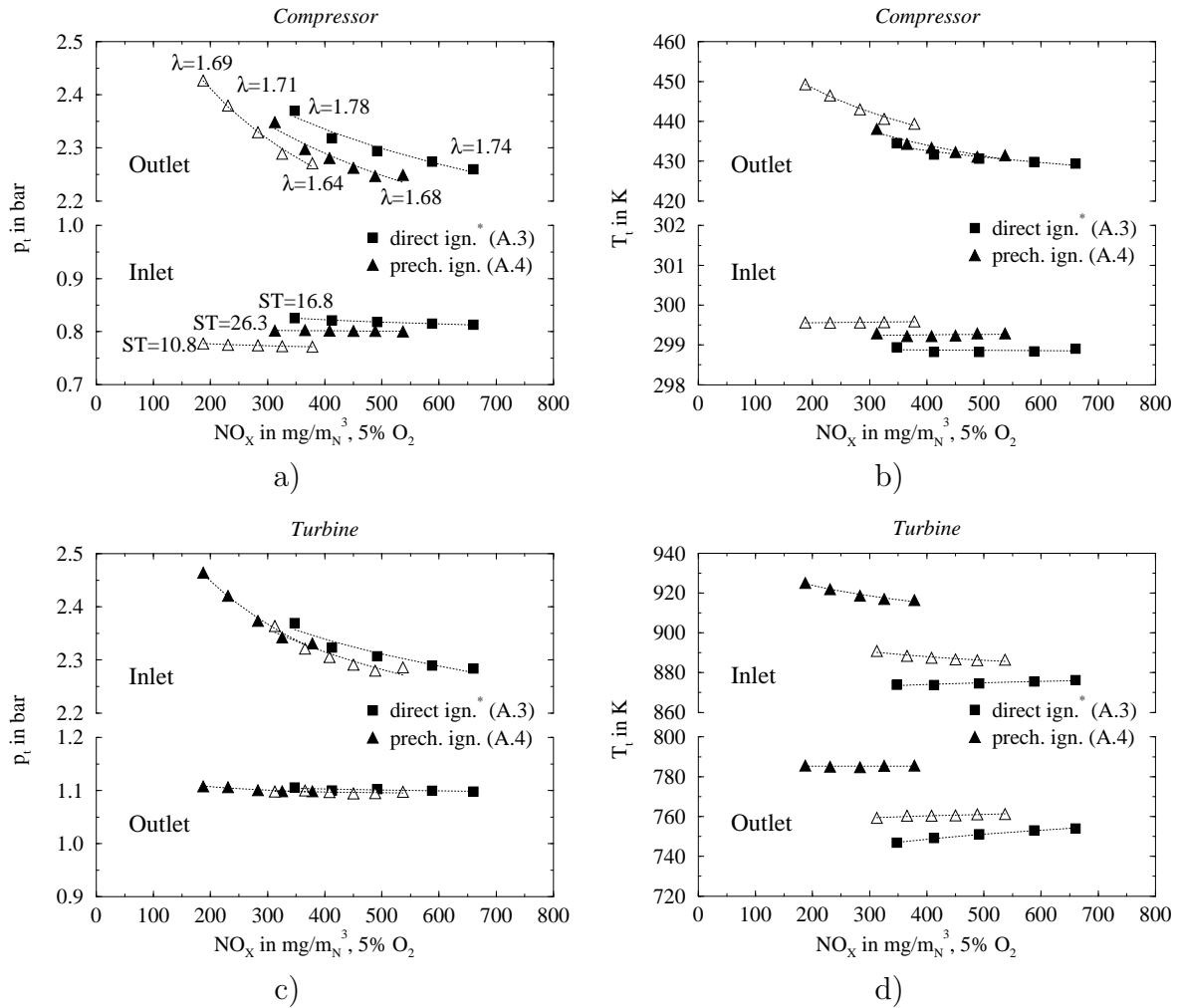


**Figure 4.7:** Effect of the prechamber on the turbocharger operating characteristics as function of  $\text{NO}_x$  emissions; a) compressor total pressure, b) compressor total temperature, c) turbine total pressure, d) turbine total temperature; Piston A,  $V_p = 4540 \text{ mm}^3$ ,  $N_n = 6$ ,  $A_n = 18.85 \text{ mm}^2$ ,  $\alpha_n \approx 62^\circ$ ,  $RH = 50$  (\*35) %, NG4.

When considering the same  $\text{NO}_x$  emissions, the transition from direct to prechamber ignition requires a reduction of the relative air to fuel ratio. This results in a decrease of the unburnt mixture mass flow rate required to achieve the nominal engine brake power output and consequently in a reduction of the boost pressure (**figure 4.7, a**). This is achieved through engine throttling and results in a decrease of the pressure at compressor inlet. The change in compressor operating conditions does however not significantly affect the temperature at compressor outlet (**figure 4.7, b**). When considering the turbine operation, the effect of the decrease in mass flow rate is to a large extent compensated by the increase in temperature at the end of the expansion stroke and therefore leads to no significant change in the pressure before turbine (**figure 4.7, c**). However, the increase of the temperature at the end of the expansion stroke yields higher temperature at turbine outlet (**figure 4.7, d**). This enables a larger heat recovery in cogeneration.

The engine operation at part throttle results in a relatively high engine pumping work, which directly affects the engine fuel economy. This means that the engine

operation close to wide open throttle with an optimised turbocharger should achieve a somewhat higher fuel conversion efficiency. This particular aspect is treated in section 4.4.10.

#### 4.4.2 Nozzle orifice cross sectional area

Following the approach considered in the numerical simulation, the total nozzle orifice cross sectional area ( $A_n$ ) was first decreased by 50% through a reduction of the nozzle orifice diameter from 2.00 ( $A_n = 18.85 \text{ mm}^2$ ) to 1.41 mm ( $A_n = 9.37 \text{ mm}^2$ ). Due to ignition instabilities, the nozzle orifice diameter was then increased to 1.73 mm ( $A_n = 14.10 \text{ mm}^2$ ), which corresponds to a 25% reduction of total nozzle orifice cross sectional area from the base prechamber. Finally, due to the relative high sensitivity of this parameter, the total cross sectional area was not increased by 50% as in the numerical simulation but by only 25% through the use of nozzle orifices of diameter 2.24 mm ( $A_n = 23.64 \text{ mm}^2$ ). The investigation was performed with piston A and prechambers featured with an internal volume of  $4540 \text{ mm}^3$  and 6 nozzle orifices, unevenly distributed and oriented at an angle of  $\approx 62^\circ$  from the prechamber axis. The engine was operated at a constant spark timing of  $10.8^\circ \text{CA}_{BTDC}$ .

#### Results summary

The reduction of the total nozzle orifice cross sectional area from 23.64 to  $9.37 \text{ mm}^2$  leads to:

- a significant intensification and acceleration of the combustion process (**figure 4.8, b** and **figure 4.9**)

and when considering the same  $\text{NO}_x$  emissions:

- similar CO and THC emissions (**figure 4.10, a**)
- a moderate or no effect on the fuel conversion efficiency (**figure 4.10, b**)
- no perceptible alteration of the cycle-by-cycle variability (**figure 4.10, b**)

Further, the results tend to indicate the existence of an optimal size of the total nozzle orifice cross sectional area close to  $18.85 \text{ mm}^2$  that achieves the lowest  $\text{NO}_x$  emissions.

#### Analysis and discussion

The results for the four different total nozzle orifice cross sectional areas are represented in **figure 4.8**, **figure 4.9** and **figure 4.10**. The reduction of the total nozzle

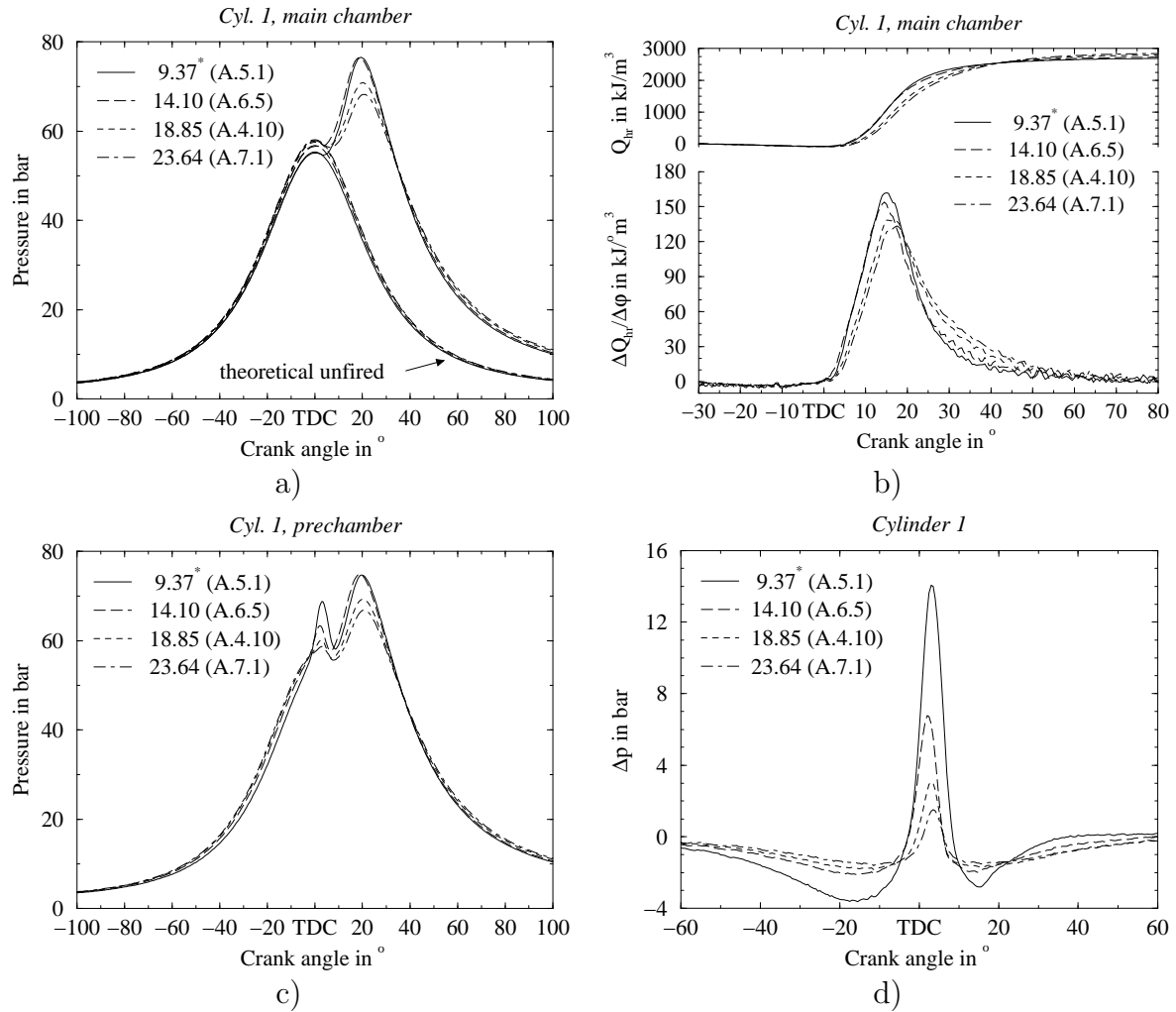


**Figure 4.8:** Influence of the total nozzle orifice cross sectional area on the engine cycle in cylinder 1 at constant relative air to fuel ratio; main chamber pressure (a), heat-release rate and integral (b), prechamber pressure (c) and pressure difference between pre- and main chamber (d); Piston  $A$ ,  $V_p = 4540 \text{ mm}^3$ ,  $N_n = 6$ ,  $\alpha_n \approx 62^\circ$ ,  $ST = 10.8^\circ\text{C}$   $A_{BTDC}$ ,  $\lambda = 1.64$  (\*1.62), NG4.

orifice cross sectional area produces an important increase in the pressure difference between pre- and main chamber (**figure 4.8, d**), which significantly accelerates and intensifies the main chamber combustion process (**figure 4.8, b**). This results in an important decrease of the combustion duration (**figure 4.9** and **figure 4.10, c**). Due to the occurrence of ignition failure, a reduction of the area to  $9.37 \text{ mm}^2$  no longer enables the engine operation at a relative air to fuel ratio above 1.62. Consequently, this strongly limits the potential to reduce the  $\text{NO}_x$  emissions. When considering the same  $\text{NO}_x$  emissions and comparing only the three larger values, the reduction of the total nozzle orifice cross sectional area leads to similar CO and THC emissions (**figure 4.10, a**). A reduction of the area from  $23.64$  to  $18.85 \text{ mm}^2$  yields an increase in fuel conversion efficiency of more than 0.5 %-point, but a further reduction from  $18.85$  to  $14.10 \text{ mm}^2$  does not significantly affect the efficiency (**figure 4.10, b**). The total nozzle orifice cross sectional area has no perceptible effect on the cycle-by-cycle variability. This is illustrated by similar values of the coefficient of variance of  $p_{mi}$ . Finally, the results indicate the existence of an optimal size of the total nozzle orifice



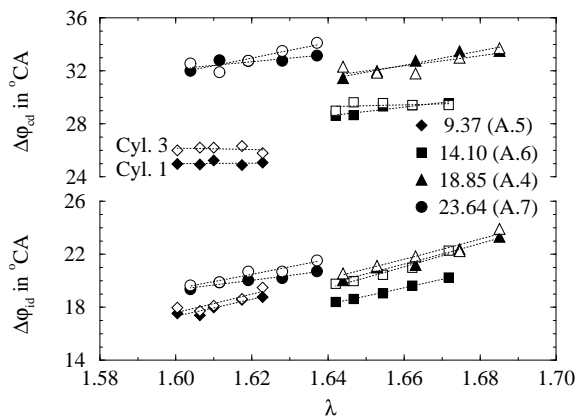


**Figure 4.9:** Influence of total nozzle orifice cross sectional area on the ignition delay and combustion duration as function of relative air to fuel ratio; Piston A,  $V_p = 4540 \text{ mm}^3$ ,  $N_n = 6$ ,  $\alpha_n \approx 62^\circ$ ,  $ST = 10.8^\circ \text{CA}_{BTDC}$ , NG4.

cross sectional area which achieves the lowest  $\text{NO}_x$  emissions. In the case of the nozzle orifice configurations tested, the optimal size is close to  $18.85 \text{ mm}^2$ .

At constant relative air to fuel ratio, the reduction of the total nozzle orifice cross sectional area yields an increase of the pressure drop between main chamber and prechamber during the compression stroke, which is more pronounced in the case of the smallest orifices (**figure 4.8, d**). Further, it results in a significant increase in prechamber pressure before main chamber ignition (**figure 4.8, c**). The combination of the following effects could contribute to this result. First, the higher turbulence generated in the prechamber by smaller orifices (**figure 3.10, b**) tends to promote the prechamber combustion process. Further, the reduction of the cross sectional area restricts the flow across the nozzle orifices and therefore tends to increase the prechamber pressure before main chamber ignition. Finally, the temperature increase produced by the pressure increase (**figure 4.8, c**) should further promote the prechamber combustion process by the acceleration of the chemical reaction kinetics. The almost exponential increase of the pressure difference between pre- and main chambers (**figure 4.8, d**) seems to indicate that the faster prechamber combustion largely over-compensates the detrimental effects of the higher pressure drop between main chamber and prechamber at spark timing and the consequent reduction of unburnt mixture transferred to the prechamber.

When considering the same relative air to fuel ratio, the increase of the pressure difference between pre- and main chambers significantly intensifies and accelerates the main chamber combustion process (**figure 4.8, b**). It results in a steeper increase of the heat-release rate at the beginning of the combustion process (**figure 4.8, b**) and in a shorter combustion duration (**figure 4.9**). In turn, the intensification and acceleration of the combustion process produces an increase in main chamber pressure (**figure 4.8, a**). As already discussed in the previous section, the larger pressure difference between pre- and main chamber is expected to generate stronger gas jets which penetrate deeper into the main combustion chamber. Based on this, the steeper increase of the heat-release rate at the beginning of the combustion process could be due to a wider main chamber initial flame front surface resulting from larger gas jet wakes. In turn, the shorter time required by a wider initial flame front to travel across the entire combustion chamber would explain the reduction of the combustion duration. The reduction of the total nozzle orifice cross sectional area from  $23.64$  to  $14.10 \text{ mm}^2$  yields a perceptible decrease of the ignition delay (**figure 4.9**). However, a further

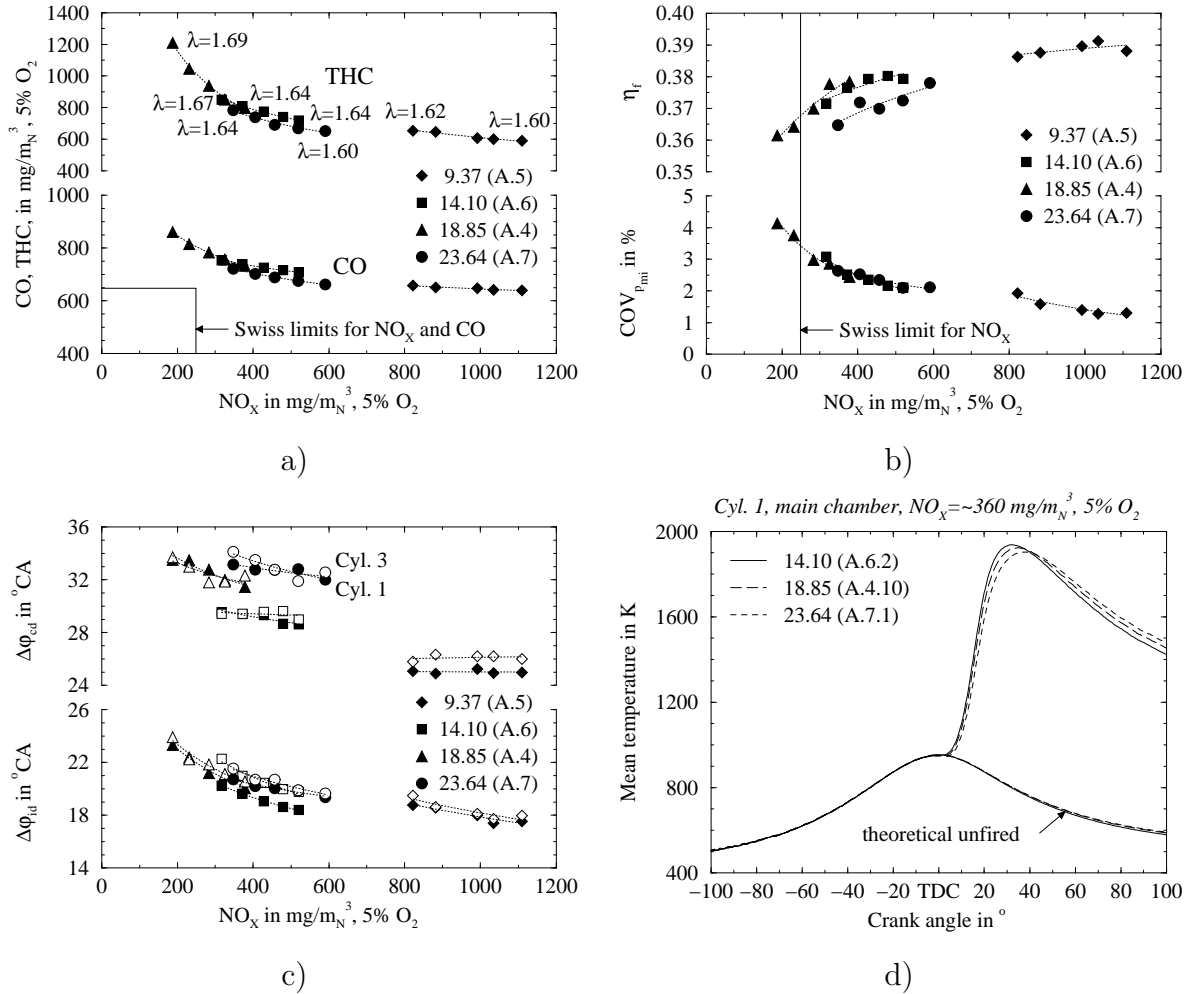


**Figure 4.10:** Influence of the total nozzle orifice cross sectional area on the engine performance and emissions as function of  $\text{NO}_x$  emissions: a) CO and THC emissions, b) fuel conversion efficiency and coefficient of variance of  $p_{mi}$ , c) ignition delay and combustion duration, d) mean combustion temperature at  $\text{NO}_x \approx 360 \text{ mg}/\text{m}^3$ , 5%  $\text{O}_2$ ; Piston A,  $V_p = 4540 \text{ mm}^3$ ,  $N_n = 6$ ,  $\alpha_n \approx 62^\circ$ ,  $ST = 10.8^\circ\text{CA}_{BTDC}$ , NG4.

decrease from 14.10 to  $9.37 \text{ mm}^2$  results in a moderate increase of the ignition delay. This may indicate that, down to a given orifice diameter, the promotion of the main chamber ignition process by stronger gas jets over-compensates the detrimental effect of a higher prechamber turbulence on the prechamber ignition. Below this value, the prechamber ignition conditions may rapidly deteriorate.

The prechamber with the smallest total nozzle orifice cross sectional area does not enable the engine operation with a relative air to fuel ratio above 1.62. From this value, prechamber ignition failure occurs at a relatively low frequency, which immediately increases the coefficient of variance of the indicated mean effective pressure far above the usually admitted maximum value of 5% (only stable operating points were measured). The occasional prechamber ignition failure seems to originate in the higher turbulence intensity at the ignition point (**figure 3.10, b**), which perturbs the arc discharge and the initial flame kernel generation [50]. The occurrence of ignition instabilities at a low value of relative air to fuel ratio strongly limits the potential to reduce the  $\text{NO}_x$

emissions (**figure 4.10, a**). Therefore, further discussion will essentially concentrate on the three larger cross sectional areas.

When considering the same  $\text{NO}_x$  emissions, the reduction of the total nozzle orifice cross sectional area results in a decrease of the ignition delay and combustion duration (**figure 4.10, c**). Despite the significant decrease in combustion duration, the reduction of cross sectional area has no perceptible effect on the engine operating stability (**figure 4.10, b**). This seems to indicate that the gain in main chamber combustion stability is balanced by the deterioration of the prechamber ignition conditions due to the increase in turbulence intensity. However, in the case of the cross sectional area of 14.10 and 23.64  $\text{mm}^2$ , a more rapid deterioration of the engine operating stability above a certain value of relative air to fuel ratio limits the potential to reduce the  $\text{NO}_x$  emissions. In the case of the cross sectional area of 14.10  $\text{mm}^2$ , this seems to be associated with the higher turbulence intensity at the ignition point, similarly to the case with 9.37  $\text{mm}^2$ . The early deterioration of combustion stability with the largest cross sectional area is thought to originate in variations of the weak gas jets, which become proportionally more sensitive to prechamber ignition and combustion fluctuations associated with the increase in relative air to fuel ratio. In consequence, this tends to indicate that there is an optimum in total nozzle orifice cross sectional area for a given prechamber configuration. The decrease of combustion duration resulting from the reduction of cross sectional area from 23.64 to 18.85  $\text{mm}^2$  leads to an increase of fuel conversion efficiency of more than 0.5 %-point (**figure 4.10, b**). However, the further decrease of combustion duration produced by the reduction of cross sectional area from 18.85 to 14.10  $\text{mm}^2$  does not significantly affect the fuel conversion efficiency. This could be a result of a higher heat transfer to the main combustion chamber wall due the deeper penetration of the gas jets.

At equal  $\text{NO}_x$  emissions, the reduction of the total nozzle orifice cross sectional area leads to no significant change in CO and THC emissions (**figure 4.10, a**). This may be explained by the offset of the two following conflicting effects: firstly, the deeper penetration of the gas jets induced by a smaller nozzle orifice cross sectional area tends to reduce the amount of unburnt mixture compressed in the combustion chamber crevices by an early arrival of the flame front at their entrance. Secondly, the intensification of the combustion process by stronger gas jets increases the cylinder pressure. On one hand, this tends to increase the quantity of unburnt mixture flowing into the crevices. On the other hand, it decreases the bulk gases temperature during expansion (**figure 4.10, d**), which is likely to reduce the proportion of unburnt hydrocarbons transformed into fully oxidised products during the secondary combustion process.

### 4.4.3 Number of nozzle orifices

When keeping a constant total nozzle orifice cross sectional area, the numerical simulation shows that an increase in the number of orifices from 6 to 8 results in a further but moderate rise in turbulence intensity at the location of the ignition point (**figure 3.16, b**). Correspondingly, a decrease from 6 to 4 orifices strongly reduces the turbulence intensity. In order to avoid a too high turbulence intensity at the ignition

point, which is suspected to produce prechamber ignition failure, only a prechamber alternative with 4 nozzle orifices was tested. However, to take advantage of stronger gas jets, the total nozzle orifice cross sectional area considered was  $14.10 \text{ mm}^2$ , which partly compensates for the decrease in prechamber turbulence intensity (**figure 3.10**). In order to keep a constant total nozzle orifice cross sectional area, the nozzle orifice diameter was increased from  $1.73 \text{ mm}$ , in the case of 6 orifices, to  $2.12 \text{ mm}$ , in the case of 4 orifices. The investigation was performed with piston *A* and prechambers featured with an internal volume of  $4540 \text{ mm}^3$  and orifices unevenly distributed and oriented at an angle of  $\approx 62^\circ$  from the prechamber axis. The engine was operated at a constant spark timing of  $10.8^\circ \text{CA}_{BTDC}$ .

## Results summary

The reduction of the number of nozzle orifices from 6 to 4, while keeping a constant total nozzle orifice cross sectional area, results in:

- a shift of the centre of gravity of the combustion process into the expansion phase (**figure 4.11, b**) and a weak decrease in combustion duration (**figure 4.12**)

and when considering the same  $\text{NO}_x$  emissions:

- a decrease of  $\approx 5\%$  and  $\approx 9\%$  in CO and THC emissions, respectively (**figure 4.13, a**)
- a slight increase in fuel conversion efficiency (**figure 4.13, b**)
- a reduction of the cycle-by-cycle variability at low  $\text{NO}_x$  emissions (**figure 4.13, b**)

## Analysis and discussion

The results corresponding to the two different cases are represented together in **figure 4.11**, **figure 4.12** and **figure 4.13**. The reduction of the number of nozzle orifices from 6 to 4, while keeping a constant total nozzle orifice cross sectional area, does not affect significantly the prechamber combustion process (**figure 4.11, c**). This results in a similar pressure difference between pre- and main chamber (**figure 4.11, d**). However, this leads to a shift of the centre of gravity of the main chamber combustion process into the expansion phase (**figure 4.11, b**) and a weak reduction of the combustion duration (**figure 4.12**). When considering equal  $\text{NO}_x$  emissions, the moderate decrease in combustion duration yields a slight increase in fuel conversion efficiency (**figure 4.13, b**). Further, the transition from 6 to 4 orifices results in reduction of  $\approx 5\%$  and  $\approx 9\%$  of the CO and THC emissions, respectively (**figure 4.13, a**). Finally, this leads to a significant improvement of the cycle-by-cycle variability, particularly at low  $\text{NO}_x$  emissions (**figure 4.13, b**).

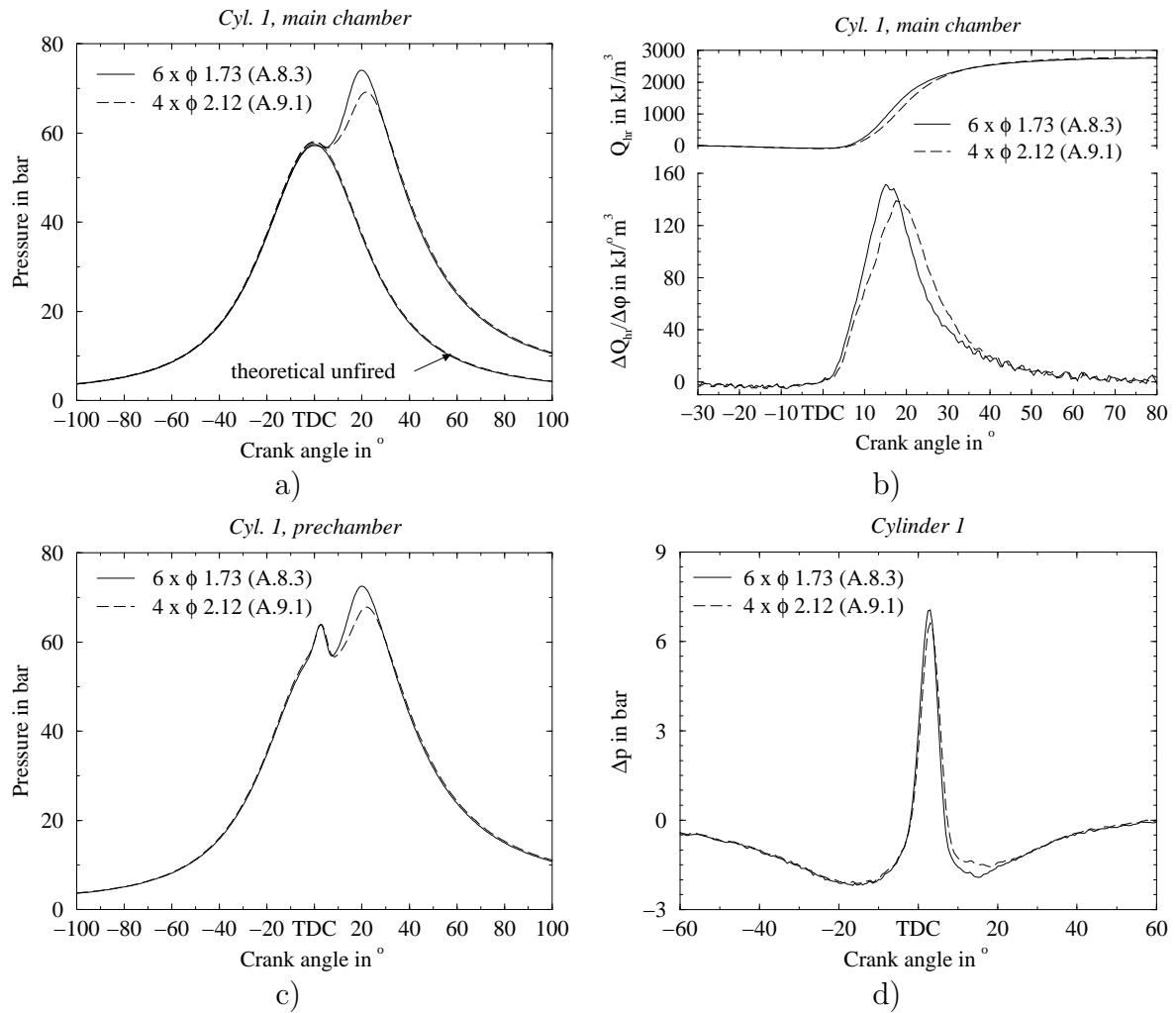


**Figure 4.11:** Influence of the number of nozzle orifices on the engine cycle in cylinder 1 at constant relative air to fuel ratio: main chamber pressure (a), heat-release rate and integral (b), prechamber pressure (c) and pressure difference between pre- and main chamber (d); Piston  $A$ ,  $V_p = 4540 \text{ mm}^3$ ,  $A_n = 14.10 \text{ mm}^2$ ,  $\alpha_n \approx 62^{\circ}$ ,  $ST = 10.8^{\circ}\text{C}A_{BTDC}$ ,  $\lambda = 1.65$ , NG5.

Due to the constant total nozzle orifice cross sectional area, the reduction of the number of orifices produces no change in the pressure drop between main chamber and prechamber during compression (**figure 4.11, d**). The lower turbulence intensity in the prechamber with 4 orifices (**figure 3.16, b**) does not significantly affect the prechamber combustion process, which results in a similar prechamber pressure evolution before main chamber combustion (**figure 4.11, c**). This probably results from the compensation of the two following effects. On one hand, the lower turbulence generated with 4 orifices is expected to attenuate the heat and mass transfer at the level of the flame front, thus slowing down its propagation. On the other hand, it is also likely to decrease the heat transfer to the prechamber wall. In turn, this tends to increase the unburnt mixture temperature and consequently to accelerate the chemical reaction kinetics.

Despite a similar prechamber combustion process, the reduction of the number of nozzle orifices yields a slower first part and a faster second part of the main chamber combustion process (**figure 4.11, b**). The second part over-compensates the effect of the slower first part, which results in a slight reduction of the combustion duration (**figure 4.12**). Further, the change in the rate of heat-release induces a shift of the centre of gravity of the combustion into the expansion phase. The reduction of the number of orifices decreases the number of main chamber distributed ignition sources. It may also to some extent reduce the turbulence generated in the main chamber by the converging flow to the orifices during the compression stroke. Therefore, a less uniform distribution of the turbulence in the vicinity of the prechamber nose and of the gas jets in the main combustion chamber may explain the lower rate of heat released during the first part of the main chamber combustion process. The acceleration of the second part of the combustion process is likely to be due to a significant increase of the initial main chamber flame front surface. This would support the assumption that the reduction of the number of nozzle orifices increases the size and penetration of the gas jets. The shift of the centre of gravity of the combustion process into the expansion phase results in a significant decrease in main chamber peak cylinder pressure (**figure 4.11, a**).

In the case of 4 nozzle orifices, the lower maximum combustion temperature resulting from the reduction of peak cylinder pressure enables the engine operation with a slightly richer fuel-air mixture to achieve equal  $\text{NO}_x$  emissions (**figure 4.13, a**). This reduces somewhat further the combustion duration (**figure 4.13, c**), which results in a slightly higher fuel conversion efficiency (**figure 4.13, b**). The lower prechamber turbulence intensity generated by 4 nozzle orifices at the ignition location (**figure 3.16, b**) tends to reduce the cycle-by-cycle variations of the prechamber combustion process. Further, the results discussed in the previous section seem to indicate that the fluctuations of the prechamber combustion process have a lower effect on the main chamber combustion process ignited by larger gas jets. This may explain why the reduction of the number of nozzle orifices yields a better main chamber combustion stability at constant  $\text{NO}_x$  emissions (**figure 4.13, b**). The reason why the improvement is greater for the highest values of relative air to fuel ratio however remains unclear.

When considering the same  $\text{NO}_x$  emissions, the transition from 6 to 4 orifices results in reduction of  $\approx 5\%$  and  $\approx 9\%$  of the CO and THC emissions, respectively (**figure 4.13, a**). At this stage, it is possible to make the following considerations. The lower cylinder pressure (**figure 4.11, a**) tends to reduce the amount of unburnt

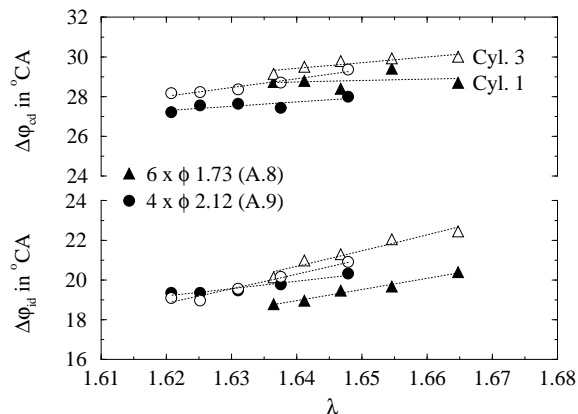


**Figure 4.12:** Influence of the number of nozzle orifices on the ignition delay and combustion duration as function of relative air to fuel ratio; Piston A,  $V_p = 4540 \text{ mm}^3$ ,  $A_n = 14.10 \text{ mm}^2$ ,  $\alpha_n \approx 62^\circ$ ,  $ST = 10.8^\circ\text{CA}_{BTDC}$ , NG5.

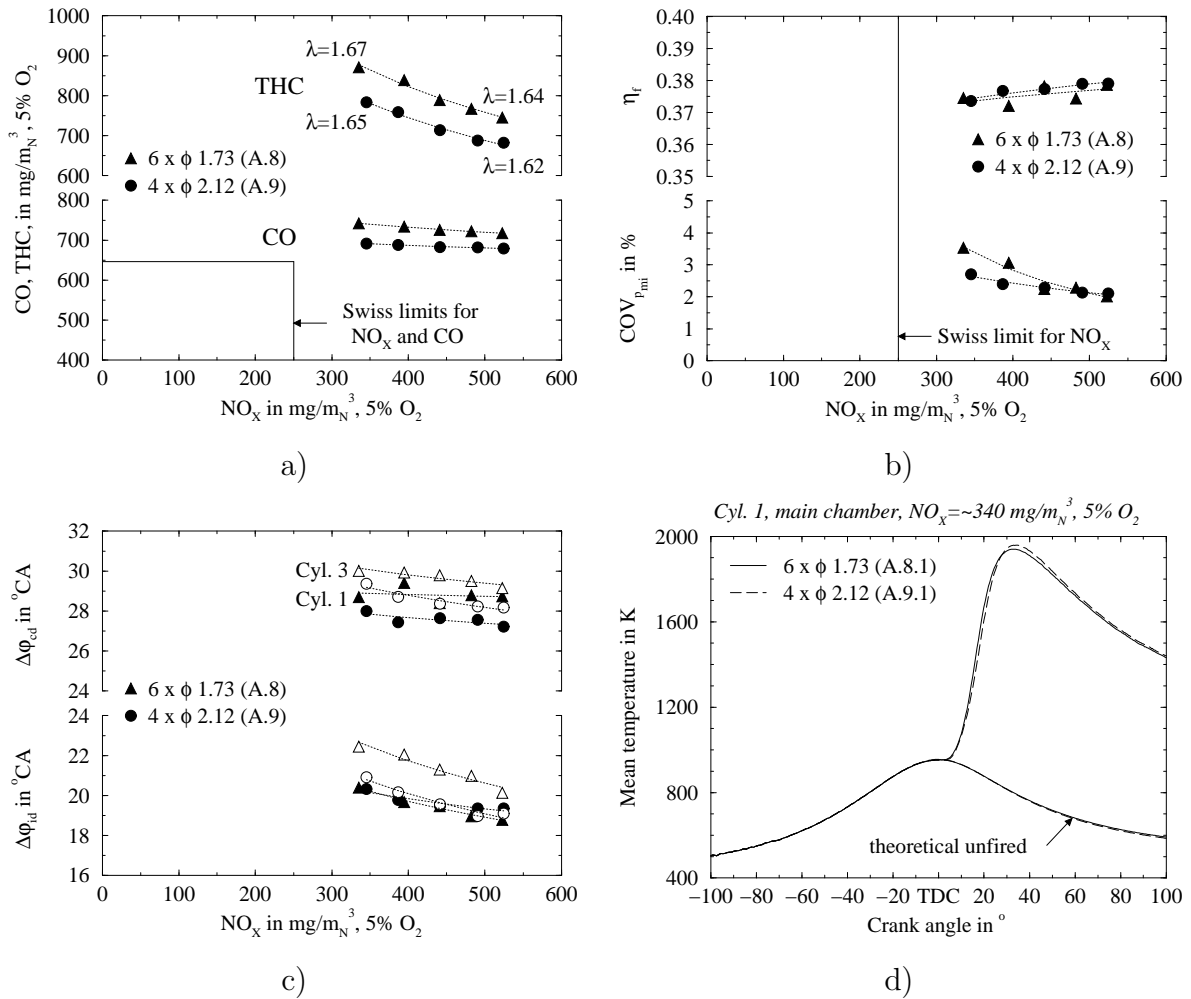


**Figure 4.13:** Influence of the number of nozzle orifices on the engine performance and emissions as function of  $\text{NO}_x$  emissions: a) CO and THC emissions, b) fuel conversion efficiency and coefficient of variance of  $p_{mi}$ , c) ignition delay and combustion duration, d) mean combustion temperature in cylinder 1 at  $\text{NO}_x \approx 340 \text{ mg}/\text{m}_N^3$ , 5%  $\text{O}_2$ ; Piston A,  $V_p = 4540 \text{ mm}^3$ ,  $A_n = 14.10 \text{ mm}^2$ ,  $\alpha_n \approx 62^\circ$ ,  $ST = 10.8^\circ\text{C}_{BTDC}$ , NG5.

mixture compressed into the combustion chamber crevices and thus escaping the primary oxidation process. Further, the deeper penetration of the gas jets should enable the flame front to reach earlier the region of the main chamber which feeds the squish region when the piston starts to move down after the end of compression. The rapid flow motion into the squish region induced by the momentary local depression is expected to promote an early arrival of the flame front at some parts of the cylinder head gasket and piston top land crevice entrances. However, the change in combustion process does not affect significantly the mean temperature during expansion (figure 4.13, d), which should lead to similar chemical reaction kinetics during the secondary oxidation process. In consequence, the lower CO and THC emissions seem to mainly originate in a reduction of the amount of unburnt mixture located in the combustion chamber crevices during the primary oxidation.

Despite the better engine operating stability with 4 nozzle orifices, the relative air to fuel ratio could not be increased beyond 1.65 in order to further reduce the  $\text{NO}_x$

emissions. Above this value, ignition failure started to occur. This phenomenon is not related to the change in prechamber configuration but to the particular spark plug used. This problem is discussed in detail in the next section.

#### 4.4.4 Nozzle orifice distribution

The azimuthal orientation of the nozzle orifices was established in order to achieve a relatively uniform distribution of the gas jets into the main combustion chamber. Due to the tilted prechamber position and its location set off from the main combustion chamber axis, this led to an uneven distribution of the nozzle orifices around the prechamber nose (**figure 4.14, a**) (see also section 2.2 and appendix A.1). In order to evaluate the influence of the nozzle orifice distribution on the combustion process, a set of prechambers with an even distribution (**figure 4.14, b**) and an orientation of  $60^\circ$  of the orifices (axisymmetrical prechamber nose) was manufactured and tested on the engine. The investigation was performed with piston *A* and prechambers featured with an internal volume of  $4540 \text{ mm}^3$  and 6 nozzle orifices<sup>3</sup> of diameter  $1.73 \text{ mm}$  ( $A_n = 14.10 \text{ mm}^2$ ). The engine was operated at a constant spark timing of  $10.8^\circ CA_{BTDC}$ .

#### Results summary

The transition from an uneven to an even distribution of the nozzle orifices leads to:

- a significant decrease in combustion duration (**figure 4.15**)

and when considering the same  $\text{NO}_x$  emissions:

- a slight increase in CO and THC emissions (**figure 4.17, a**)
- an increase in fuel conversion efficiency of  $\approx 0.5$  %-point (**figure 4.17, b**)
- a significant increase of the cycle-by-cycle variability (**figure 4.17, b**)

#### Analysis and discussion

The results discussed in this section are presented in **figure 4.15**, **figure 4.16**, **figure 4.17** and **figure 4.18**. Part of the results of cylinder 3 are also presented because they are leading to an interpretation which may be inconsistent with the one based on the results of cylinder 1. The main purpose is here to show that a clear

---

<sup>3</sup>Several series of prechamber noses were produced together in order to save manufacturing time. Therefore, it was not always possible to straightaway combine the most favourable configuration parameters



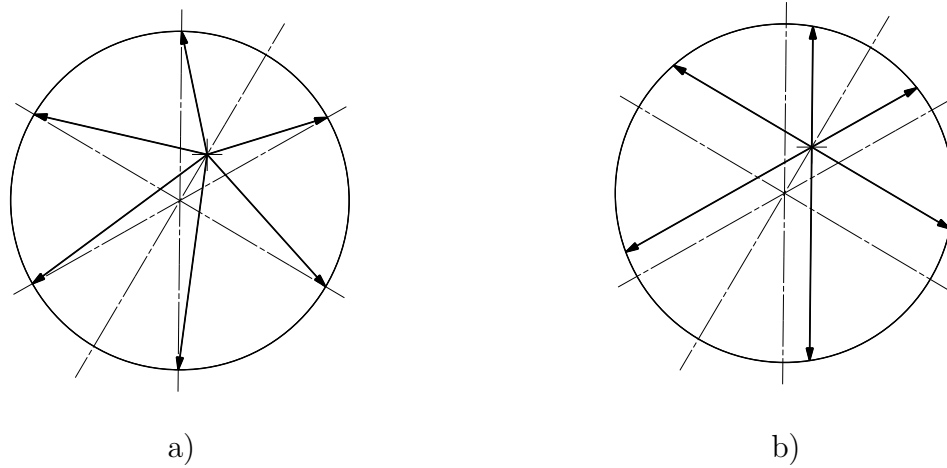


**Figure 4.14:** Theoretical path of the gas jet generated by the nozzle orifice distribution around the prechamber nose: a) uneven, b) even.

trend cannot be identified in the figures representing the evolution of the pressure, the heat-release rate and integral as well as the mean combustion temperature during the engine cycle. This consequently limits the possible interpretation of the results.

The transition from uneven to even nozzle orifice distribution does not affect the prechamber flow dynamics and combustion process prior to main chamber ignition (**figure 4.16, e**). However, this leads to a significant decrease in combustion duration (**figure 4.15**). When considering equal  $\text{NO}_x$  emissions, the transition from uneven to even nozzle orifice distribution leads to a slightly longer ignition delay and a shorter combustion duration (**figure 4.17, c**). The somewhat faster combustion more than compensates the increase in ignition delay, which results in a moderate increase in fuel conversion efficiency of  $\approx 0.5$  %-point (**figure 4.17, b**). However, the even nozzle orifice distribution yields a higher cycle-by-cycle variability. Finally, The transition from uneven to even nozzle orifice distribution leads to somewhat higher CO and THC emissions (**figure 4.17, a**).

At constant relative air to fuel ratio, the change in nozzle orifice configuration does not significantly modify the flow between the main chamber and the prechamber during compression, giving almost the same pressure drop across the orifices (**figure 4.16, e**). Further, the identical evolution of the pressure difference between pre- and main chamber after spark timing ( $10.8^\circ\text{CA}_{BTDC}$ ) shows that the prechamber combustion process is not significantly affected by the change in nozzle orifice distribution and orientation. This indicates that the trends established on the basis of the numerical simulation, considering an axisymmetrical prechamber for simplification, should not significantly be altered by the non-uniform distribution of the nozzle orifices. The large difference in ignition delay between cylinder 1 and 3 in the case of the uneven nozzle orifice distribution (**figure 4.15**) makes it difficult to evaluate the influence of the nozzle orifice distribution on the main chamber combustion process (**figure 4.16, c and d**). However, at constant relative air to fuel ratio, the even distribution of nozzle orifices clearly leads to a significant decrease of the combustion duration in both cylinders (**figure 4.15**).

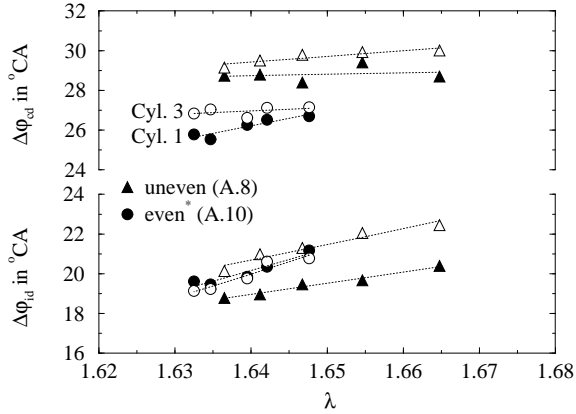


**Figure 4.15:** Influence of nozzle orifice distribution on the ignition delay and combustion duration as function of relative air to fuel ratio; Piston A,  $V_p = 4540 \text{ mm}^3$ ,  $N_n = 6$ ,  $A_n = 14.10 \text{ mm}^2$ ,  $\alpha_n \approx 62^\circ$  ( $^* = 60^\circ$ ),  $ST = 10.8 \text{ }^\circ\text{CA}_{BTDC}$ , NG5.

Considering the same nozzle orifice number and diameter as well as a similar prechamber combustion process, the main chamber combustion duration essentially depends on the distribution of the ignition source in the unburnt mixture. In turn, this distribution simultaneously depends on the distribution of the nozzle orifices and the penetration of the hot gas jets issuing from the prechamber. In the case of a deep gas jet penetration, an uneven distribution results in a better distribution of the ignition sources in the unburnt mixture located away from the prechamber nose. On the other hand, in the case of a relatively short penetration, an even distribution achieves a more uniform distribution of the ignition sources in the vicinity of the prechamber nose. The shorter combustion duration obtained with the even nozzle orifice distribution seems to indicate a relatively moderate gas jet penetration.

The somewhat faster combustion induced by the even nozzle orifice distribution requires a moderate increase in relative air to fuel ratio in order to achieve the same  $\text{NO}_x$  emissions (**figure 4.17, b**). Despite the small increase in ignition delay and combustion duration associated with the increase in relative air to fuel ratio, the transition from uneven to even nozzle orifice distribution results in a moderate increase in fuel conversion efficiency of  $\approx 0.5$  %-point. For equal  $\text{NO}_x$  emissions, the even nozzle orifice distribution yields somewhat higher CO and THC emissions (**figure 4.17, a**). Two different phenomena could contribute to this result. On one hand, the lower concentration of the gas jets in the main combustion chamber region characterised by the largest distance between prechamber nose and cylinder wall (**figure 4.14, a**) may delay the flame front arrival at the remotest location of the piston top land and cylinder head gasket crevice entrances. On the other hand, the higher cycle-by-cycle variability (**figure 4.17, b**) may indicate an increase of the frequency of bulk gas quenching. Both phenomena tend to increase the amount of unburnt mixture escaping the primary oxidation process. When considering the secondary oxidation process, the change in the main chamber combustion process does not affect significantly the mean temperature during late expansion (**figure 4.18, a and b**). This should result in a similar chemical reaction kinetics.

The engine operation with the even nozzle orifice distribution is characterised by a higher cycle-by-cycle variability which cannot directly be explained on the basis of the experimental results. As identified during a later test, the degradation of the combustion stability seems to mainly originate in the particular evolution of the spark plug behaviour after several tens of operating hours, causing an increase in the frequency

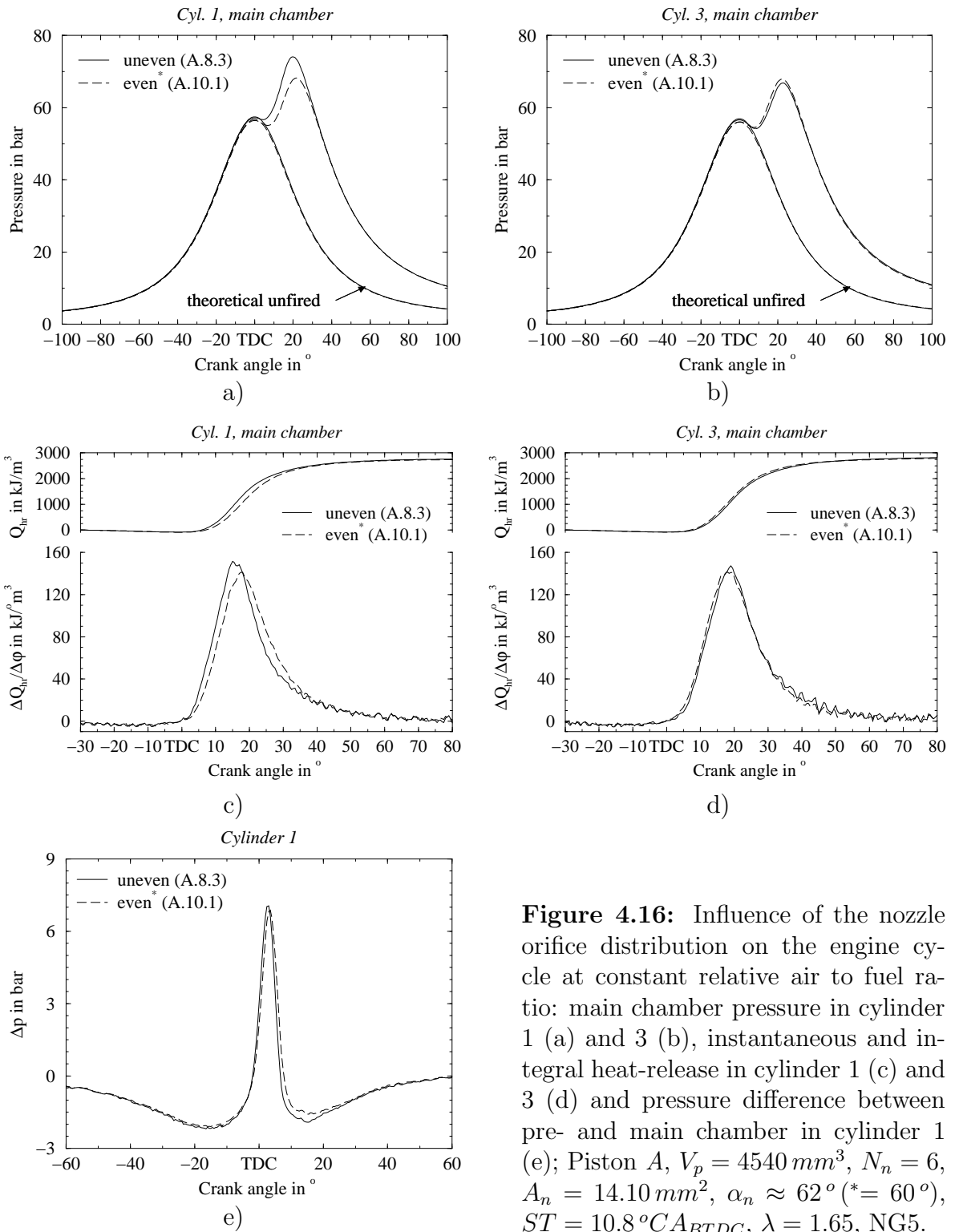


**Figure 4.16:** Influence of the nozzle orifice distribution on the engine cycle at constant relative air to fuel ratio: main chamber pressure in cylinder 1 (a) and 3 (b), instantaneous and integral heat-release in cylinder 1 (c) and 3 (d) and pressure difference between pre- and main chamber in cylinder 1 (e); Piston  $A$ ,  $V_p = 4540 \text{ mm}^3$ ,  $N_n = 6$ ,  $A_n = 14.10 \text{ mm}^2$ ,  $\alpha_n \approx 62^{\circ}$  ( $* = 60^{\circ}$ ),  $ST = 10.8^{\circ}\text{C} A_{BTDC}$ ,  $\lambda = 1.65$ , NG5.

of ignition failure. The replacement of the spark plugs by new ones dramatically improved the engine operating stability. This behaviour was encountered in a previous study [3] where small spark plugs *Bosch Super* type *FR*, characterised by a tightening hexagon of  $16 \text{ mm}$  and an internal resistance of  $6 \text{ k}\Omega$ , were also used in parallel to the standard spark plugs (*Bosch Super* type *W*). In this case, a progressive increase of the internal resistance at engine operating temperature was suspected and consequently the different small spark plugs tested were replaced at sufficiently short

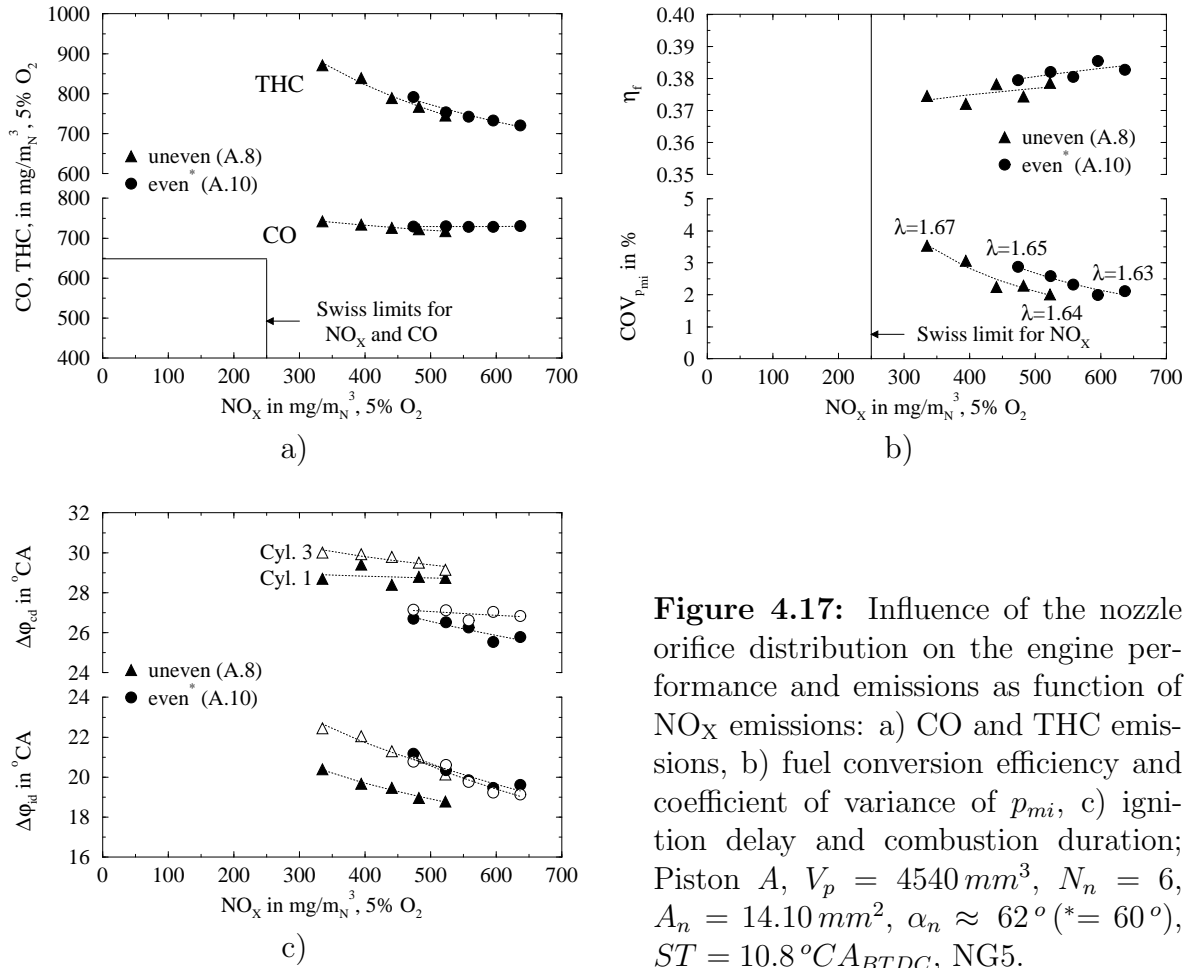


**Figure 4.17:** Influence of the nozzle orifice distribution on the engine performance and emissions as function of  $\text{NO}_x$  emissions: a) CO and THC emissions, b) fuel conversion efficiency and coefficient of variance of  $p_{mi}$ , c) ignition delay and combustion duration; Piston A,  $V_p = 4540 \text{ mm}^3$ ,  $N_n = 6$ ,  $A_n = 14.10 \text{ mm}^2$ ,  $\alpha_n \approx 62^\circ$  (\* =  $60^\circ$ ),  $ST = 10.8^\circ\text{CA}_{BTDC}$ , NG5.

intervals to avoid affecting the experimental results. In the present study, small spark plugs without internal resistance were selected because of the limited space available in the original cylinder head. Consequently, the following experiments were first carried out with spark plugs not exceeding ten operating hours. Then, standard spark plugs *Bosch Super* type *W6DC*, characterised by the same electrode configuration and thermal index as the type *F6DC*, were used. However, the fitting of the standard spark plug in the prechamber body required the milling of the tightening hexagon from 21 to 19 mm. The direct use (without modification) of standard spark plugs would necessitate the modification of the cylinder head casting. Ignition failure leads to a rapid deterioration of the engine operating stability, which results in a dramatic increase in the coefficient of variance of  $p_{mi}$ . In the case of the even nozzle orifice distribution, the early occurrence of ignition failure clearly limits the possible increase in relative air to fuel ratio in order to reduce the  $\text{NO}_x$  emissions (**figure 4.17, b**). On the other hand, the contribution of the spark plug alteration to the degradation of the combustion stability at constant  $\text{NO}_x$  emissions cannot be evaluated.

At constant  $\text{NO}_x$  emissions, the use of an even nozzle orifice distribution in comparison to an uneven distribution leads to a slight increase in fuel conversion efficiency, while producing only slightly higher CO and THC emissions. However, the results presented in section 4.4.3 indicate that a prechamber with 4 nozzle orifices enables a significant reduction of the CO and THC emissions, while not affecting the fuel conver-

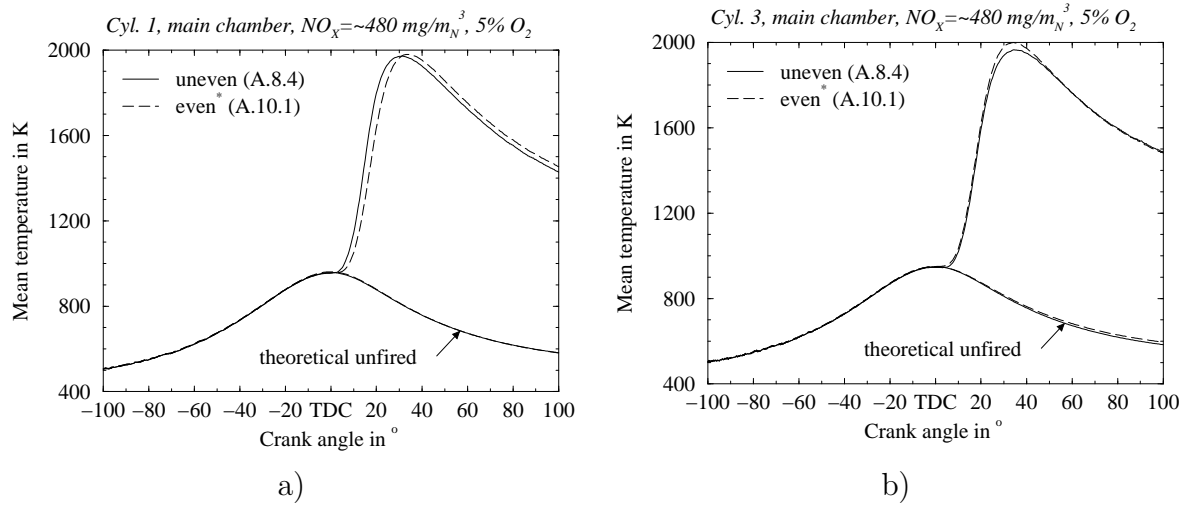


**Figure 4.18:** Influence of the nozzle orifice distribution on the mean temperature in the main combustion chamber at  $\text{NO}_X \approx 480 \text{ mg/m}_N^3$ ,  $5\% \text{ O}_2$ : a) cylinder 1, b) cylinder 3; Piston *A*,  $V_p = 4540 \text{ mm}^3$ ,  $N_n = 6$ ,  $A_n = 14.10 \text{ mm}^2$ ,  $\alpha_n \approx 62^\circ$  ( $* = 60^\circ$ ),  $ST = 10.8^\circ \text{CA}_{BTDC}$ , NG5.

sion efficiency. When now considering a lower number of nozzle orifices, it appears even more important to obtain a uniform distribution of the gas jets in the main combustion chamber. Therefore and because the general trend will be to use 4 nozzle orifices, only the uneven distribution was used for the next prechamber configurations.

#### 4.4.5 Nozzle orifice orientation

Two different orientations of the nozzle orifices, already described in section 2.2, were experimentally investigated (**figure 2.3, a**). The first orientation (*I*), characterised by an average angle from the prechamber axis of  $\approx 62^\circ$ , yields a relatively uniform distribution of the gas jets issuing from the prechamber into the volume of unburnt mixture located in the main chamber when the piston is close to TDC. The second orientation (*II*), with an average angle of  $\approx 78^\circ$ , aims to promote an early arrival of the flame front in the squish region, in order to reduce the amount of unburnt mixture compressed in the cylinder head gasket and piston top land crevices. The investigation was carried out with piston *A* and prechambers featured with an internal volume of  $4540 \text{ mm}^3$  and 6 nozzle orifices of diameter  $2.00 \text{ mm}$  ( $A_n = 18.85 \text{ mm}^2$ ), unevenly distributed. The engine was operated at a constant spark timing of  $8.3^\circ \text{CA}_{BTDC}$ . The effect and motivation of the transition from a spark timing from  $10.8$  to  $8.3^\circ \text{CA}_{BTDC}$  is discussed in section 4.4.9.

#### Results summary

The increase of the nozzle orifice angle from  $\approx 62^\circ$  to  $\approx 78^\circ$  in order to orient the gas jets towards the squish region results in:

- a significant decrease in combustion duration (**figure 4.20, c**)

and when considering the same NO<sub>X</sub> emissions:

- a significant decrease in CO and THC emissions at low NO<sub>X</sub> emissions (**figure 4.22, a**)
- an increase in fuel conversion efficiency of  $\approx 0.5$  %-point (**figure 4.22, b**)
- no significant change in cycle-by-cycle variability (**figure 4.22, b**)

Further, it leads to a fundamental change in the tradeoff between NO<sub>X</sub> and CO emissions and a significant relaxation of the tradeoff between NO<sub>X</sub> and THC emissions.

### Analysis and discussion

The results corresponding to the two different nozzle orifice orientations are given in **figure 4.19**, **figure 4.20** and **figure 4.22**. The transition from orientation *I* to *II* leads to a perceptible intensification of the prechamber combustion process (**figure 4.19, c**). This results in a moderate increase of the pressure difference between pre- and main combustion chambers (**figure 4.20, a**), which occurs somewhat earlier in the engine cycle (**figure 4.20, b**). The orientation of the nozzle orifices towards the squish region (*II*) yields a significant acceleration of the main chamber combustion process (**figure 4.19, b**). This results in a moderate decrease in ignition delay and in a shorter combustion duration (**figure 4.20, c**). In the case of orientation *II*, the more rapid combustion process leads to an increase of  $\approx 0.5$  %-point in fuel conversion efficiency at equal NO<sub>X</sub> emissions (**figure 4.22, b**). On the other hand, it produces significantly less CO and THC emissions at low NO<sub>X</sub> emissions (**figure 4.22, a**). Further, orientation *II* no longer leads to an increase in CO emissions with a decrease in NO<sub>X</sub> emissions, but in a slight decrease (this trend has been established several times). It also results in a slower increase of the THC emissions with a decrease in NO<sub>X</sub> emissions, which tends to relax the tradeoff. Finally, The orientation of the nozzle orifices towards the squish region (*II*) yields no perceptible change in cycle-by-cycle variability (**figure 4.22, b**).

In the case of orientation (*II*), the greater reorientation of the main chamber flow converging to the nozzle orifices during compression causes a slight increase in pressure drop across the orifices (**figure 4.19, c**). However, it is much smaller than predicted by the numerical simulation (**figure 3.11, d**). Orientation *II* yields a somewhat faster and more intense prechamber combustion process (**figure 4.19, c**). This results in a higher pressure difference between pre- and main chamber (**figure 4.20, a**), occurring earlier during the engine cycle (**figure 4.20, b**). The shorter prechamber ignition delay and the faster prechamber combustion may respectively originate in the slight decrease in turbulence intensity at the ignition point and the moderate increase of the velocity in the prechamber main recirculation zone indicated by the numerical simulation (**figure 3.11, a**).

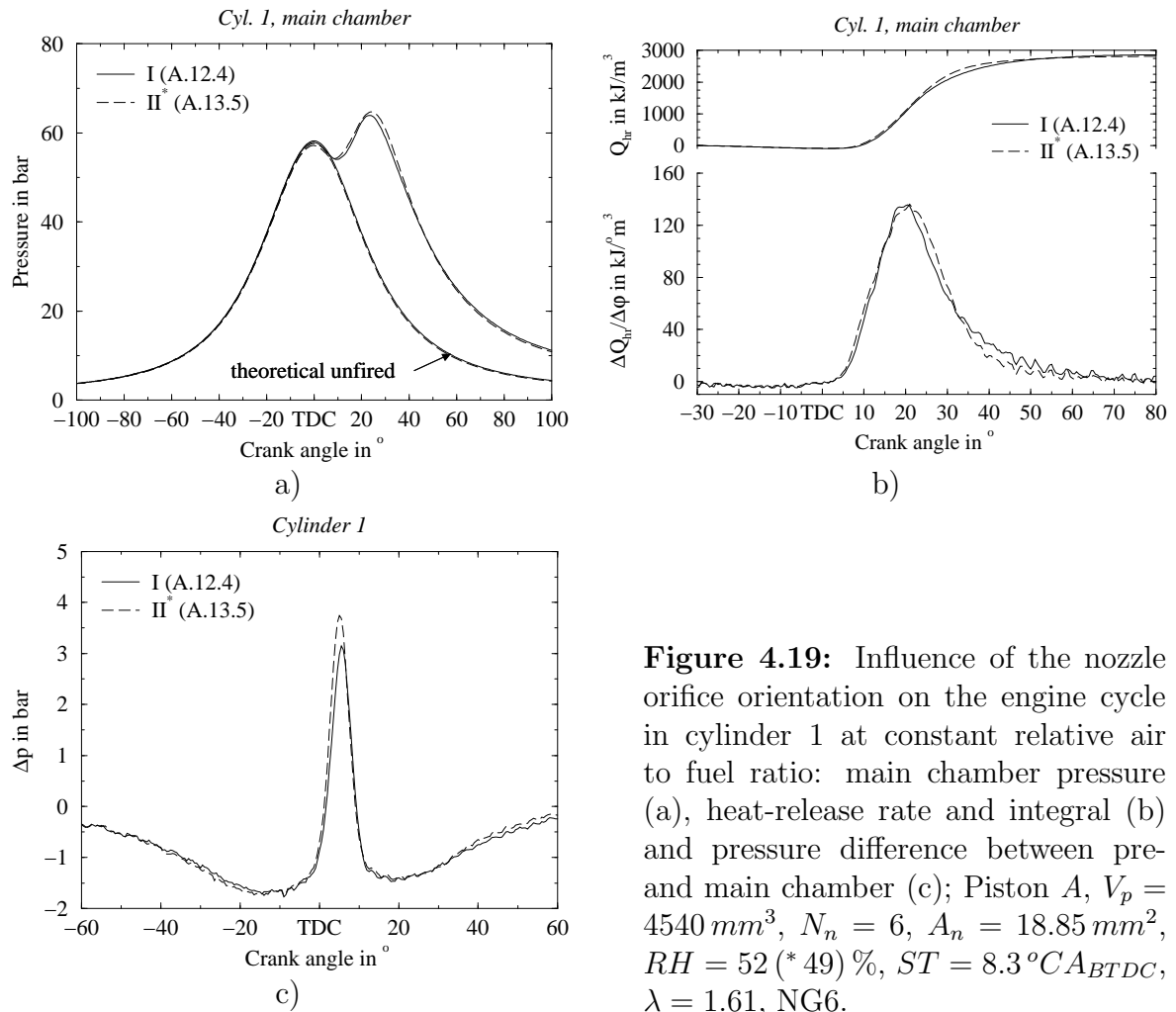


**Figure 4.19:** Influence of the nozzle orifice orientation on the engine cycle in cylinder 1 at constant relative air to fuel ratio: main chamber pressure (a), heat-release rate and integral (b) and pressure difference between pre- and main chamber (c); Piston A,  $V_p = 4540 \text{ mm}^3$ ,  $N_n = 6$ ,  $A_n = 18.85 \text{ mm}^2$ ,  $RH = 52$  (\* 49) %,  $ST = 8.3 \text{ } ^\circ\text{C}A_{BTDC}$ ,  $\lambda = 1.61$ , NG6.

When considering the same relative air to fuel ratio, the higher pressure difference between pre- and main chamber generated by orientation *II* yields a more rapid mean chamber combustion process (**figure 4.19, b**). This results in a somewhat shorter ignition delay and a significant decrease in combustion duration (**figure 4.20, c**). The slightly shorter ignition delay is expected to originate in somewhat stronger gas jets. In order to evaluate the change in interaction between the gas jet and main chamber flows, the two different theoretical gas jet paths (*I* and *II*) were superposed on the representation of the main chamber flow pattern at  $5 \text{ } ^\circ\text{C}A_{ATDC}$  (**figure 4.21**), a crank angle shortly before the pressure difference between pre- and main chamber reaches its maximum value (**figure 4.20, b**). The flow pattern of the combustion chamber without prechamber was selected for three reasons. First, because the combustion was not simulated, no gas jets are issuing from the prechamber at this particular crank angle position (even without combustion, due to the inertia, the flow through the prechamber orifices reverses only after TDC (**figure 3.4**), thus not generating significant gas jets in the main chamber before 10 to  $20 \text{ } ^\circ\text{C}A_{ATDC}$ ). Secondly, the relatively finer mesh used in the case without prechamber (8'164 instead of 7'215 cells) offers a better main chamber flow pattern resolution. Finally, when assuming that the prechamber nose tip does not affect significantly the main chamber flow shortly after TDC (at this part of the engine cycle, the flow is mainly driven by the depression created in the squish region by the piston moving down), it enables the consideration of the offset prechamber position

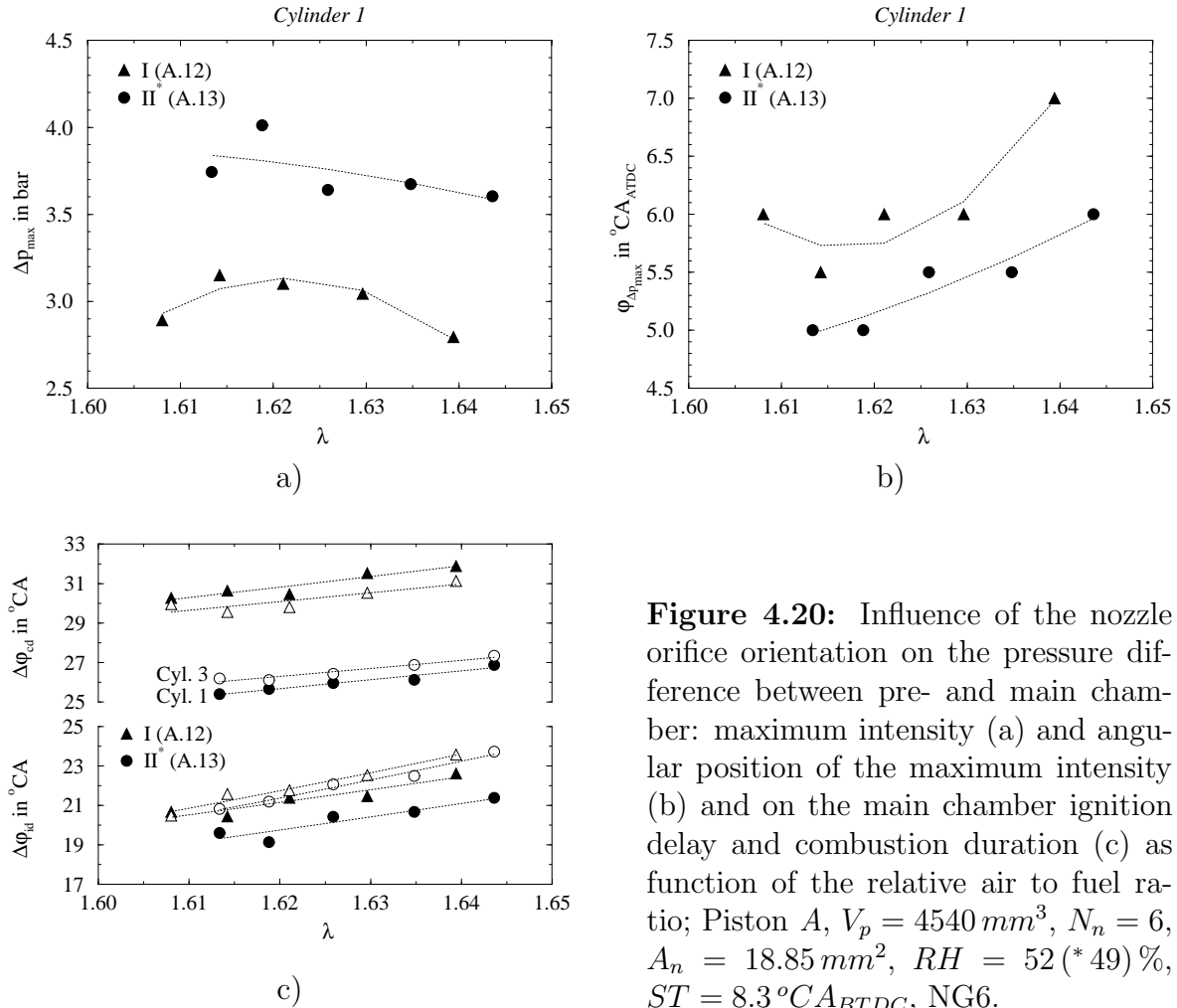


**Figure 4.20:** Influence of the nozzle orifice orientation on the pressure difference between pre- and main chamber: maximum intensity (a) and angular position of the maximum intensity (b) and on the main chamber ignition delay and combustion duration (c) as function of the relative air to fuel ratio; Piston A,  $V_p = 4540 \text{ mm}^3$ ,  $N_n = 6$ ,  $A_n = 18.85 \text{ mm}^2$ ,  $RH = 52$  (\*49)%,  $ST = 8.3 \text{ }^{\circ}C A_{BTDC}$ , NG6.

from the main combustion chamber axis. The numerical simulation indicates that in the case of the nozzle orifice orientation *II*, the gas jets develop in the main chamber regions characterised by higher flow velocities (longer arrows) and which are directly feeding the squish region. The higher velocities should accelerate the propagation of the flame front and the proximity of the squish region should promote further its early arrival at the piston top land and cylinder head gasket crevice entrances. Associated with the somewhat shorter ignition delay, this could explain the faster second part of the main chamber combustion process (figure 4.19, b) and the resulting shorter combustion

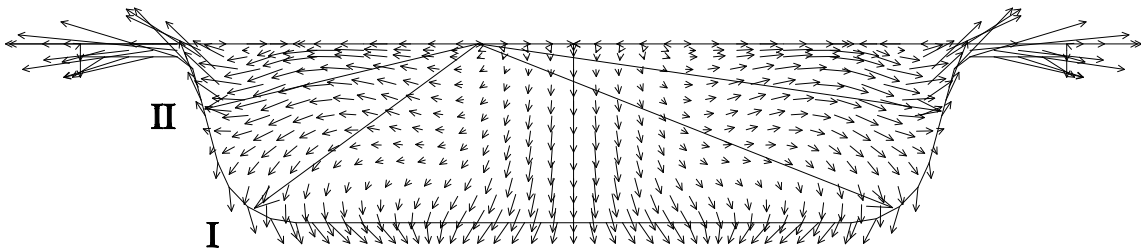


**Figure 4.21:** Simulated main chamber flow pattern at  $5 \text{ }^{\circ}C A_{ATDC}$  with the two different theoretical paths of the gas jets issuing from the prechamber.



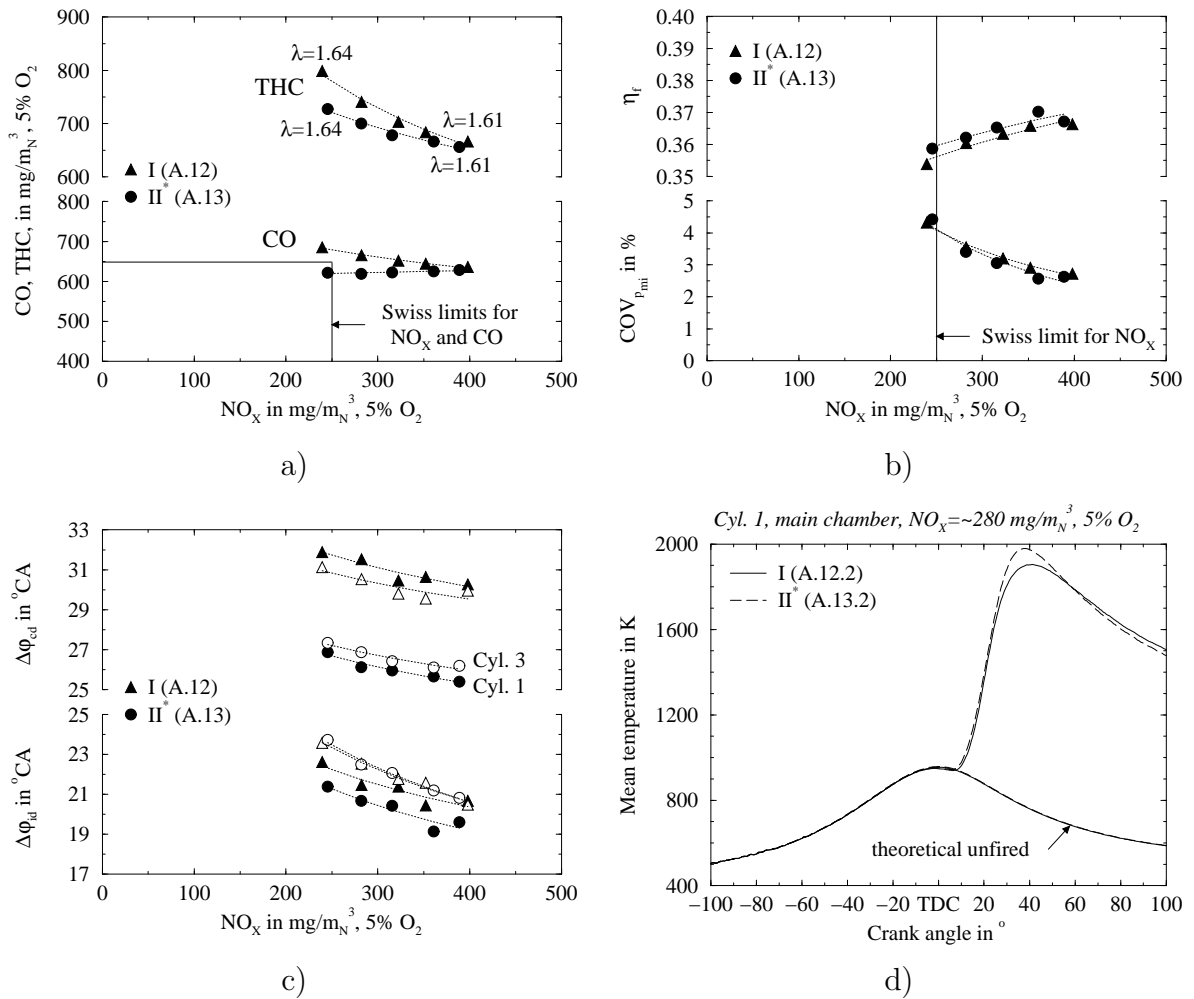


**Figure 4.22:** Influence of the nozzle orifice orientation on the engine performance and emissions as function of  $\text{NO}_x$  emissions: a) CO and THC emissions, b) fuel conversion efficiency and coefficient of variance of  $p_{mi}$ , c) ignition delay and combustion duration; d) mean combustion temperature in cylinder 1 at  $\text{NO}_x \approx 280 \text{ mg}/\text{m}_N^3, 5\% \text{O}_2$ ; Piston A,  $V_p = 4540 \text{ mm}^3$ ,  $N_n = 6$ ,  $A_n = 18.85 \text{ mm}^2$ ,  $RH = 52$  (\*49)%,  $ST = 8.3^\circ\text{CA}_{BTDC}$ , NG6.

duration (**figure 4.20, c**). On the other hand, the acceleration of the combustion process causes a slight increase of the maximum cylinder pressure (**figure 4.19, a**).

When considering the same  $\text{NO}_x$  emissions, the significantly shorter combustion duration ( $\approx 4^\circ\text{CA}$ ) combined with the somewhat reduced ignition delay induced by the nozzle orifice orientation II (**figure 4.22, c**) leads to an increase in fuel conversion efficiency of about 0.5 %-point (**figure 4.22, b**). In addition, this orientation improves slightly the combustion stability. Despite the somewhat higher peak cylinder pressure (**figure 4.19, a**) and lower temperature during late expansion (**figure 4.22, d**), the orientation of the gas jets towards the squish region results in a reduction of the CO and THC emissions (**figure 4.22, a**). The reduction is small with a relatively rich fuel-air mixture, but becomes much larger when the relative air to fuel ratio increases. Further, orientation II induces a fundamental change in the behaviour between CO and THC emissions: the CO emissions slightly decrease with the increase of relative

air to fuel ratio, while the THC emissions increase due to the degradation of the combustion stability. These results indicate that an orientation of the gas jets towards the squish region becomes more important when the relative air to fuel ratio increases (longer main chamber ignition delay and slower combustion). In turn, they tend to support the assumption that an early flame front arrival in the squish region reduces the amount of unburnt mixture compressed in the piston top land and cylinder head gasket crevices. Further, the slight decrease of the CO emissions with the increase of relative air to fuel ratio seems to indicate a progressive reduction of the amount of hydrocarbons located in the combustion chamber crevices prior to the flame front arrival. On the other hand, the increase in THC emissions should essentially result from the more frequent occurrence of bulk gas flame quenching.

The orientation of the nozzle orifices towards the squish region simultaneously reduces the THC and CO emissions, particularly when increasing the relative air to fuel ratio to decrease the  $\text{NO}_x$  emissions. In addition, it also improves somewhat the fuel conversion efficiency. For these reasons, this particular nozzle configuration was adopted to evaluate the influence of the prechamber internal volume and shape, presented in the following two sections.

#### 4.4.6 Prechamber internal volume

Two different prechamber internal volumes were experimentally evaluated. The first volume of  $4540 \text{ mm}^3$  corresponds to 2.9% of the compression volume (clearance and prechamber volumes) and was used for the majority of the experiments. The second prechamber volume of  $3010 \text{ mm}^3$  is equal to 1.9% of the compression volume. Its internal dimensions (shape *b*) corresponds to a proportional reduction of the larger prechamber (shape *a*), which results in a similar internal shape; both geometries are represented in **figure 2.3**. In order to isolate as much as possible the effect of the volume change, the nozzle orifice diameter was reduced from  $2.00 \text{ mm}$  (prechamber *a*) to  $1.63 \text{ mm}$  (prechamber *b*) to achieve approximately the same orifice flow conditions (**figure 3.22**). The orifice diameter of the prechamber *b* was determined on the basis of a constant ratio between the nozzle orifice total cross sectional area and the prechamber internal volume ( $A_n/V_p = 0.0042 \text{ mm}^{-1}$ ). The specific parameters of each prechamber are summarised in **table 4.2**. The investigation was performed with piston *A* and prechambers featured with 6 nozzle orifices unevenly distributed and oriented at  $\approx 78^\circ$ . The engine was operated at a constant spark timing of  $8.3^\circ \text{CA}_{BTDC}$ .

**Table 4.2:** Summary of the two different prechamber configurations (6 nozzle orifices)

		<b>a</b>	<b>b</b>
$V_p$	$\text{mm}^3$	4540	3010
$\% V_c$	-	2.9	1.9
$d_n$	$\text{mm}$	2.00	1.63
$A_n$	$\text{mm}^2$	18.85	12.52

### Results summary

The decrease of prechamber internal volume from  $4540\text{ mm}^3$  to  $3010\text{ mm}^3$ , while keeping a constant ratio between the nozzle orifice total cross sectional area and the prechamber internal volume, leads to:

- a moderate reduction in ignition delay and a significant increase in combustion duration (**figure 4.24**)

and when considering the same  $\text{NO}_x$  emissions:

- an increase of more than  $\approx 7\%$  and  $\approx 11\%$  in CO and THC emissions, respectively (**figure 4.25, a**)
- no perceptible change in fuel conversion efficiency (**figure 4.25, b**)
- a significant decrease in cycle-by-cycle variability (**figure 4.25, b**)

Further, it enables a large reduction in  $\text{NO}_x$  emissions far below the Swiss limits.

### Analysis and discussion

The results corresponding to the two different internal volumes are represented together in **figure 4.23**, **figure 4.24** and **figure 4.25**. The reduction of the prechamber internal volume yields a somewhat earlier and higher prechamber pressure increase (**figure 4.23, c and d**). However, this leads also to a shorter pressure pulse (**figure 4.23, d**). The corresponding change in gas jet intensity and penetration produces an earlier main chamber combustion process, characterised by a slower end (**figure 4.23, b**). This results in a shorter ignition delay and a longer combustion duration (**figure 4.24**). When considering equal  $\text{NO}_x$  emissions, the reduction of the prechamber internal volume does not affect the fuel conversion efficiency (**figure 4.25, b**). Further, the small prechamber (*b*) yields more than  $\approx 7\%$  and  $\approx 11\%$  higher CO and THC emissions, respectively (**figure 4.25, a**). Finally, the significantly lower cycle-by-cycle variability associated with prechamber *b* (**figure 4.25, b**) enables a further reduction of the  $\text{NO}_x$  emissions below  $160\text{ mg}/\text{m}_N^3$ ,  $5\% \text{ O}_2$ , thus under the Swiss limit. However in this case, the requirement regarding the CO emissions is not fulfilled.

First, the reduction of the nozzle orifice cross sectional area to maintain similar orifice flow characteristics causes a moderate increase of pressure drop between both chambers during the compression stroke (**figure 4.23, d**). Further, the small prechamber (*b*) causes an earlier start of the prechamber combustion (**figure 4.23, c**), which results in a larger pressure difference between pre- and main chamber (**figure 4.23, d**). The earlier start of prechamber combustion could originate in the strong decrease of turbulence in the vicinity of the ignition point indicated by the numerical simulation

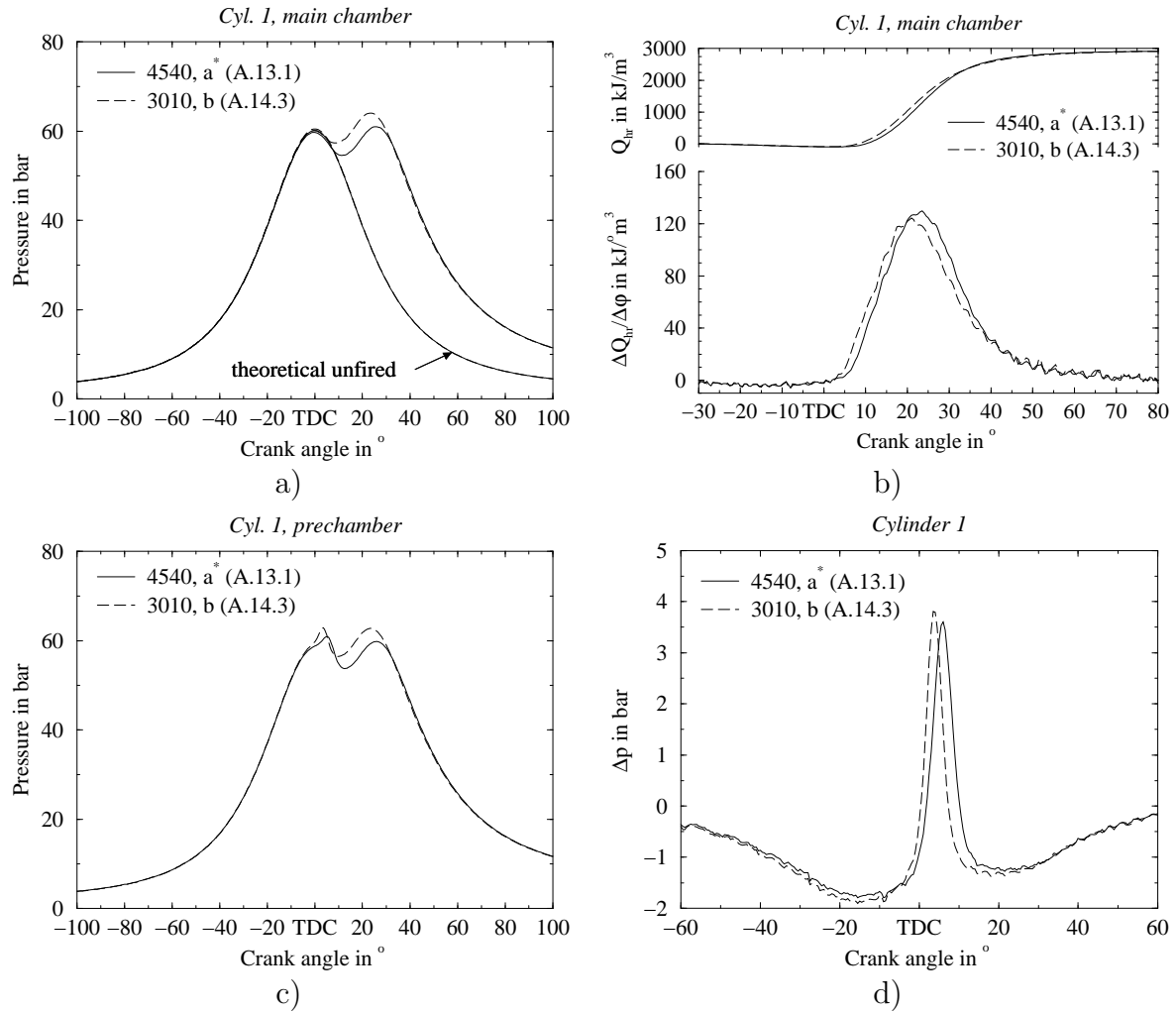


**Figure 4.23:** Influence of the prechamber internal volume on the engine cycle in cylinder 1 at constant relative air to fuel ratio; main chamber pressure (a), heat-release rate and integral (b), prechamber pressure (c) and pressure difference between pre- and main chamber (d); Piston  $A$ ,  $A_n/V_p = 0.0042 \text{ mm}^{-1}$ ,  $N_n = 6$ ,  $\alpha_n \approx 78^\circ$ ,  $RH = 50$  (\* 49) %,  $ST = 8.3^\circ \text{C A}_{BTDC}$ ,  $\lambda = 1.64$ , NG6.

(figure 3.22, b), which tends to reduce the perturbation of the flame kernel development and consequently its duration. On the other hand, the earlier prechamber combustion may benefit from a higher overall turbulence intensity (the prechamber turbulence decreases very rapidly when approaching TDC (figure 3.5)), which could explain the faster prechamber combustion. However, the combination of the smaller prechamber volume, the somewhat higher pressure drop across the nozzle orifices during compression and the earlier start of the prechamber combustion process reduces the amount of unburnt mixture flowing into the prechamber. In turn, this decreases the heat released in the prechamber and results in a shorter prechamber pressure pulse (figure 4.23, d). In consequence, the small prechamber (b) is expected to generate weaker gas jets, but which are emerging more rapidly and earlier in the engine cycle.

In the case of the small prechamber (b), the earlier and more rapid emergence of the gas jets into the main chamber causes a slight reduction of the main chamber ignition delay of approximately  $2^\circ \text{CA}$  (figure 4.24). Consequently, this leads to an earlier

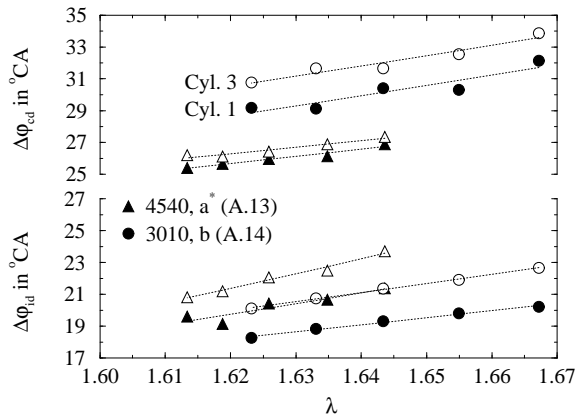


**Figure 4.24:** Influence of the prechamber internal volume on the ignition delay and combustion duration as function of relative air to fuel ratio; Piston A,  $A_n/V_p = 0.0042 \text{ mm}^{-1}$ ,  $N_n = 6$ ,  $\alpha_n \approx 78^\circ$ ,  $RH = 50$  (\*49)%,  $ST = 8.3^\circ \text{CA}_{BTDC}$ , NG6.

start of the main chamber combustion process (**figure 4.23, b**). In turn, this leads to a significant increase in peak cylinder pressure (**figure 4.23, a**). The slower end of the main chamber combustion process seems to originate in the lower penetration of the gas jets. It results in a significant increase of the main chamber combustion duration of about  $4^\circ \text{CA}$  (**figure 4.24**).

For the same  $\text{NO}_x$  emissions, the shift of the main chamber combustion process towards TDC (**figure 4.23, b**) fully compensates the detrimental effect of the longer combustion duration (**figure 4.25, c**) on the engine fuel economy. Consequently, the reduction of prechamber volume results in no perceptible change in fuel conversion efficiency (**figure 4.25, b**). The significant improvement of the cycle-by-cycle variability associated with the small prechamber (*b*) may originate in the lower turbulence in the vicinity of the spark plug electrodes indicated by the numerical simulation (**figure 3.22, b**). A lower variability of the prechamber ignition conditions is expected to promote the generation of more regular gas jets. In turn, this should stabilise the main chamber combustion process and result in a lower coefficient of variance of  $p_{mi}$ . The better combustion stability associated with the small prechamber permits an increase in the relative air to fuel ratio, which enables a further reduction of the  $\text{NO}_x$  emissions.

When considering equal  $\text{NO}_x$  emissions, the reduction of the prechamber internal volume yields significantly higher CO and THC emissions at constant  $\text{NO}_x$  emissions (**figure 4.25, a**). Further, the CO and THC emissions increase despite a better combustion stability which tends to reduce the contribution of bulk gas quenching. Moreover, the approximately equal mean combustion temperature during the late expansion phase (**figure 4.25, d**) should lead to a similar conditions for the secondary oxidation process. All these aspects tend to indicate that the increase in CO and THC emissions mainly results from the combustion chamber crevice mechanisms. On the one hand, the higher peak cylinder pressure tends to increase the amount of unburnt mixture flowing into the combustion chamber crevices. On the other hand, weaker gas jets are likely to delay the arrival of the flame front at the entrance of the piston top land and cylinder head gasket crevices. Both effects tend to increase the amount of hydrocarbons escaping the primary oxidation process. The reduction of the prechamber internal volume also causes a more rapid increase of the THC emissions and a fundamental change in the evolution of the CO emissions with the increase in relative air to fuel ratio. This particular behaviour tends to indicate that the intensity and penetration of the gas

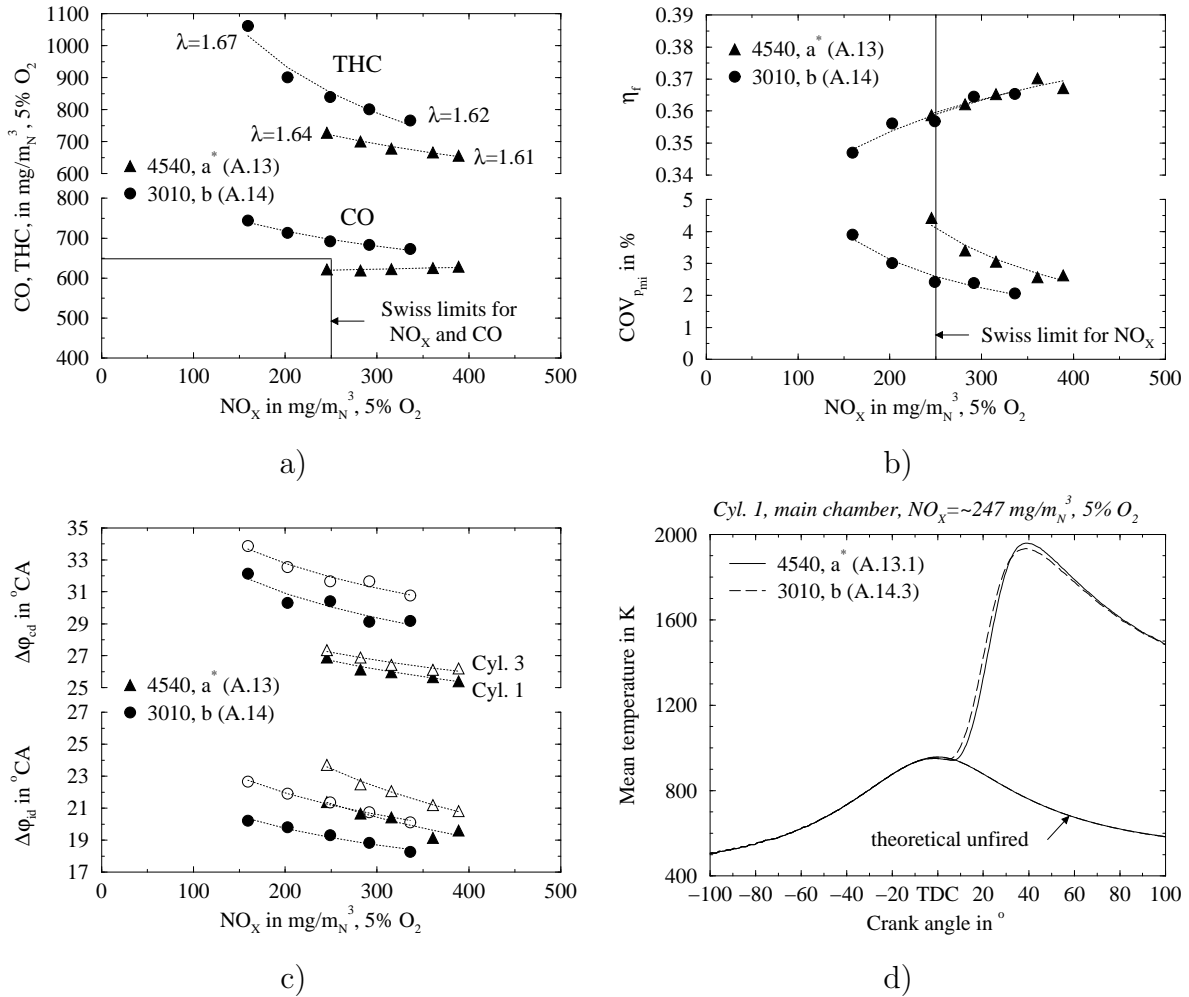


**Figure 4.25:** Influence of the prechamber internal volume on the engine performance and emissions as function of  $\text{NO}_x$  emissions: a) CO and THC emissions, b) fuel conversion efficiency and coefficient of variance of  $p_{mi}$ , c) ignition delay and combustion duration, d) mean combustion temperature at  $\text{NO}_x \approx 247 \text{ mg}/\text{m}^3$ , 5%  $\text{O}_2$ ; Piston A,  $A_n/V_p = 0.0042 \text{ mm}^{-1}$ ,  $N_n = 6$ ,  $\alpha_n \approx 78^\circ$ ,  $RH = 50$  (\*49)%,  $ST = 8.3^\circ\text{CA}_{BTDC}$ , NG6.

jets has a major influence on the exhaust gas emissions. Further, this shows that the crevice mechanism contributes to a much larger extent to the CO and THC emissions than the bulk gas effect.

The chemical energy converted into heat in the prechamber produces a sufficiently large increase in pressure (figure 4.23, c) to generate the hot gas jets required for the main chamber ignition. However, this pressure increase does not directly affect the main chamber pressure (figure 4.23, a) and thus does not produce mechanical work. The insensitivity of the fuel conversion efficiency to the variation of the prechamber volume indicates that the detrimental effect of burning a larger quantity of fuel in the prechamber without producing mechanical work is fully compensated by the acceleration of the main chamber combustion process realised by the resulting stronger gas jets. Further, the early arrival of the flame front at the piston top land and cylinder head crevice entrances promoted by the stronger gas jets yields a significant reduction of CO

and THC emissions. On the other hand, the less stable prechamber ignition process resulting from the increase in local turbulence intensity limits the possible reduction of  $\text{NO}_x$  emissions. In consequence, the greater difficulty to reduce the CO and THC than the  $\text{NO}_x$  emissions (the engine operating conditions and the main combustion chamber geometry have a larger influence on the  $\text{NO}_x$  emissions) gives preference to the large prechamber internal volume.

#### 4.4.7 Prechamber internal shape

A first insight into the influence of the prechamber internal shape was gained on the basis of two different geometries. In order to enable a sufficient variation of the internal shape without modification of the prechamber external geometry, this study was based on the small prechamber volume of  $3010 \text{ mm}^3$ . The first internal shape corresponds to the case  $b$  represented in **figure 2.3**. The second internal shape ( $c$ ) was designed in order to distribute more uniformly the volume along the prechamber axis and thus reduce the size of the main recirculation zone at the prechamber top skirt. With a size of  $14 \text{ mm}$ , the larger diameter of the upper prechamber part corresponds to the thread dimensions of the standard spark plug used. Derived from the internal shape  $b$ , the length between the point where the nozzle orifice axes converge and the prechamber top face (prechamber length) as well as the prechamber cone angle were kept constant. In comparison to the internal shape  $\alpha$  and  $\beta$  numerically simulated (see section 3.3.8) which have the same length as the prechamber with large internal volume, the length of the prechamber  $b$  and  $c$  was proportionally decreased with the reduction of volume. Although the internal shapes  $b$  and  $c$  differ somewhat (mainly in length) from  $\alpha$  and  $\beta$ , respectively, this should not significantly affect the general trends indicated by the numerical simulation. The investigation was performed with piston  $A$  and prechambers featured with 6 nozzle orifices of diameter  $1.63 \text{ mm}$  ( $A_n = 12.52 \text{ mm}^2$ ), unevenly distributed and oriented at  $\approx 78^\circ$ . The engine was operated at a constant spark timing of  $8.3^\circ \text{CA}_{BTDC}$ .

#### Results summary

A more uniform distribution of the prechamber internal volume along the prechamber axis results in:

- a significant increase in ignition delay and a slight increase in combustion duration (**figure 4.27**)

and when considering the same  $\text{NO}_x$  emissions:

- a reduction of  $\approx 11\%$  and  $\approx 13\%$  in CO and THC emissions, respectively (**figure 4.28, a**)
- a decrease of more than 0.5 %-point in fuel conversion efficiency (**figure 4.28, b**)
- a significant increase in cycle-by-cycle variability (**figure 4.28, b**)

## Analysis and discussion

The results corresponding to the two different prechamber internal shapes are represented together in **figure 4.26**, **figure 4.27** and **figure 4.28**. The transition from internal shape *b* to *c* leads to a delay of the prechamber pressure pulse and a decrease of its intensity (**figure 4.26, d**). In turn, this causes an increase of the main chamber ignition delay (**figure 4.27**), which results in a shift of the main chamber combustion process into the expansion phase (**figure 4.26, b**). Further, this yields a major decrease in the cylinder pressure during combustion (**figure 4.26, a**). At equal  $\text{NO}_x$  emissions, the shift of the combustion into the expansion phase produced by internal shape *c* causes a significant decrease of more than 0.5 %-point in fuel conversion efficiency (**figure 4.28, b**). Further, this leads to an important increase in cycle-by-cycle variability. Finally, the transition from internal shape *b* to *c* results in a reduction of  $\approx 11\%$  and  $\approx 13\%$  in CO and THC emissions, respectively (**figure 4.28, a**).

At a constant relative air to fuel ratio, the transition from internal shape *b* to *c* only moderately affects the flow across the nozzle orifices during the compression stroke (**figure 4.26, d**). This results in a slight increase of the pressure drop between prechamber and main chamber shortly before prechamber combustion starts. In consequence, this should not significantly affect the amount of turbulence generated by the flow across the nozzle orifices as indicated by the numerical simulation (**figure 3.27, b**). However, the numerical simulation shows that the lower prechamber axial flow velocity associated with the internal shape *c* (**figure 3.24**) limits the diffusion of the turbulence generated by the flow across the nozzle orifices (**figure 3.25**). In consequence, this reduces the turbulence intensity in the upper prechamber part (**figure 3.27, b**). The particularly low value achieved in the vicinity of the spark plug electrodes corresponds to typical values characterising the direct ignition operation (**figure 3.7, b**). Despite the positive effect of a lower turbulence intensity on the development of the flame kernel, the results show a less steep slope and a lower maximum intensity of the pressure pulse in the case of shape *c* (**figure 4.26, d**). This indicates a slower prechamber combustion process, which is likely to originate in the lower prechamber overall turbulence intensity. However, the detrimental effect of the lower turbulence intensity on the flame front speed may also be partly offset by a somewhat higher unburnt mixture temperature resulting from a reduced heat transfer to the prechamber wall. This tends to promote the chemical reaction kinetics and thus accelerates the flame front propagation. The longer pressure pulse observed with shape *c* results from the larger main chamber ignition delay (**figure 4.26, b**). Supported by the results already discussed in the previous sections, the slower prechamber combustion process should delay the development of the gas jets in the main chamber and attenuates their intensity and penetration.

When considering the same relative air to fuel ratio, the attenuation of the gas jet intensity and penetration resulting from the transition from shape *b* to *c* leads to an important increase in main chamber ignition delay of approximately  $3^\circ\text{CA}$  (**figure 4.27**). In turn, this results in a shift of the combustion start into the expansion phase (**figure 4.26, b**). In the case of internal shape *c*, the reduction of the gas jet penetration combined with the detrimental effect of the decreasing temperature during expansion on the chemical reaction kinetics slows down the main chamber combustion



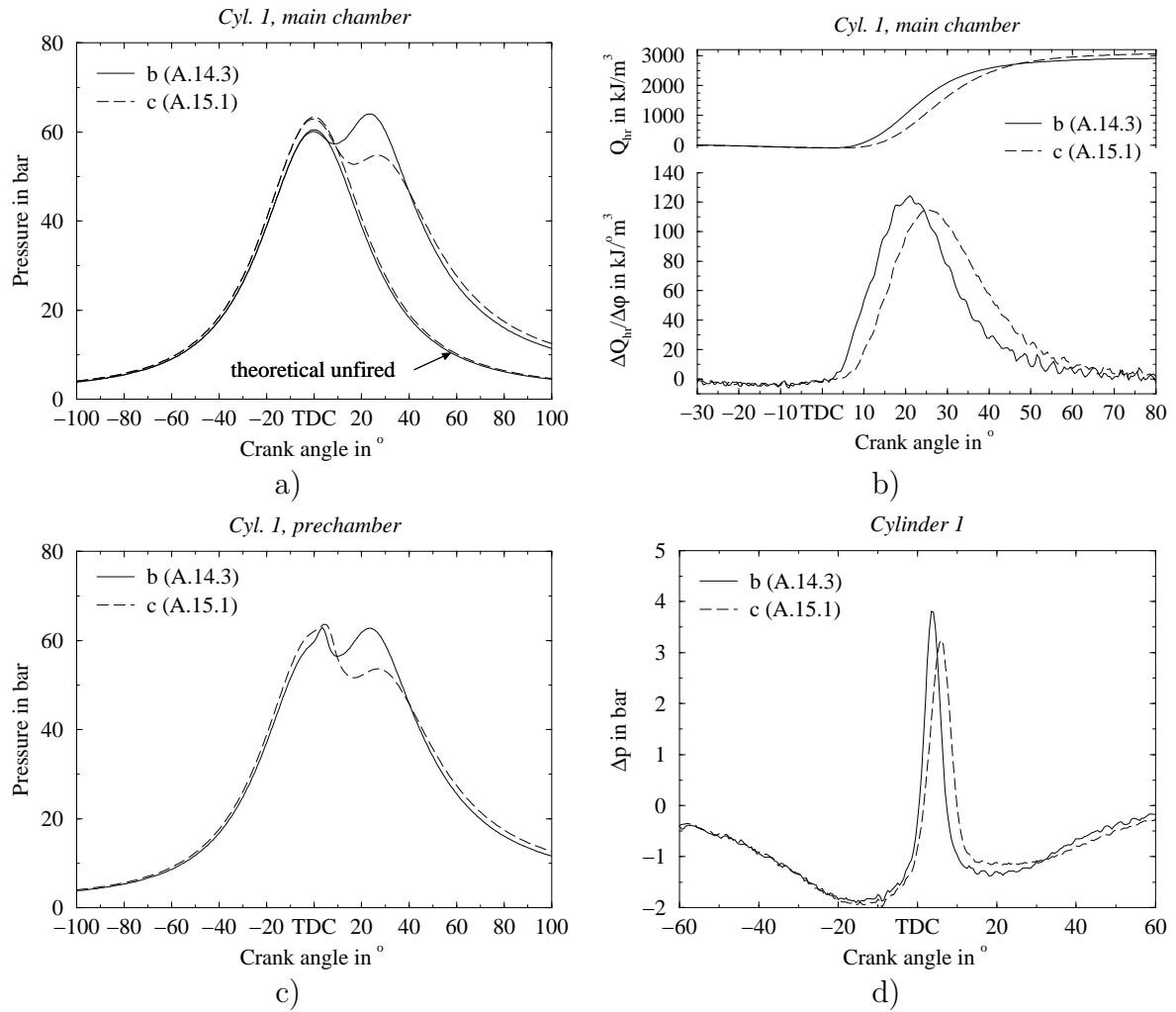


**Figure 4.26:** Influence of the prechamber internal shape on the engine cycle in cylinder 1 at constant relative air to fuel ratio; main chamber pressure (a), heat-release rate and integral (b), prechamber pressure (c) and pressure difference between pre- and main chamber (d); Piston  $A$ ,  $V_p = 3010 \text{ mm}^3$ ,  $A_n = 12.52 \text{ mm}^2$ ,  $N_n = 6$ ,  $\alpha_n \approx 78^\circ$ ,  $ST = 8.3^\circ \text{CA}_{BTDC}$ ,  $\lambda = 1.64$ , NG6.

process. This results in a larger fraction of the heat released later during expansion (illustrated by less steep slopes and a lower maximum value of the heat release rate) and consequently in a further shift of the combustion into the expansion phase. However, due to the more rapid end of combustion achieved with the internal shape  $c$ , this leads only to a moderate increase of the combustion duration of about  $1^\circ \text{CA}$  (figure 4.27). The less efficient combustion requires a larger mass flow rate of fuel-air mixture in order to achieve a constant engine power output, which results in an higher compression pressure (figure 4.26, a) and heat release integral (figure 4.26, b). The shift of the main combustion process into the expansion phase yields a significant decrease in peak combustion pressure, which becomes much smaller than the maximum value reached during compression (figure 4.26, a).

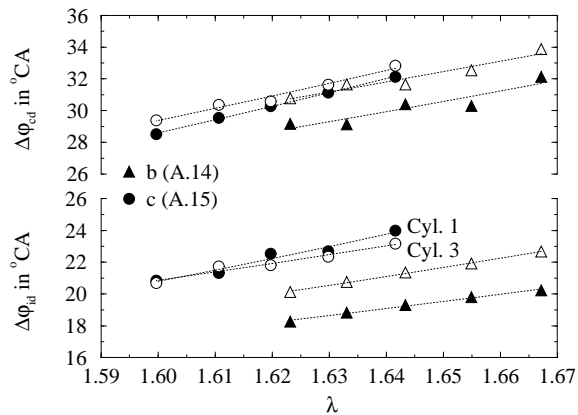


**Figure 4.27:** Influence of the prechamber internal shape on the ignition delay and combustion duration as function of relative air to fuel ratio; Piston  $A$ ,  $V_p = 3010 \text{ mm}^3$ ,  $A_n = 12.52 \text{ mm}^2$ ,  $N_n = 6$ ,  $\alpha_n \approx 78^\circ$ ,  $ST = 8.3^\circ \text{CA}_{BTDC}$ , NG6.

In comparison to the prechamber with internal shape  $b$ , the slower and later main chamber combustion process induced by internal shape  $c$  enables a reduction of the relative air to fuel ratio to achieve the same  $\text{NO}_x$  emissions (**figure 4.28, a**). In turn, this reduces the ignition delay and offsets the increase in combustion duration (compare **figure 4.27** and **figure 4.28, c**). However, in the case of internal shape  $c$ , the still longer ignition delay combined with the larger proportion of the heat released later during expansion results in an average decrease in fuel conversion efficiency of more than 0.5 %-point at constant  $\text{NO}_x$  emissions (**figure 4.28, b**). Despite the lower turbulence intensity in the vicinity of the ignition point (**figure 3.27**) and the slight decrease in relative air to fuel ratio, the later and slower combustion process associated with the shape  $c$  causes a significant increase in cycle-by-cycle variability. This is illustrated by a higher coefficient of variance of  $p_{mi}$  (**figure 4.28, b**).

When considering equal  $\text{NO}_x$  emissions, the change from shape  $b$  to  $c$  leads to significantly lower CO ( $\approx 11\%$ ) and THC ( $\approx 13\%$ ) emissions. The combination of the following effects probably contribute to this result. In the case of the shape  $c$ , the significantly lower combustion pressure (**figure 4.26, a**) tends to reduce the amount of unburnt mixture compressed in the combustion chamber crevices and thus escaping the primary oxidation process. Further, the somewhat higher mean combustion temperature during late expansion (**figure 4.28, d**) should promote a more complete secondary oxidation of the unburnt hydrocarbons into fully oxidised products. However, the less deep penetration of the gas jets retards the arrival of the flame front at the piston top land and cylinder head gasket crevice entrances. Therefore, this leaves more time available for the unburnt mixture to flow into the crevices. Finally, the deterioration of the combustion stability, resulting from the more frequent occurrence of bulk gas quenching, increases the proportion of the fuel escaping the flame front oxidation process. When considering all these aspects, the decrease in CO and THC emissions seems to mainly result from the lower combustion pressure.

The engine operation with the prechamber internal shape  $c$  yields approximately the same CO and THC emissions as with the large prechamber (shape  $a$ ), at constant  $\text{NO}_x$  emissions. On the other hand, shape  $c$  enables a further reduction of the  $\text{NO}_x$  emissions (**figure 4.28, a** and **figure 4.25, a**). However, it also leads to a decrease in fuel conversion efficiency of more than 0.5 %-point (**figure 4.28, b** and **figure 4.25, b**). Further, the effective potential to reduce the  $\text{NO}_x$  emissions sufficiently under the Swiss limits to be practical is strongly limited by the simultaneous increase of the CO

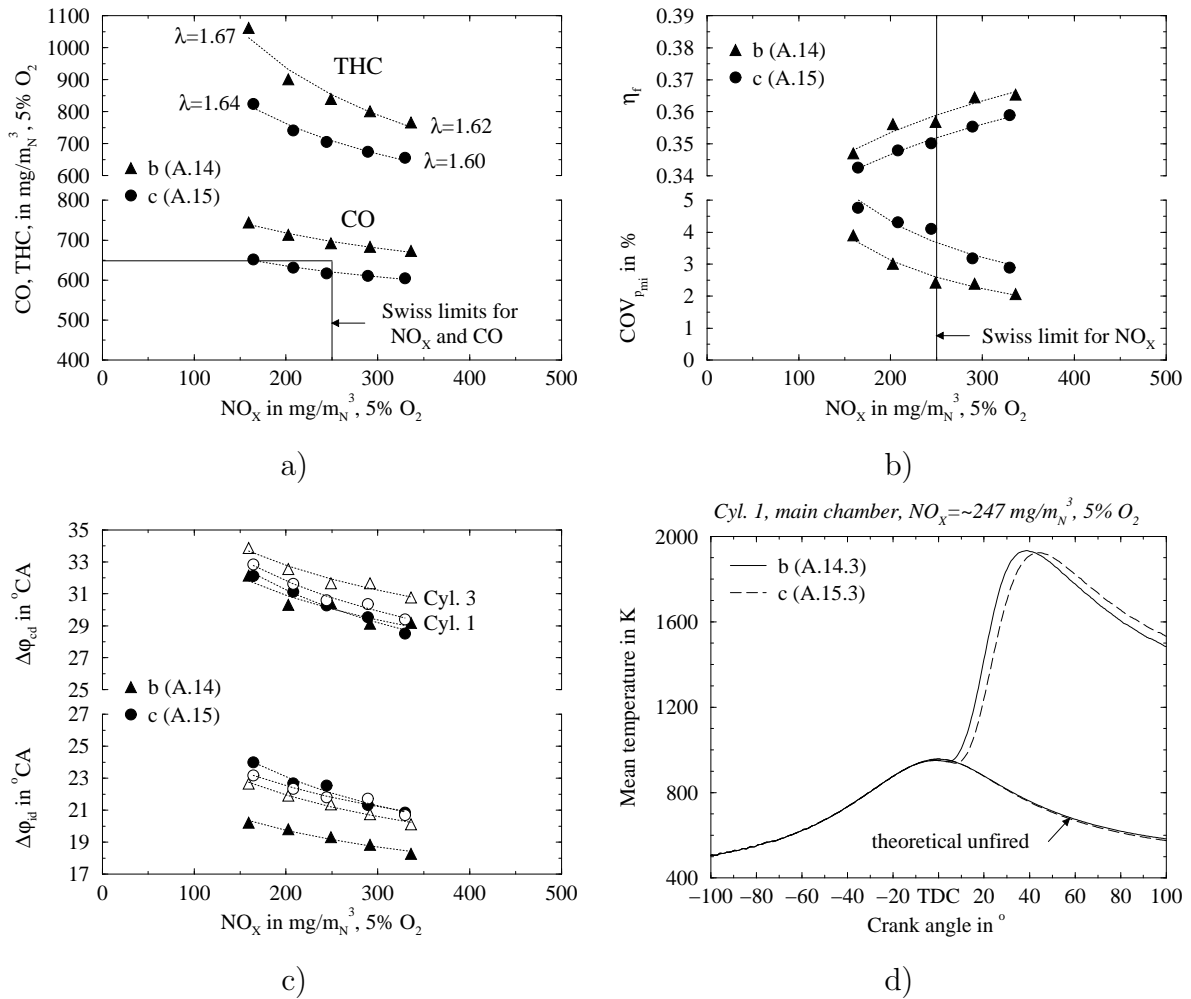


**Figure 4.28:** Influence of the prechamber internal shape on the engine performance and emissions as function of  $\text{NO}_x$  emissions: a)  $\text{CO}$  and  $\text{THC}$  emissions, b) fuel conversion efficiency and coefficient of variance of  $p_{mi}$ , c) ignition delay and combustion duration, d) mean combustion temperature at  $\text{NO}_x \approx 247 \text{ mg}/\text{m}_N^3, 5\% \text{O}_2$ ; Piston A,  $V_p = 3010 \text{ mm}^3$ ,  $A_n = 12.52 \text{ mm}^2$ ,  $N_n = 6$ ,  $\alpha_n \approx 78^\circ$ ,  $ST = 8.3^\circ\text{CA}_{BTDC}$ , NG6.

emissions. In this respect, the significantly more stable behaviour of the  $\text{CO}$  emissions characterising the engine operation with the large prechamber offers, at this stage, more potential to reduce the  $\text{CO}$  emissions to an adequate level under the Swiss limits, while keeping the highest possible fuel conversion efficiency.

#### 4.4.8 Main combustion chamber geometry

In order to perform a first evaluation of the influence of the main combustion chamber geometry on the combustion process and exhaust gas emissions, two different piston bowl configurations were investigated: the original piston (A) (figure 2.1), used in all the previous experiments, and the piston B (figure 4.3, a), generating significantly higher turbulence and already used in previous studies [3, 4, 33] (see also section 4.3). Both pistons are characterised by a volumetric compression ratio

of 12.0. The selection of piston  $B$  was principally motivated by its beneficial effect on the combustion stability, established in the context of the engine operation with direct ignition (**figure 4.2, b**). This study was realised with a new prechamber which combines all the configuration parameters studied in the previous experiments that induces a decrease in CO emissions without major prejudice to the fuel conversion efficiency. The main features are a large prechamber volume and a low number of nozzle orifices in order to increase the intensity and penetration of the gas jets as well as a large orientation angle from the prechamber axis in order to reach the main combustion zones which are feeding the squish region when the piston starts to move down after TDC. All these features contribute to an early arrival of the flame front at the piston top land and cylinder head gasket crevice entrances and thus to the reduction of the unburnt mixture fraction located in the crevice volumes during the primary oxidation process. Further, the uneven distribution of the nozzle orifices is expected to achieve a more uniform distribution of a limited number of gas jets in the main combustion chamber. Finally, the somewhat lower turbulence intensity in the vicinity of the spark plug electrodes associated with a reduced number and a larger orientation angle of the nozzle orifices enables a moderate decrease in nozzle orifice cross sectional area, in order to promote a further penetration of the gas jets. The resulting new prechamber configuration is featured with an internal volume of  $4540 \text{ mm}^3$  and 4 nozzle orifices of diameter  $2.12 \text{ mm}$  ( $A_n = 14.10 \text{ mm}^2$ ), non-evenly distributed and oriented at an angle of  $\approx 78^\circ$ . The engine was operated at a constant spark timing of  $8.3^\circ CA_{BTDC}$ .

## Results summary

The transition from the original piston ( $A$ ) to a piston generating significantly higher turbulence ( $B$ ) leads to:

- an important intensification and acceleration of the combustion process (**figure 4.29, b**), which decreases the combustion duration (**figure 4.30**)

and when considering the same  $\text{NO}_x$  emissions:

- a moderate decrease of less than  $\approx 4\%$  in CO and THC emissions at low  $\text{NO}_x$  emissions (**figure 4.32, a**)
- an increase in fuel conversion efficiency of  $\approx 0.5\%$ -point at low  $\text{NO}_x$  emissions (**figure 4.32, b**)

Further, it leads to a fundamental change in the evolution of the CO emissions as function of the  $\text{NO}_x$  emissions and to a somewhat stronger tradeoff between THC and  $\text{NO}_x$  emissions (**figure 4.32, a**).

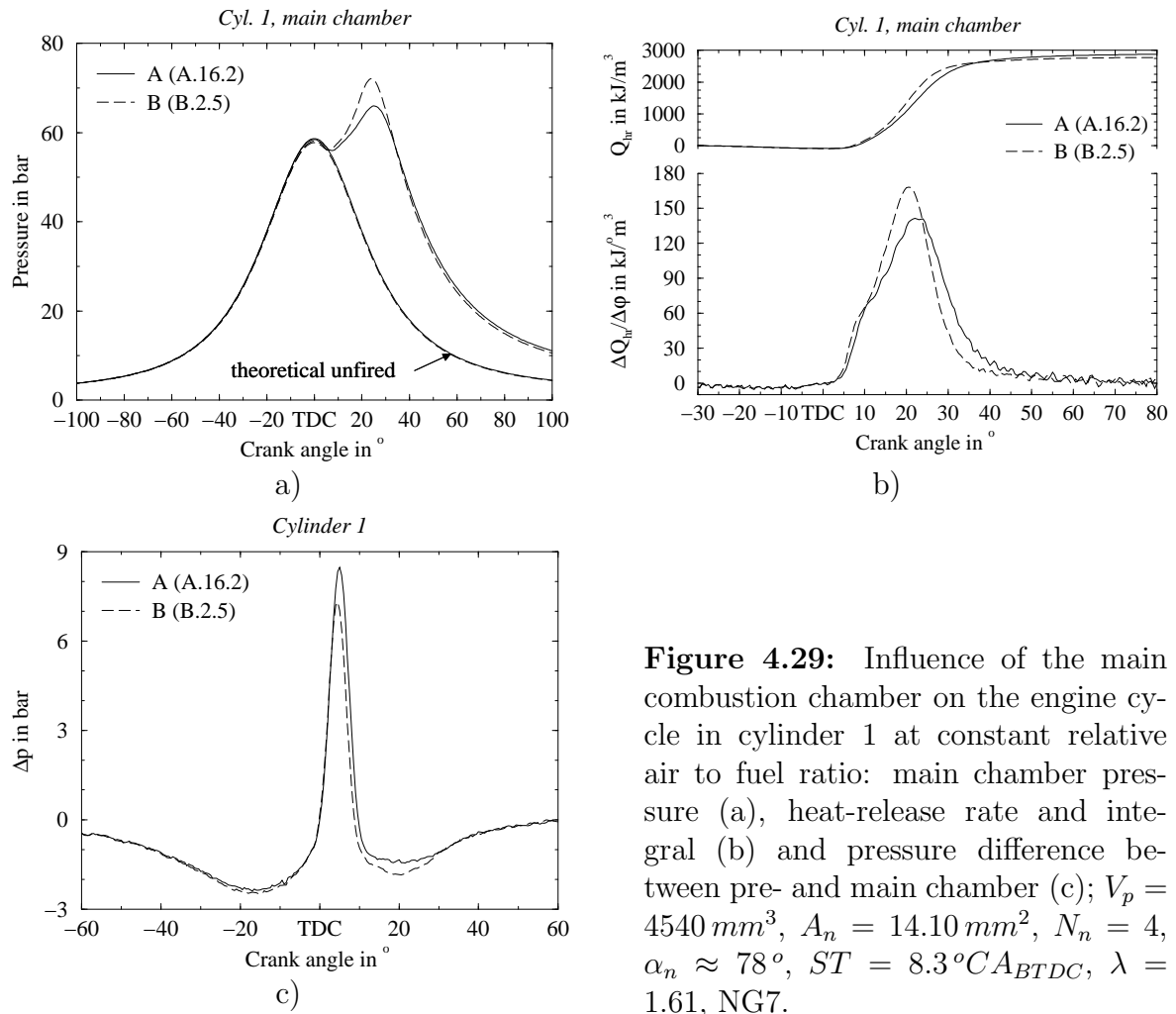


**Figure 4.29:** Influence of the main combustion chamber on the engine cycle in cylinder 1 at constant relative air to fuel ratio: main chamber pressure (a), heat-release rate and integral (b) and pressure difference between pre- and main chamber (c);  $V_p = 4540 \text{ mm}^3$ ,  $A_n = 14.10 \text{ mm}^2$ ,  $N_n = 4$ ,  $\alpha_n \approx 78^\circ$ ,  $ST = 8.3^\circ \text{C} A_{BTDC}$ ,  $\lambda = 1.61$ , NG7.

### Analysis and discussion

The results corresponding to the two different piston geometries are presented together in **figure 4.29**, **figure 4.30** and **figure 4.32**. The transition from piston A to B reduces slightly the intensity and duration of the prechamber pressure pulse (**figure 4.29, c**). However, the higher turbulence generated by piston B strongly intensifies and accelerates the main chamber combustion process (**figure 4.29, b**). This results in a significant reduction of the combustion duration (**figure 4.30**). In turn, the faster combustion process induced by piston B causes an important increase in peak cylinder pressure (**figure 4.29, a**). At equal  $\text{NO}_x$  emissions, the faster combustion generated by piston B leads to a higher fuel conversion efficiency. The difference between the pistons increases with the reduction of  $\text{NO}_x$  emissions to reach a maximum value of approximately 0.5 %-point (**figure 4.32, b**). Further, the transition from piston A to B results in somewhat lower CO and THC emissions at the same  $\text{NO}_x$  emissions (**figure 4.32, a**). However, the difference between both pistons decreases to less than  $\approx 4\%$  at low  $\text{NO}_x$  emissions. In both cases, cylinder 3 is characterised by a higher cycle-by-cycle variability (**figure 4.32, b**). Piston B yields lower and higher cycle-by-cycle variability in cylinder 1 and 3, respectively. The significantly higher cycle-by-cycle variability in cylinder 3 limits the possible reduction of the  $\text{NO}_x$  emissions (**figure 4.32, a**).

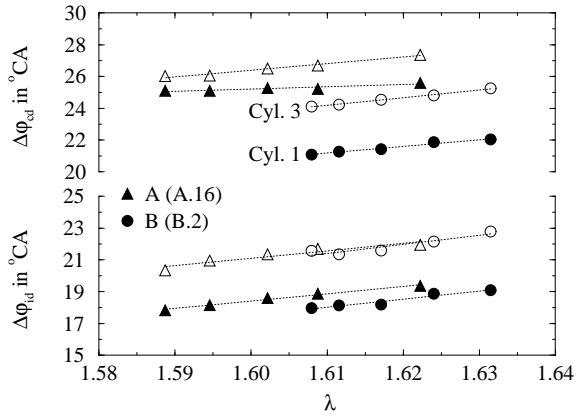


**Figure 4.30:** Influence of the main combustion chamber on the ignition delay and combustion duration as function of relative air to fuel ratio;  $V_p = 4540 \text{ mm}^3$ ,  $A_n = 14.10 \text{ mm}^2$ ,  $N_n = 4$ ,  $\alpha_n \approx 78^\circ$ ,  $ST = 8.3^\circ \text{CA}_{BTDC}$ , NG7.

At a constant relative air to fuel ratio, the change in main combustion chamber geometry does not significantly affect the flow across the nozzle orifices. This causes very similar pressure drop between the main chamber and the prechamber during compression (**figure 4.29, c**). Further, this should result in the same prechamber flow conditions and thus lead to a similar prechamber combustion process until ignition occurs in the main chamber. The higher turbulence intensity (**figure 3.8**) and flow velocities (**figure 4.31**) generated by piston *B* cause a slightly more rapid propagation of the flame front from the emerging gas jets (**figure 4.29, b**). This results in an earlier increase of the cylinder pressure, which reduces the maximum pressure difference between pre- and main chamber (**figure 4.29, c**). Consequently, this should decrease the penetration of the gas jets into the main combustion chamber.

In order to evaluate the change in the interaction between the gas jet and the main chamber flows, the theoretical gas jet paths were superposed on the representation of the flow pattern in the two different combustion chambers at  $5^\circ \text{CA}_{ATDC}$  (**figure 4.31**). The reason for considering the flow pattern without prechamber has already been discussed in section 4.4.5. The numerical simulation indicates that in the case of piston *B*, the regions of the main combustion chamber where the gas jets develop are characterised by a different flow pattern, more directly oriented towards the squish region, and by significantly higher flow velocities. This should accelerate the propagation of the flame front as well as promote an earlier arrival of the flame front at the entrance of the piston top land and cylinder gasket crevices. In the case of piston *B*, the effect of the less deep gas jet penetration may to some extent be compensated by the smaller diameter of the piston bowl entrance (the piston wall on the gas jet path is closer to the prechamber nose). The early stage of the main chamber combustion process is expected to be mainly governed by the characteristics of the gas jets and the important residual turbulence in the vicinity of the nozzle orifices (**figure 3.8**). Therefore, it is not significantly affected by the main combustion chamber geometry (**figure 4.29, b**). Consequently, the significantly higher flow velocities and turbulence generated by piston *B* (**figure 3.8**) causes only a weak decrease of the ignition delay (**figure 4.30**). The significant difference between cylinder 1 and 3 was identified later and originates in a slight leakage of water between the prechamber cooling jacket and the main chamber of cylinder 3 due to an inadequate match of machining tolerances. Because no change was made at the level of prechamber 3 during the experimentation of the two different piston geometries, the results obtained remain consistent. Further, the higher velocities and turbulence intensity produced by piston *B* cause an important

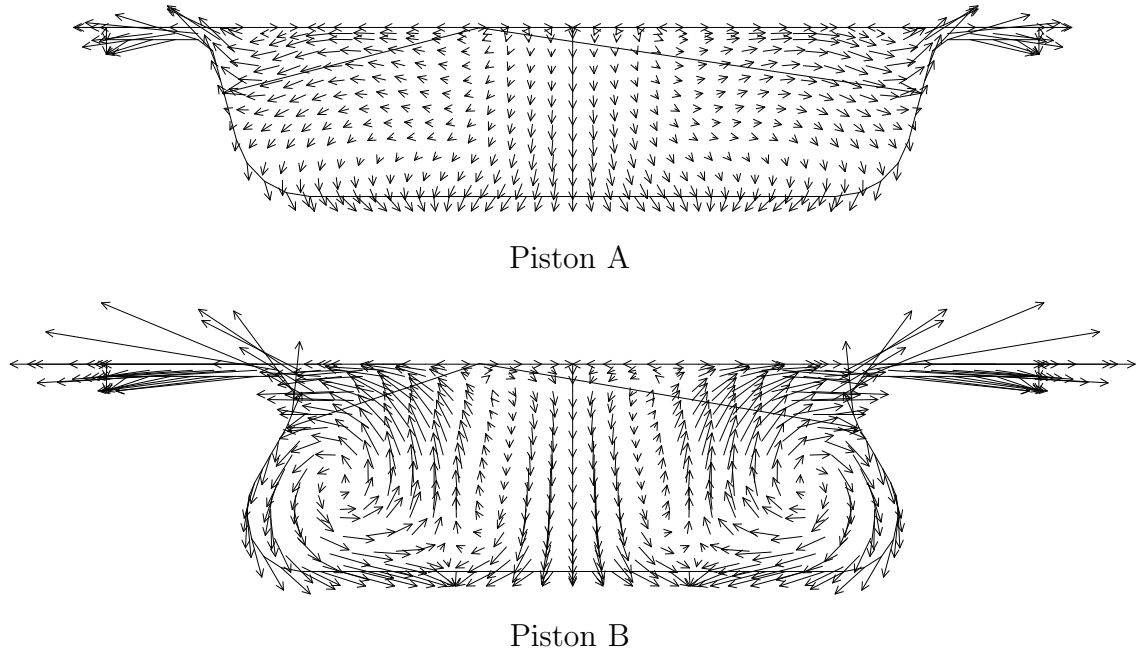


**Figure 4.31:** Simulated flow pattern in the main combustion chambers formed by piston *A* and *B* at  $5^{\circ}CA_{ATDC}$ , with the theoretical paths of the gas jets issuing from the prechamber.

acceleration and intensification of the combustion process, particularly in the late stage (**figure 4.29, b**). This results in a decrease of the combustion duration of more than  $3^{\circ}CA$  (**figure 4.30**). Consequently, the faster combustion process causes an important increase in maximum cylinder pressure (**figure 4.29, a**).

At constant  $NO_x$  emissions, the significantly shorter combustion duration characterising piston *B* (**figure 4.32, c**) causes an increase in fuel conversion efficiency, particularly for the highest values of relative air to fuel ratio (**figure 4.32, b**). Further, the more rapid late stage of the combustion process reduces slightly the cycle-by-cycle variability in cylinder 1. This is indicated by a somewhat lower coefficient of variance of  $p_{mi}$ . The opposite trend observed in cylinder 3 originates mainly in the leakage problem already mentioned previously (further experiments after improvement of the water-tightness of prechamber 3 have shown a similar combustion stability in cylinder 1 and 3).

When considering the same  $NO_x$  emissions, the transition from piston *A* to *B* causes a moderate reduction of CO and THC emissions (**figure 4.32, a**). Further, the difference between both pistons progressively decreases when increasing the relative air to fuel ratio in order to reduce the  $NO_x$  emissions. The different behaviour of the CO and THC emissions when using piston *B* seems to indicate a fundamental change in the interaction between the gas jet and the main chamber flows. This no longer gives a reduction in CO emissions while increasing the relative air to fuel ratio. Piston *B* leads to a higher peak cylinder pressure (**figure 4.29, a**) during combustion and a lower mean combustion temperature during late expansion (**figure 4.32, d**). The former effect should increase the amount of unburnt mixture located in the combustion chamber crevices during the primary oxidation process. The latter effect tends to lower

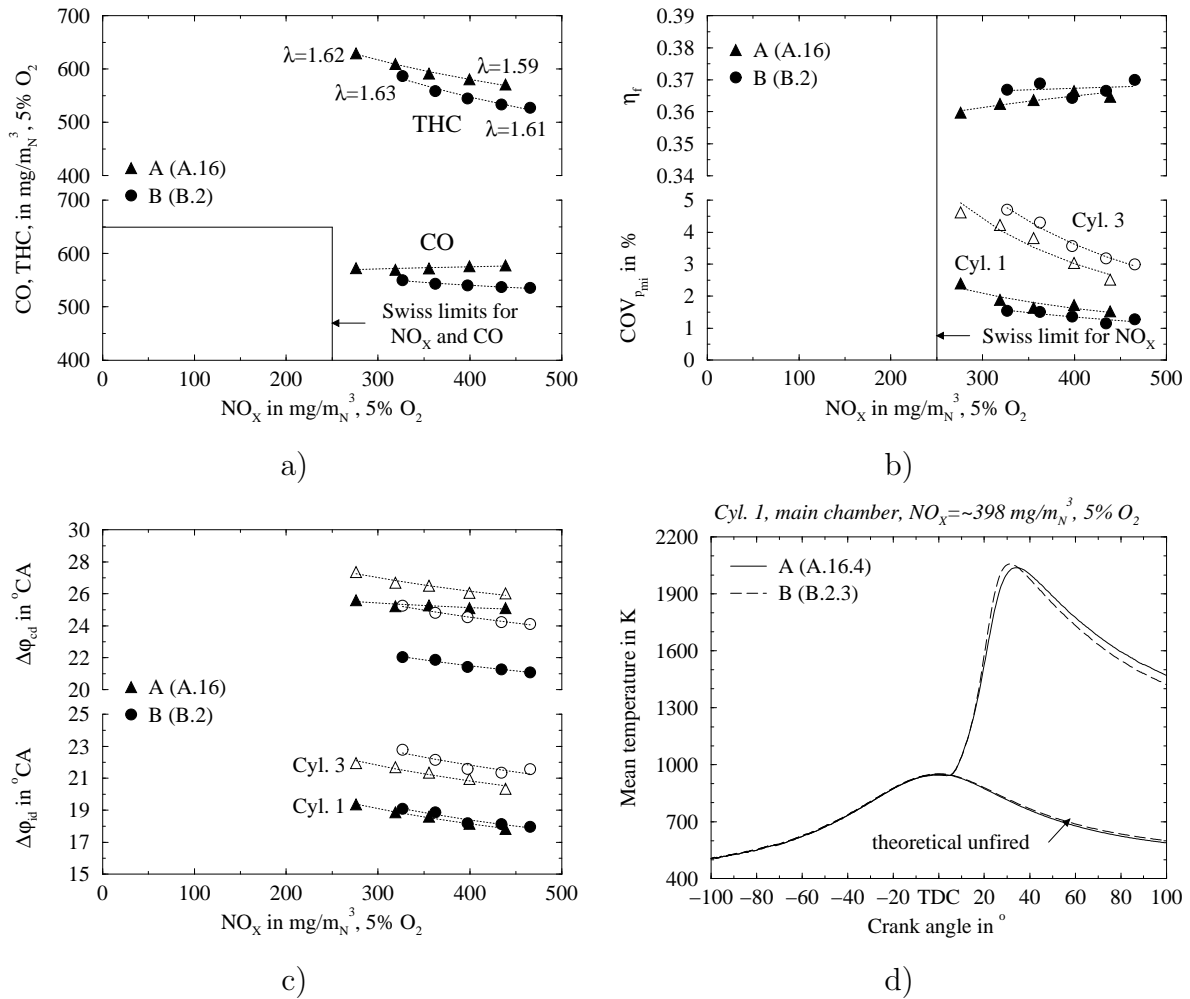


**Figure 4.32:** Influence of the main combustion chamber on the engine performance and emissions as function of  $\text{NO}_x$  emissions: a) CO and THC emissions, b) fuel conversion efficiency and coefficient of variance of  $p_{mi}$ , c) ignition delay and combustion duration; d) mean combustion temperature at  $\text{NO}_x \approx 398 \text{ mg/m}_N^3, 5\% \text{O}_2$ ;  $V_p = 4540 \text{ mm}^3$ ,  $A_n = 14.10 \text{ mm}^2$ ,  $N_n = 4$ ,  $\alpha_n \approx 78^\circ$ ,  $ST = 8.3^\circ\text{CA}_{BTDC}$ , NG7.

the extent of the secondary oxidation of the unburnt hydrocarbons emerging from these crevices. However, piston *B* tends also to promote a more rapid propagation of the flame front towards the squish region and therefore should reduce the amount of unburnt mixture flowing into the piston top land and cylinder head gasket crevices. The lower CO and THC emissions associated with piston *B* tends to demonstrate that this last effect is determinant. The increase in peak cylinder pressure induced by piston *B* results in a higher maximum combustion temperature. Consequently, this requires a moderate increase in relative air to fuel ratio in order to achieve the same  $\text{NO}_x$  emissions (figure 4.32, a). In the case of both pistons, *A* and *B*, the reduction of the  $\text{NO}_x$  emissions is essentially limited by the particularly high cycle-by-cycle variability in cylinder 3.

In comparison with piston *A*, the use of piston *B* achieves a somewhat better fuel conversion efficiency, particularly when increasing the relative air to fuel ratio in order to reduce the  $\text{NO}_x$  emissions. On the other hand, the behaviour of the CO and THC



emissions with the increase of relative air to fuel ratio seems to indicate no significant advantage of piston *B* over piston *A* at a low level of  $\text{NO}_x$  emissions. In order to clarify the real influence of the main chamber geometry on the CO and THC emissions at a low level of  $\text{NO}_x$  emissions, further experimental investigations are required after improvement of the water-tightness between the prechamber water jacket and the main chamber of cylinder 3. Due to the limited time available, they are however out of the scope of the present study. In consequence, piston *B* is used for the investigations of the turbocharger turbine and engine load.

#### 4.4.9 Spark timing

The influence of the spark timing has already been partly discussed in section 4.4.1, comparing the prechamber ignition to the direct ignition. This section discusses the effect of a further delay of the spark timing from  $10.8$  to  $8.3^\circ\text{CA}_{BTDC}$  in the case of two different nozzle orifice total cross sectional areas:  $14.10$  and  $18.85\text{ mm}^2$ . The use of a different natural gas composition has prompted a separate discussion. The experiments were performed with prechambers featured by 4 orifices oriented at  $\approx 62^\circ$ .

#### Results summary

In the case of both total nozzle orifice cross sectional areas, the delay of the spark timing from  $10.8$  to  $8.3^\circ\text{CA}_{BTDC}$  leads to:

- no major change in the intensity and velocity of the combustion process (**figure 4.33, b**)

and when considering same  $\text{NO}_x$  emissions:

- a reduction of  $\approx 10\%$  and  $\approx 14\%$  of the CO and THC emissions, respectively (**figure 4.35, a**)
- a decrease of the fuel conversion efficiency of  $\approx 0.5\%$ -point (**figure 4.35, b**)

Further, it results in a significant potential to reduce the  $\text{NO}_x$  emissions and approach the Swiss limits (**figure 4.35, a**)

#### Analysis and discussion

The results corresponding to the two different total nozzle orifice cross sectional areas and the two different spark timings are represented in **figure 4.33**, **figure 4.34**, **figure 4.35** and **figure 4.36**. The delay of the spark timing from  $10.8$  to  $8.3^\circ\text{CA}_{BTDC}$  causes a shift and a moderate increase in the intensity of the prechamber pressure pulse

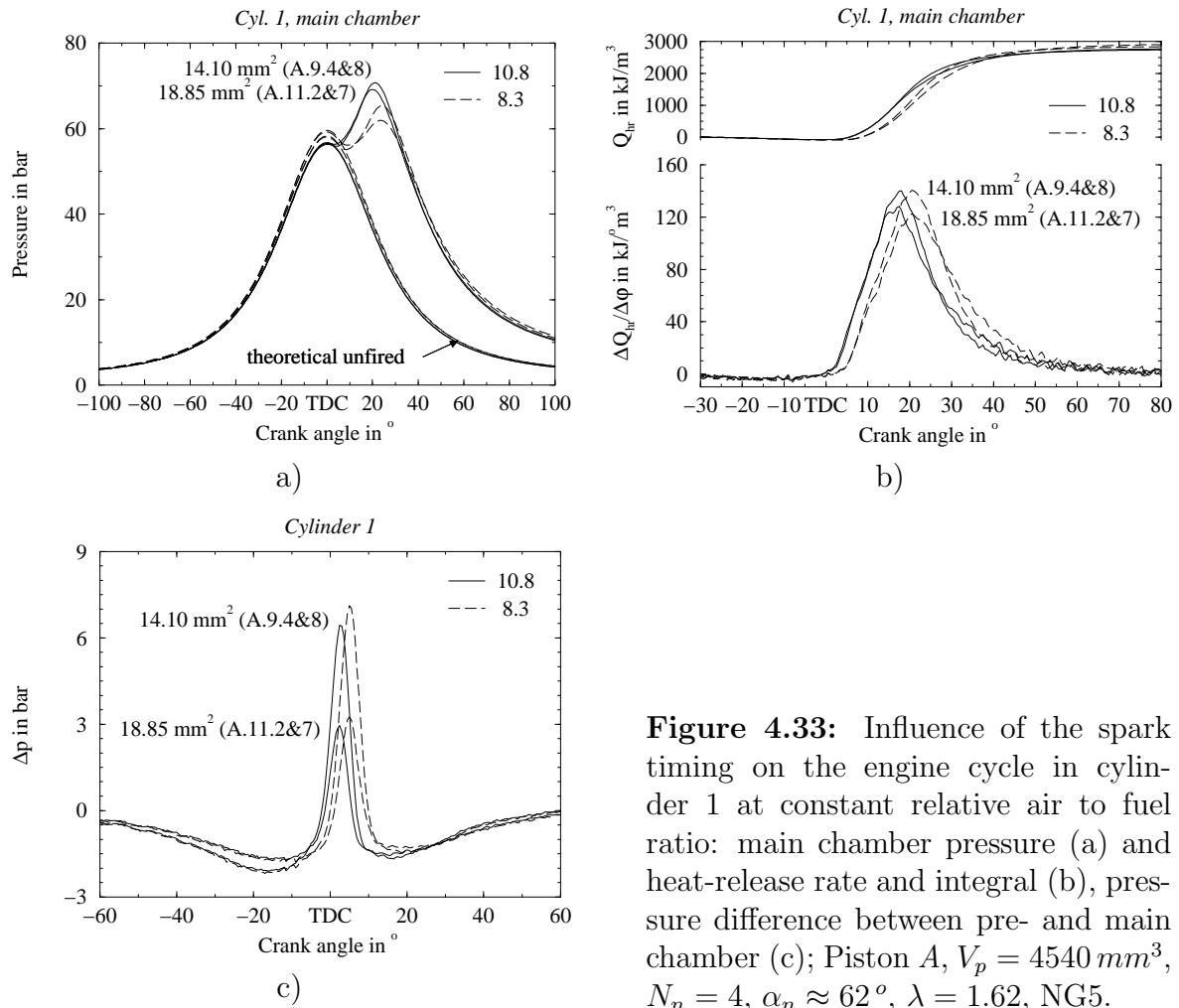


**Figure 4.33:** Influence of the spark timing on the engine cycle in cylinder 1 at constant relative air to fuel ratio: main chamber pressure (a) and heat-release rate and integral (b), pressure difference between pre- and main chamber (c); Piston A,  $V_p = 4540 \text{ mm}^3$ ,  $N_n = 4$ ,  $\alpha_n \approx 62^\circ$ ,  $\lambda = 1.62$ , NG5.

(figure 4.33, c). This results in a shift of the main chamber combustion process in the expansion phase (figure 4.33, b). However, this does not significantly affect the intensity and velocity of the combustion process and leads to a slightly longer ignition delay and a somewhat shorter combustion duration (figure 4.34). In turn, the shift of the combustion process into the expansion phase yields a significantly lower peak cylinder pressure (figure 4.33, a). When considering equal  $\text{NO}_x$  emissions, the late spark timing results in a shorter combustion duration (figure 4.35, c and d). However, the shift of the combustion process into the expansion phase causes a decrease in fuel conversion efficiency of approximately 0.5 %-point (figure 4.35, b). Further, the delay of the spark timing from 10.8 to 8.3  $^\circ\text{CA}_{BTDC}$  causes a significant reduction of  $\approx 10\%$  and  $\approx 14\%$  of the CO and THC emissions, respectively (figure 4.35, a). Finally, the late spark timing enables a significant reduction of the  $\text{NO}_x$  emissions.

When considering a constant relative air to fuel ratio, the delay of the spark timing from 10.8 to 8.3  $^\circ\text{CA}_{BTDC}$  causes a shift and a moderate increase in the intensity of the prechamber pressure pulse (figure 4.33, c). The somewhat higher pressure difference between pre- and main chamber is thought to mainly originate in the larger amount of fuel located in the prechamber at the start of prechamber combustion. This increases the quantity of chemical energy available to generate the gas jets. However, a more extended homogenisation of the unburnt mixture with the residual gas by the main annular recirculation zone located at the top of the prechamber (figure 3.6) may

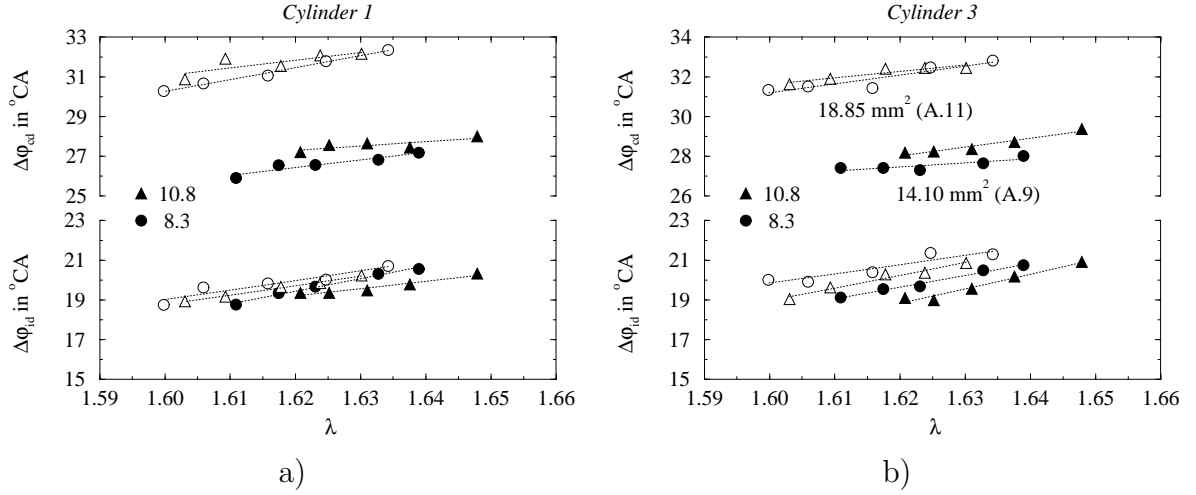


**Figure 4.34:** Influence of the spark timing on the main chamber ignition delay and combustion duration as a function of the relative air to fuel ratio in cylinder 1 (a) and 3 (b); Piston A,  $V_p = 4540 \text{ mm}^3$ ,  $N_n = 4$ ,  $\alpha_n \approx 62^{\circ}$ , NG5.

also contribute to a more rapid and complete fuel conversion during the prechamber combustion. Furthermore, the delayed start of the prechamber combustion process tends to reduce somewhat the fraction of the pressure increase used to overcome the pressure drop across the nozzle orifices. Due to the higher pressure drop across the smaller orifices during the gas jet generation, the delay of the spark timing leads to a larger increase in the pressure difference between pre- and main chamber in the case of the small nozzle orifice cross sectional area (14.10  $\text{mm}^2$ ). The higher pressure difference between pre- and main chamber is expected to result in stronger gas jets.

Despite the stronger gas jets, the delay of the spark timing from 10.8 to 8.3  $^{\circ}\text{CA}_{\text{BTDC}}$  yields a slight increase of the main chamber ignition delay (**figure 4.34**). This may be caused by the further expansion of the unburnt mixture before combustion start (in the case of both spark timings, the main chamber ignition occurs after TDC); the resulting lower temperature slows down the chemical reaction kinetics. However, the deeper penetration of the gas jets associated with the late spark timing sufficiently accelerates the main chamber combustion process to fully compensate the detrimental effect of the lower combustion temperature and of the larger amount of fuel to burn (**figure 4.33, b**) (the higher fuel consumption results from the shift of the combustion process into the expansion phase). In the case of the small nozzle orifice cross sectional area (14.10  $\text{mm}^2$ ), this is illustrated by a similar (but shifted into the expansion phase) rate of heat release up to the maximum value and by a faster second part of the combustion process. This results in a somewhat shorter combustion duration (**figure 4.34**). In the case of the large nozzle orifice cross sectional area (18.85  $\text{mm}^2$ ), the more moderate increase in the gas jet penetration leads to a somewhat lower rate of heat release during the first part of the combustion process (**figure 4.33, b**). However, this is compensated by a faster second part of the combustion process, which leads to almost the same overall combustion duration (**figure 4.34**). When considering the same relative air to fuel ratio, the higher fuel consumption requires an increase of the boost pressure in order to keep the same engine load. This consequently causes a mod-

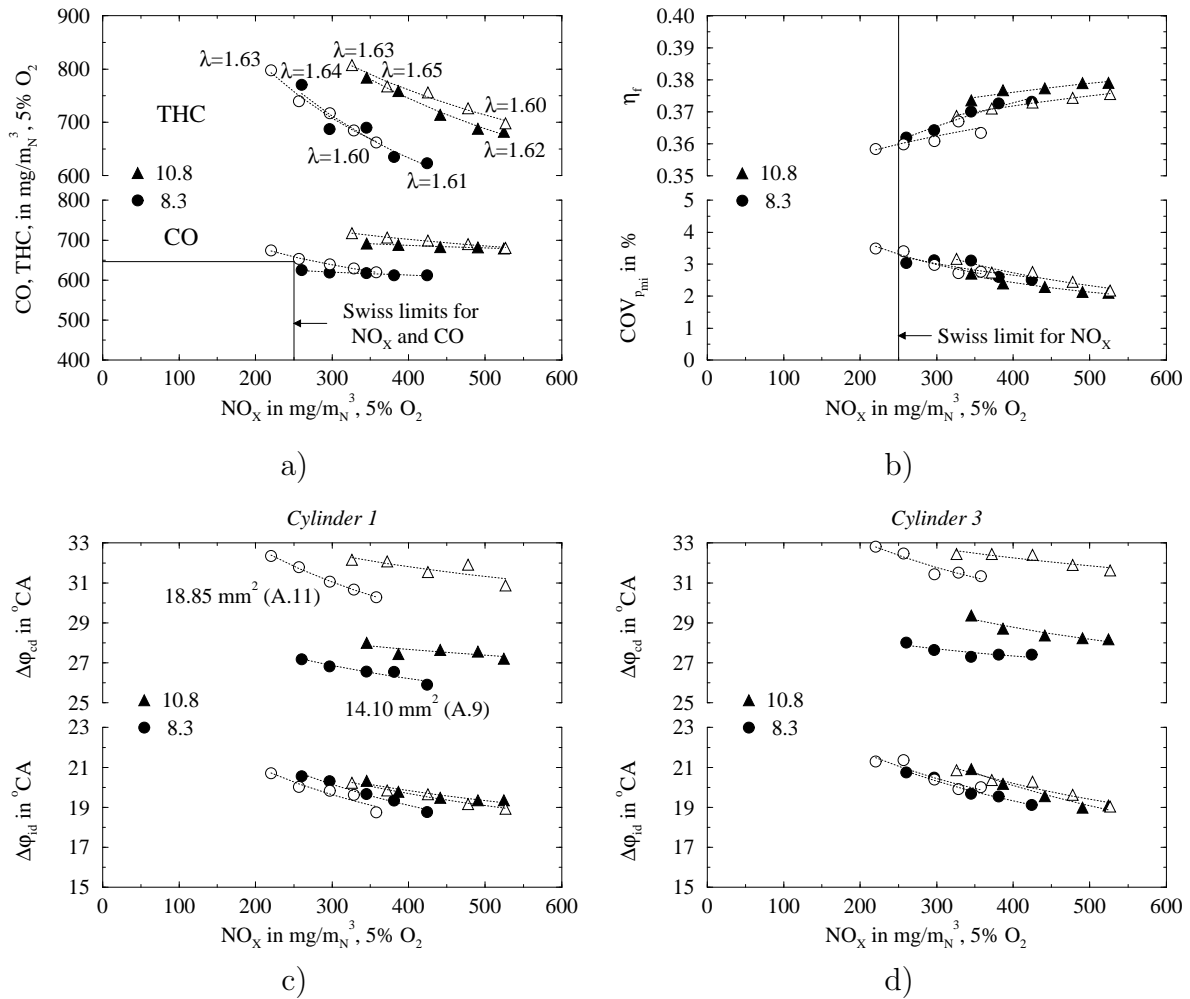


**Figure 4.35:** Influence of the spark timing on the engine emissions and performance as function of  $\text{NO}_x$  emissions: a) CO and THC emissions, b) fuel conversion efficiency and coefficient of variance of  $p_{mi}$ ; ignition delay and combustion duration in cylinder 1 (c) and 3 (d);  $V_p = 4540 \text{ mm}^3$ ,  $N_n = 4$ ,  $\alpha_n \approx 62^\circ$ , NG5.

erate increase of the maximum compression pressure (figure 4.33, a). However, the shift of the combustion process into the expansion phase leads to a significant decrease of the maximum combustion pressure.

The delay of the spark timing causes a significant reduction of the combustion temperature, which enables a decrease of the relative air to fuel ratio in order to achieve the same  $\text{NO}_x$  emissions (figure 4.35, a). This promotes a more rapid main chamber combustion process and consequently results in a shorter ignition delay and combustion duration at constant  $\text{NO}_x$  emissions (figure 4.35, c and d). The shift of the main chamber combustion process into the expansion phase tends to decrease the combustion pressure and consequently the work transferred to the piston. However, this detrimental effect is partly compensated by a shorter combustion process and therefore results in only a moderate decrease of the fuel conversion efficiency of about 0.5 %-point at constant  $\text{NO}_x$  emissions (figure 4.35, b). The intensification of the late stage of the main chamber combustion process realised through the delay of the spark timing is expected to reduce the tendency to bulk gas quenching at the end of combustion.

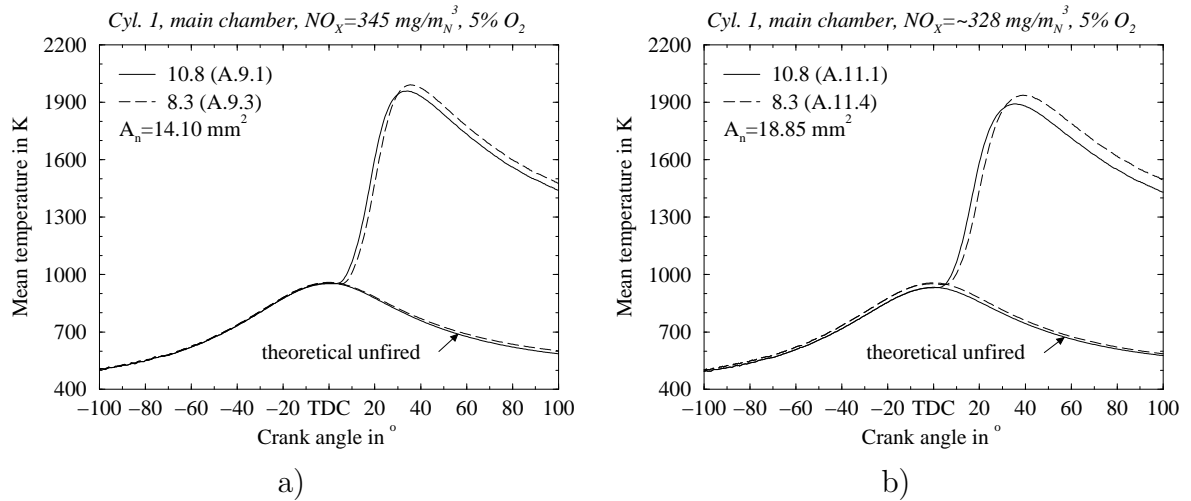


**Figure 4.36:** Influence of the spark timing on the mean combustion temperature at constant  $\text{NO}_x$  emissions in the case of a nozzle orifice total cross sectional area of  $14.10 \text{ mm}^2$  (a) and  $18.85 \text{ mm}^2$  (b); Piston  $A$ ,  $V_p = 4540 \text{ mm}^3$ ,  $N_n = 4$ ,  $\alpha_n \approx 62^\circ$ , NG5.

This may explain why both spark timings result in a similar cycle-by-cycle variability, as indicated by approximately the same coefficient of variance of  $p_{mi}$ .

The delay of the spark timing from  $10.8$  to  $8.3^\circ \text{CA}_{BTDC}$  requires a decrease in relative air to fuel ratio in order to achieve the same  $\text{NO}_x$  emissions (**figure 4.35, a**). When considering equal  $\text{NO}_x$  emissions, the delay of the spark timing causes an important decrease of approximately 10% and 14% in CO and THC emissions, respectively. Further, the behaviour of the CO and THC emissions is not significantly affected by the change in the total nozzle orifice cross sectional area. The decrease in CO and THC emissions is thought to mainly result from a reduction of the amount of fuel located in the combustion chamber crevices during the primary oxidation process. This assumption is supported by the lower combustion pressure (**figure 4.33, a**) and the somewhat deeper penetration of the gas jets induced by the later spark timing. However, the contribution of both these effects is to some extent attenuated by the slight decrease in relative air to fuel ratio required to achieve the same  $\text{NO}_x$  emissions (**figure 4.35, a**); this leads to an increase in the fuel concentration of the unburnt mixture located in the crevices. On the other hand, the higher mean combustion temperature during late expansion (**figure 4.36**) associated with the late spark timing should promote a more complete secondary oxidation. In the case of the late spark timing, the lower relative air to fuel ratio required to achieve the same  $\text{NO}_x$  emissions and the moderate cycle-by-cycle variability enables a significant reduction of the  $\text{NO}_x$  emissions (**figure 4.35, a**).

The delay of the spark timing from  $10.8$  to  $8.3^\circ \text{CA}_{BTDC}$  leads to an important reduction of the CO and THC emissions at constant  $\text{NO}_x$  emissions. Further, it enables to significantly decrease the  $\text{NO}_x$  emissions. However, this also causes a weak reduction of the fuel conversion efficiency. Considering the limited effect on the engine fuel economy, the delay of the spark timing represents a particularly effective means of reducing the exhaust gas emissions.

#### 4.4.10 Turbocharger turbine

On a turbocharged engine, the rated brake power output (maximum value at wide open throttle), is obtained through an adjustment of the turbocharger boost pressure. This is realised by an adaptation of the turbine volute throat area. The reduction of this area causes an increase of the pressure in the exhaust manifold, which is transformed in the turbine volute (in the case of the small turbocharger used, the turbine has no stator with blades) into flow kinetic energy. This energy is then converted by the turbine wheel into mechanical work. Consequently, the higher flow kinetic energy increases the mechanical work supplied to the compressor. However, an increase of the exhaust manifold pressure leads to a higher engine pumping work. When considering the same combustion process, this results in a reduction of the fuel conversion efficiency.

In the case of the turbocharger used (*KKK*, size *K27*), the turbine housing is designed with one or two volute channels, depending on the size of the total volute throat area; one channel from 6 to 16  $cm^2$  and two channels from 12 to 21  $cm^2$ . The division of the volute into two channels separates engine cylinders with overlapping exhaust phases into two different groups. These two groups each have separate exhaust manifolds which merge together only shortly before the turbine wheel inlet. This reduces the influence of the exhaust blow down phase of a cylinder, generating a high pressure pulse in the exhaust manifold, on the end of the exhaust stroke of the previous cylinder in the firing order. A low pressure in the exhaust manifold at the end of the exhaust stroke reduces the engine pumping work and thus improves the fuel conversion efficiency. The test engine is equipped with an exhaust manifold in two parts grouping cylinders 1, 2, 3 and 4, 5, 6 respectively together (firing order: 1-5-3-6-2-4).

The turbine used in all previous experiments has a single volute channel with a throat area of 11  $cm^2$ . The small size of the volute restricts the number of channels to one and thus does not enable advantage to be taken of having the exhaust manifold in two separate parts. This value was chosen for the parametric study in order to enable engine operation at the rated brake power output (150  $kW$ ) up to a relative air to fuel ratio of approximately 1.9, without modification of the turbocharger. Theoretically, an objective comparison of the performance and emissions of different engine configurations (pre- or main chamber variations) would require an adjustment of the turbocharger characteristics in order to operate the engine at wide open throttle or at least at the same compressor inlet pressure. However, this is not possible because of the too large step of 2  $cm^2$  (in most cases) between the different turbine volute throat areas available. For this reason, the control of the brake power output was realised by engine throttling.

In order to evaluate the influence of the exhaust manifold pressure on the combustion process and on the fuel conversion efficiency, the turbine volute throat area was increased to 17  $cm^2$ . This value enables engine operation very close to wide open throttle. Because this relatively large turbine is only available with two channels, the results of this particular investigation illustrate the combined effect of a simultaneous increase of the turbine volute throat area and channel number. In the case of this particular investigation, the pressure in the intake and exhaust port of cylinder 1 was measured with the high speed data acquisition system. The investigation was con-

ducted with piston  $B$  and a prechamber featured with an internal volume of  $4540 \text{ mm}^3$  and 4 nozzle orifices of diameter  $2.12 \text{ mm}$  ( $A_n = 14.10 \text{ mm}^2$ ), non-evenly distributed and oriented at an angle of  $\approx 78^\circ$ . The engine was operated at a constant spark timing of  $8.3^\circ \text{CA}_{BTDC}$ .

### Results summary

The increase of the turbine volute throat area from  $11$  to  $17 \text{ cm}^2$  in order to operate the engine close to wide open throttle results in:

- no significant change in the combustion process (**figure 4.39, b**)

and when considering the same  $\text{NO}_x$  emissions:

- an increase of  $\approx 3\%$  and  $\approx 40\%$  of the CO and THC emissions, respectively (**figure 4.40, a**). In both cases, the  $\text{NO}_x$  and CO emissions can be reduced under the Swiss limits, but however with only a narrower margin
- a significant increase of the fuel conversion efficiency of  $0.5$  to  $1\%$ -point (**figure 4.40, b**)
- no perceptible change in cycle-by-cycle variability (**figure 4.40, b**)

The major increase in THC emissions originates in significant changes in the exhaust manifold gas dynamics.

### Analysis and discussion

#### a) Breathing process and turbocharger operation

The pressure cycle measured in the intake and exhaust port of cylinder 1 is represented in **figure 4.37, a** over an entire engine cycle ( $720^\circ \text{CA}$ ). In the case of the part of the figure illustrating the exhaust port pressure, the numbers identify the peak value corresponding to the end of the blow-down phase of the different cylinders, following the firing order. The portion of the pressure cycle corresponding to the intake and exhaust strokes are represented in **figure 4.37, b** and **figure 4.37, c**, respectively. Finally, the pressure difference between intake and exhaust ports during valve overlap is given in **figure 4.37, d**.

The increase in turbine volute throat area and channel number significantly affects the exhaust port and manifold pressure dynamics (**figure 4.37, a**). These two parameters have distinct effects on the exhaust port pressure. On the one hand, the increase of the volute throat area leads to a decrease of the mean pressure during the exhaust phase. On the other hand, the complete separation of the two parts of the

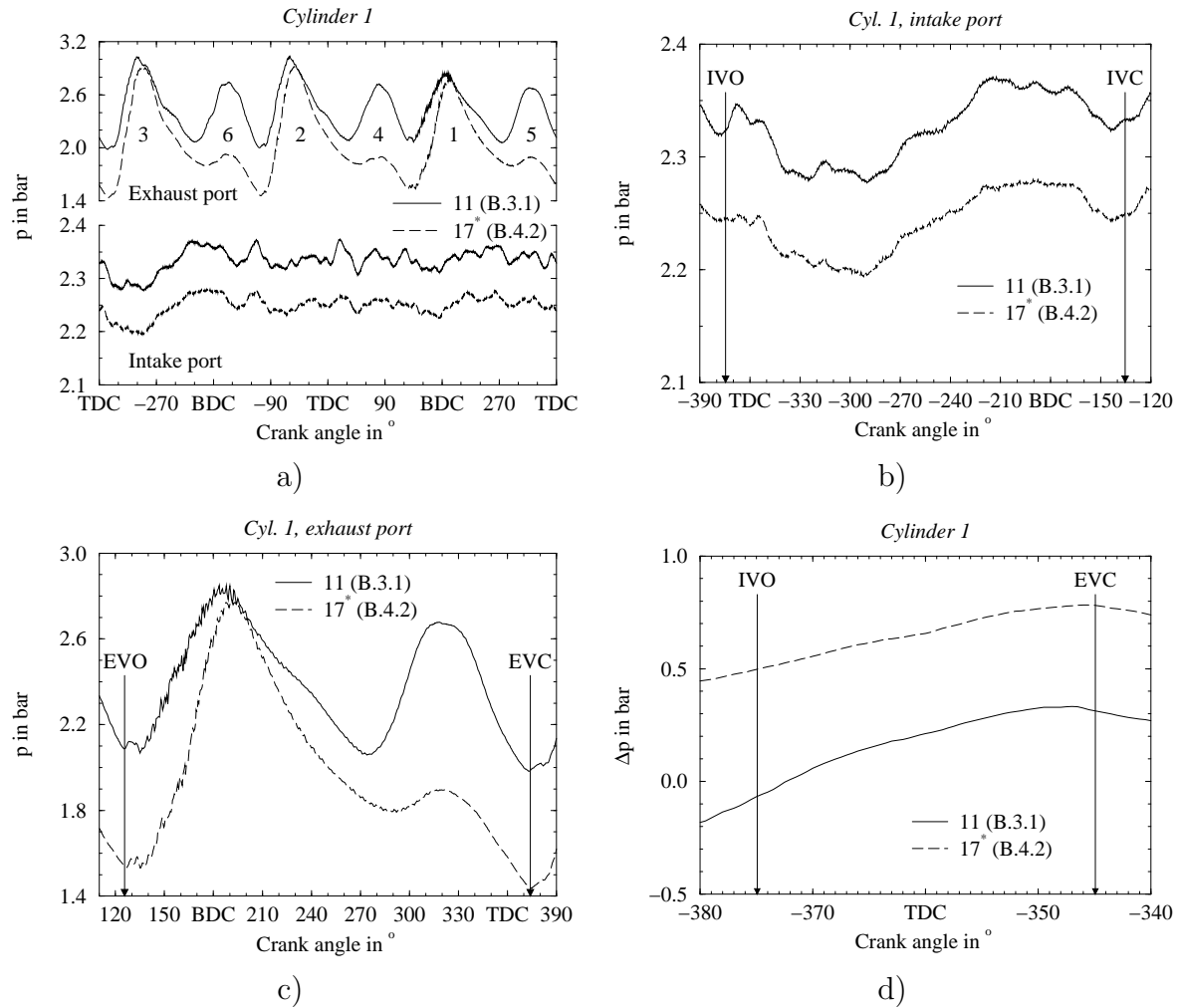


**Figure 4.37:** Influence of the turbocharger turbine volute throat area on the intake and exhaust port pressure of cylinder 1 at constant relative air to fuel ratio: intake and exhaust port pressure during the whole engine cycle (a), intake port pressure during the intake stroke (b), exhaust port pressure during the exhaust stroke (c) and pressure difference between intake and exhaust ports during valve overlap ; Piston B,  $V_p = 4540 \text{ mm}^3$ ,  $A_n = 14.10 \text{ mm}^2$ ,  $N_n = 4$ ,  $\alpha_n \approx 78^\circ$ ,  $RH = 49$  (\*47)%,  $\lambda = 1.67$ ,  $ST = 8.3^\circ \text{C A}_{BTDC}$ ,  $\lambda = 1.67$ , NG7.

exhaust manifold with a turbine housing with two distinct channels strongly damps the effect of the blow-down phase of a cylinder on the previous cylinder in the firing order (**figure 4.37, c**). This leads to a much lower pressure at the end of the exhaust stroke. However, the resulting reduction of the exhaust manifold volume (only half of the total manifold volume is available to collect the blow-down gas) causes a higher pressure increase during the blow-down phase.

The reduction of the mean exhaust port pressure (back pressure) decreases the cylinder pressure at exhaust valve closure. Thus, a lower boost pressure is required to achieve the same cylinder filling (**figure 4.37, b**). Further, the decrease in back pressure reduces the amount of residual gas trapped in the cylinder at exhaust valve closure. In comparison to the exhaust manifold, the intake manifold is characterised by much lower pressure dynamics, showing no significant interactions between the



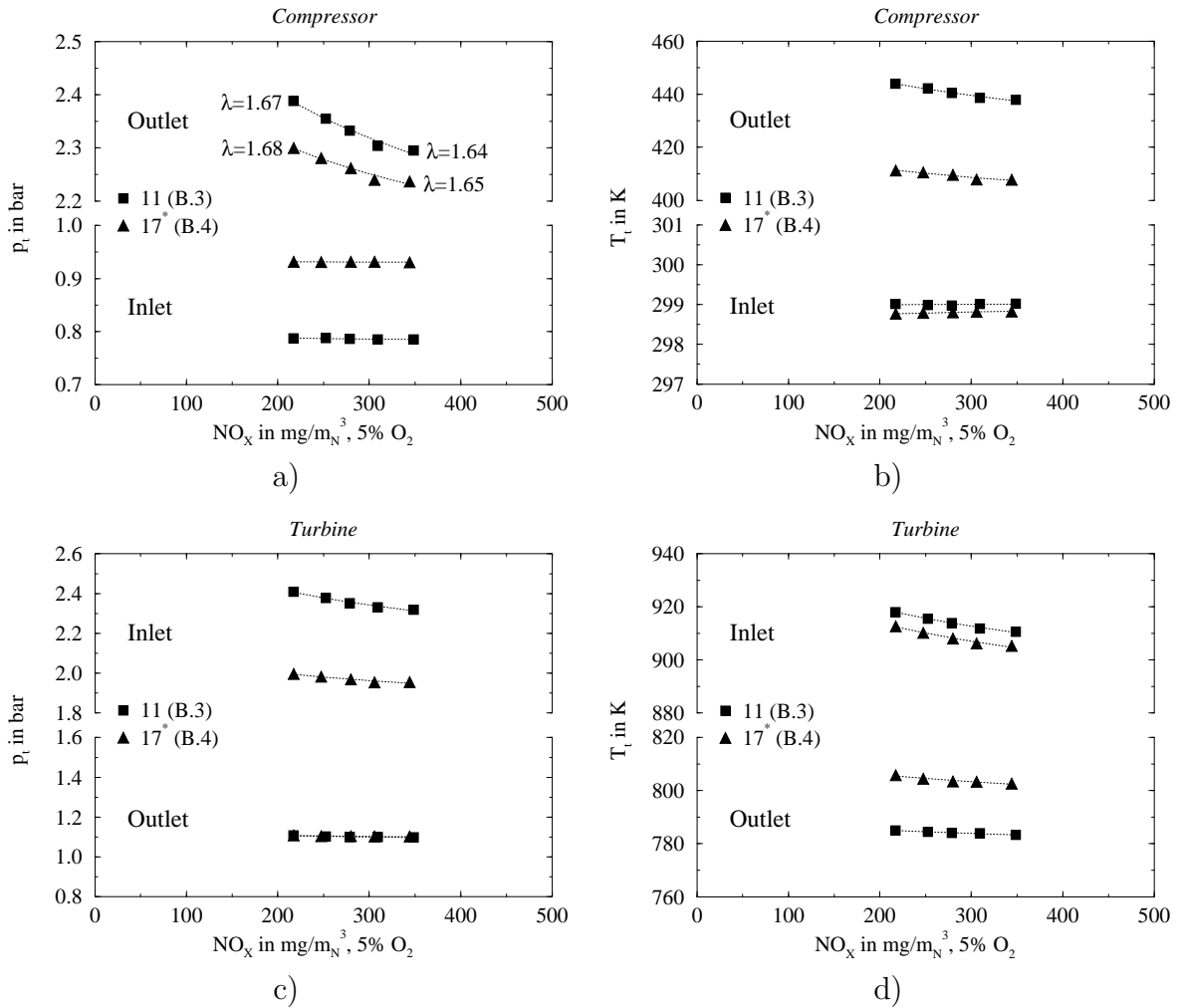


**Figure 4.38:** Influence of the turbocharger turbine volute throat area on the turbocharger operating characteristics as function of  $\text{NO}_x$  emissions: a) compressor total pressure, b) compressor total temperature, c) turbine total pressure, d) turbine total temperature; Piston  $B$ ,  $V_p = 4540 \text{ mm}^3$ ,  $A_n = 14.10 \text{ mm}^2$ ,  $N_n = 4$ ,  $\alpha_n \approx 78^\circ$ ,  $RH = 49$  (\* 47) %,  $ST = 8.3^\circ\text{C}A_{BTDC}$ , NG7.

cylinders (**figure 4.37, a**). The pressure decrease during the first part of the intake stroke (**figure 4.37, b**) originates in the rapid acceleration of the flow in the port. From mid-stroke ( $90^\circ\text{C}A_{BBDC}$ ), the piston starts to slow down and consequently the flow decelerates, resulting in an increase of the pressure to reach again the level at rest. The combination of a moderate reduction of the boost pressure and a more significant decrease of the exhaust back pressure causes an important increase of the pressure difference between intake and exhaust ports during valve overlap (**figure 4.37, d**). This tends to promote a direct transfer of unburnt mixture from the intake port to the exhaust port and thus to increase the emissions of hydrocarbons.

In order to discuss the effect of the turbine characteristics on the turbocharger operation, the total pressure and temperature at the inlet and outlet of the compressor and turbine are presented as function of  $\text{NO}_x$  emissions in **figure 4.38**. The increase in turbine volute throat area leads to a significant decrease of about  $0.4 \text{ bar}$  in mean pressure at turbine inlet (**figure 4.38, c**). This results in a reduction of the flow

kinetic energy available to the turbine wheel and thus decreases the mechanical work delivered to the compressor wheel. In order to compensate partly for the resulting reduction of the compressor pressure ratio, this requires opening the throttle valve to increase the pressure at compressor inlet (**figure 4.38, a**). The large turbine volute throat area enables engine operation very close to wide open throttle. This reduces the pressure drop across the venturi mixer and the throttle valve from 140 down to 30 *mbar* (pressure at venturi mixer inlet: 960 *mbar*). On the other hand, the reduction of the mean exhaust port pressure (**figure 4.37, a**) decreases the cylinder pressure at exhaust valve closure. Consequently, this reduces the boost pressure required to achieve the same cylinder filling by approximately 0.1 *bar* (**figure 4.38, a**). In turn, this leads to a significant decrease of about 30 *K* in temperature at compressor outlet (**figure 4.38, b**). Finally, the reduction of the mean exhaust manifold pressure causes a slight decrease in temperature at turbine inlet and results in a moderate increase of approximately 20 *K* in temperature at turbine outlet (**figure 4.38, d**).

## b) Combustion process, emissions and engine performance

The results corresponding to the two different turbine volute configurations are represented together in **figure 4.39** and **figure 4.40**. The increase in turbine volute throat area has no significant effect on the prechamber and main chamber combustion processes (**figure 4.39, c and b**). When considering equal NO<sub>x</sub> emissions, the increase in volute throat area leads to an increase between 0.5 and 1.0 %-point in fuel conversion efficiency (**figure 4.40, b**). However, this also results in a moderate increase of approximately 3% in CO emissions and a large increase of about 40% in THC emissions (**figure 4.40, a**).

As already discussed in the previous section, the reduction of the turbine volute throat area leads to a lower amount of residual gas trapped in the cylinder at exhaust valve closure. At constant relative air to fuel ratio, this reduces the total mass of gas located in the cylinder during the compression-expansion phase and results in a lower maximum compression pressure (**figure 4.39, a**). The moderate change in unburnt mixture composition and compression pressure has no perceptible effect on the prechamber combustion process (**figure 4.39, c**). Further, it does not affect significantly the main chamber combustion process (**figure 4.39, b**). The somewhat lower pressure and concentration in residual gas of the unburnt mixture slightly increases the speed of the flame front propagation [13, 58], which leads to a moderate reduction of the combustion duration (**figure 4.39, d**). The lower compression pressure results in a lower maximum combustion pressure (**figure 4.39, a**).

In the case of the large turbine volute throat area, the weak increase in flame front propagation speed results in a somewhat higher maximum combustion temperature. Therefore, a slight increase in relative air to fuel ratio is required to achieve the same NO<sub>x</sub> emissions (**figure 4.40, a**). This also fully compensates the effect of the reduction in residual gas concentration on the flame speed and consequently results in a similar combustion duration at constant NO<sub>x</sub> emissions (**figure 4.40, c**). The reduction of the exhaust back pressure causes a significant decrease of the engine pumping work, which leads to an increase of 0.5 to 1.0 %-point in fuel conversion efficiency (**figure 4.40, b**).

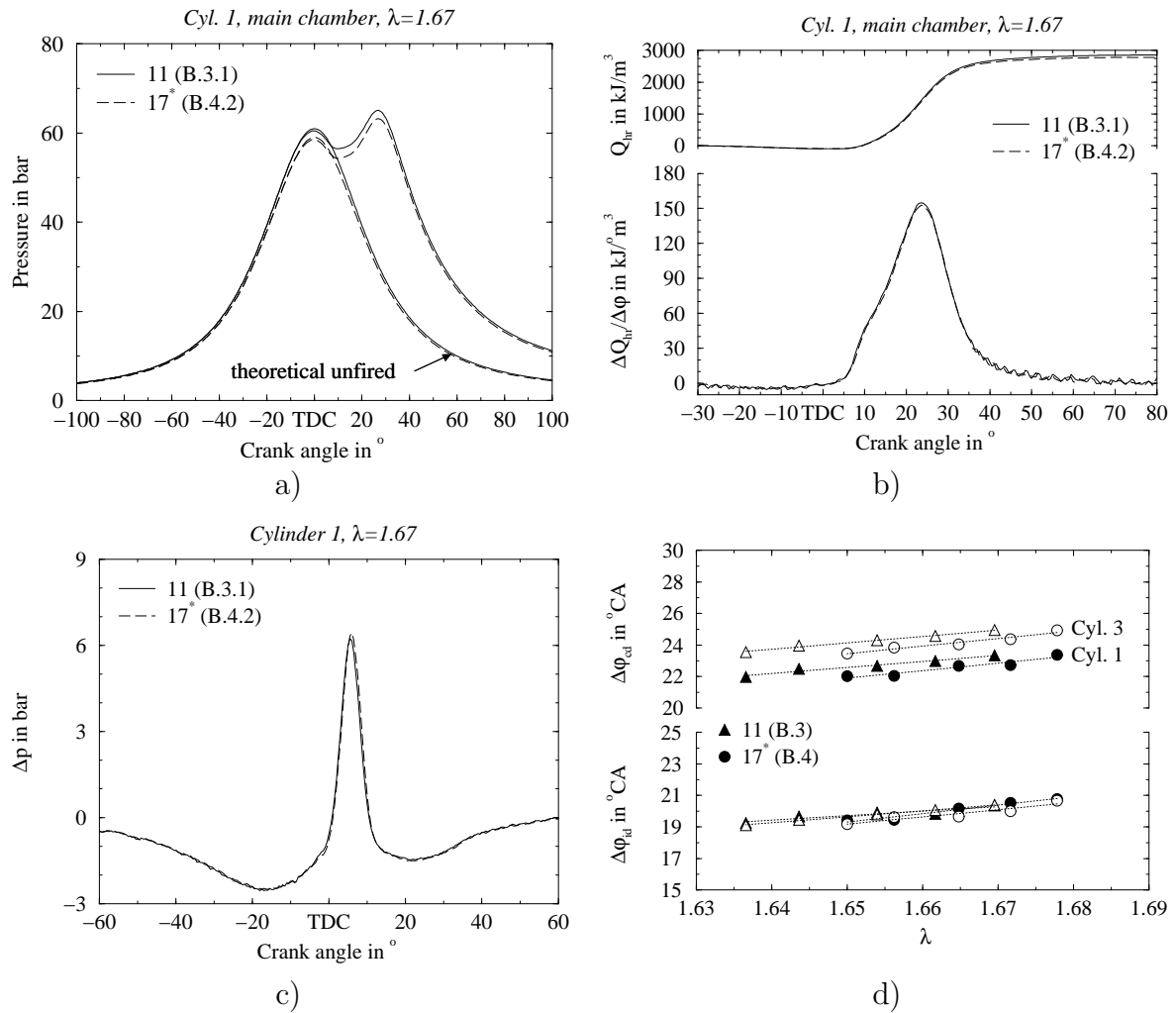


**Figure 4.39:** Influence of the turbocharger turbine volute throat area on the engine cycle in cylinder 1 at constant relative air to fuel ratio: main chamber pressure (a), heat-release rate and integral (b) and pressure difference between pre- and main chamber (c); main chamber ignition delay and combustion duration as a function of the relative air to fuel ratio (d); Piston  $B$ ,  $V_p = 4540 \text{ mm}^3$ ,  $A_n = 14.10 \text{ mm}^2$ ,  $N_n = 4$ ,  $\alpha_n \approx 78^\circ$ ,  $RH = 49$  (\* 47) %,  $ST = 8.3^\circ\text{CA}_{BTDC}$ , NG7.

Because the larger volute throat area does not affect the combustion process, it leads to a similar cycle-by-cycle variability at equal  $\text{NO}_x$  emissions. In the case of a relatively rich mixture, the similar behaviour of cylinder 1 and 3 clearly indicates that the leakage problem between the water jacket and the main combustion chamber of cylinder 3 has been solved. However, the combustion stability of cylinder 3 still more rapidly deteriorates when increasing the relative air to fuel ratio. Despite the low overall cycle-by-cycle variability in cylinder 1 and 3, the engine could not be satisfactorily operated on a leaner fuel-air mixture. The visible deterioration of the engine operating stability noticed on the test bed could originate in an increase of cycle-by-cycle variability in one or several other engine cylinders (2, 4, 5 and 6). The ignition system used does not enable a separate adjustment of the spark timing in each cylinder. Further, a previous study [3] indicated a difference of about  $0.8^\circ\text{CA}$  between the most extreme cylinders when operating the engine at a spark timing of  $20^\circ\text{CA}_{BTDC}$ . The uniformity of the spark timing of the different cylinders becomes more important when operating

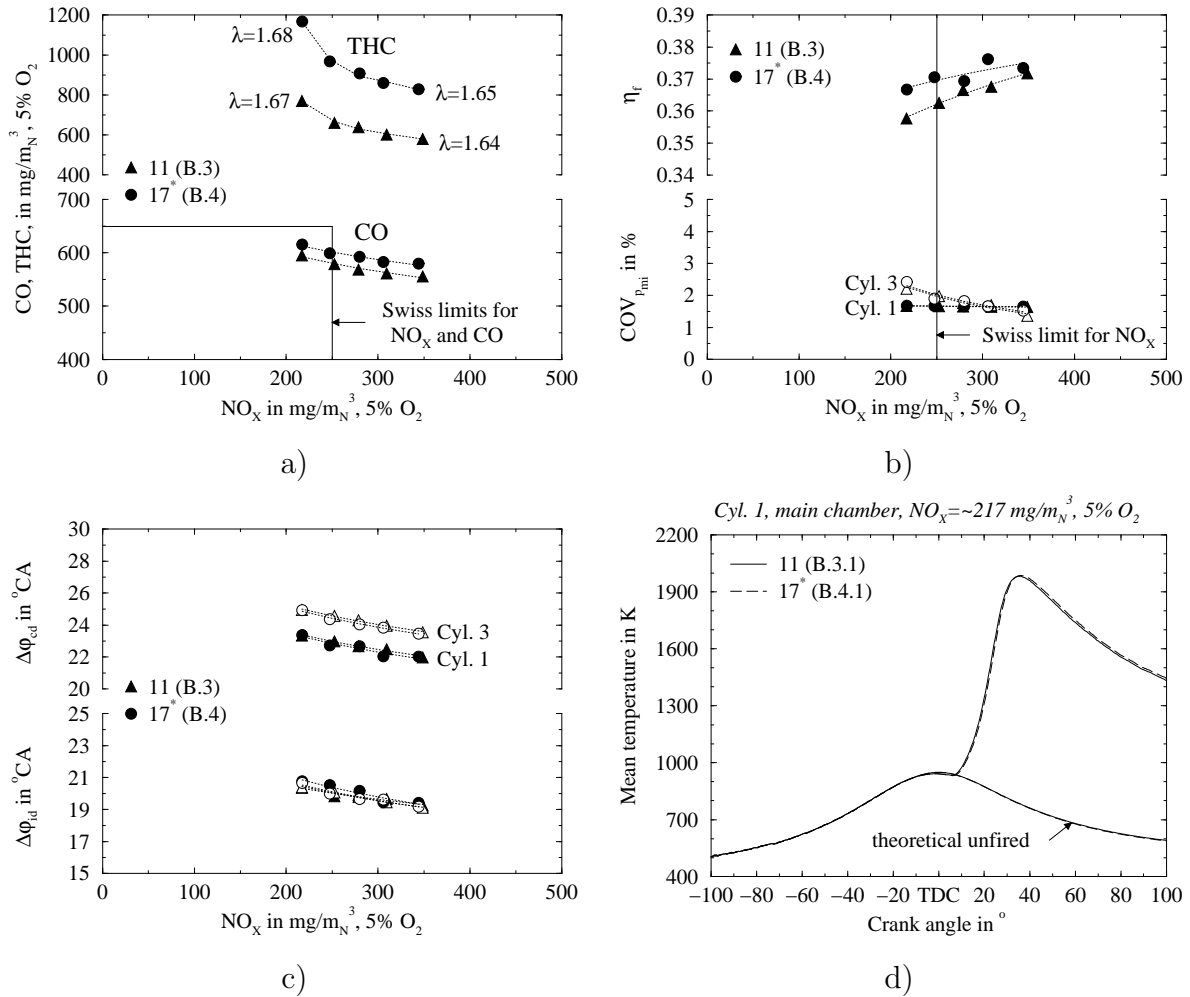


**Figure 4.40:** Influence of the turbocharger turbine volute throat area on the engine performance and emissions as function of  $\text{NO}_x$  emissions: a) CO and THC emissions, b) fuel conversion efficiency and coefficient of variance of  $p_{mi}$ , c) ignition delay and combustion duration; d) mean combustion temperature at  $\text{NO}_x \approx 217 \text{ mg}/\text{m}^3$ , 5%  $\text{O}_2$ ; Piston B,  $V_p = 4540 \text{ mm}^3$ ,  $A_n = 14.10 \text{ mm}^2$ ,  $N_n = 4$ ,  $\alpha_n \approx 78^\circ$ ,  $RH = 49$  (\*47)%,  $ST = 8.3^\circ\text{CA}_{BTDC}$ , NG7.

the engine close to the lean limit. Therefore, unequal spark timing in the different cylinders could contribute to some extent to the deterioration of the overall engine operating stability. The use of an ignition system with individual tuning of the spark timing should clarify this aspect.

When considering equal  $\text{NO}_x$  emissions, the large turbine volute throat area yields approximately 3% higher CO emissions and about 40% higher THC emissions (figure 4.40, a). This is thought to mainly result from the combination of a small decrease of the boost pressure of  $\approx 0.1 \text{ bar}$  (figure 4.37, b) and an important reduction of the exhaust back pressure at the end of the exhaust stroke of  $\approx 0.5 \text{ bar}$  (figure 4.37, c). This causes a higher pressure difference between intake and exhaust port during valve overlap (figure 4.37, d) and thus increases the amount of unburnt mixture flowing directly from the intake into the exhaust. Due to the relatively low temperature in the exhaust manifold ( $\approx 910 \text{ K}$ , (figure 4.38, d)), this unburnt mix-

ture is expected to react to a limited extent [13] and therefore should mainly remain in form of hydrocarbon emissions. Further, the significantly lower exhaust back pressure before exhaust valve closure also enables a more efficient cylinder scavenging. In consequence, a larger amount of exhaust gas with a high concentration of unburnt or partially oxidised hydrocarbons [13] (mainly resulting from the combustion chamber crevice mechanism) is transferred into the exhaust manifold. The much larger increase in THC than in CO emissions tends to indicate that the direct transfer of unburnt mixture into the exhaust system during valve overlap contributes to the largest extent.

The engine operation at rated load and wide open throttle requires the increase of the turbine volute throat area from 11 to  $17\text{ cm}^2$ , which imposes the transition from one to two volute channels. This leads to a significant decrease of the exhaust port pressure, which reduces the engine pumping work and consequently increases the fuel conversion efficiency. However, the lower exhaust port pressure promotes the direct transfer of unburnt mixture from the intake into the exhaust port during valve overlap and results in an important increase in THC emissions. In order to reduce this latter effect, two different approaches should be investigated. The first approach consists of reducing the amplitude of the exhaust pressure fluctuations through the use of a single exhaust manifold of larger internal volume (plenum chamber). This should decrease the average exhaust manifold pressure in order to reduce the engine pumping work, while avoiding an excessive pressure drop during valve overlap. The second approach consists in reducing the valve overlap duration, but without reducing the valve stroke, as in the earlier investigation described in appendix C.4.3. This should decrease part of the detrimental effect on the engine pumping work, while keeping the beneficial effect on the THC emissions. However, both approaches would require the manufacture of special parts for engine operation on gaseous fuel, thus increasing the cost of the diesel engine conversion.

#### 4.4.11 Engine load

In order to evaluate the influence of the engine load on the pre- and main chamber combustion processes, engine performance and emissions as well as on the turbocharger operating characteristics, the brake mean effective pressure was progressively reduced from 12.0 to 7.3 *bar*. This corresponds to a decrease from 100 % (150 *kW*) to 60 % (90 *kW*) of the rated engine brake power output, which covers the typical operating range of a cogeneration engine. The investigation was performed at approximately constant  $\text{NO}_x$  emissions of  $281 \pm 10\text{ mg/m}_N^3$ , 5 %  $\text{O}_2$ . This corresponds to the lowest value which enables a stable engine operation over the whole range of load. The relatively large scatter originates in the fact that the  $\text{NO}_x$  emissions are available in *ppm* on the test bed and are only later computed in  $\text{mg/m}_N^3$ , 5 %  $\text{O}_2$  during the data processing, when the exact natural gas composition is known. This study was realised with piston *B* and a prechamber featured with an internal volume of  $4540\text{ mm}^3$  and 4 nozzle orifices of diameter 2.12 *mm* ( $A_n = 14.10\text{ mm}^2$ ), non-evenly distributed and oriented at an angle of  $\approx 78^\circ$ . The turbocharger was fitted with the large turbine volute throat area of  $17\text{ cm}^2$  and the engine was operated at a constant spark timing of  $8.3^\circ\text{CA}_{BTDC}$ . The load was controlled by engine throttling and the relative air

to fuel ratio was adjusted to maintain constant  $\text{NO}_x$  emissions. When operating the engine at rated load, the exhaust gas stagnation pressure after turbine outlet was set to 1050 *mbar* through a dedicated butterfly valve located on the exhaust system. Then, when reducing the engine load, the valve was maintained at the same position in order to simulate as close as possible the conditions corresponding to a real exhaust system.

## Results summary

While maintaining constant  $\text{NO}_x$  emissions of  $\approx 281 \pm 10 \text{ mg}/\text{m}_N^3$ , 5%  $\text{O}_2$ , the brake mean effective pressure was progressively reduced from 12.0 to 7.3 *bar*. The results indicate:

- a reduction of the combustion intensity and duration (**figure 4.44, b** and **figure 4.45, c**)
- a weak decrease in CO and THC emissions (**figure 4.45, a**)
- a progressive reduction of the fuel conversion efficiency from 36.9 to 34.5% (**figure 4.45, b**)
- a turbocharger operation at an isentropic efficiency greater than 76% over the whole range of load, thus very close to the maximum value (**figure 4.42**)

When operating under conditions which are able to fulfil the Swiss limits at engine rated load, the actual combustion chamber configuration (prechamber and main chamber) does not enable a sufficiently stable practical engine operation over the whole range of load.

## Analysis and discussion

### a) Breathing process and turbocharger operation

The results corresponding to the breathing process and the turbocharger operation are represented in **figure 4.41**, **figure 4.42** and **figure 4.43**.

The reduction of the engine load from the rated value is realised through engine throttling. This causes an increase of the pressure drop across the throttle valve, which results in a decrease of the pressure at turbocharger compressor inlet (**figure 4.41, a**). At this stage, two distinct effects influence the boost pressure. On the one hand, when considering a constant compressor pressure ratio, the reduction of the pressure before compressor leads to a direct decrease of the boost pressure. On the other hand, the reduction of boost pressure and the decrease of the relative air to fuel ratio required to maintain constant  $\text{NO}_x$  emissions results in a lower cylinder charge, which causes a decrease of the exhaust gas pressure before turbine (**figure 4.41, c**). The consequent reduction of the mechanical work supplied to the compressor leads to a decrease of the

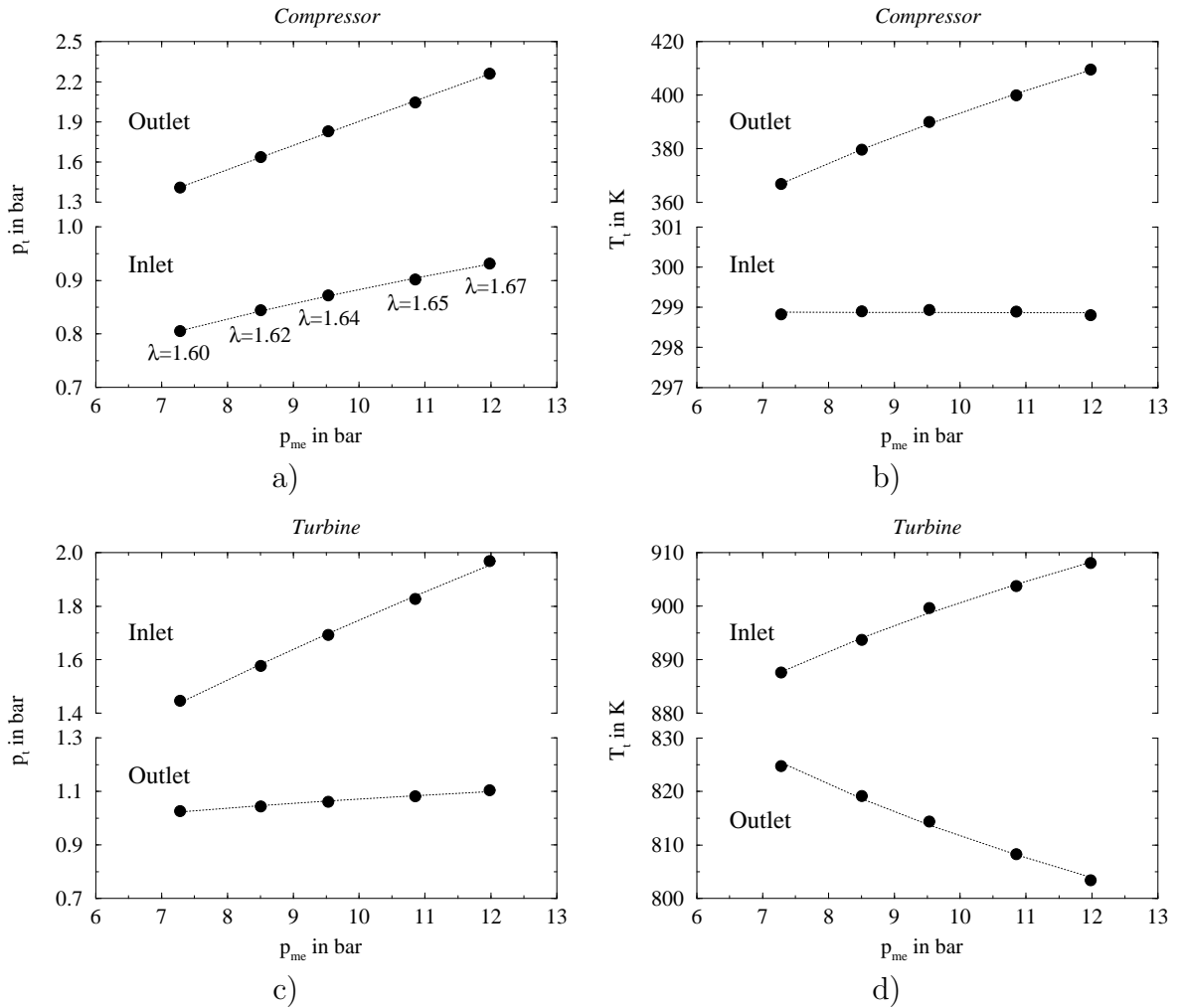


**Figure 4.41:** Effect of the brake mean effective pressure on the turbocharger operating characteristics at constant  $\text{NO}_x$  emissions of  $\approx 281 \pm 10 \text{ mg}/\text{m}_N^3$ , 5%  $\text{O}_2$ : a) compressor total pressure, b) compressor total temperature, c) turbine total pressure, d) turbine total temperature; Piston  $B$ ,  $V_p = 4540 \text{ mm}^3$ ,  $A_n = 14.10 \text{ mm}^2$ ,  $N_n = 4$ ,  $\alpha_n \approx 78^\circ$ ,  $A_t = 17 \text{ cm}^2$ ,  $RH = 47\%$ ,  $ST = 8.3^\circ\text{C} A_{BTDC}$ , NG7.

compressor pressure ratio, which induces a further reduction of the boost pressure. Due to the relatively high sensitivity of the turbocharger to mass flow variations, a moderate reduction of the pressure before compressor leads to a large reduction of the boost pressure (**figure 4.41, a**). In turn, the reduction of the boost pressure causes a significant decrease of the unburnt mixture temperature after compressor (**figure 4.41, b**). At the lowest load ( $p_{me} = 9.3 \text{ bar}$ ), the temperature at compressor outlet drops to  $365 \text{ K}$  ( $92^\circ\text{C}$ ), which no longer enables a constant unburnt mixture temperature of  $90^\circ\text{C}$  to be maintained at intake manifold inlet. In this particular case, the temperature was  $86^\circ\text{C}$ . The decrease of the mean exhaust manifold pressure (**figure 4.41, c**) resulting from the lower mass flow rate leads to a decrease of the temperature at turbine inlet (**figure 4.41, d**). Even though no detailed turbine performance map is available, the moderate increase of the temperature after turbine outlet is expected to originate in the decrease of the turbine efficiency resulting from the reduction of the expansion ratio [13]. Finally, the decrease of the mass flow rate reduces the pressure drop in the exhaust system, which results in a lower pressure at the turbine outlet (**figure 4.41, c**).

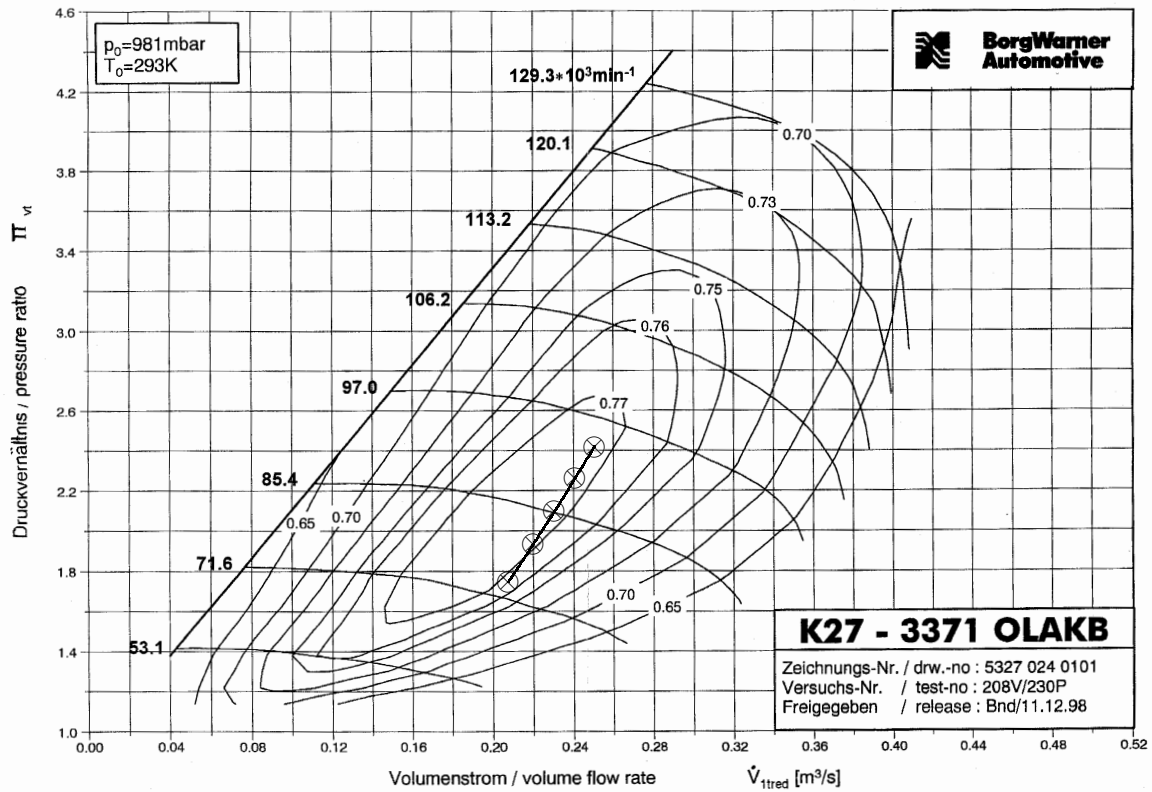


**Figure 4.42:** Turbocharger compressor performance map with superposition of the engine operating points during the variation of brake mean effective pressure; Piston  $B$ ,  $V_p = 4540 \text{ mm}^3$ ,  $A_n = 14.10 \text{ mm}^2$ ,  $N_n = 4$ ,  $\alpha_n \approx 78^\circ$ ,  $A_t = 17 \text{ cm}^2$ ,  $RH = 47\%$ ,  $ST = 8.3^\circ \text{C}_{BTDC}$ , NG7.

In order to evaluate the turbocharger compressor operating conditions, the engine operating points were superposed on the compressor performance map (figure 4.42). This figure indicates that the compressor operates between approximately 75 000 and 95 000  $\text{rpm}$ . At rated load, the compressor operates with an isentropic efficiency of 77%, which is very close to the maximum value. When reducing the engine load, the isentropic efficiency decreases only moderately and remains higher than 76%. This indicates a reasonable match between the engine and the turbocharger operating conditions. However, slightly better turbocharger performance could be achieved by selecting a somewhat larger compressor.

When reducing the engine load, the decrease in unburnt mixture mass flow rate reduces the intake port pressure variations during the intake stroke (figure 4.43, a). At part load, the lower cylinder charge decreases the overall pressure level during compression, combustion and expansion (figure 4.44, a). In turn, this reduces the pressure difference between cylinder and exhaust port when the exhaust valve opens. This significantly decreases the exhaust port pressure rise during the blow down phase and reduces the average value over the whole exhaust process (figure 4.43, b). Further, the larger decrease in intake port pressure than in exhaust port pressure lowers the pressure difference between intake and exhaust ports during valve overlap (figure 4.43, c). This tends to reduce the direct transfer of unburnt mixture into the exhaust system



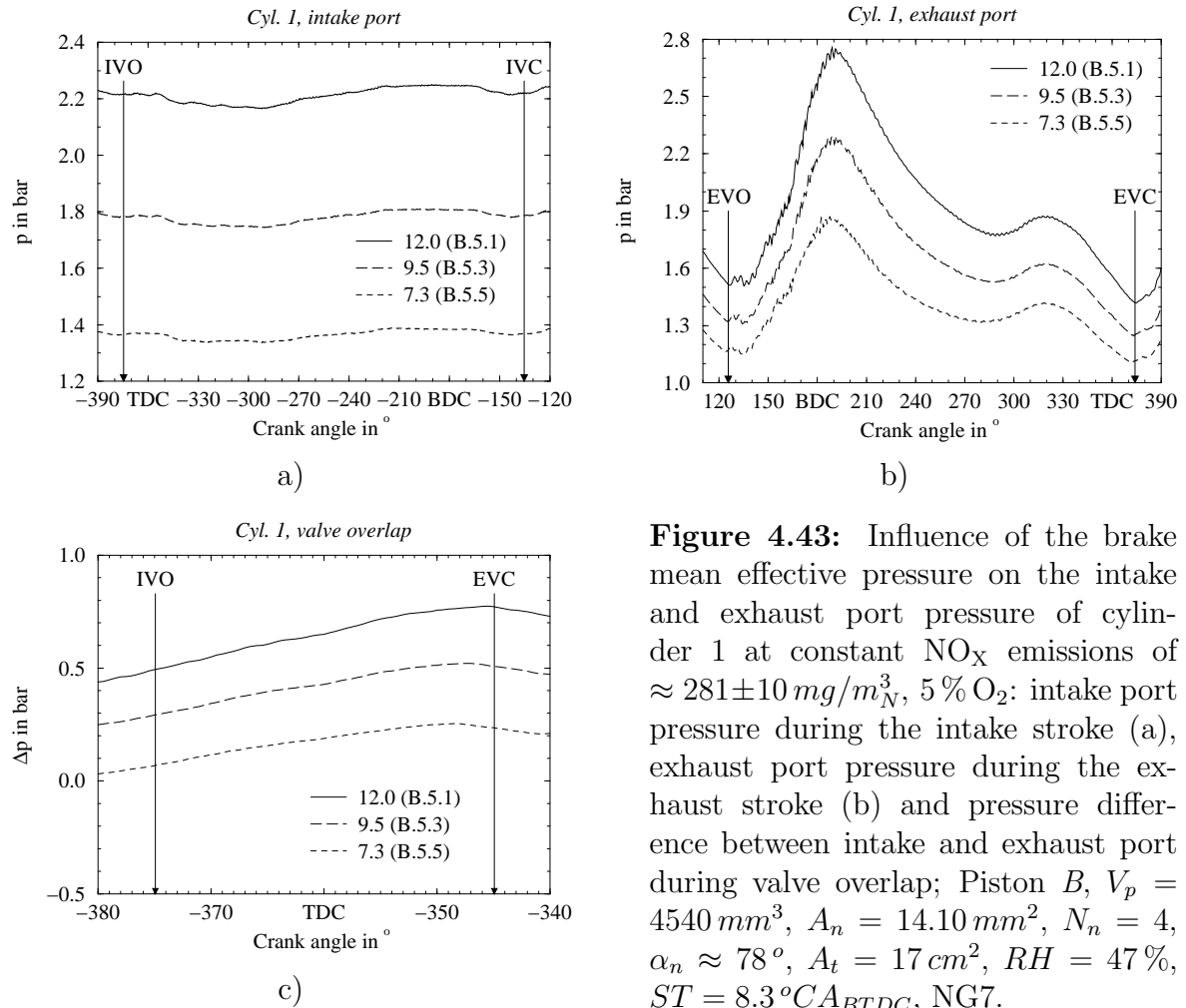


**Figure 4.43:** Influence of the brake mean effective pressure on the intake and exhaust port pressure of cylinder 1 at constant  $\text{NO}_x$  emissions of  $\approx 281 \pm 10 \text{ mg/m}_N^3$ , 5%  $\text{O}_2$ : intake port pressure during the intake stroke (a), exhaust port pressure during the exhaust stroke (b) and pressure difference between intake and exhaust port during valve overlap; Piston  $B$ ,  $V_p = 4540 \text{ mm}^3$ ,  $A_n = 14.10 \text{ mm}^2$ ,  $N_n = 4$ ,  $\alpha_n \approx 78^\circ$ ,  $A_t = 17 \text{ cm}^2$ ,  $RH = 47\%$ ,  $ST = 8.3^\circ \text{C}_{A_{BTDC}}$ , NG7.

and thus limits the waste of fuel and the consequent increase in hydrocarbon emissions.

## b) Combustion process, emissions and engine performance

The influence of the engine load on the combustion process, emissions and engine performance is represented in **figure 4.44** and **figure 4.45**. The reduction of the engine load causes an important decrease in the pressure during compression (**figure 4.44, a**). Further, this leads to a reduction of the prechamber pressure pulse intensity (**figure 4.44, c**), which results in a lower main chamber combustion intensity (**figure 4.44, b**) and duration (**figure 4.45, c**). The reduction of the engine load causes a progressive decrease in fuel conversion efficiency from 36.9 to 34.5%, but does not significantly affect the cycle-by-cycle variability (**figure 4.45, b**). Finally, it results in a weak decrease in CO and THC emissions (**figure 4.45, a**).

The achievement of a lower engine load at constant  $\text{NO}_x$  emissions requires the simultaneous reduction of the boost pressure and of the relative air to fuel ratio. This decreases the amount of unburnt mixture inducted into the cylinder and therefore results in a lower cylinder compression pressure (**figure 4.44, a**). The decrease of the compression pressure reduces the amount of unburnt mixture flowing into the

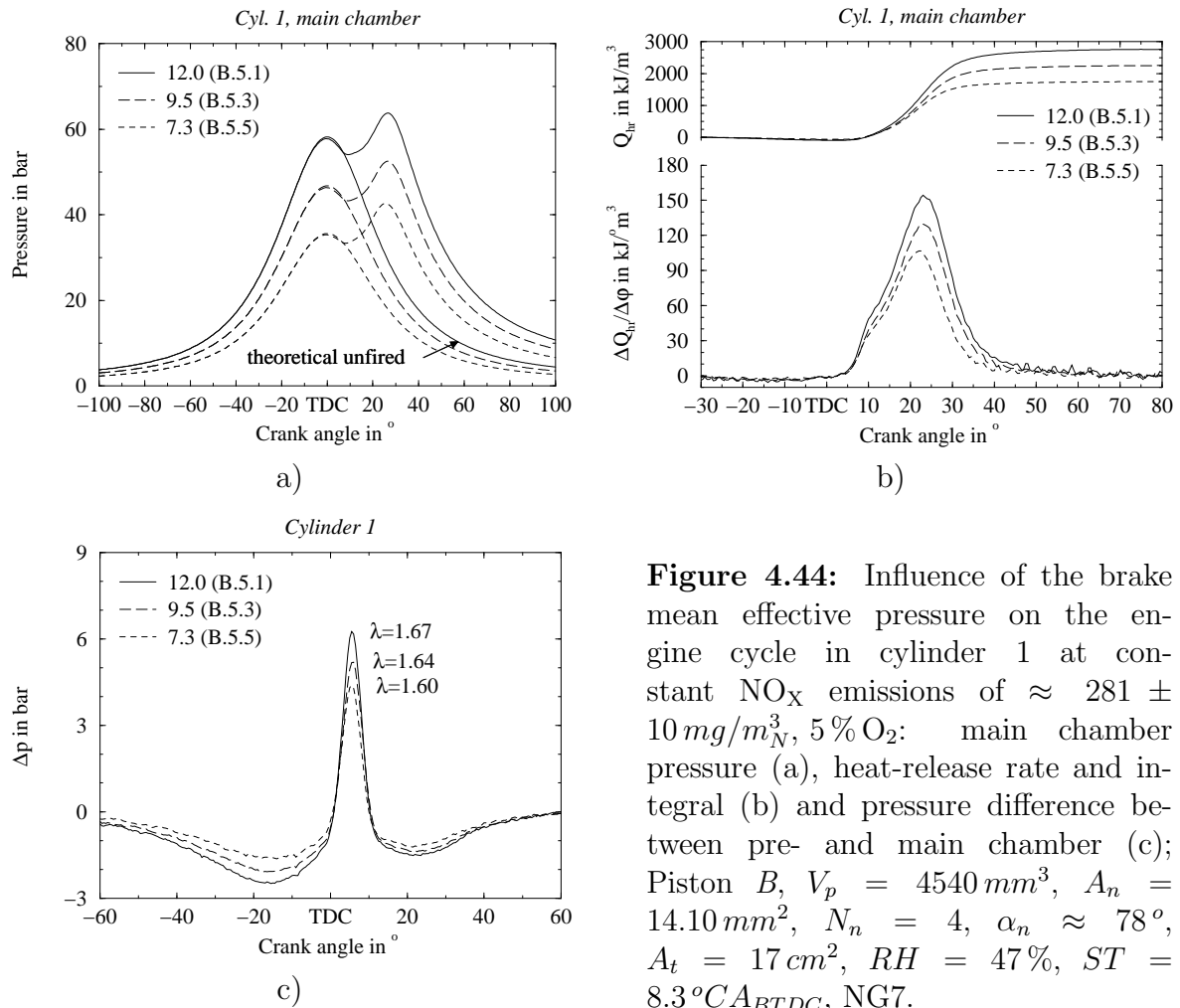


**Figure 4.44:** Influence of the brake mean effective pressure on the engine cycle in cylinder 1 at constant NO<sub>x</sub> emissions of  $\approx 281 \pm 10 \text{ mg/m}_N^3$ , 5% O<sub>2</sub>: main chamber pressure (a), heat-release rate and integral (b) and pressure difference between pre- and main chamber (c); Piston  $B$ ,  $V_p = 4540 \text{ mm}^3$ ,  $A_n = 14.10 \text{ mm}^2$ ,  $N_n = 4$ ,  $\alpha_n \approx 78^\circ$ ,  $A_t = 17 \text{ cm}^2$ ,  $RH = 47\%$ ,  $ST = 8.3^\circ \text{C} A_{BTDC}$ , NG7.

prechamber and consequently leads to a lower pressure drop across the nozzle orifices (figure 4.44, c). Despite the somewhat lower relative air to fuel ratio required to maintain constant NO<sub>x</sub> emissions, the decrease in prechamber pressure results in a lower amount of fuel located in the prechamber when combustion starts.

At part load, the lower prechamber charge results in a decrease in the intensity of the pressure pulse generated during prechamber combustion (figure 4.44, c). Several different and partly opposite effects may influence the prechamber combustion process. First, the reduction of the combustion pressure and the decrease of the relative air to fuel ratio tends to increase the burning velocity of methane [58], the main component of natural gas. Further, the larger decrease of the boost pressure than the exhaust port pressure (figure 4.43) indicates a larger reduction of the cylinder pressure at inlet valve closure than at exhaust valve closure. This is expected to increase the prechamber residual gas fraction (the pressure at exhaust valve closure governs the amount of residual gas trapped in the prechamber and the pressure at intake valve closure controls the amount of unburnt mixture admitted into the cylinder; the combination of both determines the concentration of residual gas in the prechamber mixture at a given crank angle). A higher residual gas fraction tends to reduce the burning velocity [13]. Finally, the decrease of the mass flow rate through the prechamber orifices reduces the turbulence generated and consequently transported towards the prechamber top; this acts in a similar way to an increase of the nozzle orifice diameter (figure 3.10, b). A

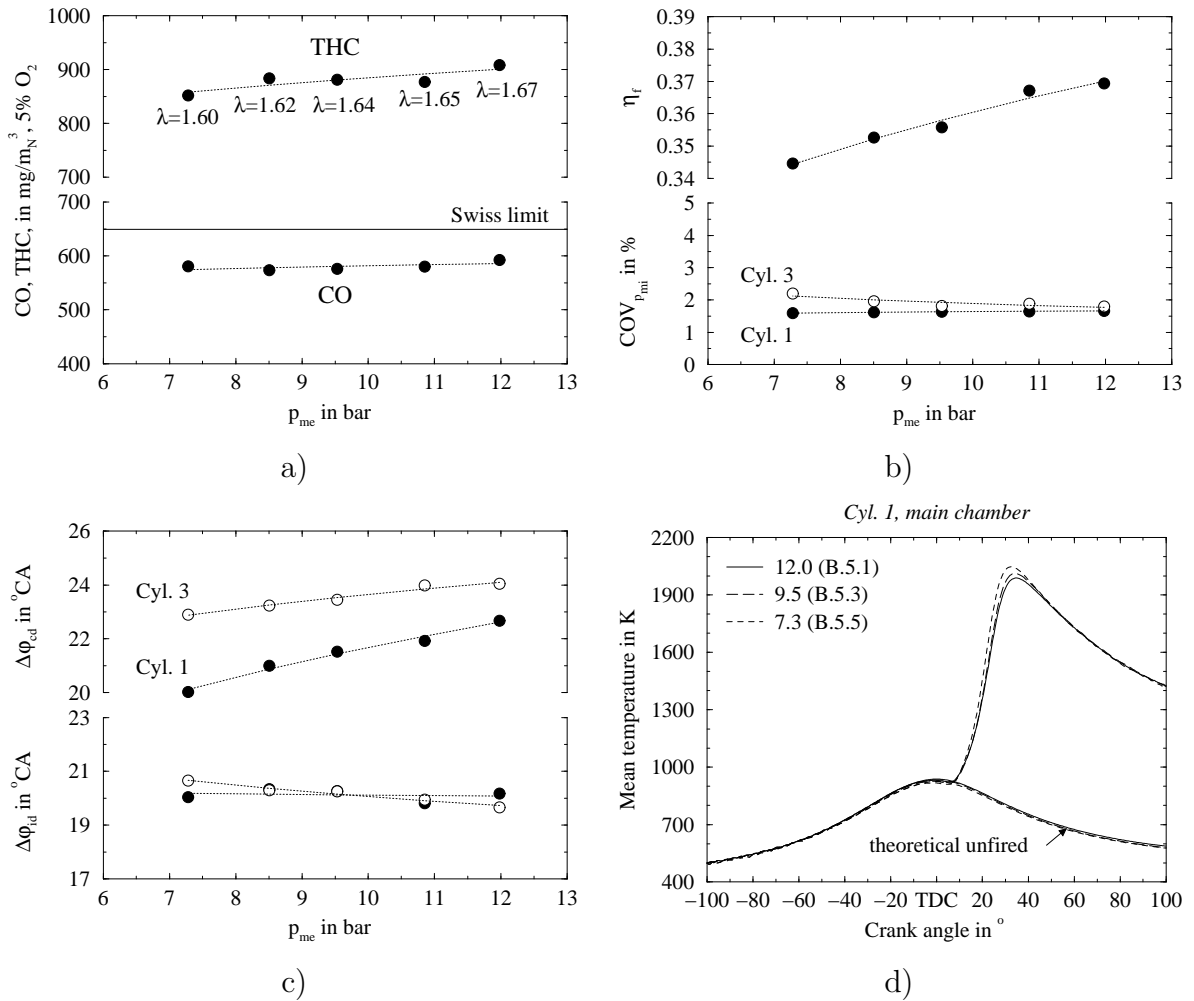


**Figure 4.45:** Influence of the brake mean effective pressure on the engine performance and emissions at constant  $NO_x$  emissions of  $\approx 281 \pm 10 mg/m^3_N$ , 5%  $O_2$ : a) CO and THC emissions, b) fuel conversion efficiency and coefficient of variance of  $p_{mi}$ , c) ignition delay and combustion duration; d) mean combustion temperature; Piston  $B$ ,  $V_p = 4540 mm^3$ ,  $A_n = 14.10 mm^2$ ,  $N_n = 4$ ,  $\alpha_n \approx 78^\circ$ ,  $A_t = 17 cm^2$ ,  $RH = 47\%$ ,  $ST = 8.3^\circ CA_{BTDC}$ , NG7.

decrease of prechamber turbulence tends to reduce the perturbation of the early stage of the flame kernel development, but also slows down the propagation of the flame front. The reduction of the prechamber rate of pressure increase following the decrease in engine load (**figure 4.44, c**) shows a slowing down of the prechamber combustion process. This seems to indicate that the beneficial effect of the lower prechamber pressure and the slightly richer unburnt mixture is more than compensated by the detrimental effect of a higher unburnt mixture residual gas concentration and a lower prechamber turbulence intensity. At part load, the lower maximum pressure difference between pre- and main chamber should mainly originate in the reduced amount of fuel admitted into the prechamber. This is expected to reduce the gas jet intensity and penetration. Finally, the less rapid decrease of the pressure difference between pre- and main chamber originates in the slower main chamber pressure increase resulting from the consequent slowing down of the main chamber combustion process (**figure 4.44, b**).

During the first part of the main chamber combustion process, the reduction of the gas jet intensity and penetration largely offsets the positive effect of the lower combustion pressure and richer unburnt mixture on the burning velocity and leads to a moderate decrease of the rate of heat release (**figure 4.44, b**). However, once the flame front is established, the higher burning velocity associated with the lower pressure and the richer unburnt mixture promotes a more rapid propagation of the flame front throughout the main combustion chamber. The more rapid second part of the combustion process largely compensates the slowing down of the first part and thus tends to shift the centre of gravity of the combustion process towards TDC. Further, this results in a moderate decrease of the combustion duration (**figure 4.45, c**).

At part load, the shift of the main chamber combustion process towards TDC and the somewhat shorter combustion duration (**figure 4.45, c**) tends to increase the engine fuel conversion efficiency. However, a reduction of the engine load also leads to a decrease in mechanical efficiency [13] (at a constant crankshaft rotational speed, the engine total friction losses decrease when the load decreases, but however proportionally less than the positive work delivered to the crankshaft), which decreases the fuel conversion efficiency. The larger effect of the latter causes a progressive reduction of the fuel conversion efficiency from 36.9 to 34.5% (**figure 4.45, b**). When keeping constant  $\text{NO}_x$  emissions, the reduction of the engine load does not significantly affect the cycle-by-cycle variability. This results in an approximately constant coefficient of variance of  $p_{mi}$  in cylinder 1 and 3.

The reduction of the engine load results in a weak decrease in CO and THC emissions (**figure 4.45, a**). This seems to mainly result from a balance between two opposite effects on the amount of fuel located in the combustion chamber crevices during the primary oxidation process. On the one hand, the lower cylinder pressure (**figure 4.44, a**) reduces the quantity of unburnt mixture compressed in the crevices. However, this effect is partly compensated by the somewhat lower relative air to fuel ratio. On the other hand, weaker gas jets delay the arrival of the flame front at the crevice entrances. This assumption is also partly supported by the fact that the mean combustion temperature during late expansion (**figure 4.45, d**) does not vary. This should therefore lead to a similar secondary oxidation process.

When maintaining constant  $\text{NO}_x$  emissions of  $\approx 281 \pm 10 \text{ mg}/\text{m}_N^3$ , 5%  $\text{O}_2$ , the reduction of the engine load from 12.0 to 7.3 bar (100% to 60% of the rated power output of 150 kW) causes a decrease of the engine fuel conversion efficiency from 36.9 to 34.5%. Further, this leads to a slight decrease of the CO and THC emissions, while not affecting significantly the engine cycle-by-cycle variability. However, the actual combustion chamber configuration (prechamber and main chamber) does not enable a sufficiently stable practical engine operation over the whole range of load under conditions which simultaneously reduce the  $\text{NO}_x$  and CO emissions below the Swiss limits. Nevertheless, a progressive advancing of the spark timing with the decrease of the load, while adjusting the relative air to fuel ratio, may improve the engine operating stability and therefore could enable operation at lower  $\text{NO}_x$  emissions.

## 4.5 Conclusion

The engine operation with prechamber ignition was experimentally investigated in order to evaluate the potential to reduce the exhaust gas emissions, particularly the CO emissions, under the Swiss limits, without exhaust gas after treatment. Variations of prechamber configuration, piston geometry, turbocharger characteristics and engine operating parameters were carried out to determine their influence on the engine performance and emissions. The principal experimental results and a direct comparison between direct and prechamber ignition operation are presented in this section.

### Prechamber

In comparison to the direct ignition, the prechamber ignition enables to strongly intensifies and accelerates the combustion process. This results from the distribution of ignition sources in the main combustion chamber by the means of jets of combustion products issuing from the prechamber. The penetration of the gas jets into the main chamber dramatically increases the initial flame front surface and therefore reduces the time required for combustion. The intensity of the gas jets mainly depends on the amount of fuel admitted into the prechamber during the compression process. Therefore, the generation of substantial gas jets requires a delay of the spark timing of at least  $10^{\circ}CA$  in comparison with direct ignition ( $26.7^{\circ}CA_{BTDC}$ ). Further, the prechamber ignition leads to a large reduction of CO and THC emissions. This is deduced to mainly originate from:

- a much lower combustion pressure resulting from the delay of the spark timing
- an early arrival of the flame front in the squish region due to the penetration of the gas jets in the main combustion chamber

These two factors contribute to a reduction of the amount of unburnt mixture compressed into the piston top land and cylinder head gasket crevices during the primary oxidation process. However, the reduction of CO and THC emissions may also partly result from:

- a significantly higher mean combustion temperature during late expansion resulting from the delay of the spark timing

This promotes the secondary oxidation of unburnt mixture emerging from the combustion chamber crevices during the expansion stroke.

The prechamber geometrical parametric study indicates that the following trends have a beneficial effect on the penetration of the gas jets and/or promote an early arrival of the flame front at the piston top land and cylinder head gasket crevice entrances:

- a small total nozzle orifice cross sectional area. However, the reduction of this area is limited by the occurrence of ignition failure, likely to result from an excessive increase in turbulence intensity at the ignition point. There is an optimum area, which enables minimum  $\text{NO}_x$  emissions to be achieved for a given nozzle orifice configuration.
- a limited number of nozzle orifices (4 instead of 6)
- an orientation of the nozzle orifices towards the squish region ( $\approx 78^\circ$  instead of  $\approx 62^\circ$ )
- a relatively large prechamber internal volume (2.9 instead of 1.9% of  $V_c$ )

On the other hand, the investigation of the nozzle orifice azimuthal distribution indicates no clear trend regarding the CO and THC emissions. However, these results are based on a prechamber with 6 orifices and are therefore not necessarily valid for a smaller number of orifices. Further, the parametric study shows a large influence of the prechamber internal shape.

The combination of all the positive features results in a prechamber with an internal volume of  $4540 \text{ mm}^3$  ( $V_c = 2.9\%$ ) and 4 nozzle orifices of diameter  $2.12 \text{ mm}$  ( $A_n = 14.10 \text{ mm}^2$ ), non-evenly distributed and oriented at an angle of  $\approx 78^\circ$ . However, due to the limited number of variations performed for each geometrical parameter investigated, the final prechamber configuration obtained does not represent the global optimum. The research of the global optimum was out of the scope of this study and therefore would require further investigation. Nevertheless, the final prechamber configuration obtained should be relatively close to the global optimum.

## Main chamber

In comparison to the original piston (*A*), the use of a piston generating significantly more turbulence (*B*) results in approximately 0.5%-point higher fuel conversion efficiency. Further, it yields somewhat lower CO and THC emissions. However, the emission benefit of piston *B* decreases when reducing the  $\text{NO}_x$  emissions and tends to vanish at low  $\text{NO}_x$  emissions. This mainly results from the particular ability of piston *A* to suppress the tradeoff between CO and  $\text{NO}_x$  emissions (CO emissions decrease slightly with the reduction of the  $\text{NO}_x$  emissions) and relax the tradeoff between THC and  $\text{NO}_x$  emissions. This change in emission behaviour is expected to originate from a significant change in the interaction between gas jet and main chamber flows.

## Spark timing

The delay of the spark timing strongly reduces the exhaust gas emissions. However, it only leads to a relatively weak decrease in fuel conversion efficiency. The engine achieves the lowest  $\text{NO}_x$ , CO and THC emissions at a spark timing of  $8.3^\circ \text{CA}_{BTDC}$ . A further delay results in a rapid increase of the cycle-by-cycle variability.

## Turbocharger

The characteristics of the turbocharger turbine were adjusted in order to operate the engine at wide open throttle and thus to reduce the pumping work. This required an increase in the volute throat area from 11 to 17  $cm^2$ , which also imposed the transition from one to two volute channels (not available with a single channel). The enlargement of the volute throat area causes an increase of about 1 %-point in fuel conversion efficiency at the lowest  $NO_x$  emissions. However, this leads to a moderate increase of 3 % in CO emissions and a large increase of 40 % in THC emissions. The much higher THC emissions mainly result from the transition from one to two volute channels. This induces a fundamental change in the exhaust manifold gas dynamics which is expected to cause an increase of the amount of unburnt mixture directly bypassed from the intake port into the exhaust port during valve overlap.

## Engine load

When maintaining approximately constant  $NO_x$  emissions of 280  $mg/m_N^3$ , 5 %  $O_2$ , the progressive decrease of the engine specific power output from 150 to 90  $kW$  results in a reduction of the fuel conversion efficiency from 36.9 to 34.5 %. On the other hand, this leads to a slight decrease in CO and THC emissions. However, when operating under conditions which are able to fulfil the Swiss requirements at engine nominal load, the actual combustion chamber configuration (prechamber and main chamber) does not enable a sufficiently stable practical engine operation over the whole range of load. Nevertheless, a progressive advancing of the spark timing with the decrease of the load, while adjusting the relative air to fuel ratio, may improve the engine operating stability and therefore could enable operation at lower  $NO_x$  emissions.

## Comparison between direct and prechamber ignition

In order to compare the direct and prechamber ignition operation as objectively as possible, the corresponding experimental results obtained with piston *B* are represented together in **figure 4.46**. It must be noted, however, that the experimental conditions were somewhat different in several respects. First, the natural gas blend used in the case of the direct ignition has significantly higher concentrations of high order hydrocarbons (mainly  $C_2H_6$  and  $C_3H_8$ ). This promotes ignition [59, 60, 61] and accelerates the combustion process [54]. Further, the direct ignition operation was performed with an air-fuel mixture temperature of 50 °C instead of 90 °C. This has, however, only a very limited effect on the engine performance and emissions [3, 4]. Finally, the intake air relative humidity was 30 and 50 % for the direct and prechamber operation, respectively. An increase in air relative humidity causes a moderate decrease in the rate of combustion and in the  $NO_x$  emissions and increases somewhat the CO and THC emissions [62].

In the case of the prechamber ignition, the results corresponding to the two different turbocharger configurations are represented in order to clearly distinguish the effect of

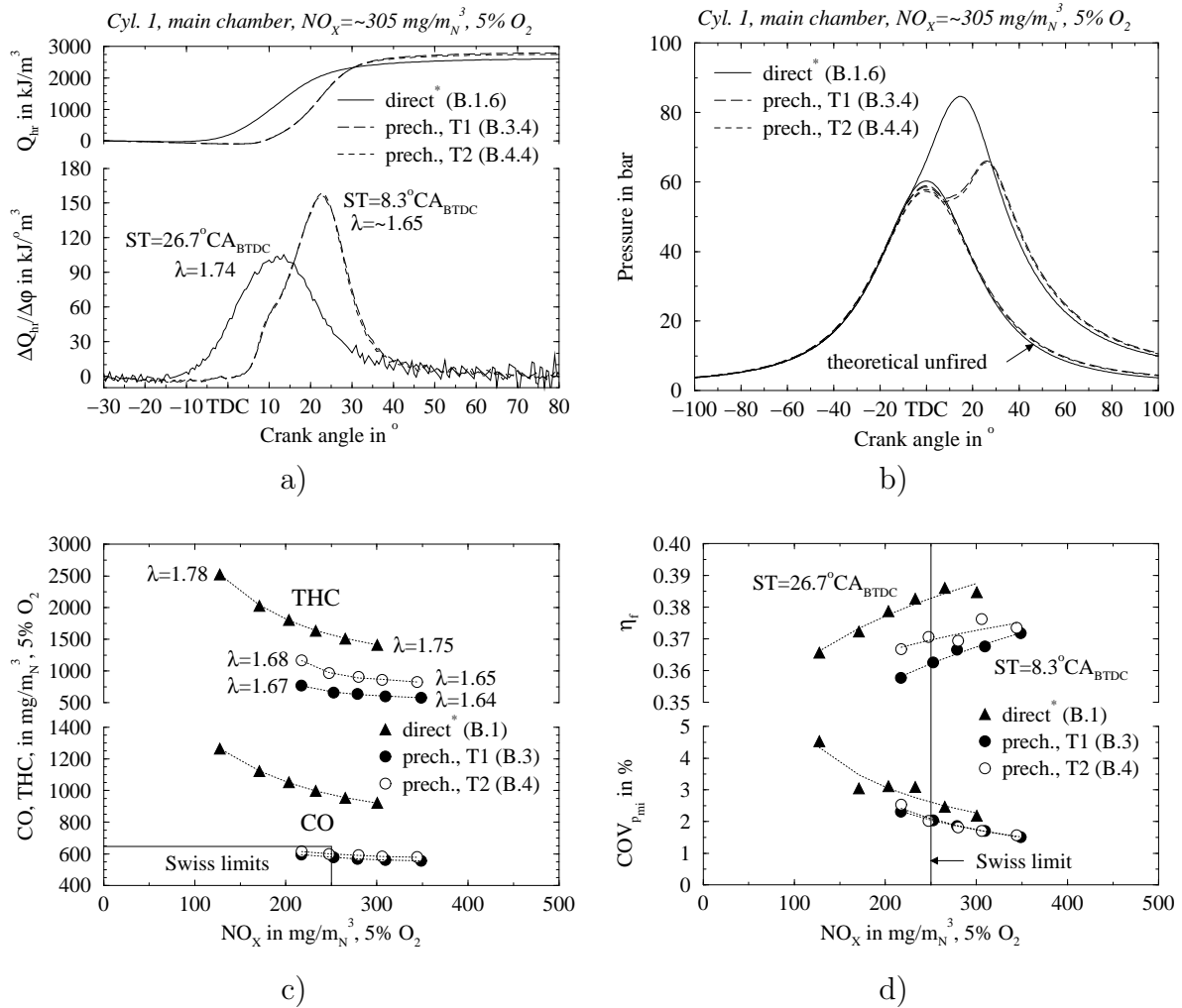


**Figure 4.46:** Final comparison between direct and prechamber ignition; engine cycle in cylinder 1: heat-release rate and integral (a), main chamber pressure (b); engine performance and emissions as function of  $NO_x$  emissions: CO and THC emissions (c), fuel conversion efficiency and coefficient of variance of  $p_{mi}$  (d); Piston  $B$ ,  $V_p = 4540 \text{ mm}^3$ ,  $A_n = 14.10 \text{ mm}^2$ ,  $N_n = 4$ ,  $\alpha_n \approx 78^\circ$ ,  $A_t = 9$  (\*), 11 (T1), 17 (T2)  $\text{cm}^2$ ,  $T_{mixt} = 90$  (\* = 50)  $^\circ\text{C}$ ,  $RH \approx 48$  (\* = 30) %, NG7 (\*NG1).

the prechamber on the THC emissions from the effect of the change in exhaust manifold gas dynamics.

In comparison with the direct ignition, the prechamber ignition dramatically intensifies and accelerates the combustion process (figure 4.46, a). The important delay of the spark timing required to operate the engine with prechambers results in a large decrease in cylinder pressure (figure 4.46, b). Further, the prechamber ignition yields approximately 40 % and 55 % less CO and THC emissions, respectively (figure 4.46, c). This enables the Swiss requirements to be fulfilled, but however with a narrow margin. The lower potential to reduce the  $NO_x$  emissions partly results from the different natural gas composition<sup>4</sup>. The prechamber ignition operation leads to a

<sup>4</sup>the major influence of the natural gas composition on the lean operating limit has been established several times on the test bed, when switching from the network to the high pressure storage



reduction of slightly more than 2 %-point in fuel conversion efficiency (**figure 4.46, d**). However, an adequate adjustment of the turbocharger characteristics, in order to operate the engine close to wide open throttle, causes an increase of approximately 1 %-point in fuel conversion efficiency. When operating the engine under the Swiss limits, the prechamber ignition achieves a fuel conversion efficiency higher than 36.5%. Finally, the prechamber ignition is characterised by a lower cycle-by-cycle variability and thus enables a more stable engine operation.



# Chapter 5

## Conclusions

In the context of cogeneration with internal combustion engines, the operation with prechamber ignition was investigated in order to evaluate the potential to reduce the exhaust gas emissions, particularly the CO emissions, below the Swiss limits ( $\text{NO}_x$  and CO emissions: 250 and  $650 \text{ mg}/\text{m}_N^3$ , 5 %  $\text{O}_2$ , respectively), without exhaust gas after treatment. The investigation was carried out on a small size six cylinder turbocharged *Liebherr* diesel engine type 926 converted for natural gas and biogas operation. This required the development of cooled prechambers and the modification of the engine cylinder heads. The approach was essentially experimental, but included a numerical simulation based on the CFD-code *KIVA-3V*. The objective of the numerical simulation was to guide the selection of the prechamber configurations for the experimentation in order to come close to the optimum more quickly and to help with the interpretation of the experimental results.

The numerical simulation was carried out in order to evaluate the effects and consequences of transferring the ignition point of the conventional combustion chamber (direct spark ignition in a single combustion chamber) into a small prechamber connected to the main combustion chamber through small orifices. The prechamber flow characteristics at the location of the gap between the spark plug electrodes and in the crank angle period where the ignition is expected to occur (between  $30^\circ \text{CA}_{BTDC}$  and TDC) were compared to the corresponding conditions in the conventional combustion chamber at the experimental spark timing for minimum  $\text{NO}_x$  exhaust emissions ( $\approx 27^\circ \text{CA}_{BTDC}$ ). The influence of the prechamber geometrical configuration was evaluated through variations of the nozzle orifice diameter, number and orientation, as well as prechamber volume and internal shape.

The results show that the velocity magnitude at the ignition point is mainly dependent on the prechamber shape, and that it is generally of the same order as with direct ignition. The turbulence intensity varies strongly with the geometrical configuration and reaches, in most cases, a much higher value in the prechamber. High turbulence intensity promotes rapid prechamber combustion, but also perturbs the ignition process and the early stage of the flame kernel growth, which is expected to increase the probability of ignition failure. The partial dilution of the unburnt mixture with unscavenged prechamber residual gas generally leads to a slightly lower fuel to air equivalence

ratio. However, nozzle orifices imparting a swirl motion or a prechamber shape with an almost uniform cross section can result in fuel concentration very close to or beyond the flammability limit. In most cases, the mixture temperature is not significantly affected by changes in the prechamber geometrical configuration. However, depending on the prechamber spark timing, the mixture temperature can be similar to or much higher ( $\approx 100\text{ K}$ ) than in the case of direct ignition. The prechamber charge, and thereby the amount of energy available for the main chamber ignition, depends mainly on the prechamber volume, but is significantly affected by the pressure drop across the nozzle orifices. Finally, the strong turbulence generated in the main chamber by the flow towards the nozzle orifices is expected to promote a rapid propagation of the flame front in the early stage of the main chamber combustion process.

Based on the results of the numerical simulation, the most promising prechamber configuration parameters were selected for experimentation. Then, variations of the selected prechamber configuration parameters, as well as the piston geometry, the turbocharger characteristics and the engine operating parameters, were carried out to determine their influence on the engine performance and emissions. The main experimental results are the following:

- in comparison with the direct ignition, the prechamber ignition strongly intensifies and accelerates the combustion process; this results from the distribution of ignition sources in the main combustion chamber by means of jets of combustion products issuing from the prechamber; the penetration of the gas jets into the main chamber dramatically increases the initial flame front surface
- when comparing with the direct ignition, the prechamber ignition requires a significant delay of the spark timing in order to generate substantial gas jets; in turn, this strongly reduces the maximum cylinder pressure and results in an important decrease in  $\text{NO}_x$ , CO and THC emissions; minimum emissions are achieved at a spark timing of about  $8^\circ\text{CA}_{BTDC}$
- the prechamber geometrical parametric study indicates that trends which increase the penetration of the gas jets and/or promote an early arrival of the flame front at the piston top land and cylinder head gasket crevice entrances are beneficial to reduce the CO and THC emissions
- in comparison to the original piston, the use of a piston generating significantly more turbulence leads to an approximately 0.5 %-point higher fuel conversion efficiency; however, it induces no significant change in the CO and THC emissions at low  $\text{NO}_x$  emissions
- in comparison with the direct ignition, the prechamber ignition yields approximately 40 % and 55 % less CO and THC emissions, respectively; however, this also leads to a reduction of about 2 %-point in fuel conversion efficiency
- the adjustment of the turbocharger characteristics in order to operate the engine at wide open throttle results in an increase of about 1 %-point in fuel conversion efficiency; however, a consequent change in the exhaust manifold gas dynamics causes an increase of approximately 40 % in THC emissions

- at the rated power output, the prechamber ignition operation fulfils the Swiss requirements for emissions and achieves a fuel conversion efficiency higher than 36.5 %

In comparison with the combined EGR-lean burn mode with direct ignition, the prechamber ignition achieves similar performances and emissions, when operating the engine below the Swiss limits. However, the potential improvement of the exhaust manifold gas dynamics is expected to cause a decrease of 20 % in THC emissions and consequently to lead to a value below  $800 \text{ mg}/\text{m}_N^3$ , 5 %  $\text{O}_2$ . Finally, the use of the prechamber ignition results in a significant relaxation of the tradeoff between CO and  $\text{NO}_x$  emissions.



# Chapter 6

## Further work

This chapter presents several proposals of complementary investigations, which are expected to lead to further improvements in engine performance and emissions or are required in order to treat aspects which were beyond the scope of the present study.

### Experimental

#### Exhaust manifold configuration and cam shaft profile

The increase of the turbocharger turbine volute throat area in order to reduce the engine pumping work requires the change from one to two volute channels, which results in a fundamental change in the exhaust manifold gas dynamics (the exhaust manifold is in two distinct parts). Combined with the decrease in average exhaust manifold pressure, this causes an increase of the pressure difference between the intake and the exhaust port during valve overlap and leads to a large increase in THC emissions. This is believed to result from an increase in the amount of unburnt mixture bypassing the cylinder during valve overlap. This effect can be reduced through two different approaches, which may also be combined. The first approach consists of decreasing the valve overlap duration through a change of the cam shaft profile, but without significantly increasing the engine pumping work in order to avoid a reduction of fuel conversion efficiency. The second approach consists of reducing the exhaust pressure fluctuations through the use of a single exhaust manifold of larger internal volume (plenum chamber).

#### Piston geometry

The present study indicates that the piston geometry directly affects the trade-offs between CO and NO<sub>x</sub> emissions as well as between THC and NO<sub>x</sub> emissions. Therefore, the optimisation of the interaction between the gas jets emerging from the prechamber and the main chamber flow requires a thorough investigation of the influ-

ence of the piston geometry. In addition, variations of the compression ratio should also be performed in order to determine its influence on the engine performance and emissions.

### Prechamber cooling

The present study was carried out with a constant prechamber cooling water flow rate. Because this parameter is expected to have a significant influence on the prechamber ignition and combustion process, it should also be investigated in detail. For this purpose, the cylinder heads have already been modified in order to enable the installation of special plugs with calibrated orifice in the channel feeding the prechamber cooling jacket.

### Ignition system

The reduction of the  $\text{NO}_x$  emissions through an increase in relative air to fuel ratio is limited by the consequent increase in cycle-by-cycle variability. The cycle-by-cycle variability depends on the mixture composition and on the flow conditions in the vicinity of the ignition point. When operating close to the lean limit, the overall engine stability is also affected by differences in the ignition timing of the individual cylinders. The ignition system used for the present investigation is characterised by spark timing differences larger than  $0.5^\circ\text{CA}$  between cylinders and does not enable individual cylinder spark timing. Therefore, the use of a new ignition system featured with individual cylinder spark timing is expected to increase the engine operating stability, which is likely to enable a moderate further decrease in  $\text{NO}_x$  emissions.

Another approach, in order to improve the engine operating stability, would be to replace the conventional electrical spark by a micro injection of diesel or a similar auto-ignitable fuel as ignition source for the prechamber. An investigation of the direct ignition with pilot fuel injection indicates that the quantity injected should not exceed 0.5 to 1 % of the amount of fuel required to achieve the rated power output, in order to limit the amount of  $\text{NO}_x$  generated by the ignition process [63]. The main advantage of an ignition system based on the auto-ignition of a small amount of fuel is the large ignition energy delivered when compared to spark ignition. This reduces the sensitivity to variations of the local flow conditions and enables the ignition of leaner air-fuel mixtures in comparison to spark ignition. Another advantage of an ignition system based on a diesel injection system is the corresponding high reliability and long lifetime. Due to the relatively rapid wear of the electrodes, the lifetime of a conventional spark plug is limited to about 1000 *h*. The principal challenge associated with a micro injection system is the achievement of a reasonably fine atomisation of a very small amount of liquid fuel.



## Biogas operation

Although the engine is intended for operation on natural gas as well as on biogas, it was exclusively operated on natural gas during the present study. Therefore, a dedicated investigation performed with synthetic biogas is required in order to determine the ability of the prechamber ignition to comply with the Swiss requirements for exhaust gas emissions and to evaluate the engine performance.

## Field testing

Finally, the evaluation of the reliability of the prechamber ignition requires an endurance test over several thousands of operating hours under practical cogeneration conditions.

## Numerical simulation

The extension of the numerical method with a combustion model is necessary in order to simulate the interaction between the main chamber and the gas jet flows. This should enable the study of the influence of the piston geometry and help in selection of the most promising cases for experimental investigation. However, the numerical method used, based on the CFD program *KIVA-3V*, has been developed for sequential resolution on a single processor and is not suitable for parallel implementation based on loop decomposition. For this reason, the simulation without combustion leads already to a relatively long computation time of approximately 30 CPU hours. Therefore, the numerical simulation with combustion process modelling requires an important modification of *KIVA-3V* or the use of another numerical method which enables parallel computation (*Star-CD* by *Computational Dynamics Ltd* in London (UK), *Fire* by *AVL GmbH* in Graz (Austria) or the extension of a code partially developed at *EPFL*), in order to avoid taking a prohibitive execution time.



# References

- [1] Le Conseil fédéral suisse; *Ordonnance sur la protection de l'air (OPair)*; du 16 décembre 1985 (Etat au 12 octobre 1999).
- [2] Bundesregierung Deutschland; *Technische Anordnung zur Luftreinheit (TA-Luft)*; 1986 (Stand in 1992).
- [3] Roethlisberger, R. P., Leyland, G., Paschoud C.-A. and Favrat, D.; *Swiss Motor, Modification d'un moteur Diesel pour le fonctionnement avec mélange stœchiométrique ( $\lambda = 1$ ) et pauvre ( $\lambda \gg 1$ )*; Swiss Federal Office of Energy, Final Report, 1998.
- [4] Roethlisberger, R. P., Leyland, G., Favrat, D. and Raine, R. R.; *Study of a Small Size Cogeneration Gas Engine in Stoichiometric and Lean Burn Modes: Experimentation and Simulation*; SAE Paper 982451 and SP-1391, 1998.
- [5] Nellen C. and Boulouchos, K.; *Aufgeladene Gasmotoren mit AGR und Dreiwege-Katalysator - der Weg zu niedrigsten Emissionen bei hohem Wirkungsgrad und großer Leistungsdichte*; MTZ Motortechnische Zeitschrift, Vol. 61, pp. 54–62, 2000.
- [6] Dietrich, W. R. and Grundmann, W.; *Die homogene Magergemischaufladung der DEUTZ MWM-Ottogasmotoren - Teil 2*; MTZ Motortechnische Zeitschrift, Vol. 50, pp. 231–236, 1989.
- [7] Quirchmayr, G.; *Der Jenbacher Magermotor - Eine schadstoffarme Variante des Gas-Ottomotors*; MTZ Motortechnische Zeitschrift, Vol. 52, pp. 16–21, 1991.
- [8] Kingston Jones, M. G. and Heaton, D. M.; *Nebula Combustion System for Lean Burn Spark Ignited Gas Engines*; SAE Paper 890211, 1989.
- [9] Chmela, F. and Kapus, P.; *Das TRI-FLOW-Verbrennungsverfahren für den Magerbetrieb von Gasmotoren*; MTZ Motortechnische Zeitschrift, Vol. 55, pp. 526–535, 1994.
- [10] Bruch, K. L.; *Caterpillar G3500 High Efficiency Engine Development*; ASME, Fall Technical Conference, ICE-Vol. 25-3, pp. 115–123, 1995.
- [11] Boulouchos, K., Zbiorczyk, A., Inhelder, J. and Frouzakis, C.; *Optimale Auslegung umweltfreundlicher Gasmotoren mit Hilfe von Simulationswerkzeugen*; MTZ Motortechnische Zeitschrift, Vol. 58, pp. 486–499, 1997.

- [12] Bhargava, S., Clark, N. N. and Hildebrand, M. W.; *Exhaust Gas Recirculation in a Lean Burn Natural Gas Engine*; SAE Paper 981395, 1998.
- [13] Heywood, J. B.; *Internal Combustion Engine Fundamentals*; McGraw-Hill International Editions, Automotive Technology Series, ISBN 0-07-100499-8, 1988.
- [14] Goto, S., Itoh, Y., Higuchi, Y. and Nagai, T.; *NIIGATA Ultra Lean Burn SI Gas Engines - Achieving High Efficiency and Low NO<sub>x</sub> Emissions*; SAE Paper 901608, 1990.
- [15] Šauperl, I., Laiminger, S., Sams, T., Herdin, G. and Plohberger, D.; *CFD unterstützte Optimierung eines Großgasmotors*; Institute for Internal Combustion Engines and Thermodynamics, Graz University of Technology, Austria, 6<sup>th</sup> Symposium On The Working Process Of The Internal Combustion Engine, pp. 141–155, 1997.
- [16] Reinbold, E. O.; *The AT27GL: A Continuing Development of the Waukesha AT Series Gas Engine*; ASME, ICE-Vol. 22, Heavy Duty Engines: A Look at the Future, pp. 23–30, 1994.
- [17] Nakazono, T. and Natsume, Y.; *Effect of Dimensions of Prechamber on Lean Burn Gas Engine*; Transactions of the JSME, JSME International Journal, Series B, Vol. 37, No. 4, pp. 951–956, 1994.
- [18] Schiffgens, H.-J., Brandt, D., Rieck, K. and Umiersky, M.; *Development of the New MAN B&W 28/32 SI Stationary Gas Engine*; ASME, Fall Technical Conference, ICE-Vol. 25-3, pp. 89–102, 1995.
- [19] Chrisman, B. M. and Freen, P. D.; *Development of the 2400G Stationary Gas Engines*; Transactions of the ASME, Journal of Engineering for Gas Turbines and Power, Vol. 117, pp. 810–819, 1995.
- [20] Crane, M. E. and King, S. R.; *Emission Reductions through Pre-Combustion Chamber Design in a Natural Gas, Lean Burn Engine*; ASME, ICE-Vol. 15: Fuels, Controls, and Aftertreatment for Low Emissions Engines, pp. 73–81, 1991.
- [21] Nakazono, T.; *Study of Lean Burn Gas Engine (Effect of Main Chamber)*; Transactions of the JSME, JSME International Journal, Series B, Vol. 37, No. 3, pp. 677–682, 1994.
- [22] Nakazono, T.; *Characteristics of Unburned HC from a Lean-Burn Prechamber Gas Engine*; Transactions of the Japan Society of Mechanical Engineers (JSME), in Japanese, Series B, Vol. 60, pp. 335–340 (569), 1994.
- [23] Czerwinski, J.; *Über die Zündung und Verbrennung im 4-Takt-Ottomotor mit unterteiltem Brennraum*; Fortschritt-Berichte des Vereins Deutscher Ingenieure (VDI), Reihe 6: Energietechnik/Wärmetechnik, Nr. 176, 1985.
- [24] Ohtsu, A., Ryu, H. and Asanuma, T.; *Visualization of Flame Propagation in a Spark Ignition Engine with an Unscavenged Prechamber*; Transactions of the JSME, JSME International Journal, Series II, Vol. 32, No. 1, pp. 127–133, 1989.

- [25] Mavinahally, N. S., Assanis, D. N., Govinda Mallan, K. R. and Gopalakrishnan, K. V.; *Torch Ignition: Ideal for Lean Burn Premixed-Charge Engines*; Transactions of the ASME, Journal of Engineering for Gas Turbines and Power, Vol. 116, pp. 793–798, 1994.
- [26] Geiger, J., Böwing, R., Koß, H.-J. and Thiemann, J.; *Zündsysteme für Ottomotoren mit hoher Ladungsverdünnung*; 3. Stuttgarter Symposium über Kraftfahrzeugwesen und Verbrennungsmotoren, Art. 5.3, pp. 267–281, 1999.
- [27] Nellen C, Laboratory for Internal Combustion Engines and Combustion (LVV) of the Swiss Federal Institute of Technology of Zürich; *personal communication*; 1998.
- [28] Snyder, W. E. and Dexter, S.G.; *Looking into a Lean Burn Spark Ignited Gas Engine*; The Thirteenth Annual Energy-Sources Technology Conference and Exhibition, New Orleans, Louisiana, January 14–18, pp. 67–75, 1990.
- [29] Sakurai, T. and Shoji, F.; *Study on Mixture Formation in Prechamber of Lean Burn Gas Engine*; ASME, Spring Technical Conference, ICE-Vol. 26-1, pp. 43–51, 1996.
- [30] Liebherr Machine Bulle S.A., Rue de l'Industrie 19, CH-1630 Bulle, Switzerland; [www.liebherr.com](http://www.liebherr.com).
- [31] Motortech GmbH, Hogrevestraße 21, D-29223 Celle, Germany; [www.motortech.de](http://www.motortech.de)
- [32] RMG Regel + Messtechnik GmbH, Postfach 102967, D-34029 Kassel, Germany; [www.rmg.de](http://www.rmg.de)
- [33] Roethlisberger, R. P., Raine, R. R., Kleemann, R. and Favrat, D.; *Experimental Results and Modelling of Carbon Monoxide Emissions from a Natural Gas Fuelled Spark-Ignition Cogeneration Engine*; IMechE International Conference on Computational and Experimental Methods in Reciprocating Engines, IMechE Conference Transactions, ISBN 1-86058-275-3, pp. 127-138, 2000.
- [34] Kühnle, Kopp & Kausch AG, Hessheimer Straße 2, D-67227 Frankenthal, Germany; [www.agkkk.de](http://www.agkkk.de)
- [35] Structural Dynamics Research Corporation (SDRC); *I-DEAS Master Series, Version 6.m.1*; [www.sdrc.com](http://www.sdrc.com), 1998.
- [36] Böhler Edelsthal GmbH, Mariazeller Straße 25, A-8605 Kapfenberg, Austria
- [37] Kistler Instrumente AG, CH-8408 Winterthur, Switzerland; [www.kistler.ch](http://www.kistler.ch).
- [38] Kuratle, R.; *Motorenmeßtechnik*; Vogel Fachbuch, ISBN 3-8023-1553-7, 1995.
- [39] Amsden, A. A.; *KIVA-3V: A Block-Structured KIVA Program for Engines with Vertical and Canted Valves*; Los Alamos National Laboratory report LA-13313-MS, 1997.
- [40] ICEM CFD Engineering; *Hexa: Automated Hexahedral Meshing, Version 4.0.7*; [www.icemcfd.com](http://www.icemcfd.com), 2000.

- [41] Computational Engineering International (CEI), Inc; *EnSight, Version 6.2.1*; [www.ensight.com](http://www.ensight.com), 2000.
- [42] ICEM CFD Engineering; *SDRC Mesher Interface, Version 1.0.9*; [www.icemcfd.com](http://www.icemcfd.com), 1999.
- [43] ICEM CFD Engineering; *Mesh Editor, Version 4.0.7*; [www.icemcfd.com](http://www.icemcfd.com), 2000.
- [44] Nordin, N.; *KIVA to EnSight Interface*; Dept. of Thermo & Fluid Dynamics, Chalmers University of Technology, Gothenburg, Sweden, [www.tfd.chalmers.se/~nordin/ensight.html](http://www.tfd.chalmers.se/~nordin/ensight.html), 1998.
- [45] Amsden, A. A., O'Rourke, P. J. and Butler T. D.; *KIVA-II: A Computer Program for Chemically Reactive Flows with Sprays*; Los Alamos National Laboratory report LA-11560-MS, 1989.
- [46] Amsden, A. A.; *KIVA-3: A KIVA Program with Block-Structured Mesh for Complex Geometries*; Los Alamos National Laboratory report LA-12503-MS, 1993.
- [47] Amsden, A. A.; *KIVA-3V, Release 2, Improvements to KIVA-3V*; Los Alamos National Laboratory report LA-UR-99-915, 1999.
- [48] Chase, M.W., Jr., Davie, C.A., Downey, J.R., Jr., Frurip, D.J., McDonald R.A. and Syverud A.N.; *JANAF Thermochemical Tables, Third Edition, Part I and II*; Journal of Physical and Chemical Reference Data, vol. 14, suppl. 1, 1985.
- [49] Yasar, O. and Zacharia, T.; *Distributed implementation of KIVA-3V on the Intel Paragon*; Parallel Computational Fluid Dynamics, Implementations and Results Using Parallel Computers, Proceedings of the Parallel CFD'95 Conference, Pasadena, CA, pp. 81–88, 1995.
- [50] Chigier, N.; *Energy, Combustion and Environment*; McGraw-Hill International Editions, Energy, Combustion and Environment Series, ISBN 0-07-010766-1, 1981.
- [51] International norm ISO 3046/1; *Reciprocating internal combustion engines - Performance - Part 1: Standard reference conditions and declarations of power, fuel consumption and lubricating oil consumption*; Third edition, 1986-08-15, 1986
- [52] Filterwerk Mann + Hummel GmbH, Hindenburgstraße 45, D-71638 Ludwigsburg, Germany; *Technical documentation*; [www.mann-hummel.com](http://www.mann-hummel.com)
- [53] Bach, C., Heeb, N., Mattrel, P. and Mohr, M.; *Effect-based Assessment of Automotive Emissions*; MTZ Motortechnische Zeitschrift, Vol. 59, issue 11, 1998.
- [54] Nellen C. and Boulouchos, K.; *Natural Gas Engines for Cogeneration: Highest Efficiency and Near-Zero-Emissions through Turbocharging, EGR and 3-Way Catalytic Converter*; SAE Paper 2000-01-2825, 2000.
- [55] Ryhming, I. L.; *Dynamique des Fluides*; Presses Polytechniques Romandes, première édition, ISBN 2-88074-068-1, 1985.
- [56] Cheng, W. K., Hamrin, D., Heywood, J. B., Hochgreb, S., Min, K. and Norris, M.; *An Overview of Hydrocarbon Emissions Mechanisms in Spark-Ignition Engines*; SAE Paper 932708, 1993.

- [57] Alkidas, A. C.; *Combustion-chamber crevices: the major source of engine-out hydrocarbon emissions under fully warmed conditions*; Progress in Energy and Combustion Science, vol. 25, pp. 253–273, Pergamon, Elsevier, 1999.
- [58] Lewis, B. and von Elbe, G.; *Combustion, Flames and Explosions of Gases*; Third Edition, Academic Press, ISBN 0-12-446751-2, 1987.
- [59] Lifshitz, A., Sheller, K., Burcat, A. and Skinner, G. B.; *Shock-Tube Investigation of Ignition in Methane-Oxygen-Argon Mixtures*; Combustion and Flame, vol. 16, pp.311-321, 1971.
- [60] Eubank, C. S., Rabinowitz, M. J., Gardiner, W. C., Jr. and Zellner, R. E.; *Shock-Initiated Ignition of Natural Gas-Air Mixtures*; The 18<sup>th</sup> Symposium (International) on Combustion, The Combustion Institute, Pittsburgh, pp.1767-1774, 1981.
- [61] Tan, Y., Dagaut, P., Cathonnet, M. and Boettner, J. C.; *Natural Gas and Blends Oxidation and Ignition: Experiments and Modelling*; Paper submitted for the 25<sup>th</sup> Symposium (International) on Combustion at the University of California, Irvine, 1994.
- [62] Kubesh, J. T. and Podnar, D. J.; *Humidity Effects and Compensation in a Lean Burn Natural Gas Engine*; SAE Paper 971706, 1997.
- [63] Nakagawa, K., Sakurai, T. and Shoji, F.; *Study of Lean Burn Gas Engines Using Pilot Fuel For Ignition Source*; SAE Paper 982480, 1998.
- [64] Han, Z. and Reitz, R. D.; *Turbulence Modeling of Internal Combustion Engines Using RNG  $k-\epsilon$  Models*; Combustion Science and Technology, Vol. 106, pp. 267–295, 1995.
- [65] Vibro-Meter SA, Rte de Moncor 4, Case postale 71, CH-1700 Fribourg, Switzerland; [www.vibro-meter.com](http://www.vibro-meter.com)
- [66] Hewlett Packard Compagny, 3000 Hanover Street, Paolo Alto, California 94304, USA; [www.hp.com](http://www.hp.com)
- [67] National Instruments; *Labview*; [www.ni.com](http://www.ni.com), 1996.
- [68] Philips Industrial Electronics AG, Riedstrasse 12, Postfach 360, CH-8953 Dietikon 1, Switzerland; [www.philips.com](http://www.philips.com)
- [69] Jaquet AG, Thannerstrasse 15, CH-4009 Basel, Switzerland; [www.jaquet.com](http://www.jaquet.com)
- [70] Trimec Industries, 5/23 Resolution Drive, Caringbah NSW 2229, Australia; [www.trimecind.com.au](http://www.trimecind.com.au)
- [71] ABB Kent-Taylor Ltd., St Neots, Cambs, England PE19 3EU; [www.abb.com](http://www.abb.com)
- [72] Rotronic AG, Grindelstrasse 6, Postfach, CH-8303 Bassersdorf, Switzerland; [www.rotronic.ch](http://www.rotronic.ch)
- [73] Asch, G.; *Les capteurs en instrumentation industrielle*; Editions Dunod, ISBN 2-10-000220-1, 1991.

- [74] Haenni Instruments AG, Bernstrasse 59, CH-3303 Jegenstorf, Switzerland; [www.haenni-instr.com](http://www.haenni-instr.com)
- [75] AVL List GmbH; *Manuel for AVL 620 Indiset (docking station 6162) and IndiWin software version 1.40*; [www.avl.com](http://www.avl.com), 1998.
- [76] Johnson Controls, Inc., 5757 N. Green Bay Avenue, P.O. Box 591, Milwaukee, WI 53201, USA; [www.johnsoncontrols.com](http://www.johnsoncontrols.com)
- [77] Meriam Instrument Compagny, 10920 Madison Avenue, Cleveland, OH 44102, USA; [www.meriam.com](http://www.meriam.com)
- [78] Société Suisse de l'Industrie du Gaz et des Eaux (SSIGE); *Communications*; Gas Wasser Abwasser (gwa), 1989-94.
- [79] Karl Dungs GmbH & Co., Siemensstrasse 6-10, D-73660 Urbach, Germany; [www.dungs.de](http://www.dungs.de)
- [80] Coverad Heat Transfer Ltd., Sir Henry Parkes Road, Canley, Coventry, CV5 6BN, England
- [81] Honeywell, 101 Columbia Road, Morristown, NJ 07962, USA; [www.honeywell.com](http://www.honeywell.com)
- [82] Watlow Electric Manufacturing Compagny, 12001 Lackland Road, St. Louis, Missouri 63146, USA; [www.watlow.com](http://www.watlow.com)
- [83] Gaznat S.A., Zone Industrielle Les Isles, CH-1860 Aigle, Switzerland; *Société pour l'approvisionnement et le transport de gaz naturel en Suisse Romande, Centre de surveillance*.
- [84] NIST Chemistry WebBook; [webbook.nist.gov](http://webbook.nist.gov)
- [85] Kee, R. J., Rupley, F. M. and Miller, J. A.; *CHEMKIN thermodynamic data base*; Sandia National Laboratories, Livermore, CA 94550, Report SAN87-8215B, 1990.
- [86] Borel, L.; *Thermodynamique et Energétique*; Presses Polytechniques Romandes, première édition, ISBN 2-88074-025-8, 1984.
- [87] Chan, S. H. and Zhu, J.; *Divergence Analysis of an Emissions-Based Air-Fuel Ratio Model and Exhaust Oxygen Estimation*; Proceedings of the Institution of Mechanical Engineers (IMEchE), Part D, Journal of automobile engineering, vol. 211, n. 2, pp. 137-144, 1997.
- [88] Rassweiler, G. M. and Withrow, L.; *Motion Pictures of Engine Flames Corraleted with Pressure Cards*; SAE Paper 800131 (originally presented in 1938), 1980.
- [89] Thompson, N. D. and Wallace, J. S.; *Effect of Engine Operating Variables and Piston and Ring Parameters on Crevice Hydrocarbon Emissions*; SAE Paper 940480, 1994.



# Notation

## Symbols

$A$	Area	$m^2$
$A_n$	Total nozzle orifice cross sectional area	$mm^2$
$A_t$	Turbine inlet area	$cm^2$
$B$	Cylinder bore	$m$
$COV$	Coefficient of variance	-
$c$	Mass fraction	-
$\tilde{c}$	Mole fraction	-
$\dot{c}$	Emission concentration	$ppm$
$\check{c}$	Emission concentration	$mg/m^3$
$\breve{c}$	Emission concentration	$mg/kWh$
$c_p$	Specific heat at constant pressure	$J/(kg K)$
$c_v$	Specific heat at constant volume	$J/(kg K)$
$d_n$	Nozzle orifice diameter	$mm$
$E$	Mechanical work	$J$
$\dot{E}$	Engine break power output	$kW$
$f$	Emission correction factor	-
$f_\nu$	Intake to exhaust molar ratio	-
$h$	Specific enthalpy	$J/kg$
$k$	Turbulence kinetic energy	$m^2/s^2$
	Heat transfer coefficient	$W/(m^2 K)$
$L$	Connecting rod length	$m$
$M$	Engine torque	$Nm$
$m$	Specific mass	-
$\dot{m}$	Mass flow rate	$kg/s$
$\tilde{m}$	Molar mass	$kg/kmole$
$N_n$	Number of nozzle orifices	-
$n$	Crankshaft rotational speed	$rpm$
	Number of mole	-
	Polytropic coefficient	-
$p_{me}$	Brake mean effective pressure	$bar$
$p_{mi}$	Indicated mean effective pressure	$bar$
$p$	Pressure	$bar$
$p''$	Pressure of saturation	$bar$
$Q$	Heat	$J$

$R$	Gas constant	$J/(kg K)$
$\mathcal{R}$	Universal gas constant	$J/(kmole K)$
$RH$	Relative humidity	%
$S$	Piston stroke	$m$
$S_p$	Piston speed	$m/s$
$T$	Temperature	$K$
$U$	Internal energy	$J$
$u$	Specific internal energy	$J/kg$
$v$	Flow velocity	$m/s$
	Number of carbon atoms	-
	Specific volume	-
$\dot{v}$	Volume flow rate	$m^3/s$
$V$	Volume	$m^3$
$V_c$	Clearance volume	$mm^3$
$V_s$	Swept volume	$m^3$
$V_p$	Prechamber volume	$mm^3$
$w$	Number of hydrogen atoms	-
	Specific water content per unit of dry air	-
$x$	Number of oxygen atoms	-
$y$	Number of nitrogen atoms	-
$z$	Number of cylinders	-
$\alpha_n$	nozzle orifice mean orientation angle	$^\circ$
$\Delta h_0$	Specific heating value	$kJ/kg$
$\Delta \tilde{h}_0$	Molar heating value	$kJ/kmole$
$\Delta \dot{h}_0$	Volumetric heating value	$kJ/m_N^3$
$\Delta_f^0 \tilde{h}$	Molar standard heat of formation	$kJ/kmole$
$\Delta p$	Pressure difference	$bar$
$\Delta \varphi$	Crank angle interval	$^\circ$
$\epsilon$	Volumetric compression ratio	-
	Rate of dissipation of the turbulence kinetic energy	-
$\eta_f$	Fuel conversion efficiency	-
$\gamma$	Isentropic coefficient	-
$\lambda$	Relative air to fuel ratio	-
$\nu$	Stoichiometric coefficient	-
$\omega$	angular velocity	$rad/s$
$\phi$	Fuel to air equivalence ratio	-
$\varphi$	Crank angular position	$^\circ$
$\pi$	Compression ratio	-
$\psi$	Air relative humidity	-
$\rho$	Density	$kg/m^3$
$\sigma$	Standard deviation	-

## Subscripts and superscripts

<i>ABDC</i>	After bottom dead centre
<i>AST</i>	After spark timing
<i>ATDC</i>	After top dead centre
<i>air</i>	Dry air
<i>BBDC</i>	Before bottom dead centre
<i>BTDC</i>	Before top dead centre
<i>c</i>	Compression
<i>cd</i>	Combustion duration
<i>corr</i>	Corrected
<i>cp</i>	Combustion products
<i>e</i>	End
<i>ea</i>	Excess air
<i>eg</i>	Exhaust gas
<i>f</i>	Formation
<i>h</i>	Humidity
<i>hr</i>	Heat released
<i>hum</i>	Humid
<i>IVC</i>	Inlet valve closure
<i>id</i>	Ignition delay
<i>in</i>	Inlet or intake
<i>L</i>	Lower
<i>m</i>	Measured
<i>main</i>	Main combustion chamber
<i>min</i>	Minimum
<i>mixt</i>	Fuel-air mixture
<i>N</i>	Normal conditions: $p = 1.013 \text{ bar}$ , $T = 273.15 \text{ K}$
<i>n</i>	Net
<i>ng</i>	Natural gas
<i>out</i>	Outlet
<i>pre</i>	Combustion prechamber
$Q_{5\%}$	5% of combustion heat-release integral
$Q_{90\%}$	90% of combustion heat-release integral
<i>s</i>	Start
<i>st</i>	Spark timing
<i>t</i>	Total
<i>U</i>	Upper
<i>unf</i>	Unfired
0	Reference conditions: $p = 1.013 \text{ bar}$ , $T = 298.15 \text{ K}$

## Abbreviations

<i>CA</i>	Crank angle
<i>CNG</i>	Compressed natural gas
<i>CPU</i>	Central Processing Unit
<i>Cyl.</i>	Cylinder
<i>EGR</i>	Exhaust gas recirculation
<i>IVC</i>	Inlet valve closure
<i>MBT</i>	Maximum brake torque
<i>ST</i>	Spark timing
<i>TDC</i>	Top dead centre
<i>vol</i>	Volume

# List of Figures

1.1	Schematic representation of a spark plug prechamber . . . . .	7
2.1	Schematic representation of the original combustion chamber . . . . .	16
2.2	Combustion prechamber . . . . .	18
2.3	Schematic representation of the combustion chamber with prechamber .	19
2.4	Cylinder head instrumentation for high pressure indication . . . . .	21
2.5	Cylinder head instrumentation for low pressure indication . . . . .	22
2.6	Instrumented cylinder 1 with prechamber . . . . .	22
3.1	CFD simulation procedure . . . . .	27
3.2	Blocking of the computational domain . . . . .	29
3.3	Mesh of the computational domain . . . . .	30
3.4	Evolution of the prechamber flow pattern and velocity magnitude . . .	33
3.5	Evolution of the prechamber turbulence kinetic energy . . . . .	34
3.6	Evolution of the prechamber fuel to air equivalence ratio . . . . .	35
3.7	Comparison between direct and prechamber ignition . . . . .	36
3.8	Turbulence kinetic energy in the main combustion chamber at TDC . .	37
3.9	Reference locations in the combustion prechamber . . . . .	38
3.10	Influence of the total nozzle orifice cross sectional area . . . . .	39
3.11	Influence of the nozzle orifice orientation . . . . .	40
3.12	Effect of a prechamber swirl motion on the flow pattern and velocity .	42
3.13	Effect of a prechamber swirl motion on the turbulence kinetic energy .	42

3.14	Effect of a prechamber swirl motion on the fuel to air equivalence ratio	43
3.15	Effect of a prechamber swirl motion . . . . .	44
3.16	Influence of the number of nozzle orifices . . . . .	45
3.17	Effect of a coaxial nozzle orifice . . . . .	46
3.18	Effect of a coaxial nozzle orifice on the turbulence kinetic energy . . . .	47
3.19	Influence of the prechamber bottom geometry on the flow pattern and velocity . . . . .	48
3.20	Influence of the prechamber bottom geometry on the turbulence kinetic energy . . . . .	48
3.21	Influence of the prechamber bottom geometry . . . . .	49
3.22	Influence of the prechamber volume . . . . .	50
3.23	Influence of the prechamber volume on the turbulence kinetic energy .	51
3.24	Influence of the prechamber shape on the flow pattern and velocity . .	53
3.25	Influence of the prechamber shape on the turbulence kinetic energy . .	53
3.26	Influence of the prechamber shape on the fuel to air equivalence ratio .	54
3.27	Influence of the prechamber shape . . . . .	55
4.1	Test bed with gas engine <i>Liebherr G 926 TI</i> . . . . .	58
4.2	Performance and emissions with direct ignition . . . . .	62
4.3	High turbulence and low compression combustion chambers . . . . .	63
4.4	Effect of the prechamber on the engine cycle at constant relative air to fuel ratio . . . . .	67
4.5	Effect of the prechamber on the engine cycle at constant NO <sub>x</sub> emissions . . . . .	69
4.6	Effect of the prechamber on the engine performance and emissions . . .	71
4.7	Effect of the prechamber on the turbocharger operating characteristics	74
4.8	Influence of the total nozzle orifice cross sectional area on the engine cycle . . . . .	76
4.9	Influence of the total nozzle orifice cross sectional area on the ignition delay and combustion duration . . . . .	77

4.10	Influence of the total nozzle orifice cross sectional area on the engine performance and emissions . . . . .	78
4.11	Influence of the number of nozzle orifices on the engine cycle . . . . .	81
4.12	Influence of the number of nozzle orifices on the ignition delay and combustion duration . . . . .	82
4.13	Influence of the number of nozzle orifices on the engine performance and emissions . . . . .	83
4.14	Geometrical distribution of the nozzle orifices around the prechamber nose . . . . .	85
4.15	Influence of the nozzle orifice distribution on the ignition delay and combustion duration . . . . .	86
4.16	Influence of the nozzle orifice distribution on the engine cycle . . . . .	87
4.17	Influence of the nozzle orifice distribution on the engine performance and emissions . . . . .	88
4.18	Influence of the nozzle orifice distribution on the mean combustion temperature . . . . .	89
4.19	Influence of the nozzle orifice orientation on the engine cycle . . . . .	91
4.20	Influence of the nozzle orifice orientation on the pressure difference between pre- and main chamber and on the ignition delay and combustion duration . . . . .	92
4.21	Simulated main chamber flow pattern at $5^{\circ}CA_{ATDC}$ . . . . .	92
4.22	Influence of the nozzle orifice orientation on the engine performance and emissions . . . . .	93
4.23	Influence of the prechamber internal volume on the engine cycle . . . . .	96
4.24	Influence of the prechamber internal volume on the ignition delay and combustion duration . . . . .	97
4.25	Influence of the prechamber internal volume on the engine performance and emissions . . . . .	98
4.26	Influence of the prechamber internal shape on the engine cycle . . . . .	101
4.27	Influence of the prechamber internal shape on the ignition delay and combustion duration . . . . .	102
4.28	Influence of the prechamber internal shape on the engine performance and emissions . . . . .	103

4.29	Influence of the main combustion chamber on the engine cycle . . . . .	105
4.30	Influence of the main combustion chamber on the ignition delay and combustion duration . . . . .	106
4.31	Simulated main chamber flow pattern at $5^{\circ}CA_{ATDC}$ . . . . .	107
4.32	Influence of main combustion chamber on the engine performance and emissions . . . . .	108
4.33	Influence of the spark timing on the engine cycle . . . . .	110
4.34	Influence of the spark timing on the ignition delay and combustion duration . . . . .	111
4.35	Influence of the spark timing on the engine emissions and performance . . . . .	112
4.36	Influence of the spark timing on the mean combustion temperature . . . . .	113
4.37	Influence of the turbocharger turbine volute throat area on the intake and exhaust port pressure of cylinder 1 . . . . .	116
4.38	Influence of the turbocharger turbine volute throat area on the turbocharger operating characteristics . . . . .	117
4.39	Influence of the turbocharger turbine volute throat area on the engine cycle . . . . .	119
4.40	Influence of the turbocharger turbine volute throat area on the engine performance and emissions . . . . .	120
4.41	Effect of the brake mean effective pressure on the turbocharger operating characteristics . . . . .	123
4.42	Turbocharger compressor performance map . . . . .	124
4.43	Effect of the brake mean effective pressure on the engine breathing process . . . . .	125
4.44	Influence of the brake mean effective pressure on the engine cycle . . . . .	126
4.45	Influence of the brake mean effective pressure on the engine performance and emissions . . . . .	127
4.46	Final comparison between direct and prechamber ignition . . . . .	132
A.1	Orientation of the nozzle orifices in the main combustion chamber . . . . .	162
B.1	Reference locations in the combustion chamber . . . . .	186



B.2	Influence of the main chamber mesh resolution on the main chamber flow . . . . .	187
B.3	Influence of the main chamber mesh resolution on the prechamber flow	187
B.4	Influence of the prechamber mesh resolution on the prechamber flow . .	188
B.5	Influence of the turbulence model on the main chamber flow . . . . .	189
B.6	Influence of the turbulence model on the prechamber flow . . . . .	190
B.7	Influence of the initial turbulence intensity on the main chamber flow .	191
B.8	Influence of the initial turbulence intensity on the prechamber flow . . .	191
B.9	Influence of the initial turbulence intensity on the conventional combustion chamber flow . . . . .	192
B.10	Influence of the initial temperature difference between prechamber and main chamber . . . . .	193
C.1	Diagram of the testing facilities . . . . .	198
C.2	Low speed acquisition system . . . . .	202
C.3	High speed acquisition system . . . . .	204
C.4	Air conditioning system and laminar flow meter . . . . .	205
C.5	Compressed natural gas expansion system . . . . .	206
C.6	Fuel-air mixer and throttle . . . . .	207
C.7	Turbocharger . . . . .	208
C.8	Air-fuel mixture intercooler . . . . .	209
C.9	Intake piping with measurement section before the intake manifold . .	210
C.10	Exhaust system . . . . .	211
C.11	Engine and dynamometer cooling water conditioning systems . . . . .	212
C.12	Engine lubricating oil conditioning system . . . . .	212
C.13	Instantaneous polytropic coefficient . . . . .	229
C.14	Combustion chamber model for heat release calculation . . . . .	231
C.15	Combustion chambers with different volumetric compression ratios . . .	238

C.16 Influence of the volumetric compression ratio . . . . .	239
C.17 Influence of the volumetric compression ratio on the combustion process . . . . .	240
C.18 Intake and exhaust valve strokes . . . . .	241
C.19 Influence of the valves overlap on the emissions and performance . . . .	242
C.20 Influence of the valve overlap on the pumping loop . . . . .	243
C.21 First compression ring location . . . . .	244
C.22 Influence of the piston top land height . . . . .	245

# List of Tables

2.1	Main engine specifications . . . . .	15
2.2	Summary of the prechamber configurations . . . . .	20
2.3	Main specifications of the pressure transducers . . . . .	23
3.1	Main calculation and initial conditions of the numerical simulation . . . . .	30
4.1	General experimental conditions . . . . .	59
4.2	Summary of the prechamber configurations . . . . .	94
A.1	List of the prechamber and cylinder head drawings . . . . .	163
A.2	List of the drawings of the instrumentation holders . . . . .	176
C.1	Main specifications of the measurement instrumentation . . . . .	200
C.2	Main specifications of the exhaust gas analysers . . . . .	201
C.3	Main specifications of the piezoresistive pressure transducers . . . . .	203
C.4	Natural gas composition and properties . . . . .	215
C.5	Molecular weight and standard heat of formation . . . . .	216
C.6	Tabulated direct ignition experimental data . . . . .	246
C.7	Tabulated prechamber ignition experimental data . . . . .	247
C.8	Absolute errors on the engine performance and emissions . . . . .	249



# Appendix A

## Design

### A.1 Orientation of the nozzle orifices

The orientation of the nozzle orifices was established in order to achieve a relatively uniform distribution of the jets of combustion products in the main chamber, considering the offset of the prechamber location from the piston axis. The chosen approach consists in orienting the nozzle orifices to equally distributed positions on a curve located on the piston bowl surface at TDC, in a plane parallel to the cylinder head surface. The global orientation pattern is defined in order to obtain a symmetrical distribution. In the case of 6 nozzle orifices, the principle is described in **figure A.1**. The angle  $\beta$  represents the orientation from the prechamber positioning pin. The angles  $\beta$  and  $\lambda$  are required for the construction of the nozzle orifices in the CAD model.

The nozzle orifices were designed to converge to a single point located on the plane containing the cylinder head bottom surface. This point is offset from the combustion chamber axis by the following values in the referential  $xy$  attached to the cylinder head surface:

$$\begin{aligned} a &= 6.5 \text{ mm} \\ b &= -11 \text{ mm} \end{aligned}$$

The angle  $\mu$  gives the angular distribution of theoretical jet impact points on the defined piston bowl curve from the symmetry plane of the global jet pattern. In the case of 6 nozzle orifices, the values are  $30^\circ$ ,  $90^\circ$ ,  $150^\circ$ ,  $210^\circ$ ,  $270^\circ$ ,  $330^\circ$ . The partial prechamber symmetry plane (including the axis of the positioning pin) is oriented by  $20^\circ$  from the cylinder head main reference plane, which is imposed by the original cylinder head design. The symmetry plane of the global jet pattern is oriented from the cylinder head main reference plane by the following angle:

$$\delta = \arctan\left(\frac{a}{-b}\right) = 30.58^\circ \quad (\text{A.1})$$

The curve on the piston bowl surface can be arbitrarily chosen and is defined by its radius  $r$  and relative position  $h$  from the cylinder head surface. The position of the

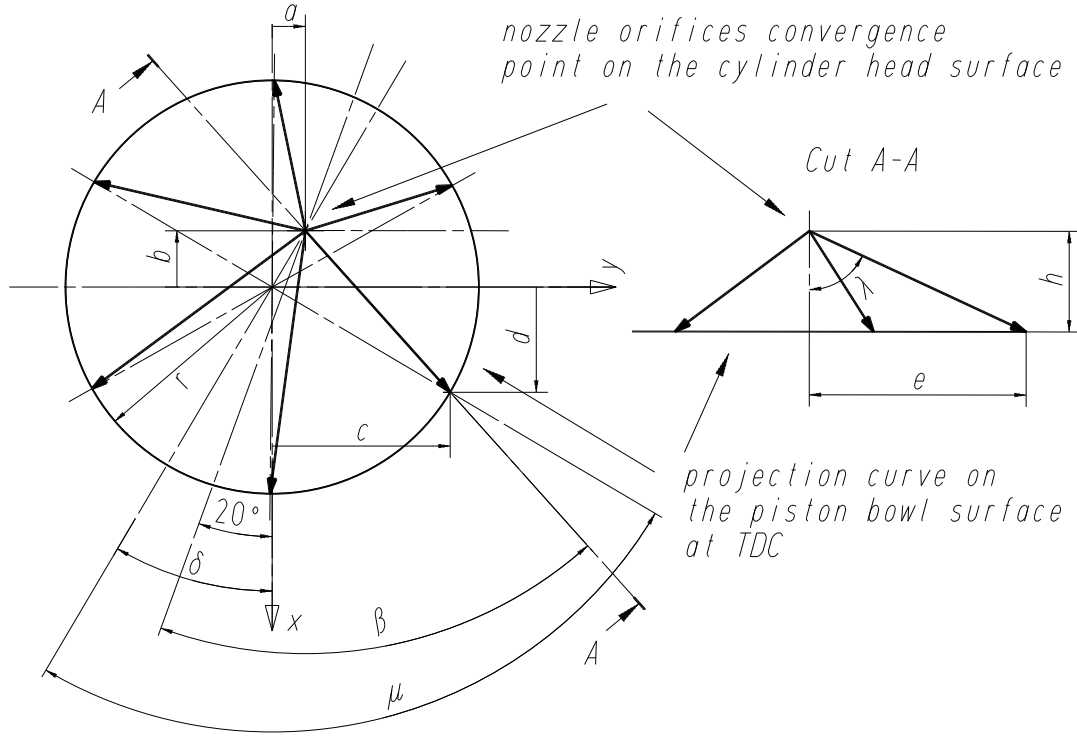


**Figure A.1:** Geometrical orientation of the nozzle orifices in the main combustion chamber

theoretical jet impact points in the main combustion chamber referential is:

$$c = \sin(\mu - \delta)r \quad (\text{A.2})$$

$$d = \cos(\mu - \delta)r \quad (\text{A.3})$$

It is then possible to determine the projected theoretical jet length:

$$e = \sqrt{(c - a)^2 + (d - b)^2} \quad (\text{A.4})$$

and finally the both orientation angles:

$$\beta = \arctan \left[ \frac{(c - a)}{(d - b)} \right] + 20^\circ \quad (\text{A.5})$$

$$\lambda = \arctan \left( \frac{e}{h} \right) \quad (\text{A.6})$$

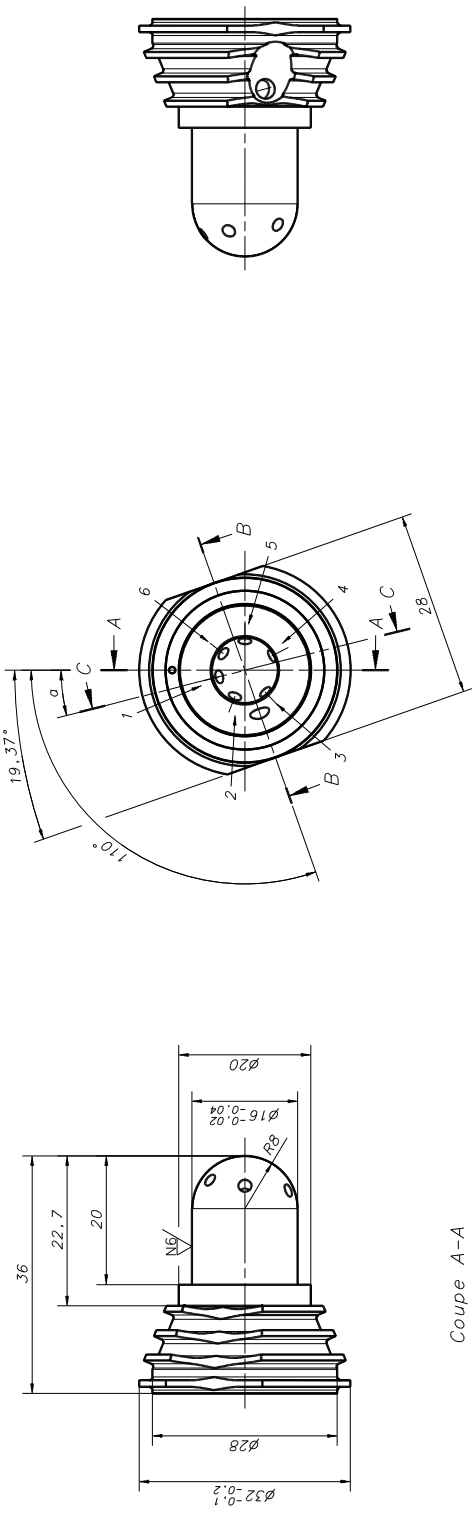
$\beta$  and  $\lambda$  are referred to the partial prechamber symmetry plane in the plane containing the cylinder head surface and to the axis perpendicular to the cylinder head surface and passing by the nozzle orifice convergence point, respectively. These angles are used in the CAD model to orient the reference planes required to cut the orifices in the prechamber nose. They are different from the one ( $a$  and  $b$ ) indicated in the drawings given in appendix A.2, which are referred to the partial prechamber symmetry plane in a plane perpendicular to the prechamber axis and containing the nozzle orifice convergence point and to the prechamber axis, respectively. The latter were directly measured in the CAD model to suit the specific requirements for machining the orifices.

## A.2 Prechamber and cylinder head drawings

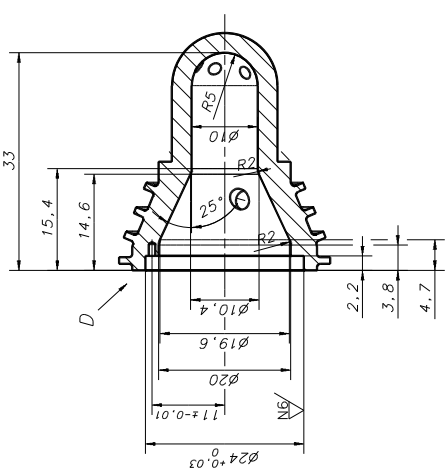
This section contains the drawings of the different parts composing the combustion prechamber as well as a partial representation of the modified cylinder head. The prechamber drawings represent the main geometrical features of the different configurations. Most of the configurations tested were however made out of the combination of these features or of simple modifications, like the variation of the nozzle orifice diameter. All arrangements are therefore not represented here. The cylinder head drawing describes the required modifications to enable the fitting of the prechamber, its cooling with engine water and its instrumentation for pressure cycle measurement in the main- and prechamber as well as in the intake and exhaust ports. The different drawings (commented in French) are summarised in the following table:

**Table A.1:** List of the prechamber and cylinder head drawings

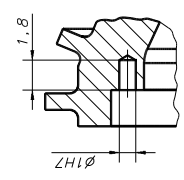
Designation	Page
Prechamber nose, 6 orifices, orientation angle $\approx 62^\circ$ , 4540 $mm^3$	164
Prechamber nose, 6 orifices, orientation angle $\approx 78^\circ$ , 4540 $mm^3$	165
Prechamber body, 4540 $mm^3$	166
Prechamber nose, 4 orifices, orientation angle $\approx 62^\circ$ , 3010 $mm^3$ , proport. red.	167
Prechamber body, proportional reduction, 3010 $mm^3$	168
Prechamber nose, 4 orifices, orientation angle $\approx 78^\circ$ , 3010 $mm^3$ , shape var.	169
Prechamber body, shape variation, 3010 $mm^3$	170
Prechamber fixing clamp	171
Cylinder head for instrumentation of cylinder 1 (partial representation)	172
Plug of the cooling channel (only for cylinder 1)	173
Copper joint between prechamber body and nose	174
Copper joint between prechamber nose and cylinder head	175



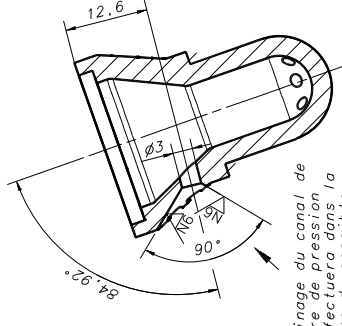
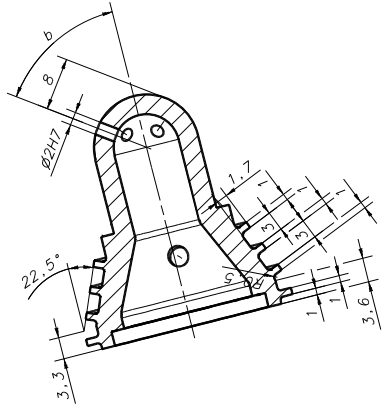
Coupe A-A



Détail D (5:1)



Coupe C-C



Coupe B-B

L'usinage du canal de mesure de pression s'effectuera dans la mesure du possible au montage.

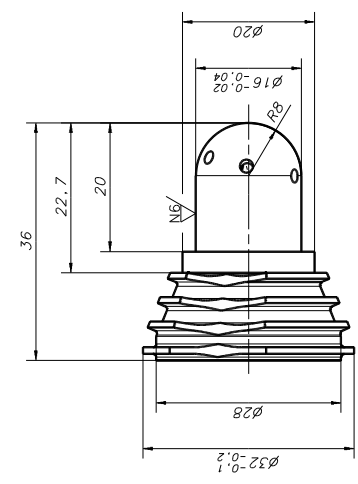
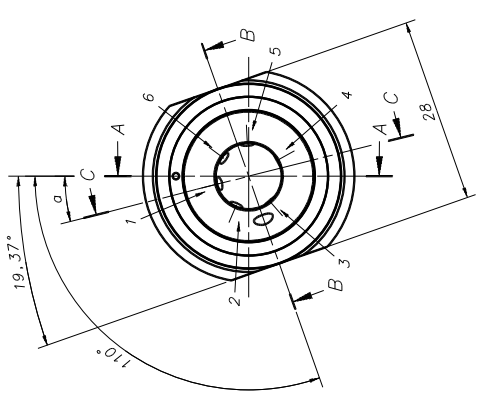
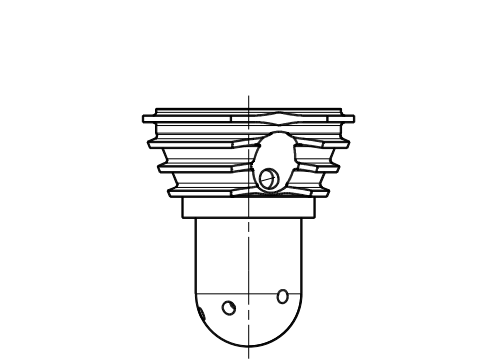
N°	a	b
1	14.19°	54.59°
2	69.19°	58.81°
3	133.36°	66.47°
4	207.93°	69.77°
5	269.82°	64.17°
6	322.03°	56.99°

NB/ (N6/)

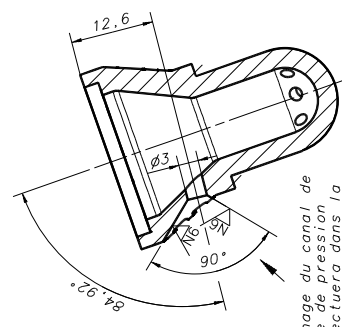
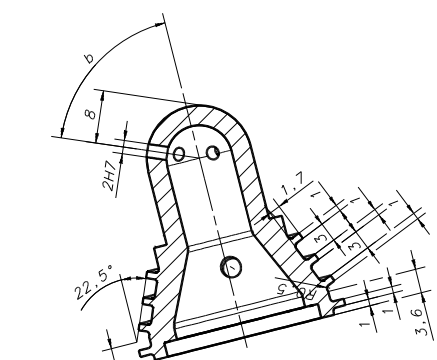
X15CRNiSi25-20		Matériau																																					
Requis	Quantité	Unité	Dimensionnement																																				
			9.7.99																																				
			2 : 1																																				
<table border="1"> <tr> <td>Revisité</td> <td>Revisé</td> <td>Revisé</td> <td>Revisé</td> </tr> <tr> <td></td> <td></td> <td></td> <td></td> </tr> <tr> <td></td> <td></td> <td></td> <td></td> </tr> <tr> <td></td> <td></td> <td></td> <td></td> </tr> <tr> <td></td> <td></td> <td></td> <td></td> </tr> <tr> <td></td> <td></td> <td></td> <td></td> </tr> <tr> <td></td> <td></td> <td></td> <td></td> </tr> <tr> <td></td> <td></td> <td></td> <td></td> </tr> <tr> <td></td> <td></td> <td></td> <td></td> </tr> </table>				Revisité	Revisé	Revisé	Revisé																																
Revisité	Revisé	Revisé	Revisé																																				
N° de dessin		PRE-1.1																																					





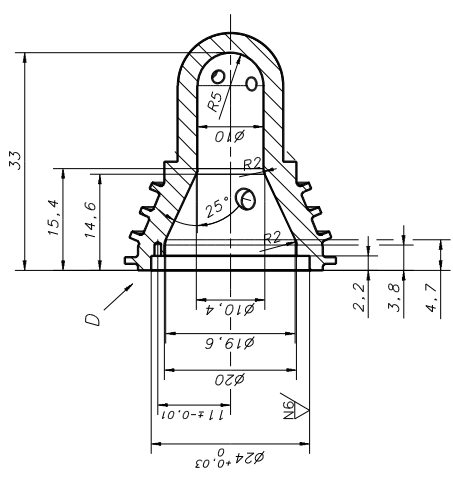


Coupe C-C

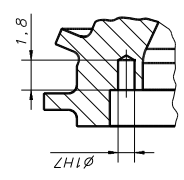


Coupe B-B

L'usinage du canal de mesure de pression s'effectuera dans la mesure du possible au montage



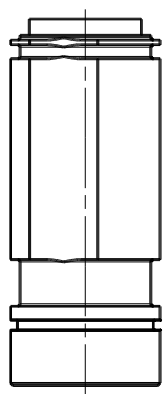
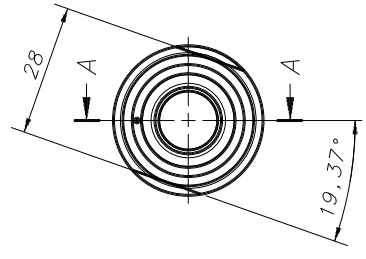
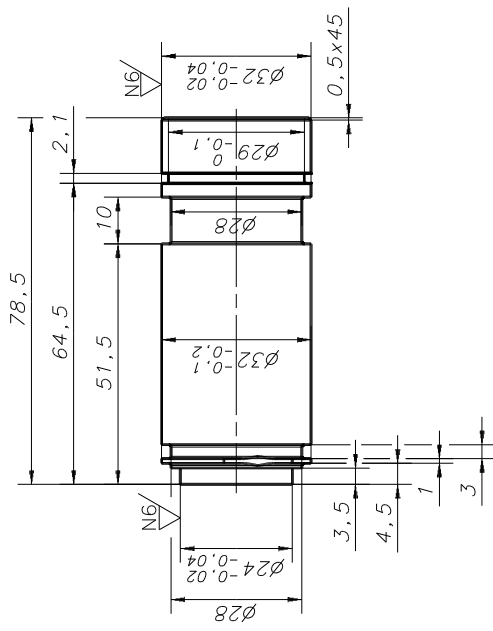
Détail D (5:1)



X15CrNiSi25-20		Métre		Diamètre caractéristique	
Pos.	Quantité	Unité	Dessiné	4. 2.00	Exécuté
			Contrôlé		2: 1
			Cont. au nom:		
			Bas pour référence		
			N° de commande		
			Etat:		
			N° de pièce		
			Etat:		
			N° de série		
			Etat:		
			N° de série		
			Etat:		

N°	a	b
1	13.98°	67.47°
2	66.95°	74.20°
3	130.64°	86.92°
4	209.01°	90.36°
5	272.31°	79.51°
6	323.63°	69.79°

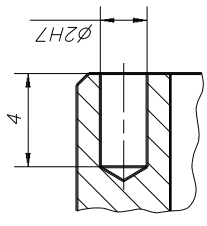
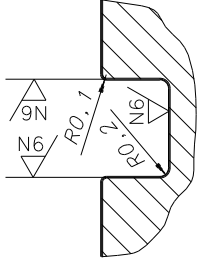
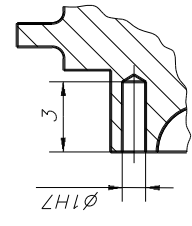
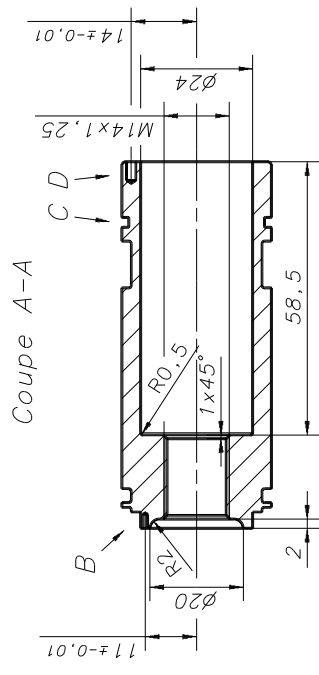
Préchambre de combustion PRE-1.1.2



Détail B (5:1)


Détail C (5:1)

Détail D (5:1)

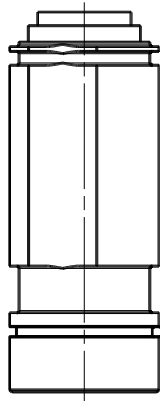
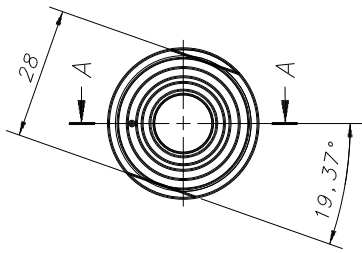
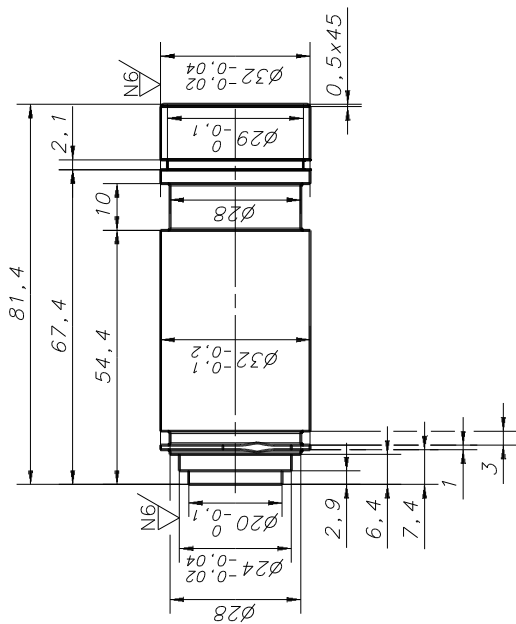


NB (N6)

Rayons non-cotés: 0,5

Pis.	Quantité	Unité	Matériau	Dénomination/caractéristiques	Échelle
			X15CrNiSi25-20	Reinforcing	21.9.99
Mod.				Essaié	1:1
				Contrôlé	
				Conf. aux normes	
				Bon pour exécution	
				N° de commande	
				Origine	
				Remarque	
Sans nomenclature séparée				Nb. feuilles	
Numér. séq. de mise N°				Feuille N°	
Numér. séq. de N° différent				N° de dessin	
				Dénomination	
				Corps préchambre de combustion	
				PRE-1.2	

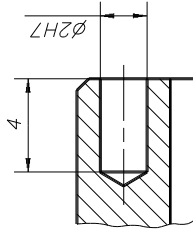
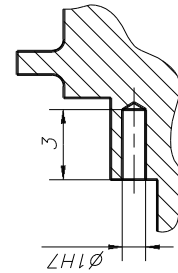
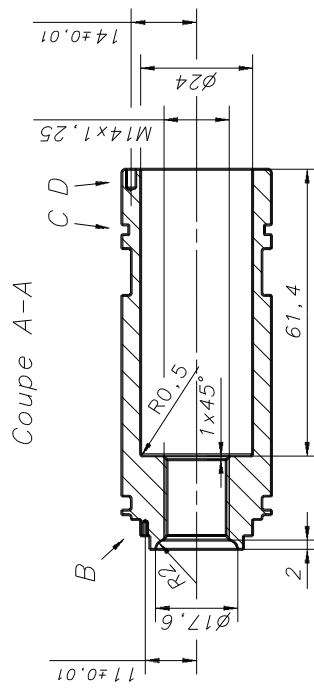




Détail B (5:1)

Détail C (5:1)

Détail D (5:1)

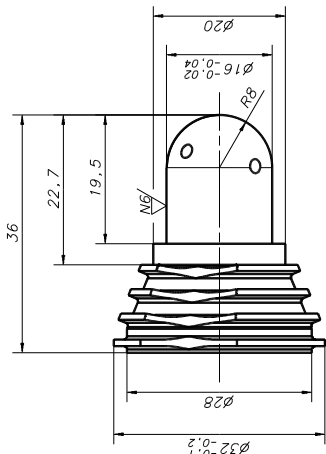
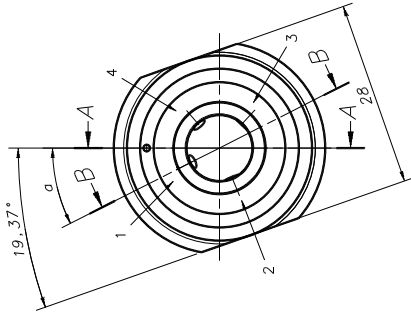
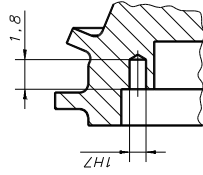


N6 (N6)

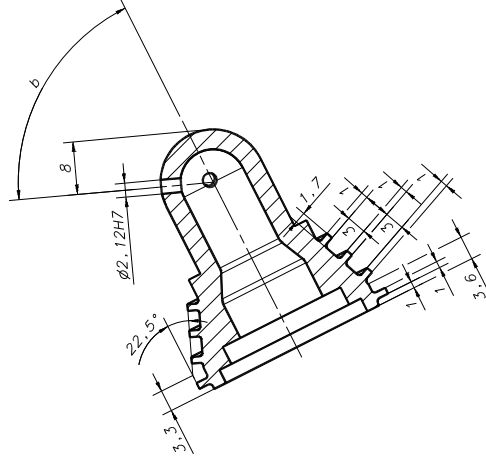
Rayons non-cotés: 0,5

Pos.	Quantité	Unité	Matériau	Dénomination/caractéristiques	Échelle
			X15CrNiSi25-20	Bessiné Rein / isbergé	1:3.5.00
Mod.				Contrôle	1:1
				Conf. aux normes	
				Bon pour exécution	
				N° de commande	
				Origine	Nb. feuilles
				Remarque	Feuille N°
Sans nomenclature séparée Numérot. sep. de mme N° Numérot. sep. de N° différent				N° d'ident.	
				Dénomination	N° de dessin
Corps préchambre de combustion					PRE-1.2.2

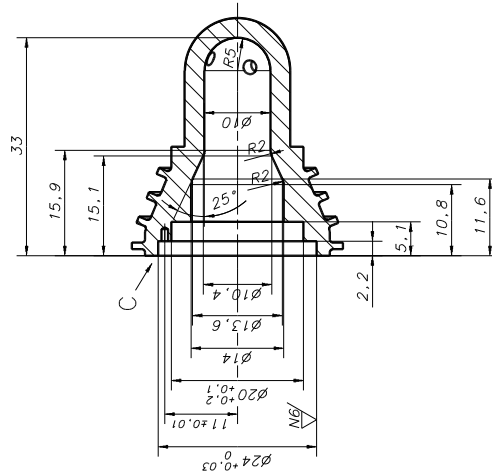
Détail C (5:1)



Coupe B-B



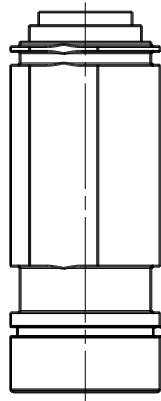
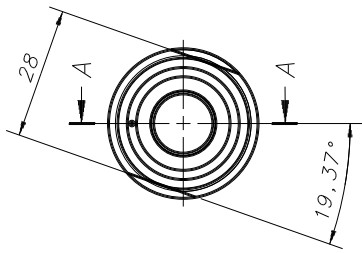
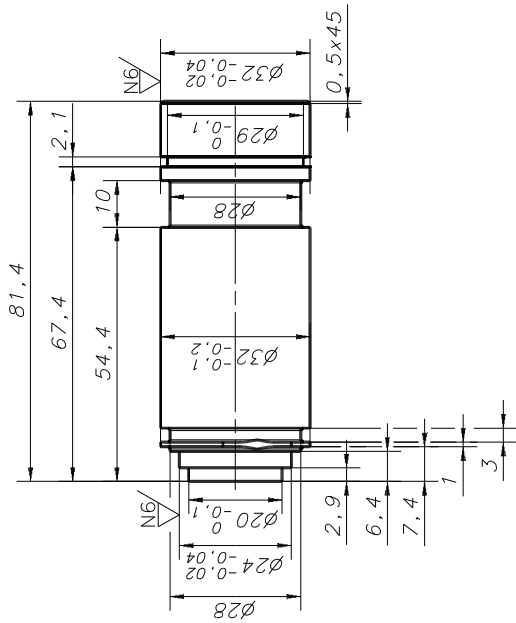
Coupe A-A



N°	a	b
1	26.84°	68.32°
2	112.89°	83.73°
3	226.86°	88.26°
4	311.14°	71.67°

N6/ (N6/)

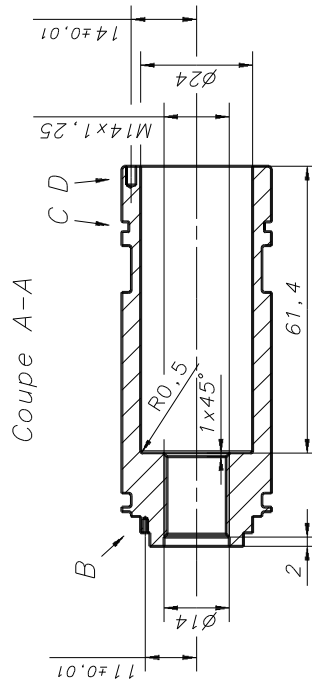
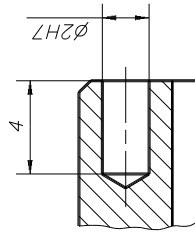
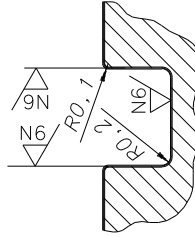
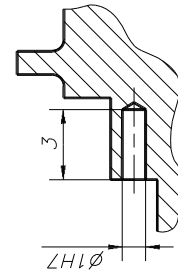
Pos.	Quantité	Unité	Matériau	Désignation caractéristique	Exécuté
				X15CRNiSi25-20	3.8.00
Mat.			Mat.	Mat./réviser	2:1
Sanctionné spécifiquement par le service de R. & D.			N° d'essai	N° de contrôle	N° de vérification
N° de dessin			N° de dessin	N° de dessin	N° de dessin
Désignation			Préchambre de combustion		
N° de dessin			PRE-1.1.4		



Détail B (5:1)


Détail C (5:1)

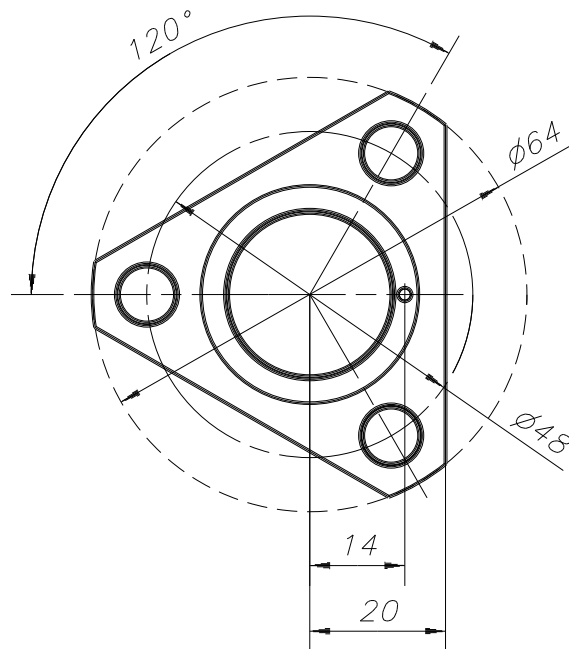
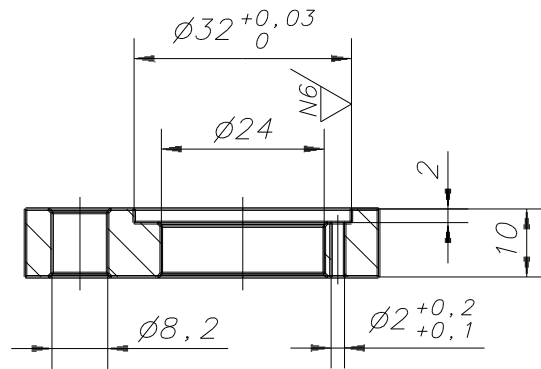
Détail D (5:1)



N6 (N6)

Rayons non-cotés: 0,5

Pos.	Quantité	Unité	Matériau	Dénomination/caractéristiques	Échelle
			X15CrNiSi25-20		1:1
Mod.				Revisé	4.9.00
				Contrôlé	
				Conf. aux normes	
				Bon pour exécution	
				N° de commande	
				Origine	
				Remplace	
Sans nomenclature séparée			N° d'ident.	Nb. feuilles	Feuille N°
Nomencl. sep. de n° différent			Dénomination	N° de dessin	
			Corps préchambre de combustion		
			PRE-1.2.3		

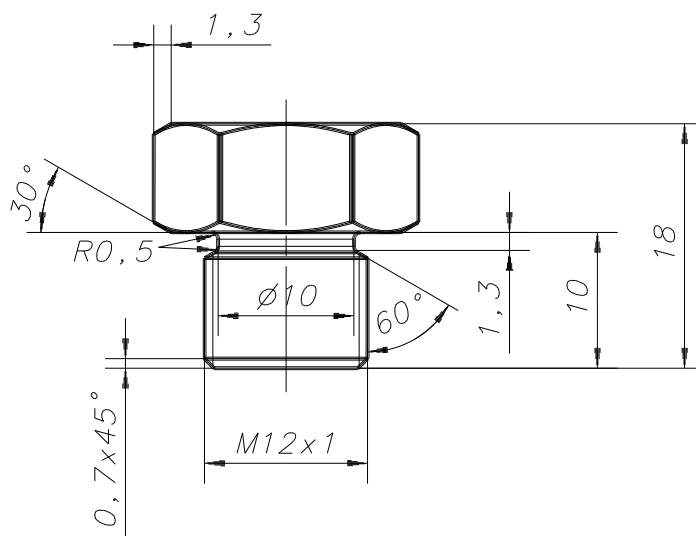


Chamfreins non-cotés: 0,5x45°

			Ac inox décolt.						
Pos.	Quantité	Unité	Matière	Dénomination/caractéristiques					
Mod.			Mod.		Dessiné	Röthlisberger	21.9.99	Echelle	
					Contrôlé			1:1	
					Conf. aux normes				
					Bon pour exécution				
Sans nomenclature séparée				N° de commande					
Nomencl. sép. de même N°				Origine		Nb. feuilles	Feuille N°		
Nomencl. sép. de N° différent				N° d'ident.	Remplace				
				Dénomination	Bride fixation préchambre de combustion			N° de dessin	PRE-1.3

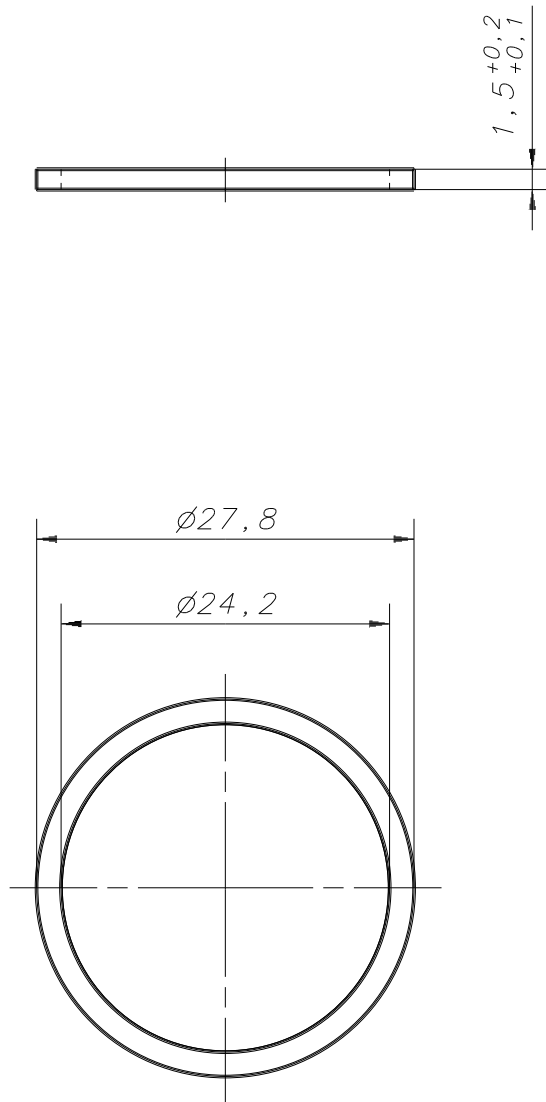






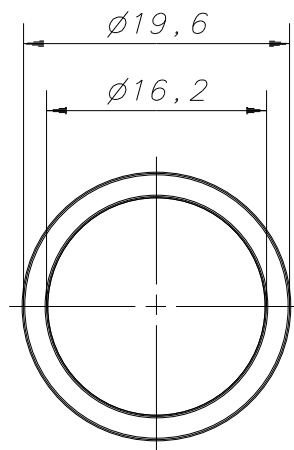
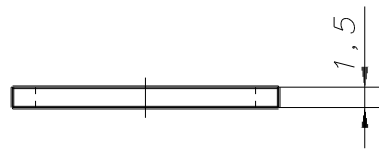
N8/

			Ac inox décollt.					
Pos.	Quantité	Unité	Matière		Dénomination/caractéristiques			
Mod.			Mod.		Dessiné	Röthlisberger	21.9.99	Echelle
					Contrôlé			2:1
					Conf. aux normes			
					Bon pour exécution			
Sans nomenclature séparée				N° de commande				
Nomencl. sép. de même N°				Origine		Nb. feuilles	Feuille N°	
Nomencl. sép. de N° différent				N° d'ident.		Remplace		
			Dénomination			N° de dessin		
			Bouchon canal refroidissement préchambre			RPR-1.1		



N8/

		<i>Cuivre recuit</i>							
Pos.	Quantité	Unité	Matière		Dénomination/caractéristiques				
Mod.			Mod.		Dessiné	<i>Röthlisberger</i>	<i>21.9.99</i>	Echelle <b>2:1</b>	
						Contrôlé			
						Conf. aux normes			
						Bon pour exécution			
Sans nomenclature séparée				N° de commande					
Nomencl. sép. de même N°				Origine		Nb. feuilles	Feuille N°		
Nomencl. sép. de N° différent				N° d'ident.	Remplace				
				Dénomination <i>Joint préchambre de combustion</i>			N° de dessin <i>PRE-1.4</i>		



N8/

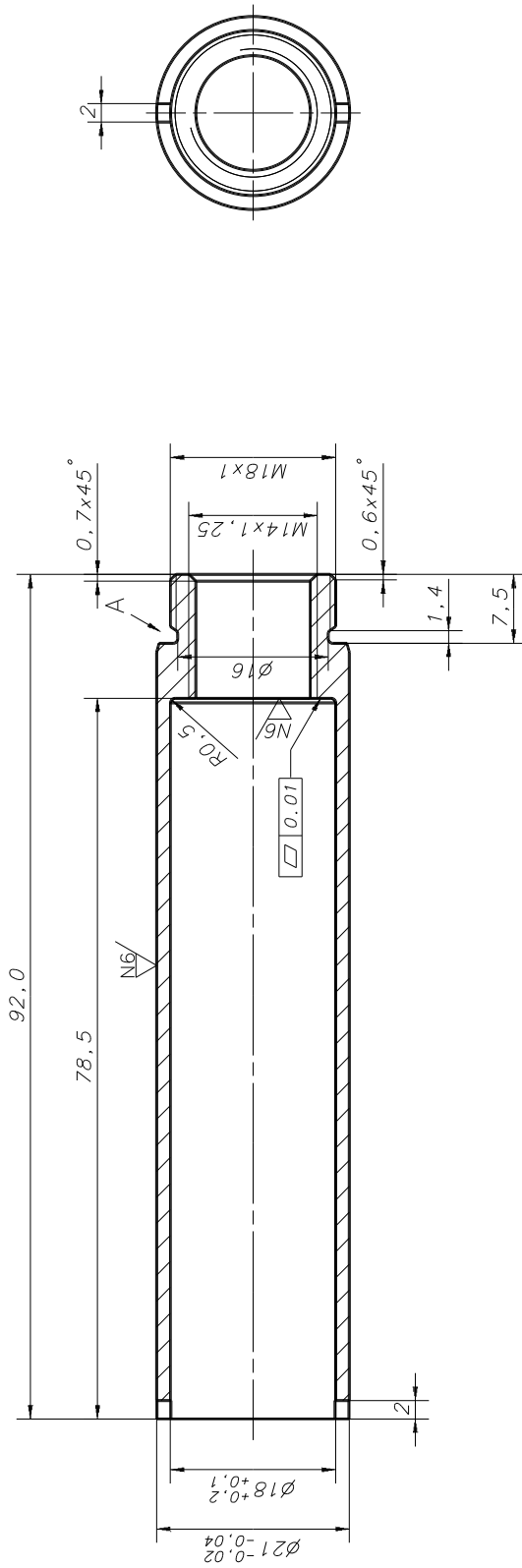
				<i>Cuivre recuit</i>					
Pos.	Quantité	Unité	Matière		Dénomination/caractéristiques				
Mod.			Mod.		Dessiné	<i>Röthlisberger</i>	<i>21.9.99</i>	Echelle <b>2:1</b>	
					Controlé				
					Conf. aux normes				
Sans nomenclature séparée					Bon pour exécution				
Nomencl. sép. de même N°					N° de commande				
Nomencl. sép. de N° différent				N° d'ident.	Origine		Nb. feuilles		Feuille N°
				Dénomination <i>Joint préchambre-culasse</i>			N° de dessin <i>PRE-1.5</i>		

### A.3 Drawings of the instrumentation holders

This section contains the drawings of holders required to fit the measurement instrumentation onto cylinder 1 and partially cylinder 3. These adapters are intended for piezoelectric transducers for main- and prechamber pressure indication as well as for water-cooled adapters for piezoresistive transducers for pressure measurement in the intake and exhaust ports. The different drawings (commented in French) are summarised in the following table:

**Table A.2:** List of the drawings of the instrumentation holders

<b>Designation</b>	<b>Page</b>
Holder for the main chamber pressure transducer	177
Holder for the prechamber pressure transducer	178
Guide for the prechamber pressure transducer holder	179
Holder for the intake port pressure transducer	180
Holder for the exhaust port pressure transducer	181
Copper joint for the main chamber pressure transducer holder	182
Copper joint for the intake port pressure transducer holder	183
Copper joint for the exhaust port pressure transducer holder	184

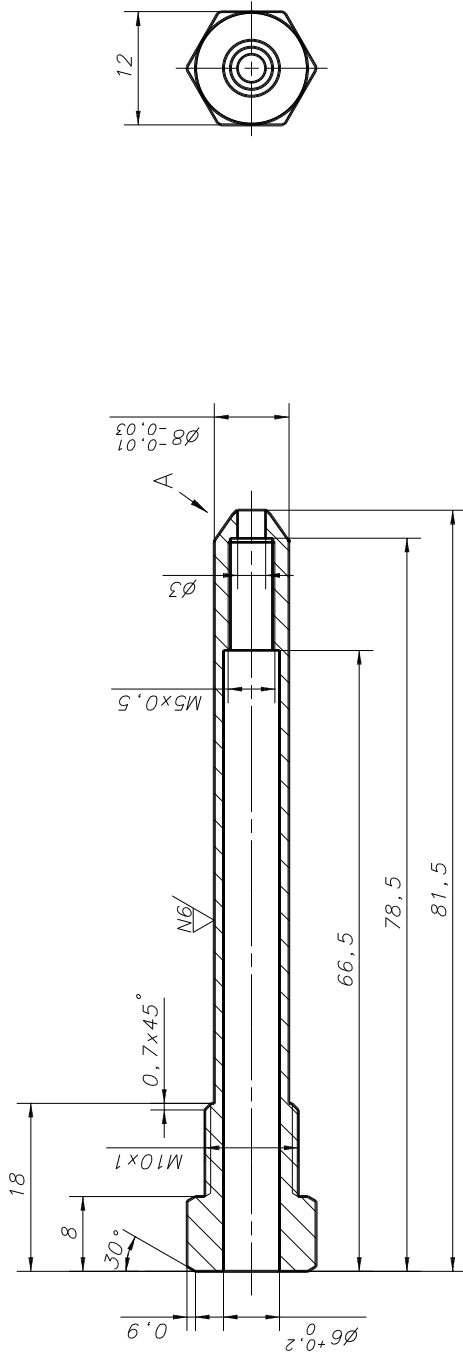


Détail A (10:1)

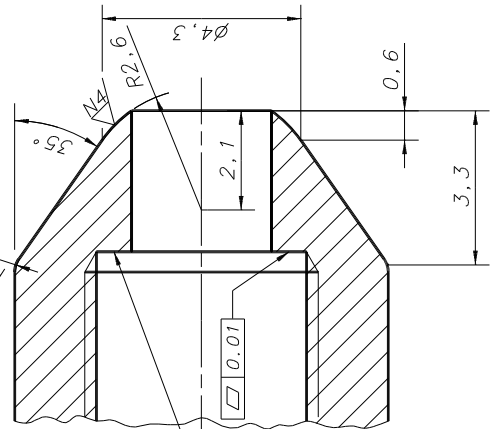
N8 (N6)

Pos.	Quantité	Unité	Matériau	Dénomination/caractéristiques	Revised/Revised	27.9.99	Echelle	2:1	
Mod.									
Sans nomenclature séparée				Dessiné					
Nomencl. sep. de série N°				Contrôlé					
Nomencl. sep. de N° d'élément				Contr. sur nom					
				Bon pour exécution					
				N° de commande					
				Origine					
				Remplace					
				N° d'ident.					
				Nb. feuilles					
				Dénomination: Adaptateur pour montage capteur de pression Kistler 7061B dans culasse avec préchambre				N° de dessin MCP-2.1	





Détail A (10:1)



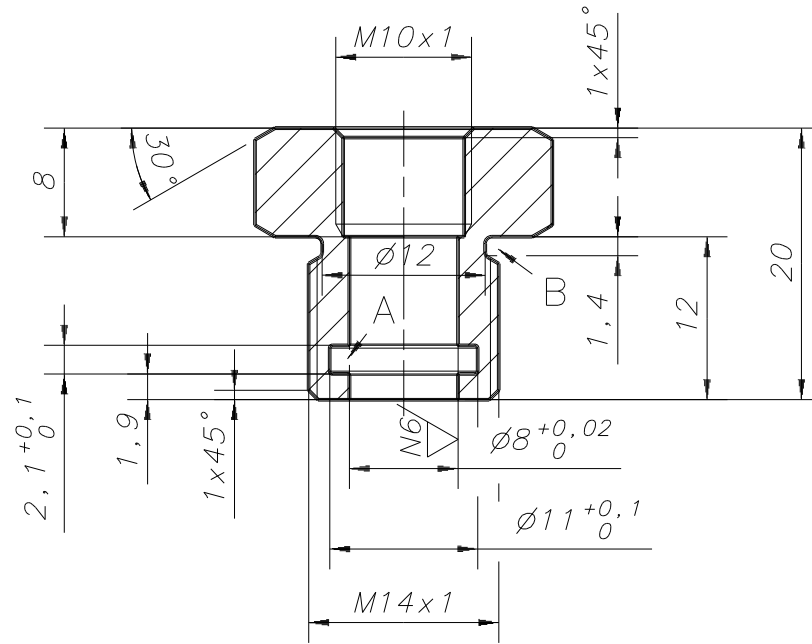
Face dressée avec l'outil spécial KISTLER 1300A79001 après taraudage M5x0.5

L'usinage des perçages de Ø4.5 pour le taraudage de M5x0.5 et de Ø3 seront effectués simultanément à l'aide de l'outil spécial KISTLER type 1300A53. Le taraudage de M5x0.5 sera effectué à l'aide de l'outil spécial KISTLER 1357A.

NS (N6, N4)

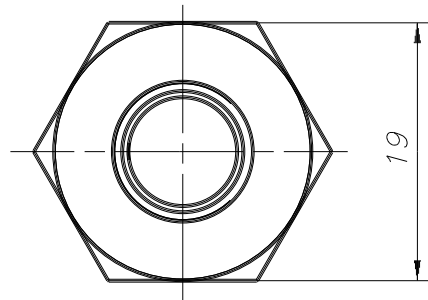
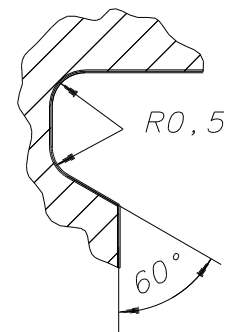
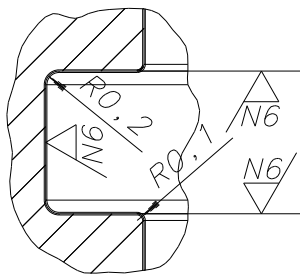
Pos.	Quantité	Unité	Matériau	Dénomination/caractéristiques	Échelle
			Ac inox décolt.		2:1
Mod.				Röthlisberger	21.9.99
Dessiné				Contrôlé	
Mod.				Contr. aux normes	
Sans nomenclature séparée				Bon pour exécution	
Nomencl. sep. de même N°				N° de commande	
Nomencl. sep. de N° d'ilérent				Origine	
N° d'ilérent				Remplace	Nb. feuilles
Dénomination				N° de dessin	
Adaptateur pour capteur de pression KISTLER 6053				MCP-3.1	





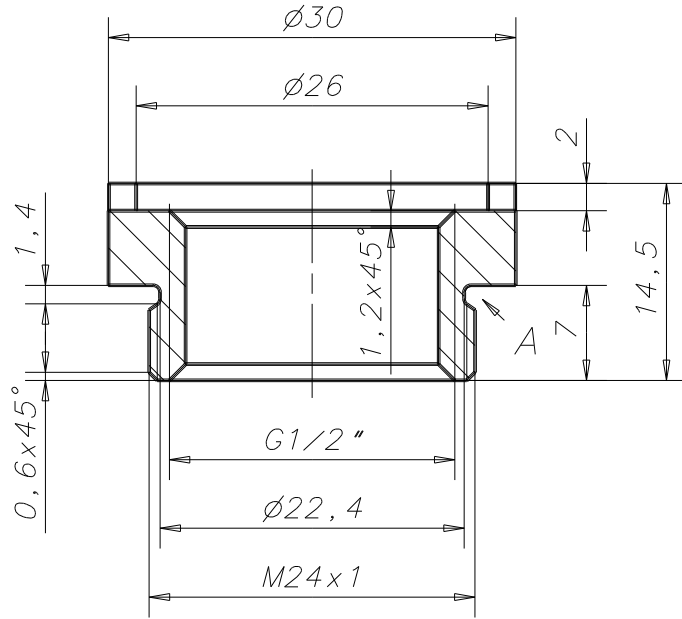
Détail A (10:1)

Détail B (10:1)

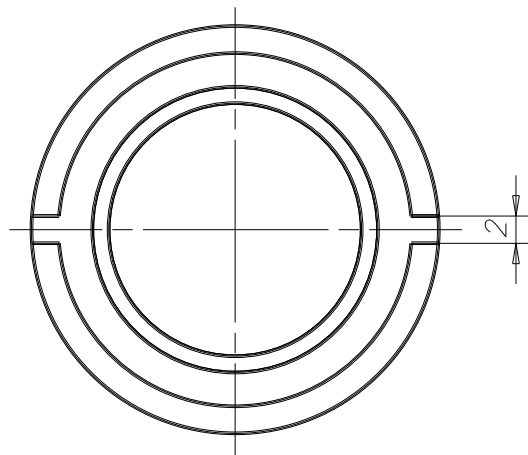
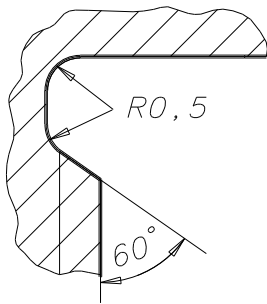


N8/ (N6/)

		Ac inox décolt.					
Pos.	Quantité	Unité	Matière	Dénomination/caractéristiques			
Mod.			Mod.	Dessiné	Röthlisberger	21.9.99	Echelle 2:1
				Contrôlé			
				Conf. aux normes			
Sans nomenclature séparée				Bon pour exécution			
Nomencl. sep. de même N°				N° de commande		Nb. feuilles	
Nomencl. sep. de N° différent			N° d'ident.	Remplace			
			Dénomination	Guide adaptateur pour capteur KISTLER 6053		N° de dessin MCP-3.2	



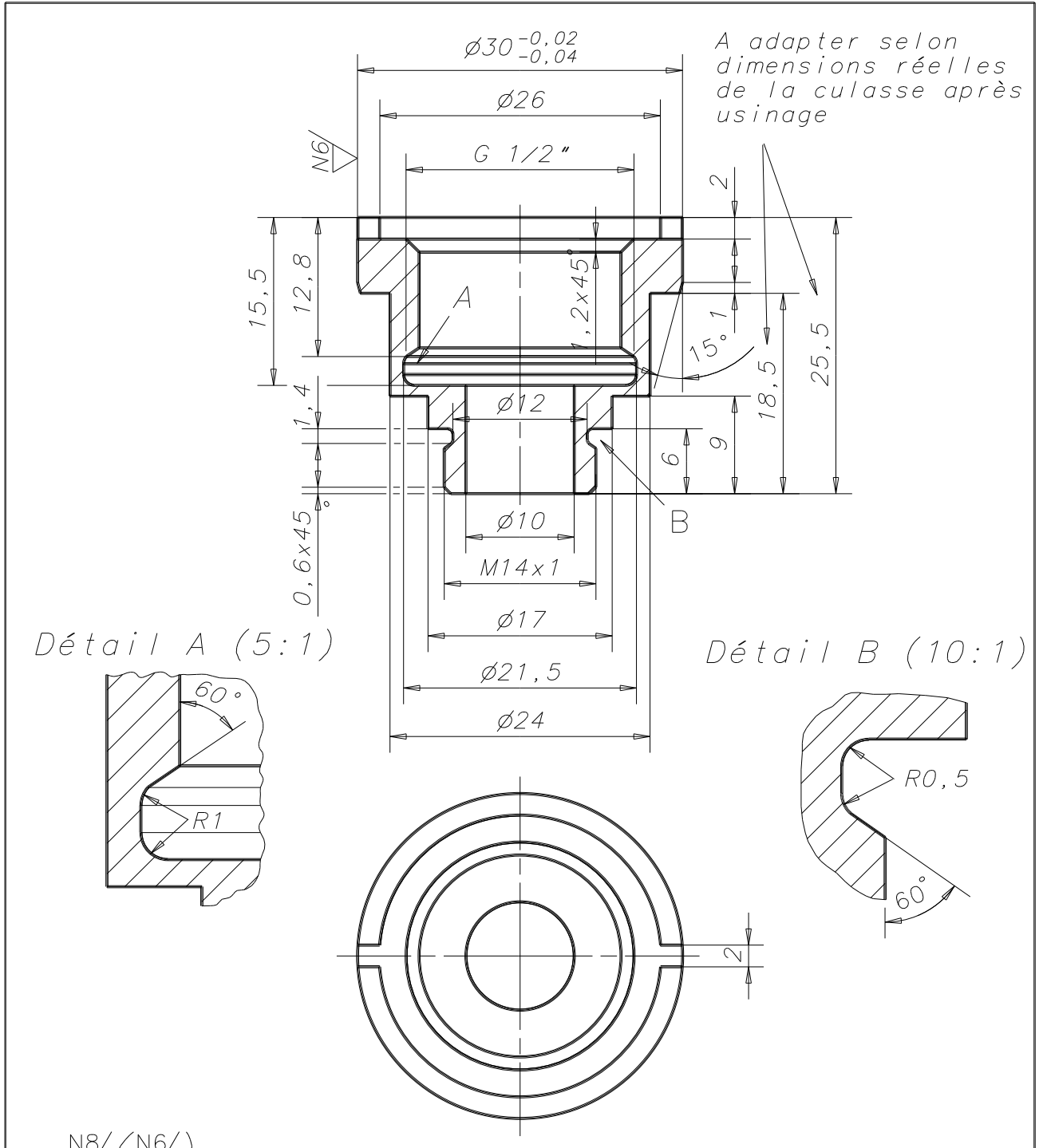
Détail A (10:1)



N8/

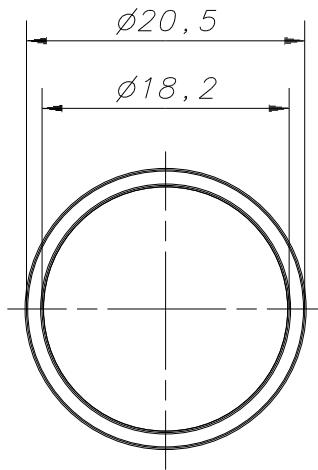
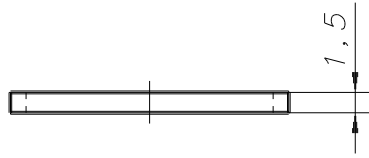
		Ac Inox décolt.					
Pos.	Quantité	Unité	Matière	Dénomination/caractéristiques			
Mod.			Mod.	Dessiné	Röthlisberger	21.9.99	Echelle
				Contrôlé			2:1
				Conf. aux normes			
				Bon pour exécution			
Sans nomenclature séparée				N° de commande			
Nomencl. sép. de même N°				Origine		Nb. feuilles	Feuille N°
Nomencl. sép. de N° différent			N° d'ident.	Remplace			
				Dénomination		N° de dessin	
				Support d'adaptateur refroidi pour capteur Kistler 4045 sur canal d'admission		MCP-4.1	





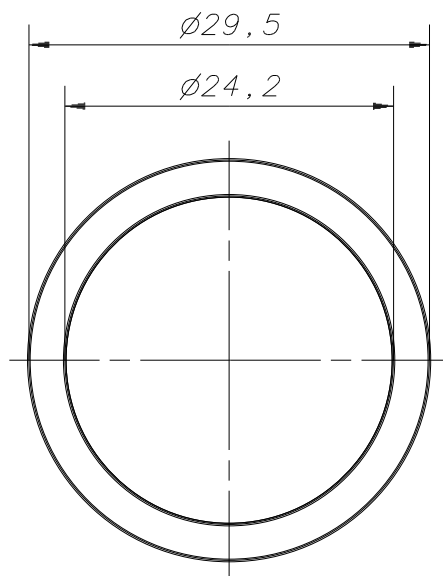
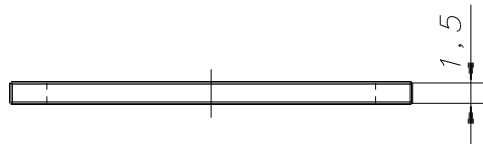
N8/ (N6/)

		Ac inox décollt.					
Pos.	Quantité	Unité	Matière	Dénomination/caractéristiques			
Mod.			Mod.	Dessiné	Röthlisberger	21.9.99	Echelle 2:1
				Contrôlé			
				Conf. aux normes			
				Bon pour exécution			
Sans nomenclature séparée				N° de commande			
Nomencl. sep. de même N°				Origine		Nb. feuilles	Feuille N°
Nomencl. sep. de N° différent				N° d'ident.	Remplace		
			Dénomination Support d'adaptateur refroidi pour capteur Kistler 4045 sur canal d'échappement			N° de dessin MCP-5.1	



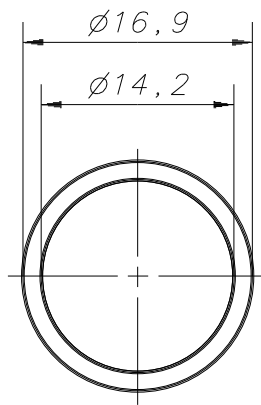
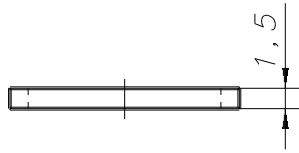
N8/

		<i>Cuivre recuit</i>					
Pos.	Quantité	Unité	Matière	Dénomination/caractéristiques			
Mod.			Mod.	Dessiné	<i>Röthlisberger</i>	<i>1.7.99</i>	Echelle <i>2:1</i>
				Contrôlé			
					Conf. aux normes		
Sans nomenclature séparée				N° de commande			
Nomencl. sép. de même N°				Origine		Nb. feuilles	Feuille N°
Nomencl. sép. de N° différent			N° d'ident.	Remplace			
			Dénomination <i>Joint adaptateur pour montage capteur de pression Kistler 7061B</i>			N° de dessin <i>MCP-2.2</i>	



N8/

		<i>Cuivre recuit</i>					
Pos.	Quantité	Unité	Matière	Dénomination/caractéristiques			
Mod.			Mod.	Dessiné	<i>Röthlisberger</i>	<i>21.9.99</i>	Echelle <i>2:1</i>
				Contrôlé			
				Conform. aux normes			
				Bon pour exécution			
Sans nomenclature séparée				N° de commande		Nb. feuilles	Feuille N°
Nomencl. sép. de même N°				Origine			
Nomencl. sép. de N° différent			N° d'ident.	Remplace			
			Dénomination <i>Joint support d'adaptateur refroidi pour capteur Kistler 4045 sur canal d'admission</i>			N° de dessin <i>MCP-4.2</i>	



N8/

		<i>Cuivre recuit</i>						
Pos.	Quantité	Unité	Matière	Dénomination/caractéristiques				
Mod.			Mod.	Dessiné	<i>Röthlisberger</i>	<i>21.9.99</i>	Echelle <i>2:1</i>	
				Contrôlé				
				Conf. aux normes				
Sans nomenclature séparée				Bon pour exécution				
Nomcl. sép. de même N°				N° de commande		Nb. feuilles		Feuille N°
Nomcl. sép. de N° différent			N° d'ident.	Origine				
			Dénomination <i>Joint support d'adaptateur refroidi pour capteur Kistler 4045 sur canal d'échappement</i>			N° de dessin <i>MCP-5.2</i>		

# Appendix B

## Numerical simulation

### B.1 Sensitivity analysis

A sensitivity analysis was performed on the mesh resolution, the turbulence model and the initial kinetic energy, as well as on the prechamber initial temperature, in order to evaluate their influence on the numerical solution and define the conditions for the main study. The influence of these parameters was evaluated at three different locations in the prechamber and also partially at three other positions in the main chamber (**figure B.1**). The first location in the prechamber (I) corresponds to the position between the electrodes of a standard ignition spark plug (*Bosch Super F6DC*). Even though the spark plug electrodes are not modelled, the flow characteristics at this particular location give an indication on the conditions that prevail during the ignition process and the early stage of the flame kernel growth. The second position in the prechamber (II) has been chosen at three quarter of the distance separating the ignition point (I) and the nearest lateral wall. This point is located close to the middle of the main prechamber recirculation zone and is consequently a sensitive indicator of changes in the flow pattern. The third point in the prechamber (III) is situated in the middle of the nozzle orifice and gives information on the flow conditions at this particular position. The first point in the main chamber (IV) is located at a distance of 10 times the orifice diameter from the nozzle exit, along its axis. The second (V) and the third (VI) points are respectively positioned on each side of the first point at a distance of 2.5 times the orifice diameter, perpendicularly to the nozzle axis. These three points are situated in the region which provides the mixture that flows into the prechamber during the compression stroke and where the jet issuing from the nozzle develops during the expansion stroke. These points enable the evaluation of the effect of the mesh resolution on the development of the jet along its theoretical axis (IV), on the influence of the flow issuing from the squish region (V) and on the influence of the piston bowl wall (VI).

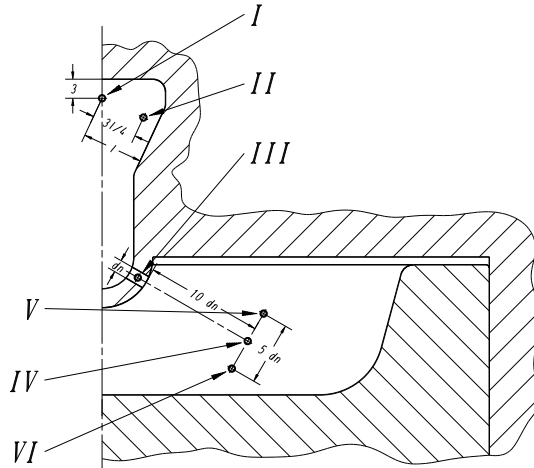


**Figure B.1:** Reference locations in the combustion chamber.

### B.1.1 Mesh resolution

The influence of the main- and prechamber mesh resolution were evaluated. The calculation conditions are those described in section 3.1.3. The starting mesh comprised 2259 cells in the prechamber and 1800 cells in the main chamber. The simulation execution time was 18 CPU hours.

An increase in the number of cells in the main chamber to 6045, while keeping the prechamber mesh unchanged, has a significant effect on the turbulence kinetic energy and the velocity magnitude in the main chamber (**figure B.2**). On the other hand, this has only a very weak influence on the turbulence kinetic energy and velocity magnitude in the nozzle orifice (III) as well as on the velocity magnitude in the prechamber recirculation zone (II) (**figure B.3**). These results show that the nozzle orifice acts as a filter, which obliterates the majority of the large scale flow characteristics of the main chamber. The increase of the main chamber mesh resolution increases the execution time to 34 CPU hours.

From its starting value of 2259, the number of cells in the prechamber was decreased to 1345 and respectively increased to 3844. In the latter case, the main chamber mesh resolution could not be maintained constant because of the diffusion of prechamber grid lines into the main chamber, through the nozzle orifice. Therefore the number of cells in the main chamber increased from 6045 to 6832. The execution time decreased to 19 CPU hours with the reduction to 1345 cells and increased to 73 CPU hours with the increase to 3844 cells. The results of the two most extreme cases are represented in **figure B.4**; the one of the starting case lays in between. The weak effect of the mesh variation indicates that the lowest number of cells already offers an adequate resolution.

In order to obtain a sufficient resolution in the prechamber and in the upper part of the main chamber mesh (fixed part of the mesh) while keeping a reasonable computing time of about 24 CPU hours, the final mesh comprises 1499 cells in the prechamber and

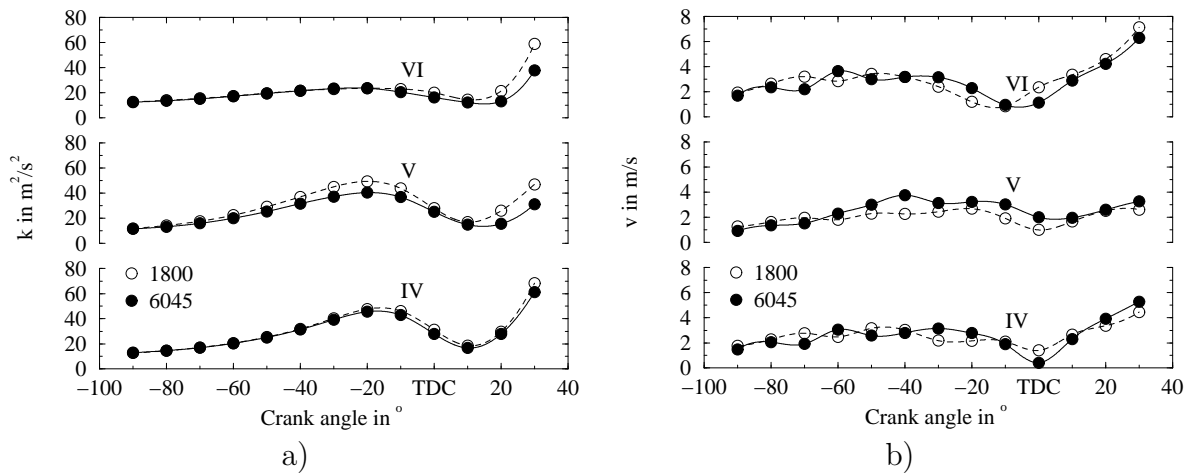


**Figure B.2:** Influence of the main chamber mesh resolution on the main chamber flow, prechamber mesh 2259 cells: a) turbulence kinetic energy, b) velocity magnitude.

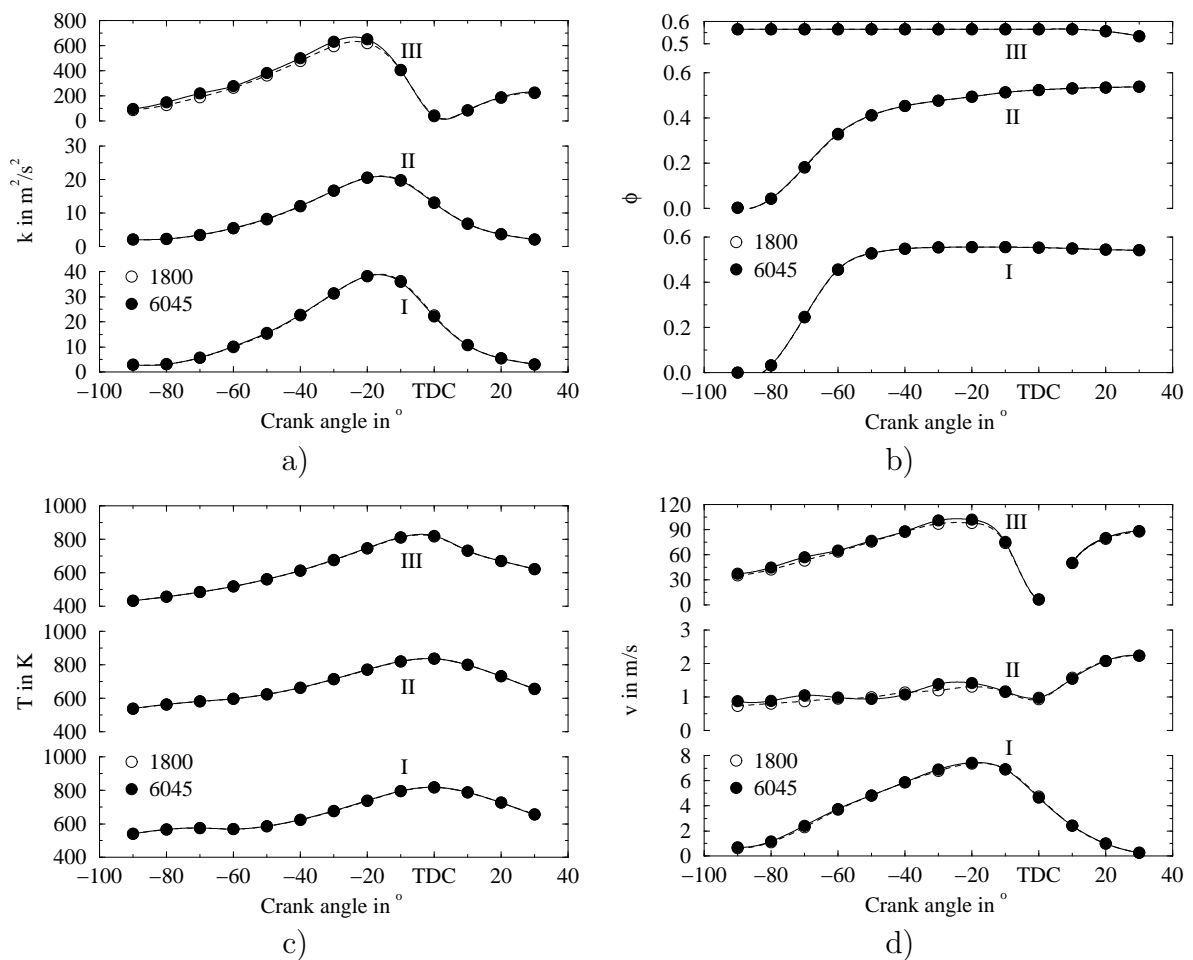


**Figure B.3:** Influence of the main chamber mesh resolution on the prechamber flow: a) turbulence kinetic energy, b) fuel to air equivalence ratio, c) temperature, d) velocity magnitude.

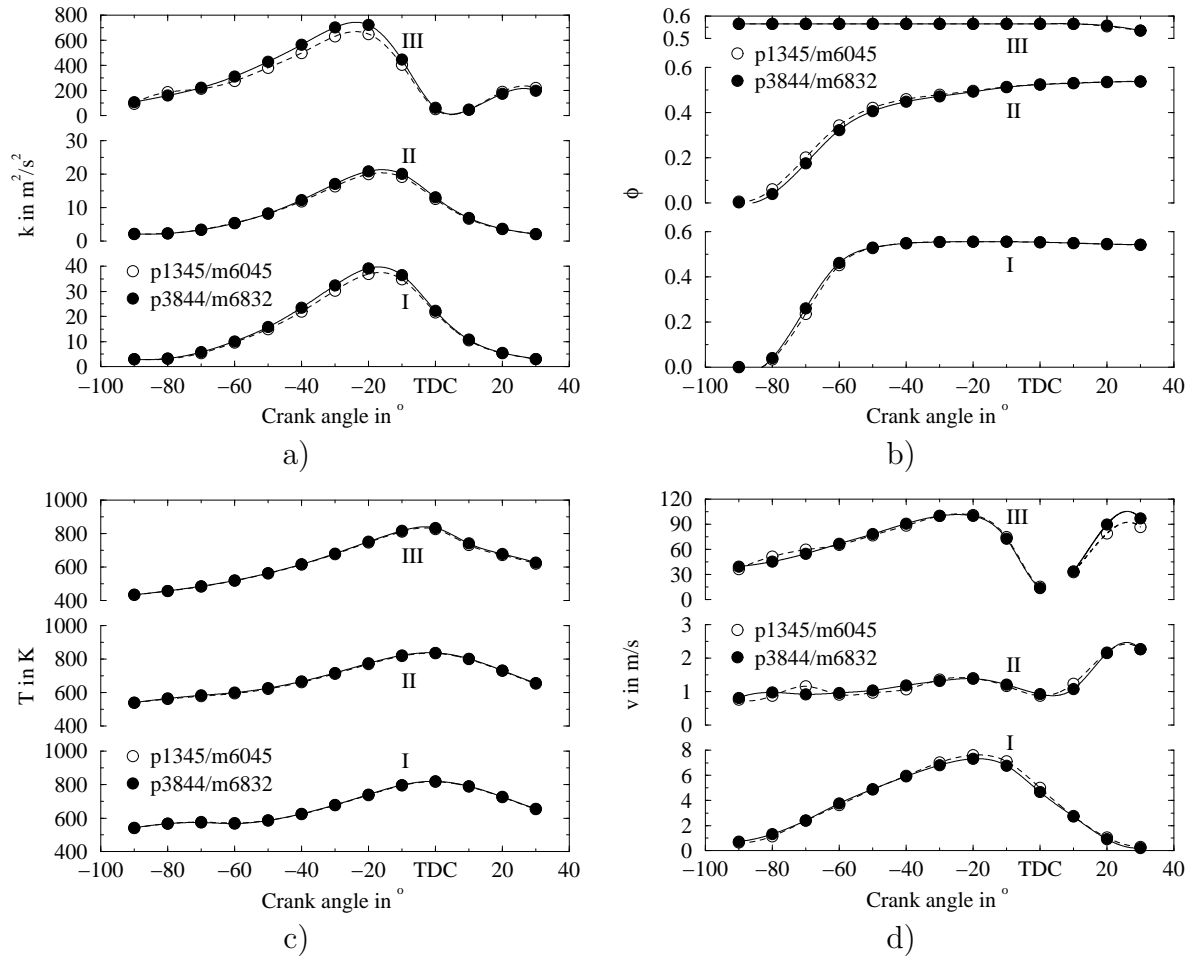


**Figure B.4:** Influence of the prechamber mesh resolution on the prechamber flow: a) turbulence kinetic energy, b) fuel to air equivalence ratio, c) temperature, d) velocity magnitude.

7215 cells in the main chamber (2574 cells forming the fixed part), making up a total of 8714 cells. The constant and relatively high resolution of the fixed part of the main chamber mesh (**figure 3.3**) allows the evaluation of the influence of the prechamber on the piston bowl flow motion prior to ignition.

### B.1.2 Turbulence model and initial turbulence intensity

On the basis of a mesh comprising 2259 cells in the prechamber and 1800 cells in the main chamber, the standard and the renormalised group (RNG) theory  $k-\epsilon$  models were alternatively used and the results compared. The RNG  $k-\epsilon$  model corresponds to the standard  $k-\epsilon$  model with the addition of a new term which accounts for the ratio of the turbulent to the mean-strain time scale. The standard  $k-\epsilon$  constants are also slightly modified. The influence of the turbulence model at the reference locations (**figure B.1**) are presented in **figure B.5** for the main chamber and in **figure B.6** for the prechamber. These results show a moderate effect on the main chamber numerical solution. On the other hand, the numerical solution of the prechamber is more significantly affected by the turbulence model used. In absence of experimental data to



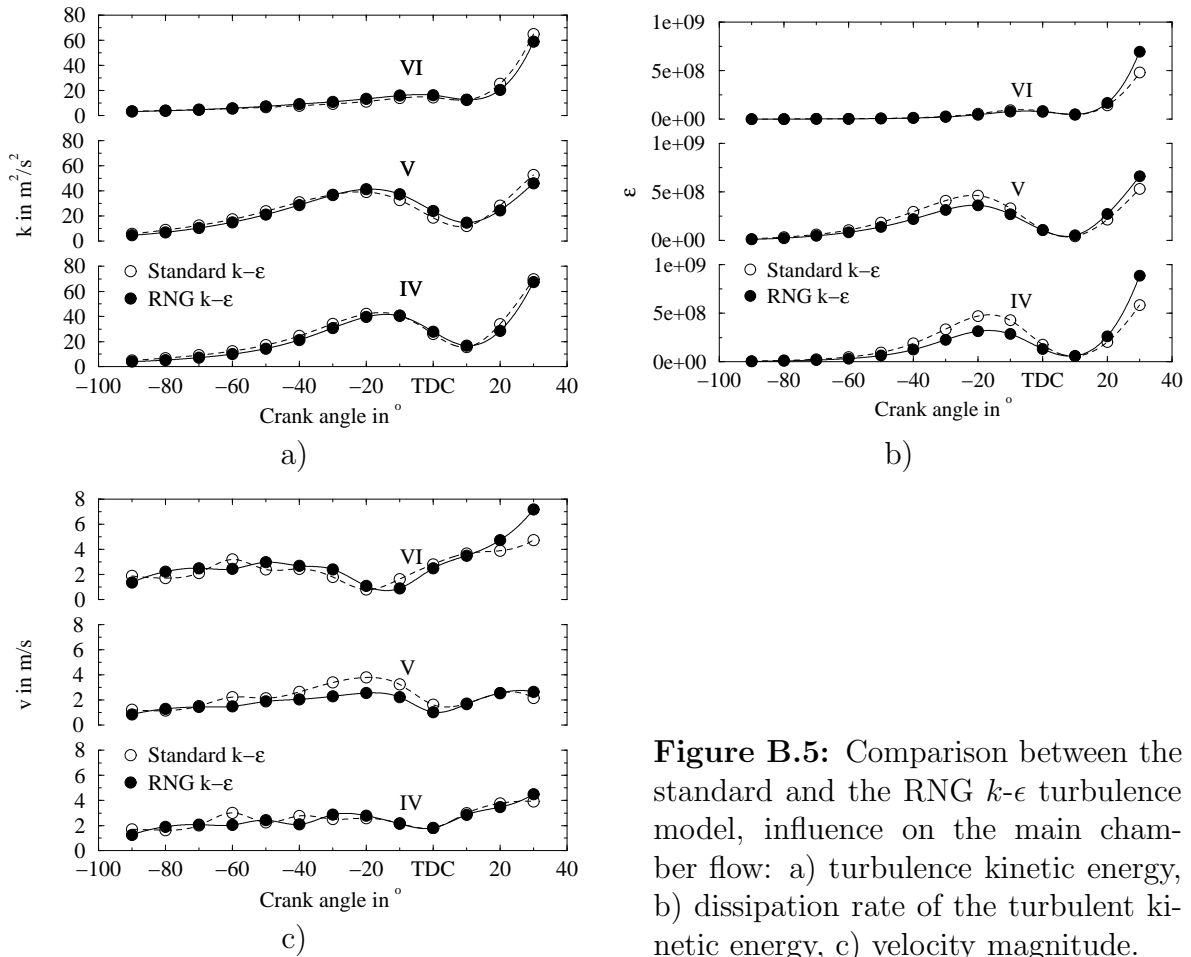


**Figure B.5:** Comparison between the standard and the RNG  $k-\epsilon$  turbulence model, influence on the main chamber flow: a) turbulence kinetic energy, b) dissipation rate of the turbulent kinetic energy, c) velocity magnitude.

compare with and thus validate either models, the RNG  $k-\epsilon$  model was selected because of its better ability to predict large flow structures which are affected by the squish and fuel spray [64]. This model is expected to simulate more accurately the influence of the gas jets generated by the nozzle orifices, in the prechamber during compression and in the main chamber during expansion, which has an entrainment effect on the large scale flow similar to a fuel spray.

The initial level of turbulence intensity must be evaluated and represents typically a fraction of the kinetic energy based on the mean piston speed that is turbulence kinetic energy. The turbulence intensity after inlet valve closure depends on the characteristics of the flow through the intake port and valve, and is therefore engine specific. The influence on the numerical solution of two different initial levels of turbulence intensity, 10 % and 50 % of the value based on the mean piston speed (7.1  $m/s$  at 1500  $rpm$ ), were evaluated. The comparison of the results show a significant effect on the main chamber flow (**figure B.7**) and a very weak effect on the prechamber flow (**figure B.8**), at the beginning of the compression stroke. The low sensitivity of the prechamber flow originates in the rapid generation of a large scale fluid motion, which obliterates the initial uniform small scale flow characteristics. The same phenomenon can be noticed in the main chamber first when the flow generated by the squish starts to form while the piston approaches TDC and also after TDC when the jet issuing from the nozzle orifice emerges and develops in the piston bowl. Despite the relative insensitivity of the prechamber numerical solution to the initial turbulence intensity, the choice of an adequate value is required to enable an objective comparison of the prechamber

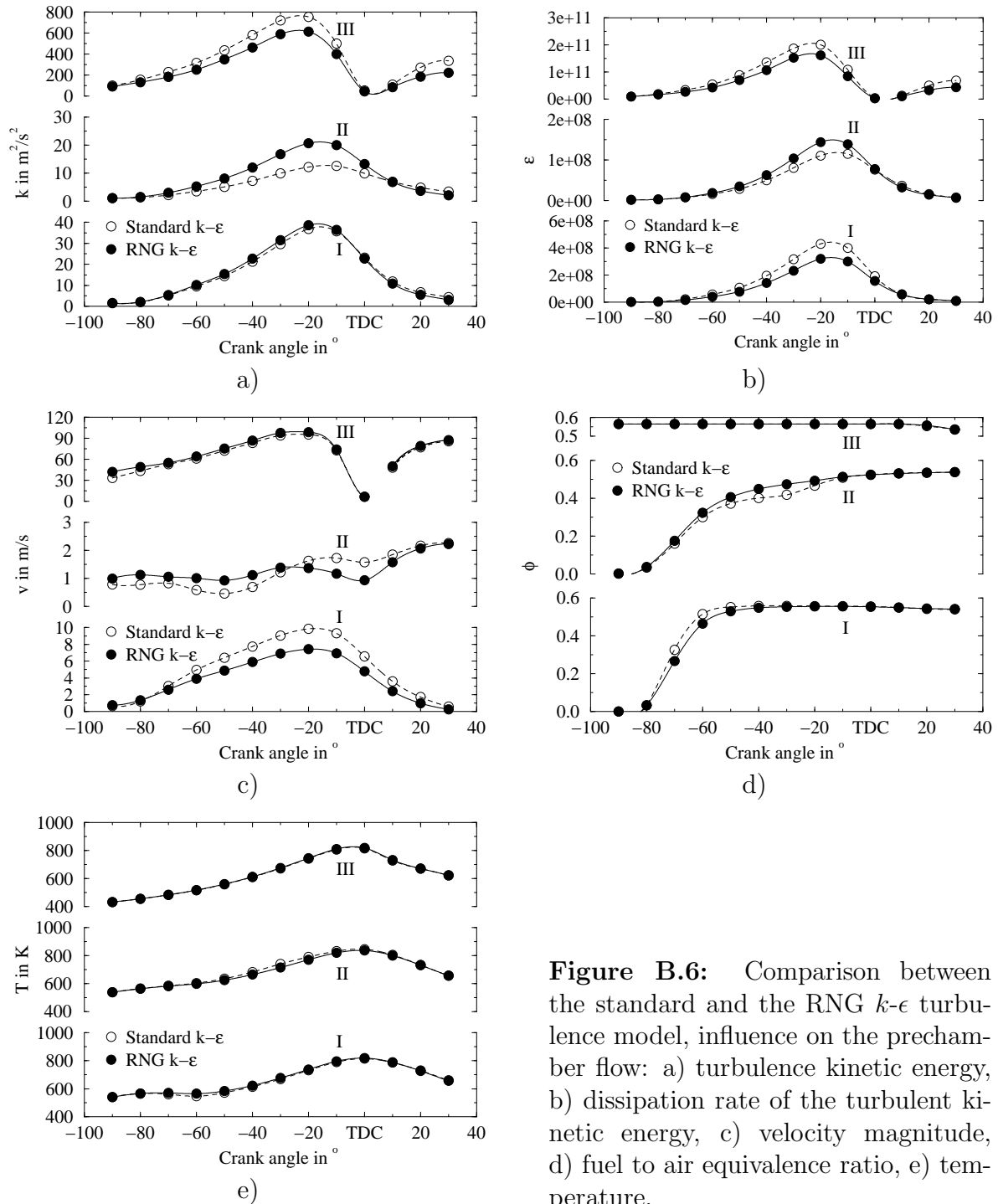


**Figure B.6:** Comparison between the standard and the RNG  $k-\epsilon$  turbulence model, influence on the prechamber flow: a) turbulence kinetic energy, b) dissipation rate of the turbulent kinetic energy, c) velocity magnitude, d) fuel to air equivalence ratio, e) temperature.

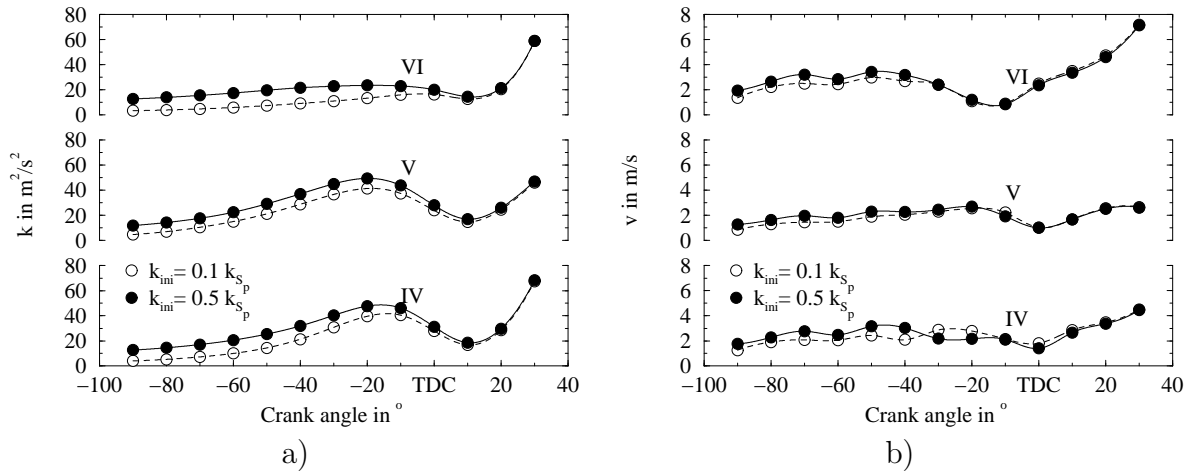


Figure B.7: Influence of the initial turbulence kinetic energy on the main chamber flow: a) turbulence kinetic energy, b) velocity magnitude.

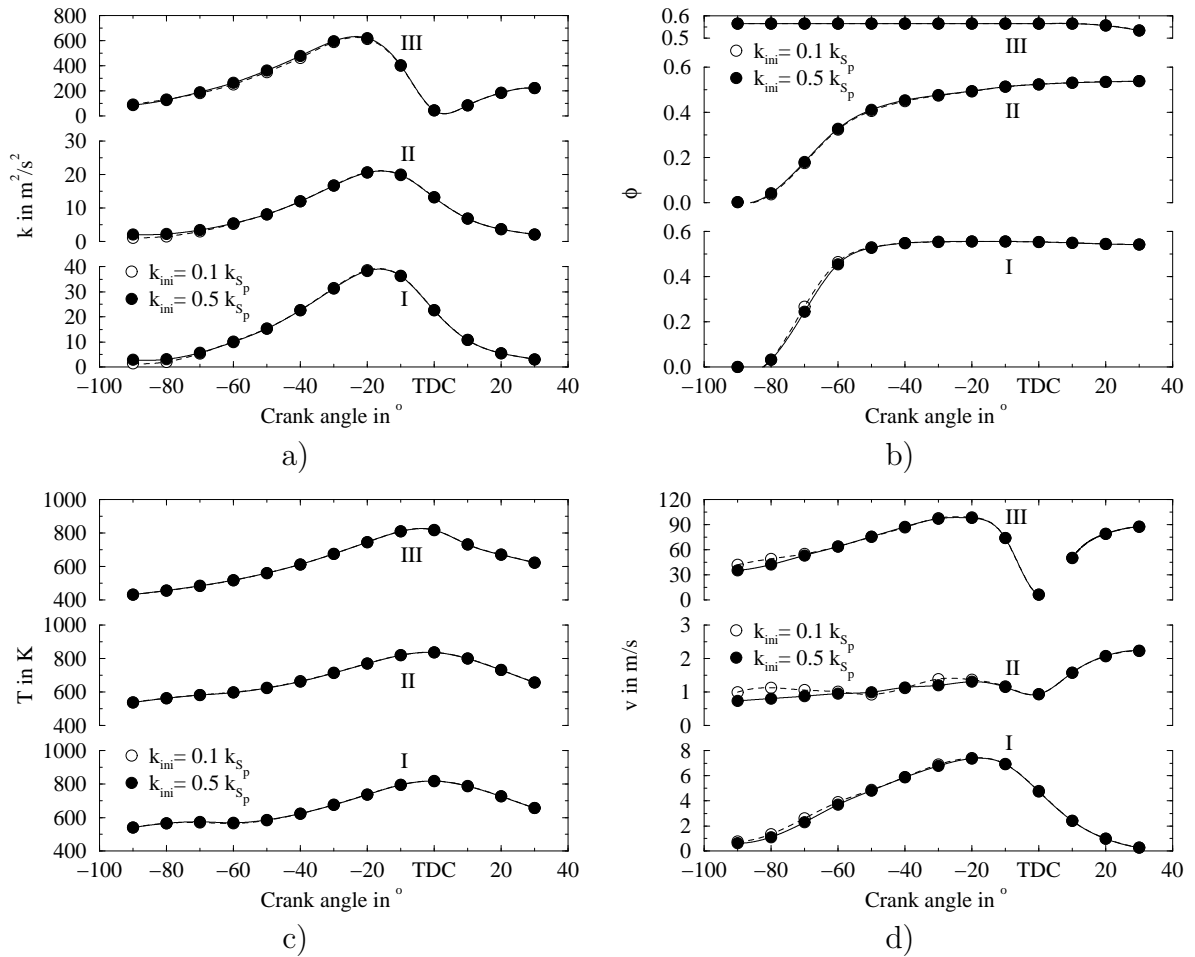
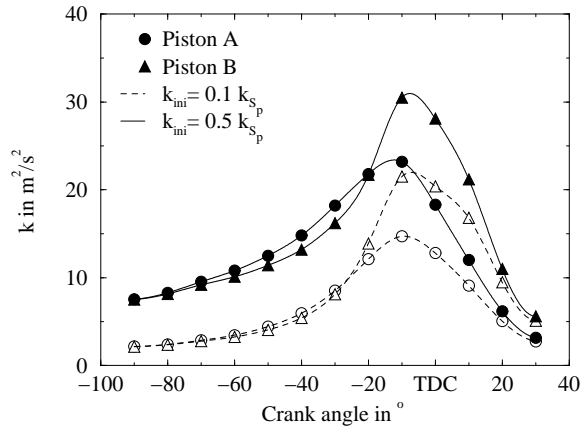


Figure B.8: Influence of the initial turbulence kinetic energy on the prechamber flow: a) turbulence kinetic energy, b) fuel to air equivalence ratio, c) temperature, d) velocity magnitude.



**Figure B.9:** Influence of the initial turbulence kinetic energy on the internal flow of the engine equipped with two different pistons.

ignition conditions with the one characterising the engine with conventional direct spark ignition. For this purpose, the flow in the conventional engine (without prechamber) equipped with the original piston with bathtub bowl (*A*) (**figure 2.3**) and alternatively with a high turbulence generating piston with re-entrant bowl (*B*) (**figure 4.3, a**) was simulated with the two different levels of initial turbulence intensity. The mesh density was kept similar to the prechamber case and all the other initial conditions were held constant. The corresponding turbulence kinetic energy at the point located between the spark plug electrodes is represented in **figure B.9**. Comparison with a compilation of experimental results from different engine flow configurations and combustion chamber geometry [13, Figure 8-11] indicates that the high initial turbulence intensity leads to a more realistic prediction of the turbulence kinetic energy at TDC, when considering the high swirl motion generated by the intake port (2.0) (table 2.1) and the intense turbulence produced by the squish. Therefore the initial level of turbulence intensity of 50% of the value based on the mean piston speed was considered throughout the numerical study.

### B.1.3 Initial prechamber temperature

The temperature of the residual combustion gas located in the prechamber after inlet valve closure depends principally on the prechamber cooling characteristics. This temperature determines the amount of combustion products trapped in the prechamber at the beginning of the compression stroke. In the absence of experimental data, the estimation of this temperature is very difficult. This temperature was first estimated to be 100 *K* above the main chamber initial value and the simulation performed with a mesh formed by 1345 cells in the prechamber and 6045 cells in the main chamber. This temperature difference was then increased to 200 *K* and the results were compared. The magnitude of the temperature difference has a significant influence on the local values of the prechamber temperature and fuel to air equivalence ratio, as well as a perceptible effect on the flow velocity (**figure B.10**). Nevertheless, this influence is essentially limited to the part of the compression stroke prior to ignition, which is expected to occur after 30°*CA*<sub>BTDC</sub>. The decrease of the influence of the initial temperature difference during the compression stroke is due to the progressive replacement of residual combustion gas by fresh mixture flowing from the main cham-

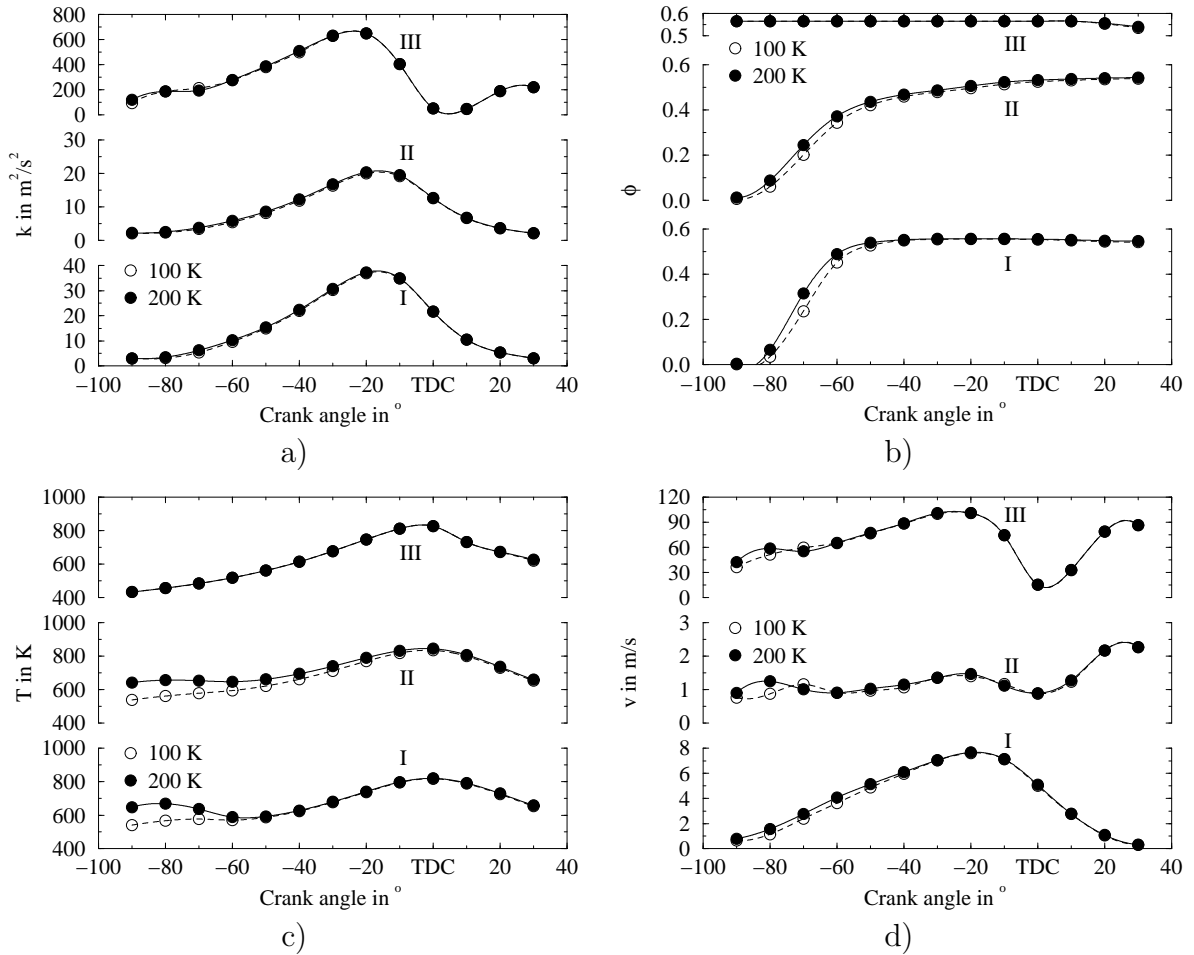


**Figure B.10:** Influence of the initial temperature in the prechamber: a) turbulence kinetic energy, b) fuel to air equivalence ratio, c) temperature, d) velocity magnitude.

ber (ex: points I and III) or by strong dilution (ex: point II). The rapid and almost complete obliteration of the prechamber initial conditions originates in the high volumetric compression ratio ( $\epsilon = 12$ ) and in the low relative prechamber volume ( $\approx 3\%$  of the compression volume). The results finally show that the initial prechamber temperature has no major effect on the flow conditions during ignition and the early stage of flame kernel development. In consequence, a temperature difference of 100 K was considered throughout the numerical simulation.

## B.2 *KIVA-3V* input file (itape5)

Case028, 3.5.00, Roethlisberger, pre017, mesh 60 deg

```
  irest      0
  nohydro    0
  lwall      1
  lpr        0
  irez       2
ncfilm 999999
  nctap8     500
nclast 999999
ncmon 999999
ncaspec 13
  -90.0, -80.0, -70.0, -60.0, -50.0, -40.0, -30.0, -20.0, -10, 0.0, 10.0,
  20.0, 30.0
  gmv        0.0
  cafilm     9.99e+9
  cafin      30.0
  angmom     0.0
  pgssw      1.0
  dti        1.0e-8
  dtmxca     9.99e+9
  dtmax      2.0e-7
  tlimd      1.0
  twfilm     9.99e+9
  twfin      9.99e+9
  fchsp      0.25
  bore       12.2
  stroke     14.2
  squish     0.123
  rpm        1.5e+3
  atdc       -130.0
  datdct     0.0
  revrep     2.0
  conrod     22.8
  swirl      0.0
  swipro     3.11
  thsect     60.0
  sector     1.0
  epsy       1.0e-3
  epsv       1.0e-3
  epsp       1.0e-4
  epst       1.0e-3
  epsk       1.0e-3
  epse       1.0e-3
  gx         0.0
  gy         0.0
```

gz	0.0
tcylwl	453.0
thead	453.0
tpistn	523.0
pardon	0.0
a0	0.0
b0	1.0
artvis	0.0
ecnsrv	0.0
adia	0.0
anu0	0.0
visrat	-.66666667
tcut	800.0
tcute	1200.0
epschm	0.02
omgchm	1.0
turbsw	2.0
sgsl	0.0
trbchem	0.0
capa	18.0
pmplict	0.0
lospeed	0.0
airmu1	1.457e-5
airmu2	110.0
airla1	252.0
airla2	200.0
prl	0.74
rpr	1.11
rsc	1.11
xignit	0.0
tlign	-1.0
tdign	-1.0
calign	-27.0
cadign	9.6
xignl1	0.25
xignr1	0.75
yignf1	0.0
yignd1	0.238
zignb1	11.75
zignt1	12.50
xignl2	0.0
xignr2	0.0
yignf2	0.0
yignd2	0.0
zignb2	0.0
zignt2	0.0
kwikeq	0
numnoz	1

```

numvel      1
injdistrib  1
kolide      0
tlinj      -1.0
tdinj      -1.0
calinj     210.0
cadinj     12.672
tspmas     0.0
pulse      1.0
tnparc    400.0
tpi       350.0
turb       1.0
breakup    0.0
evapp      0.0
drnoz     0.0
dznoz    13.021934
dthnoz     0.0
tiltxy     0.0
tiltxz     0.0
cone       62.5
dcone     12.5
anoz       1.0
smr       5.00e-4
amp0       0.0
           0.0
nsp        5
  ch4
  o2      mw2  31.9988  htf2  0.0000
  n2      mw3  28.0134  htf3  0.0000
  co2     mw4  44.0100  htf4 -93.9653
  h2o     mw5  18.0153  htf5 -57.1035
stoifuel   1.0
stoio2     2.0
nreg       2
'presi',   0.263374E+07  0.263374E+07
'tempi',  377.7          477.7
'tkei',    0.50          0.50
'scli',    0.0           0.0
'er',      0.564972     0.0
'mfracfu', 0.028678       0.000000
'mfraco2', 0.212276       0.097876
'mfracn2', 0.743149       0.743149
'mfracco2', 0.008741       0.087412
'mfracch2o', 0.007156     0.071564
nrk        0
nre        0
nvalves    0
isoot      0

```



# Appendix C

## Experimentation

### C.1 Testing facilities

The realisation of the gas engine project required the construction of a new test bed especially developed for the study of this type of engine. The test bed is equipped with a direct natural gas supply from the network as well as from an intermediate storage tank at high pressure (200 *bar*). The storage tank is used to keep the natural gas composition constant over several series of experiments. The testing facilities consist of a test bed equipped with a dynamometer, several conditioning systems for the engine and dynamometer fluids, a control system as well as measurement instrumentation and two data acquisition systems. The testing facilities have already been described thoroughly in the report of the previous study [3]. However, the main features of the testing facilities and particularly the measurement instrumentation are presented here for completeness.

#### C.1.1 Test bed

The test bed consists of a steel tubular frame in two parts mounted on vibration dampers (**figure 4.1**). The first part supports an eddy-current dynamometer Vibro-Meter type 3 WB 25 [65], which generates a torque to brake the engine and dissipates the mechanical work into heat. The torque is measured with a strain gauge transducer and the rotational speed is determined with an inductive transducer and a toothed wheel. The dynamometer can operate between 10 and 10 000 *rpm* and the maximum brake torque is 1472 *Nm* at 1750 *rpm*, which corresponds to a rated power of 270 *kW*. More details on the dynamometer characteristics and on its control unit are given in [3]. In order to enable the test of engines of different sizes and configurations, the second part of the frame has a modular design based on mobile traverses and screw-jacks. The vibration isolation between engine and frame is realised with dampers mounted on the top of the screw-jacks. Further, T-grooves on the frame and on the traverses enable the mounting of complementary devices. The transmission between engine and dynamometer is realised with a cardan shaft and a flexible coupling.

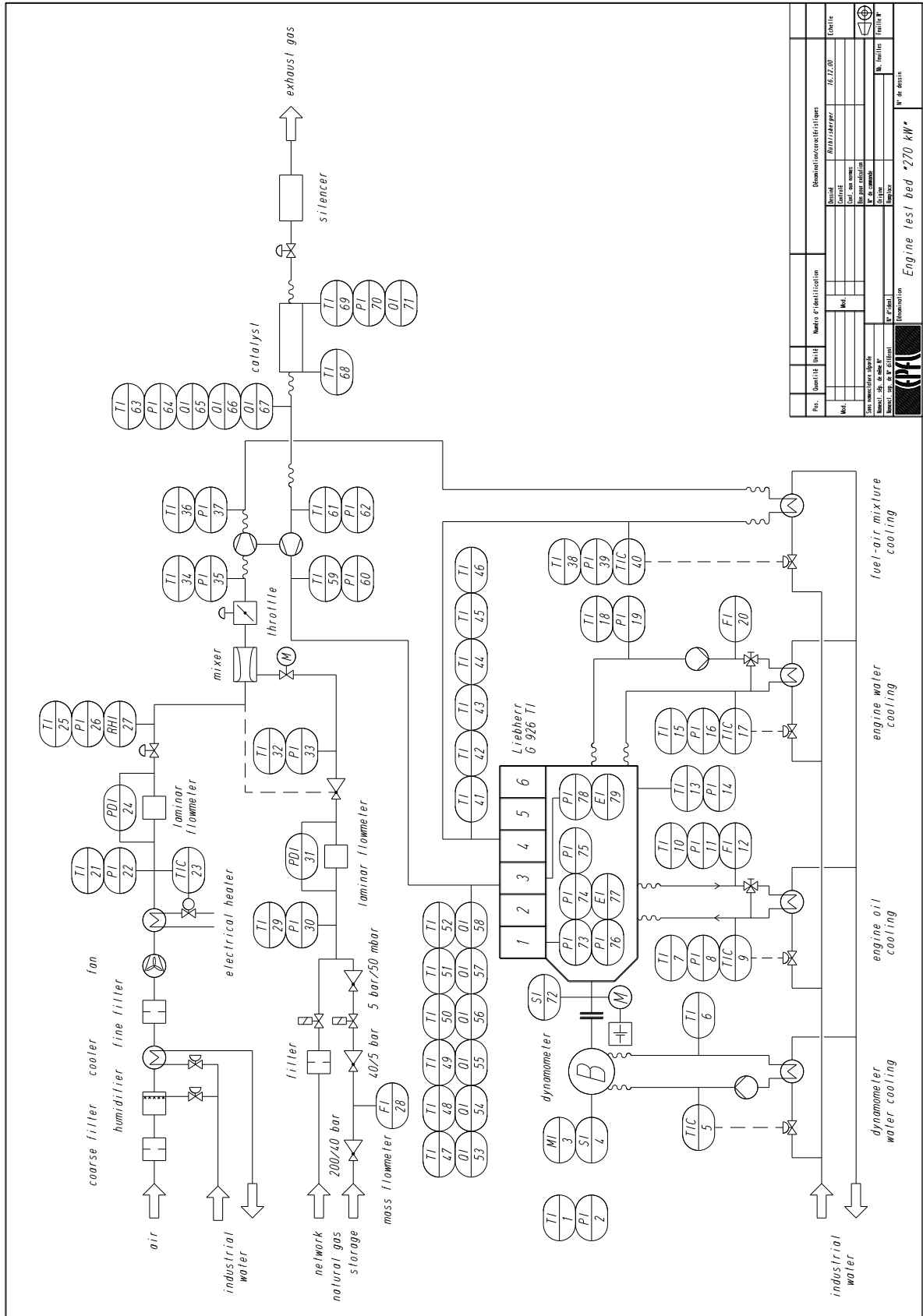


Figure C.1: Diagram of the testing facilities with the location of the measurement instrumentation.

## C.1.2 Measurement instrumentation and acquisition systems

The testing facilities with the measurement instrumentation is represented in **figure C.1**. The variables measured, the type of transducers used, the measurement ranges and the relative errors are given for each measurement location in **table C.1**. The description of the exhaust gas analysers is given in **table C.2**.

Two different data acquisition systems are used to collect the measurements. A low speed acquisition system records the steady state variables which are not significantly varying during an engine cycle, such as the engine torque, the engine water temperature and the fuel mass flow rate. In parallel, a high speed data acquisition system is used for cylinder pressure indication and spark timing measurement.

### Low speed data acquisition system

The low speed data acquisition system records all temperatures, all pressures except the ones indicated, air relative humidity, engine torque, crankshaft rotational speed, natural gas and engine cooling water mass flow rates, engine lubricating oil volume flow rate, relative air to fuel ratio and exhaust gas composition. A diagram of this acquisition system is shown in **figure C.2**. It is based on a data acquisition system *Hewlett Packard* type *3852A* [66], equipped with a voltmeter *HP 44701A*, two modules *HP 44708A* with 20 channels for measurement with thermocouples and two modules *HP 44705A* with 20 channels for the measurement of voltage signals. The recorded values are transferred to a computer *Macintosh* type *PowerPC 7100/66AV* through a *GPIB* connection and are processed with the program *Labview* [67]. The *GPIB* connection is made with a *National Instruments NB-GPIB/TNT* card.

The piezoresistive transducers for absolute and differential pressure measurements *Haenni* deliver a current signal. The transfer to the module *HP 44705A* requires a preliminary conversion into voltage, which is realised with precision resistances in a current-voltage converter. The description of this converter is given in [3]. The steady state pressure transducers and the thermocouple connections are installed in a box supported by an articulated arm over the test bed. In order to keep constant transducer temperature for accuracy, the box is ventilated with air at about 20 °C.

The thermocouples measuring temperatures below 150 °C are calibrated. The calibration was performed between 10 and 150 °C, every 10 °C, using a quartz thermometer *Hewlett Packard* type *2804A* [66] as a reference. The calibration curves were approximated by numerical regressions, which were then introduced into *Labview*. For convenience, all the thermocouples were calibrated together on the same temperature range. The relative error corresponds to the difference between the reference value and the measured value after correction with the regression. Because it is significantly larger on the lowest side of the temperature range, the value given in **table C.1** for each thermocouple corresponds to the part of the range effectively used during experimentation. The relatively large error on the exhaust gas temperature measurements results from the technique used. Due to the great temperature difference between the exhaust gas stream and the exhaust piping, heat radiates from the thermocouple located in

**Table C.1:** Main specifications of the measurement instrumentation

No	Variable	Transducer			Range	Error <sup>1</sup> ±%
		Principle	Producer	Type		
1	ambient temperature	tc	Phillips	2AB25DIN	10-150 °C	0.4
2	atmospheric pressure	piezoresistive	Haenni	ED510/454.211/025	0.93-1.01 bar	0.05
3	engine torque	strain gauges	Vibrometer	3 WB 25	0-1300 Nm	0.2
4	engine rotational speed	inductive	Jaquet	DFE 410	60-10000 rpm	0.3 <sup>2</sup>
5	dynamom. regulation temp.	tc	Phillips	2AB25DIN	*	*
6	dynamometer outlet temp.	tc	Phillips	2AB25DIN	10-150 °C	1
7	oil inlet temperature	tc	Phillips	2AB25DIN	10-150 °C	0.2
8	oil inlet absolute pressure	piezoresistive	Haenni	ED510/454.211/065	1.0-6.8 bar	2
9	oil regulation temperature	tc	Phillips	2AB25DIN	*	*
10	oil outlet temperature	tc	Phillips	2AB25DIN	10-150 °C	0.2
11	oil outlet absolute pressure	piezoresistive	Haenni	ED510/454.211/065	1.0-6.8 bar	2
12	oil volume flow rate	volumetric	Trimec	MP50S	0.2-5.6 l/s	0.5 <sup>2</sup>
13	sump oil temperature	tc	Phillips	2AB25DIN	10-150 °C	0.2
14	sump absolute pressure	piezoresistive	Haenni	ED510/454.211/055	0.93-1.07 bar	0.05
15	water inlet temperature	tc	Phillips	2AB25DIN	10-150 °C	0.2
16	water inlet absolute pressure	piezoresistive	Haenni	ED510/454.211/055	1.0-3.5 bar	0.8
17	water regulation temperature	tc	Phillips	2AB25DIN	*	*
18	water outlet temperature	tc	Phillips	2AB25DIN	10-150 °C	0.2
19	water outlet abs. pressure	piezoresistive	Haenni	ED510/454.211/055	1.0-3.5 bar	0.8
20	water mass flow rate	coriolis	ABB	K-Flow K500	2-3 kg/s	0.2 <sup>2</sup>
21	air flow-meter inlet temp.	tc	Phillips	2AB25DIN	10-150 °C	0.4
22	air flow-meter inlet abs. pres.	piezoresistive	Haenni	ED510/454.211/035	0.93-1.05 bar	0.05
23	air regulation temperature	*	Johnson	TS-9100-8213	*	*
24	air flow-meter diff. pressure	piezoresistive	Haenni	ED572/522.281/A36	0-20 mbar	0.1
25	air temperature before mixer	tc	Phillips	2AB25DIN	10-150 °C	0.4
26	air abs. pres. before mixer	piezoresistive	Haenni	ED510/454.211/035	0.93-1.05 bar	0.05
27	air humidity before mixer	capacitive	Rotronic	I1000/HygromerC94	0-100 %	5 <sup>2</sup>
28	ng mass flow rate	coriolis	ABB	K-Flow K5	4-11·10 <sup>-3</sup> kg/s	0.5 <sup>2</sup>
29	ng flow-meter inlet temp.	tc	Phillips	2AB25DIN	10-150 °C	1
30	ng flow-meter inlet abs. pres.	piezoresistive	Haenni	ED510/454.211/035	0.93-1.05 bar	0.05
31	ng flow-meter diff. pressure	piezoresistive	Haenni	ED572/522.281/A36	0-20 mbar	0.1
32	ng temperature before mixer	tc	Phillips	2AB25DIN	10-150 °C	1
33	ng abs pres. before mixer	piezoresistive	Haenni	ED510/454.211/035	0.93-1.05 bar	0.05
34	compressor inlet temp.	tc	Phillips	2AB25DIN	10-150 °C	0.4
35	compressor inlet abs. pres.	piezoresistive	Haenni	ED510/454.211/055	0.87-1.02 bar	0.05
36	compressor outlet temp.	tc	Phillips	2AB25DIN	10-150 °C	0.2
37	compressor outlet abs. pres.	piezoresistive	Haenni	ED510/454.211/025	1.0-3.5 bar	0.5
38	mixt. temp. b. int. manifold	tc	Phillips	2AB25DIN	10-150 °C	0.2
39	mixt. abs. pres. b. int. man.	piezoresistive	Haenni	ED510/454.211/025	1.0-3.5 bar	0.5
40	mixture regulation temp.	tc	Phillips	2AB25DIN	*	*
41	mixture temp. before cyl. 1	tc	Phillips	2AB25DIN	10-150 °C	†
42	mixture temp. before cyl. 2	tc	Phillips	2AB25DIN	10-150 °C	†
43	mixture temp. before cyl. 3	tc	Phillips	2AB25DIN	10-150 °C	†
44	mixture temp. before cyl. 4	tc	Phillips	2AB25DIN	10-150 °C	†
45	mixture temp. before cyl. 5	tc	Phillips	2AB25DIN	10-150 °C	†
46	mixture temp. before cyl. 6	tc	Phillips	2AB25DIN	10-150 °C	†
47	exhaust temp. after cyl. 1	tc	Phillips	2AB25DIN	10-1000 °C	†
48	exhaust temp. after cyl. 2	tc	Phillips	2AB25DIN	10-1000 °C	†
49	exhaust temp. after cyl. 3	tc	Phillips	2AB25DIN	10-1000 °C	†
50	exhaust temp. after cyl. 4	tc	Phillips	2AB25DIN	10-1000 °C	†
51	exhaust temp. after cyl. 5	tc	Phillips	2AB25DIN	10-1000 °C	†
52	exhaust temp. after cyl. 6	tc	Phillips	2AB25DIN	10-1000 °C	†
53	exhaust comp. after cyl. 1	‡	‡	‡	‡	‡
54	exhaust comp. after cyl. 2	‡	‡	‡	‡	‡
55	exhaust comp. after cyl. 3	‡	‡	‡	‡	‡
56	exhaust comp. after cyl. 4	‡	‡	‡	‡	‡

continued on next page

**Table C.1:** Main specifications of the measurement instrumentation (continued)

No	Variable	Transducer			Range	Error <sup>1</sup> ±%
		Principle	Producer	Type		
57	exhaust comp. after cyl. 5	‡	‡	‡	‡	‡
58	exhaust comp. after cyl. 6	‡	‡	‡	‡	‡
59	turbine inlet temperature	tc	Phillips	2AB25DIN	10-1000 °C	10
60	turbine inlet abs. pressure	piezoresistive	Haenni	ED510/454.211/025	1.0-3.5 bar	0.5
61	turbine outlet temperature	tc	Phillips	2AB25DIN	10-1000 °C	10
62	turbine outlet abs. pressure	piezoresistive	Haenni	ED510/454.211/035	0.97-1.07 bar	0.05
63	exhaust temp. after engine	tc	Phillips	2AB25DIN	10-1000 °C	10
64	exh. abs. pres. after engine	piezoresistive	Haenni	ED510/454.211/035	0.97-1.07 bar	0.05
65	exhaust comp. after engine	‡	‡	‡	‡	‡
66	lambda sensor	galvanic	Horiba	Mexa-110λ	1.5-2.0	0.5
67	lambda sensor	galvanic	Bosch	LSM 11	1-2	§
68	exhaust temp. bef. catalyst	tc	Phillips	2AB25DIN	10-1000 °C	10
69	exhaust temp. after catalyst	tc	Phillips	2AB25DIN	10-1000 °C	10
70	exh. abs. pres. after catalyst	piezoresistive	Haenni	ED510/454.211/035	0.97-1.07 bar	0.05
71	exhaust comp. after catalyst	‡	‡	‡	‡	‡
72	crankshaft angular position	opto-electronic	AVL	364	0-360 °CA	4 <sup>2,3</sup>
73	relative pressure in cyl. 1	piezoelectric	Kistler	7061B	0-250 bar	●
74	rel. pressure in cyl. 1 prech.	piezoelectric	Kistler	6053Csp90	0-250 bar	●
75	int. port abs. pres. in cyl. 1	piezoresistive	Kistler	4045 A5	1-5 bar	0.2
76	exh. port abs. pres. in cyl. 1	piezoresistive	Kistler	4045 A5	1-5 bar	0.2
77	ignition signal of cyl. 1	inductive	AVL	3080	-	*
78	relative pressure in cyl. 3	piezoelectric	Kistler	7061B	0-250 bar	●
79	ignition signal of cyl. 3	inductive	AVL	3080	-	*

tc thermocouple K (chromel/alumel) *Philips Thermocoax* type *TKI* [68]

ng natural gas

1 the relative error is valid for the part of the range used and is given for an interval of confidence of 99 % based on a normal Gaussian distribution

2 given by the manufacturer for the measurement range (*Jaquet* [69], *Trimec* [70], *ABB* [71], *Rotronic* [72])

3 of the crank angle resolution of 0.5 °CA, thus ±0.02 °CA

\* only for regulation; value set on the basis of the measurement made with the calibrated instrumentation (see figure C.1)

‡ only for comparison; because of the pulsating flow, the measured value corresponds to the average thermocouple temperature

‡ see table C.2

§ only to get the signal of an industrial transducer

● see table 2.3

\* the error is given by the one of the crankshaft angular position (no 72)

**Table C.2:** Main specifications of the exhaust gas analysers

Component	Analyser			Range	Error <sup>1</sup> ±%
	Principle	Producer	Type		
O <sub>2</sub>	paramagnetic	Servomex	Xentra 4900	0-25 %	2.5
CO <sub>2</sub>	infrared	Servomex	Xentra 4900	0-20 %	3.5
CO	infrared	Servomex	Xentra 4900	0-3000 ppm	3.5
NO <sub>x</sub>	chemiluminescence	Ecophysics	CLD 700 EL ht	0-10 000 ppm	5.0
THC	flame ionization	Signal	FID 3001	0-10 000 ppm	4.0

1 estimated over the effective range of measurement

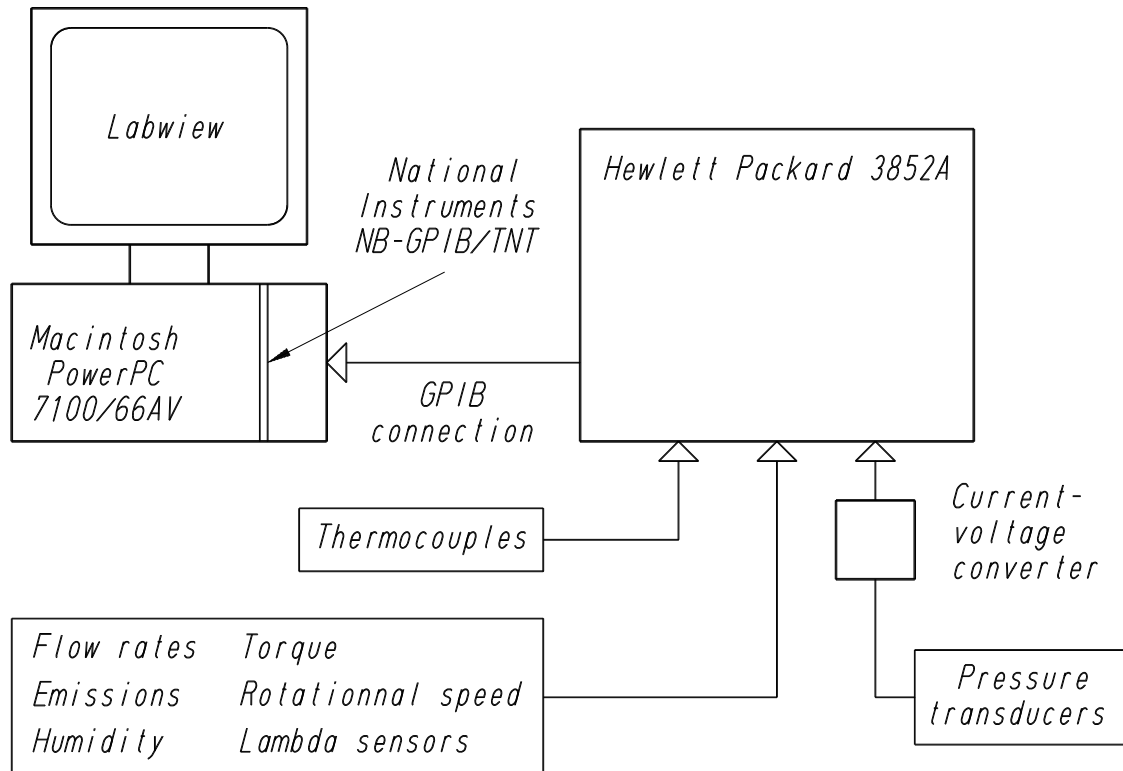


**Figure C.2:** Low speed acquisition system for steady state variables.

the middle of the stream towards the walls. This leads to a thermocouple temperature (measured value) which is lower than the effective exhaust gas flow temperature. The literature [73] indicates that at least three successive shields should be used in order to reduce significantly the measurement error. However, this cannot easily be implemented in the case of a practical system.

The characteristics of the steady state pressure transducers are given in **table C.3**. They were calibrated in two different ways. The transducers measuring close to the atmospheric pressure ( $\approx \pm 100 \text{ mbar}$ ) and the differential pressure transducers were calibrated with a water column on the range over which they are used. The transducers measuring a higher pressure were calibrated with a manometric balance between 1.0 and 3.5 *bar*, except the one measuring the engine lubricating oil pressure which was calibrated between 1.0 and 6.8 *bar*. Ten points were recorded on the measurement range and a numerical regression was performed to approximate the calibration curve. The regression was then introduced into *Labview*. Similarly to the temperature measurements, the relative error given in **table C.1** for each transducer measuring far above atmospheric pressure corresponds to the part of the range effectively used during experimentation.

The dynamometer torque was calibrated between 0 and 1300 *Nm*, every 100 *Nm*, using weights. The calibration curve was approximated by a numerical regression, which was introduced into *Labview*. The exhaust gas analysers were calibrated before each series of measurements with calibration gases. The relatively large error on the

**Table C.3:** Main specifications of the piezoresistive pressure transducers *Haenni* [74]

	ED 510/454.211				ED 572/522.281
	025	035	055	065	A36
Range	0-1 bar	0-1.6 bar	0-4 bar	0-6 bar	0-20 mbar
Non-linearity in % FS	0.15				
Hysteresis and repeatability in % FS	0.1				0.15
Temperature zero point drift in % FS/10 K	0.3				0.2
Temperature sensitivity in % FS/10 K	0.25				0.2
Signal output in mA	4-20				

NO<sub>x</sub> concentration measurement is partially due to the switch between two different scales during experimentation. Therefore, it takes into account that part of the measurements were made at the lowest end of the upper scale. Further, this error also takes into account that no H<sub>2</sub>O and CO<sub>2</sub> signal quenching corrections were performed. The relatively large error on the THC concentration measurement results from the use of the analyser in the first third of the scale used.

The acquisition procedure consists of recording ten successive scans of all the measurements, which takes approximately five minutes. The data is then processed with software developed for this purpose and the average values are considered for the analysis and interpretation of the results. The main engine parameters calculated from the measurement data by the software are detailed in appendix C.3. However, the variance corresponding to each acquisition channel is taken into account for the evaluation of the absolute error. This evaluation procedure is detailed in [3] and typical absolute errors on the engine emissions and performance based on the two last series of experiments are given in **table C.8**.

### High speed data acquisition system

The high speed data acquisition system is intended for pressure indication and spark timing measurement and is based on a device *AVL* type *Indiset 620* [75] (**figure C.3**). This system consists of a docking station *AVL 6161* with eight channels. The data storage capacity (RAM) is 8 MB and the maximum data transfer rate is 1 MHz. The docking station is fitted with two double charge amplifiers *AVL 3066 A01* for piezoelectric pressure transducers, two ignition timing modules *AVL 3080 A01* and a double multipurpose amplifier for piezoresistive pressure transducers. Further, it is equipped with an angle encoder *AVL 364* with light pulse converter which enables the selection of a crank angle resolution of 0.1, 0.2, 0.5 or 1 °CA and an inductive sensor *AVL 428* for accurate TDC-measurement. The recorded data is transferred to a personal computer *MEM Pentium I* over an *RS232* connection to be visualised with the software *IndWin v.1.4* by *AVL*. The data is then processed separately with software developed for this purpose and the main variables calculated are detailed in appendix C.3. The system is completed with a cooling system for cooled piezoelectric transducers and piezoresistive adapters.

The crank angle resolution used in this study was 0.5 °CA and 100 consecutive cycles were recorded. The angular position of the TDC in cylinder one was measured with the inductive sensor *AVL 428*. The values in the other cylinders were calculated with the

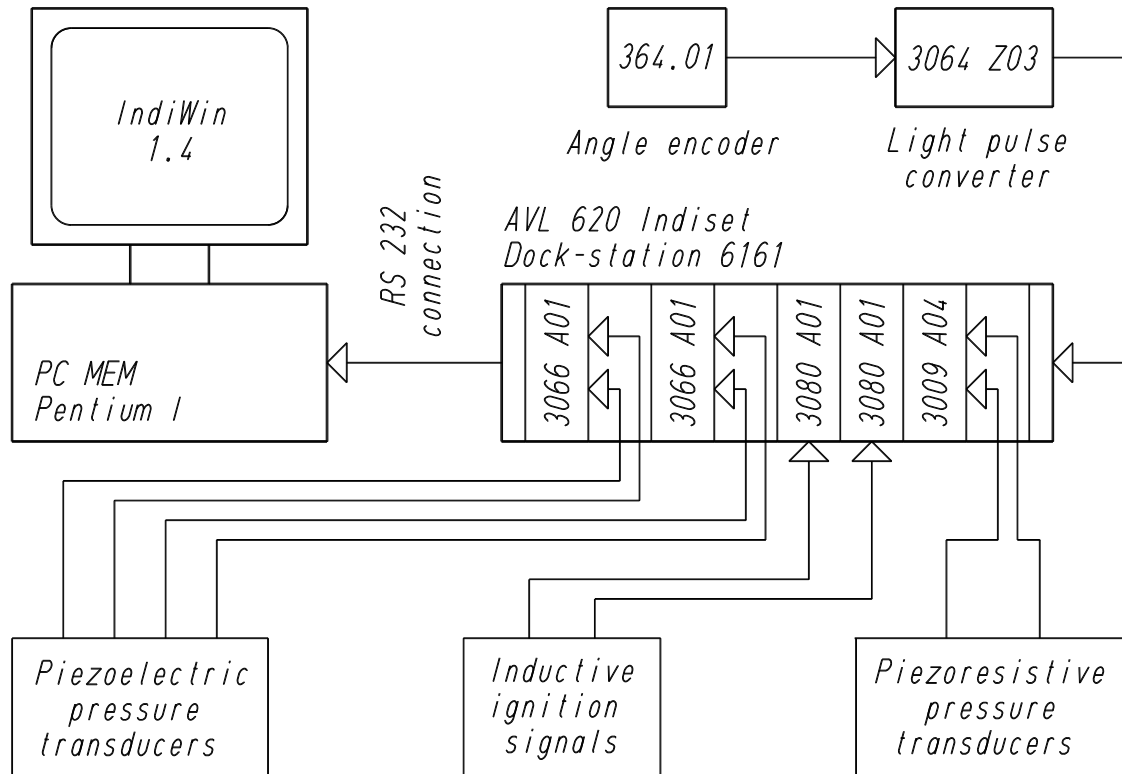


**Figure C.3:** High speed acquisition system for pressure indication and spark timing measurements.

theoretical intervals based on the firing order. The characteristics of the transducers used are detailed in **table 2.3**. The piezoelectric transducers were calibrated by the manufacturer and the piezoresistive transducers with the manometric balance. The latter were calibrated between 1 and 5 *bar* at intervals of 0.5 *bar*. The calibration curve was approximated by a numerical regression, which was then introduced into the software *IndWin*.

### C.1.3 Conditioning of the engine and dynamometer fluids

Several systems were developed and implemented to condition the engine and dynamometer fluids. They are described in detail in the following sections and their configurations are represented in **figure C.1**; the numbers given into brackets correspond to the measurement locations indicated on this figure.

#### Combustion air

The conditioning of the combustion air is performed with a multi-bloc standard air conditioning system (**figure C.4**). The air goes first through a coarse filter (0.3  $\mu\text{m}$ , efficiency 60%) before passing through an humidifier. Due to its position before the





**Figure C.4:** Air conditioning system and laminar flow meter installed on the piping.

heater, the humidifier only allows an increase in relative humidity of 20 % from the ambient value. However, it enables a constant value to be maintained during a series of measurements. The air goes then across a heat exchanger, which enables cooling with or without condensation, followed by a fine filter ( $0.3 \mu m$ , efficiency 99.9 %). Finally, it is blown by a fan through an electrical heater. In order to allow the stabilisation of the operating conditions before engine start, the piping is equipped with a bypass valve to the room. A temperature sensor coupled to an industrial regulator *Johnson Control* type *DX 9100* [76] controls the air temperature (23). The regulation is set in order to obtain a given temperature before the air-fuel mixer (25). The air flow rate is measured with a laminar flow meter *Meriam* type *50MR2-6* [77]. The mass flow rate is calculated from the inlet temperature (21) and pressure (22) as well as the differential pressure across the measurement element (24) and the calibration curve established by the manufacturer. Due to the very small influence of the relative humidity on the dynamic viscosity ( $\eta_{hum}/\eta_{dry} \leq 0.999$ ) at the experimentation conditions ( $\approx 25^\circ C$ , 30-60 % *RH*), no humidity correction is performed. Finally, a butterfly valve is installed on the piping in order to control the pressure before the air-fuel mixer (26).



**Figure C.5:** Compressed natural gas expansion system: 40 to 5 bar (bottom, left), 5 to 50 mbar (middle, right) and connection to the network supply.

Thus, this enables a constant value to be maintained independently from variations in atmospheric pressure. The air temperature (25), pressure (26) and relative humidity (27) are measured before the air-fuel mixer.

### Natural gas

The testing facilities are supplied with natural gas from two different sources. The first source is the low pressure network (50 mbar) and the second source consists of a storage unit formed by four clusters of cylinders at a pressure of 200 bar. The total storage volume of  $48 \times 50 \text{ l}$  represents a natural gas capacity of  $440 \text{ m}^3$  at 1013 mbar and  $0^\circ\text{C}$ . The refilling is realised at a CNG refuelling station, which requires the transportation of the cylinder clusters. Important variations of the network natural gas composition can occur over a short period of time. This motivated the creation of the storage unit in order to keep a constant composition over several series of experiments. The storage unit is located outside the building.

The natural gas from the storage unit is first expanded to 40 bar before passing through a mass flow meter (28). In order to keep a sufficient mass flow measurement accuracy, the storage is not emptied below 40 bar. Natural gas is then expanded from 40 to 5 bar and from 5 to 50 mbar before the connection with the network supply piping (**figure C.5**). Natural gas from the network passes through a  $50 \mu\text{m}$  filter before this connection (natural gas from the storage unit is filtered at the refuelling station). The selection of the natural gas source is realised by the alternative commutation of two

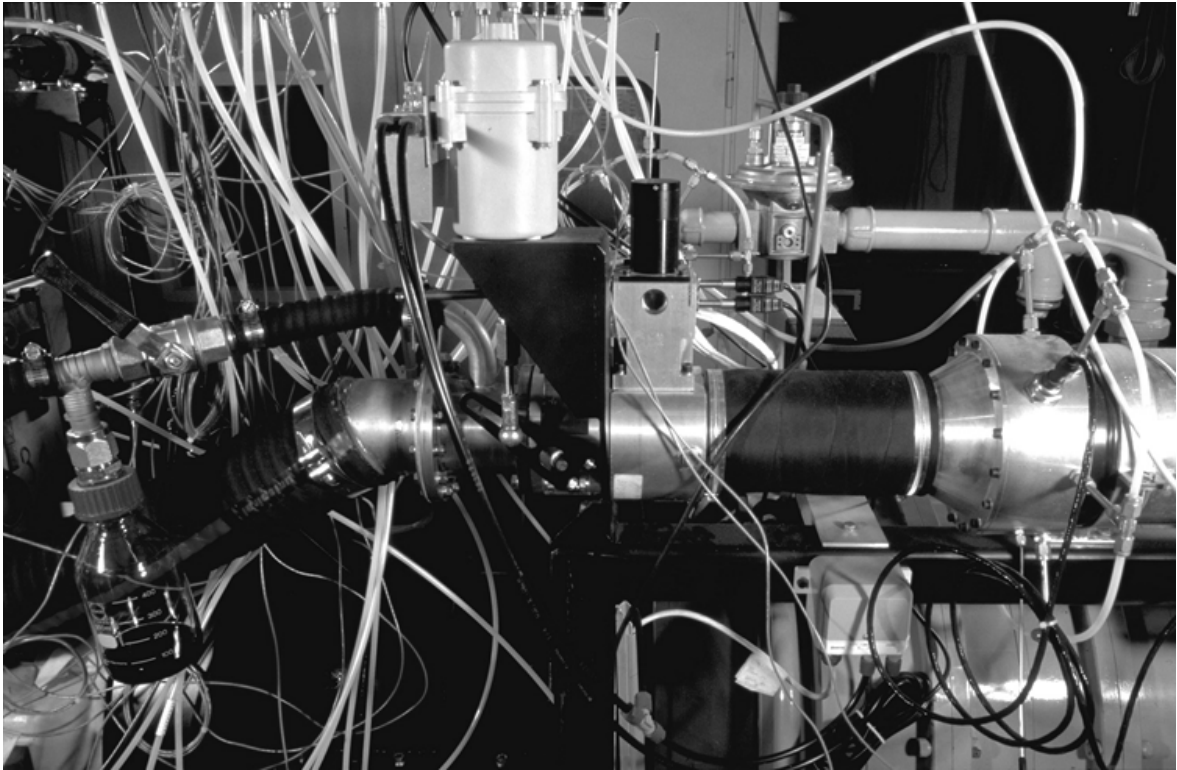


**Figure C.6:** Air-fuel mixer with motored valve to adjust the relative air to fuel ratio (middle, right side) and pneumatic controlled throttle valve (middle, left side).

electro-valves; only one is open at a time. The engine warm up and the stabilisation of the operating conditions are performed with natural gas from the network. The natural gas from the storage unit is exclusively used for measurements.

The natural gas at low pressure then flows into a laminar flow meter *Meriam* type  $50MW20-1^{1/2}$  [77]. The mass flow rate is calculated from the inlet temperature (29) and pressure (30) as well as the differential pressure across the measurement element (31) and the calibration curve established by the manufacturer. Because the calibration curve was established for air, the volume flow rate is corrected with the ratio between the dynamic viscosity of dry air and the one of natural gas [78]. This flow meter is mainly intended for the natural gas supplied from the network. Finally, the natural gas is expended through a zero pressure regulator *Dungs* type *FRNG 515* [79] to the pressure at the air inlet of the air-fuel mixer. Its temperature (32) and pressure (33) are measured just after the zero pressure regulator. This regulator keeps the air and natural gas volumetric flow rates approximately proportional when the engine load or rotational speed are varied.

### Air-fuel mixture

The air-fuel mixture is prepared with a venturi type mixer *RMG* type *980-140/65-36-1.1* [32] (**figure C.6**). The relative air to fuel ratio is adjusted through a valve located on the natural gas side and activated by a stepper motor. The control of the stepper motor is detailed in [3]. The engine load is controlled through a throttle valve



**Figure C.7:** Turbocharger *KKK* type *K27* instrumented for temperature and pressure measurements at the inlet and outlet of the compressor and turbine.

*RMG* type *981b-140/96* [32] actuated by a pneumatic jack, located directly after the mixer. In order to evacuate the blowby gases, a pipe connects the engine sump to the intake piping just after the throttle valve. A trap is installed on the pipe in order to prevent oil vapour, which may have condensed, from flowing into the intake piping.

The mixture is compressed by the turbocharger (**figure C.7**). The temperature and pressure are measured as close as possible to the inlet (34,35) and outlet (36,37) of the compressor. The mixture is then cooled with a heat exchanger *Covrad* type *CA 40188* [80] connected to the industrial cooling water circuit of the *EPFL* (**figure C.8**) before flowing into the engine. Its temperature (38) and pressure (39) are measured at a short distance from the intake manifold inlet (**figure C.9**). In order to keep a constant temperature at this location, the intercooler water flow rate is regulated

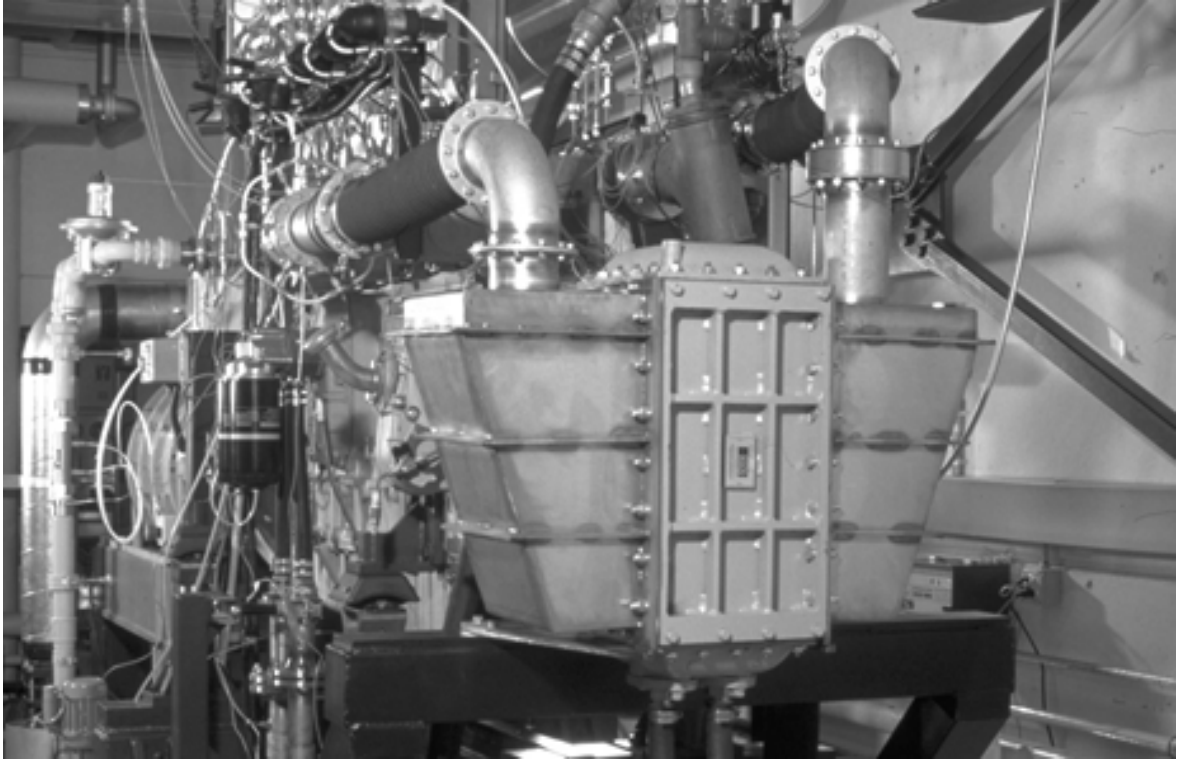


**Figure C.8:** Air-fuel mixture intercooler transferring heat to the industrial cooling water circuit.

through a control valve actuated by an industrial regulator *Honeywell* type *UDC 3000* [81] (40). Finally, the intake manifold is fitted with thermocouples located close to the inlet of each cylinder head intake port (41-46). Due to the pulsating flow at these locations and the thermal inertia of the thermocouples, the values measured correspond to the thermocouple temperatures and not to the local flow values. However, these temperature measurements enable a qualitative comparison of the intake conditions of the different cylinders.

### Exhaust gas

The exhaust system is shown in **figure C.10**. The exhaust manifold is fitted with thermocouples (47-52) and gas sampling probes (53-58) located close to the outlet of each cylinder head exhaust port. This allows a qualitative comparison of the combustion in the different cylinders. Part of the exhaust gas kinetic energy is recovered by the turbocharger and the temperature and pressure are measured as close as possible to the inlet (59,60) and to the outlet (61,62) of the turbine. Further, the exhaust gas temperature (63), pressure (64) and composition (65) are measured at a location on the exhaust piping sufficiently away from the turbine outlet to insure a good exhaust gas homogeneity. This measurement section is also fitted with an accurate (66) and an industrial (67) lambda sensor. The exhaust system is equipped with an oxidation catalyst. The catalyst is instrumented for temperature measurement at the inlet (68) and for temperature (69), pressure (70) and exhaust gas composition (71) measurements at the outlet. However, the exhaust gas composition was only measured before

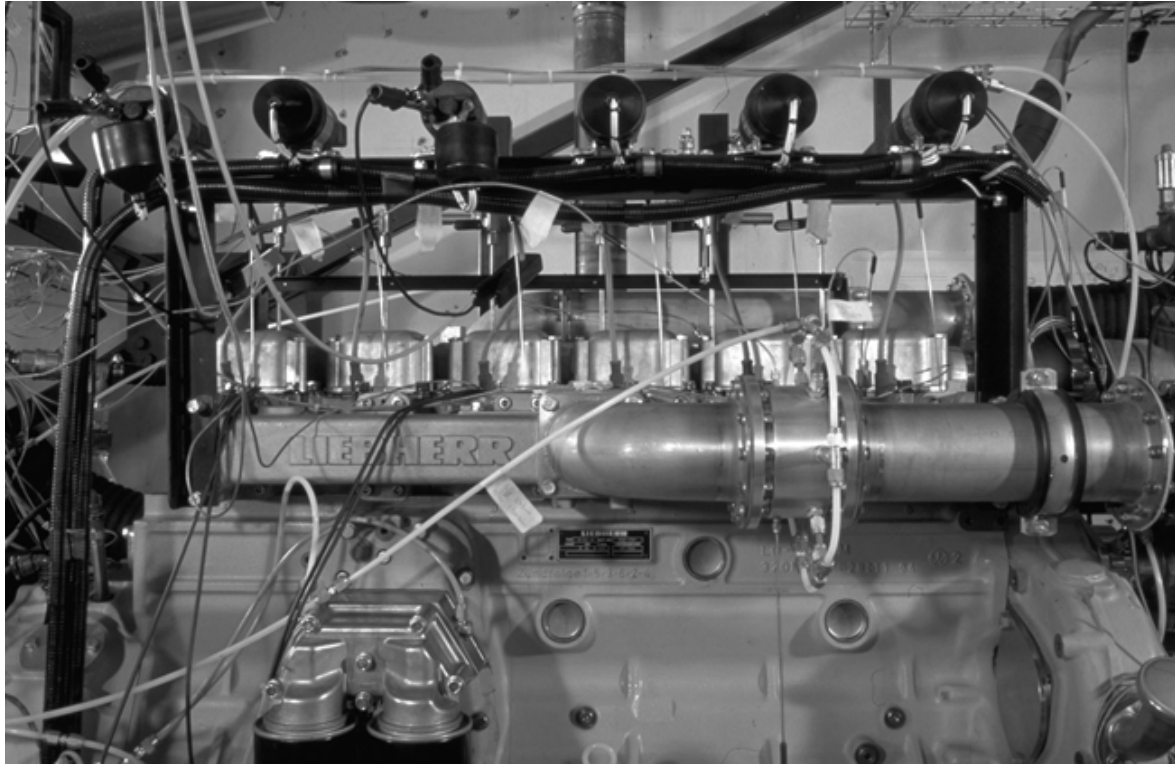


**Figure C.9:** Intake piping with measurement section before the intake manifold.

catalyst in the present study. Finally, a butterfly valve actuated by a pneumatic jack is installed on the exhaust piping just before the silencer in order to adjust the back pressure.

### Engine cooling water

The engine is cooled by the means of a water conditioning system (**figure C.11**). The heat generated by the engine is transferred to the industrial cooling water circuit through an heat exchanger. In order to keep a constant temperature at the engine inlet, the industrial cooling water mass flow rate is regulated with a control valve actuated by an industrial regulator *Watlow* type 988 [82] (17). Because the engine has no integrated water pump, the cooling water is circulated with an electrical centrifugal pump. The engine cooling water mass flow rate is adjusted by a valve located on the circuit. The circuit pressure is set to 2 bar and the thermal expansion is absorbed by a closed expansion vessel. The temperature and pressure at the engine inlet (15,16) and outlet (18,19) as well as the engine cooling water mass flow rate (20) are measured.

### Engine lubricating oil

In order to control the engine oil temperature, the original engine internal oil/water heat exchanger was removed. The oil flow is diverted after the filter and is cooled separately with industrial water by the means of an external heat exchanger (**figure C.12**),

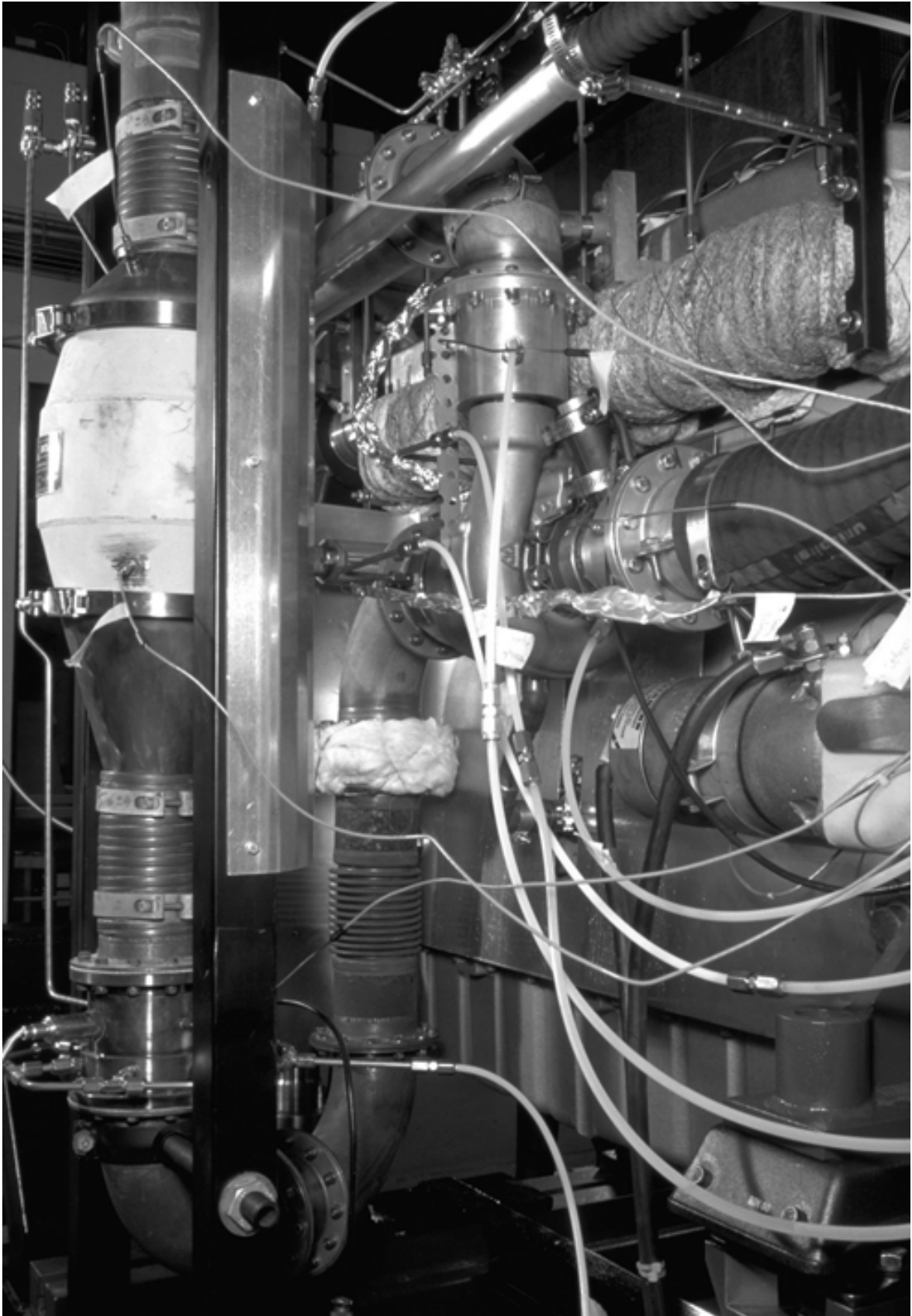


**Figure C.10:** Exhaust system with insulated manifold, turbocharger, measurement section (bottom, left) and oxidation catalyst.

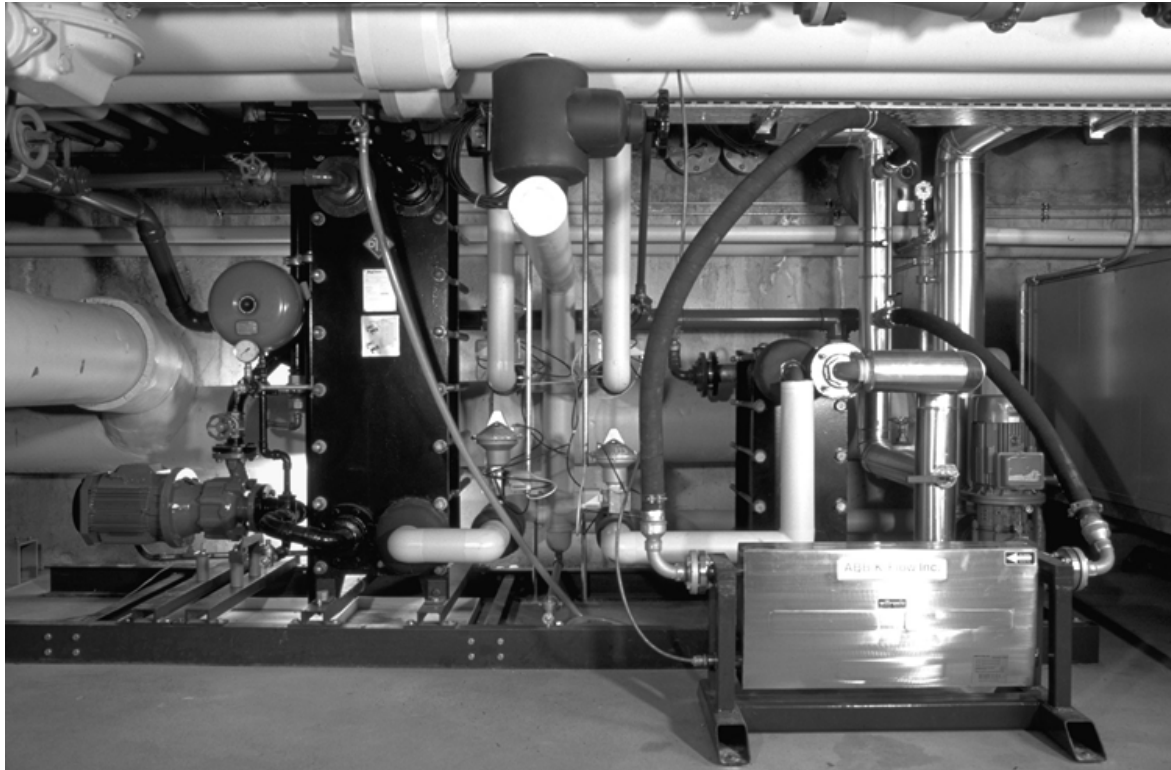


**Figure C.11:** Engine (right) and dynamometer (left) cooling water conditioning systems; engine cooling water mass flow meter (foreground, right) and industrial cooling water control valves (middle).

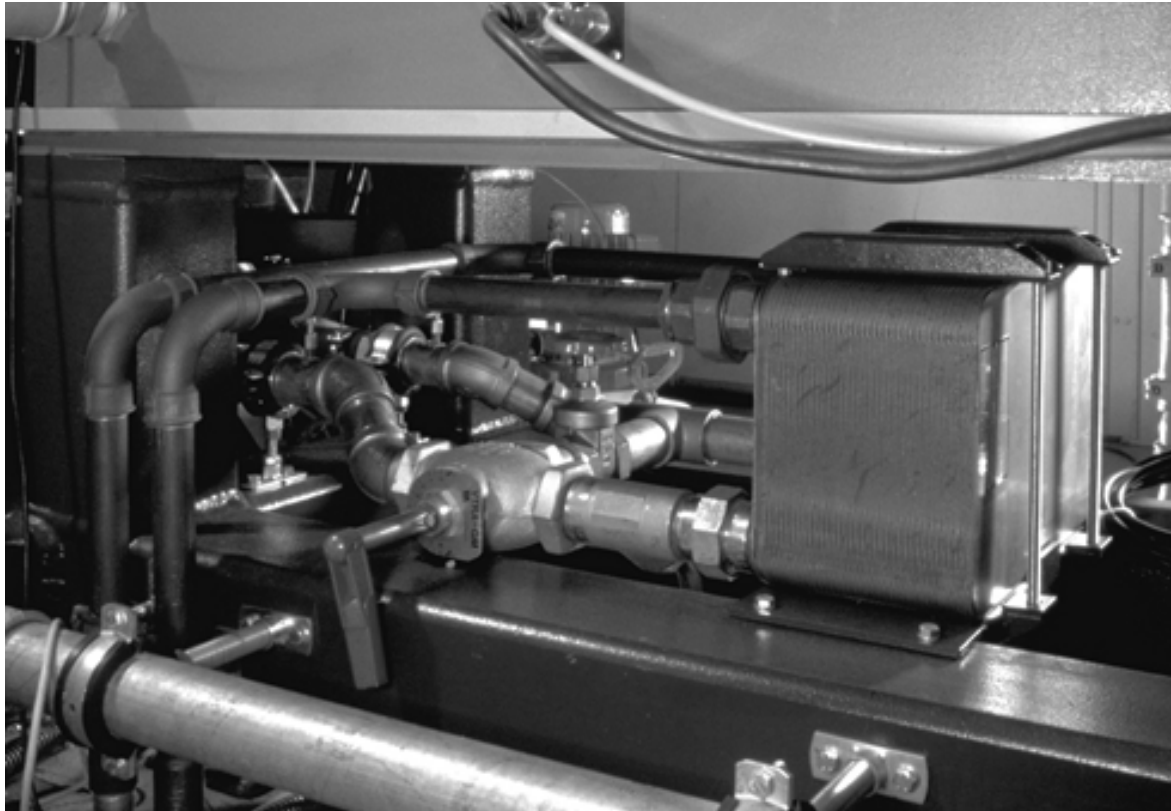


**Figure C.12:** Engine lubricating oil conditioning system transferring heat to the industrial cooling water circuit.



before returning to the engine. The oil temperature at the engine inlet is regulated with a control valve installed on the industrial cooling water circuit and actuated by an industrial regulator *Watlow* type *988* [82] (9). The temperature and pressure at the engine inlet (7,8) and outlet (10,11) as well as the oil volume flow rate (12) are measured.

### **Dynamometer cooling water**

The heat generated by the dynamometer is transferred to a closed cooling circuit. It is then further transferred to the industrial cooling water circuit through a heat exchanger (**figure C.11**). The dynamometer cooling water is circulated with an electrical centrifugal pump. The circuit pressure is set to *2 bar* and the thermal expansion is absorbed by a closed expansion vessel. In order to prevent air humidity condensation in the dynamometer and thus avoid corrosion problems as well as insure a good measurement accuracy, the inlet cooling water temperature is regulated to  $20\text{ }^{\circ}\text{C}$  with a control valve installed on the industrial cooling water circuit and actuated by an industrial regulator *Watlow* type *988* (5). The outlet cooling water temperature is measured and used to ensure that no dynamometer overheating occurs.

## C.2 Natural gas composition and properties

Natural gas is a blend of several gaseous hydrocarbons, nitrogen and carbon dioxide. It contains mainly methane, but also substantial amounts of ethane, propane, as well as small quantities of butane, pentane, hexane and higher hydrocarbons. The natural gas composition varies substantially, depending of its origin. Switzerland is supplied simultaneously with natural gas from Russia, the North Sea and North Africa. Due to the pipeline interconnection, the composition varies with time, depending on the local consumption. This can lead to important concentration changes, even during a single hour [3], which motivated the creation of a storage unit. The chemical composition and properties of the natural gas blends used are given in **table C.4**.

The composition was determined by gas chromatography on a sample from the storage by the natural gas supplier *GAZNAT* [83]. The properties are calculated as follows, considering the higher hydrocarbons  $C_6^+$  as n-hexane (n- $C_6H_{14}$ ):

Regarding the natural gas as formed by  $n$  molecules  $i$  of type  $C_{v_i}H_{w_i}O_{x_i}N_{y_i}$ , it is possible to determine the variables  $v$ ,  $w$ ,  $x$  and  $y$  of a synthetic hydrocarbon molecule  $C_vH_wO_xN_y$  from the molar (or volumetric) concentrations  $\tilde{c}_i$  of the individual components:

$$v = \sum_{i=1}^n \tilde{c}_i v_i, \quad w = \sum_{i=1}^n \tilde{c}_i w_i, \quad x = \sum_{i=1}^n \tilde{c}_i x_i, \quad y = \sum_{i=1}^n \tilde{c}_i y_i \quad (C.1)$$

The corresponding molar mass is:

$$\tilde{m}_{C_vH_wO_xN_y} = v\tilde{m}_C + w\tilde{m}_H + x\tilde{m}_O + y\tilde{m}_N \quad \text{in} \quad \frac{kg}{kmole} \quad (C.2)$$

where the individual molar masses of the elementary elements C, H, O and N are given in **table C.5**.

It is then possible to determine the ideal gas constant:

$$R_{C_vH_wO_xN_y} = \frac{\mathcal{R}}{\tilde{m}_{C_vH_wO_xN_y}} \quad \text{in} \quad \frac{J}{kg K} \quad (C.3)$$

where  $\mathcal{R}$  is the molar universal ideal gas constant, equal to  $8'314 \frac{J}{kmole K}$

Based on the ideal gas law, the gas density at normal conditions ( $p = 1.013 \text{ bar}$  and  $T = 273.15 \text{ K}$ ) is:

$$\rho_{C_vH_wO_xN_y} = \frac{1.013 \cdot 10^5}{R_{C_vH_wO_xN_y} 273.15} \quad \text{in} \quad \frac{kg}{m^3} \quad (C.4)$$

The hydrogen to carbon ratio is given by:

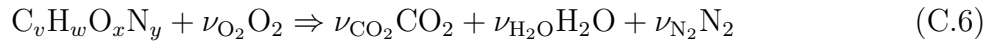
$$H/C = \frac{w}{v} \quad \text{in} \quad \frac{kmole_H}{kmole_C} \quad (C.5)$$

**Table C.4:** Chemical composition and properties of the natural gas blends used

		NG1	NG2	NG3	NG4	NG5	NG6	NG7
CH <sub>4</sub>	% vol.	92.17	95.90	97.45	93.01	95.68	96.06	95.78
C <sub>2</sub> H <sub>6</sub>	% vol.	3.48	1.77	0.88	3.28	1.76	1.70	1.95
C <sub>3</sub> H <sub>8</sub>	% vol.	0.86	0.46	0.26	0.84	0.50	0.40	0.49
i-C <sub>4</sub> H <sub>10</sub>	% vol.	0.13	0.07	0.04	0.14	0.08	0.07	0.08
n-C <sub>4</sub> H <sub>10</sub>	% vol.	0.15	0.08	0.05	0.15	0.09	0.07	0.07
i-C <sub>5</sub> H <sub>12</sub>	% vol.	0.03	0.02	0.02	0.04	0.02	0.03	0.02
n-C <sub>5</sub> H <sub>12</sub>	% vol.	0.00	0.01	0.01	0.03	0.02	0.01	0.02
C <sub>6</sub> <sup>+</sup>	% vol.	0.05	0.00	0.00	0.04	0.00	0.00	0.00
N <sub>2</sub>	% vol.	2.35	1.42	1.30	1.84	1.54	1.47	1.34
CO <sub>2</sub>	% vol.	0.79	0.27	0.00	0.64	0.31	0.19	0.25
$\tilde{m}^*$	kg/kmole	17.44	16.75	16.45	17.32	16.80	16.70	16.77
$R^*$	J/(kg K)	477	497	506	480	495	498	496
$\rho^*$	kg/m <sub>N</sub> <sup>3</sup>	0.778	0.747	0.734	0.773	0.749	0.745	0.748
H/C <sup>*</sup>	kmole <sub>H</sub> /kmole <sub>C</sub>	3.85	3.93	3.97	3.86	3.92	3.93	3.92
$\nu_{O_2, min}^*$	kmole <sub>O<sub>2</sub></sub> /kmole <sub>NG</sub>	2.033	2.016	2.001	2.044	2.015	2.013	2.021
$m_{air, min}^*$	kg <sub>air</sub> /kg <sub>NG</sub>	16.05	16.57	16.75	16.25	16.52	16.59	16.60
$\nu_{air, min}^*$	m <sub>N<sub>air</sub></sub> <sup>3</sup> /m <sub>N<sub>NG</sub></sub> <sup>3</sup>	9.70	9.62	9.55	9.76	9.62	9.60	9.65
$\Delta h_{0,L}^*$	MJ/kg	46.84	48.32	48.82	47.42	48.16	48.38	48.40
$\Delta \check{h}_{0,L}^*$	MJ/m <sub>N</sub> <sup>3</sup>	36.44	36.10	35.82	36.64	36.08	36.05	36.20
$\Delta h_{0,U}^*$	MJ/kg	51.88	53.57	54.15	52.54	53.40	53.64	53.66
$\Delta \check{h}_{0,U}^*$	MJ/m <sub>N</sub> <sup>3</sup>	40.37	40.02	39.73	40.59	40.01	39.97	40.13

\* C<sub>6</sub><sup>+</sup> considered as n-C<sub>6</sub>H<sub>14</sub>

Considering the following one step combustion reaction to fully oxidised products:



the molar minimum theoretical oxygen required per *kmole* of natural gas is:

$$\nu_{O_2, min} = v + \frac{w}{4} - \frac{x}{2} \quad \text{in} \quad \frac{kmole_{O_2}}{kmole_{C_v H_w O_x N_y}} \quad (C.7)$$

Based on a practical air composition of 79.05% *vol* of molecular nitrogen (N<sub>2</sub>) and 20.95% *vol* of molecular oxygen (O<sub>2</sub>) [13], which represents 3.773 *kmole*<sub>N<sub>2</sub></sub>/*kmole*<sub>O<sub>2</sub></sub>, the molar minimum theoretical air required per *kmole* of natural gas is:

$$\nu_{air, min} = (1 + 3.773) \nu_{O_2, min} = 4.773 \left( v + \frac{w}{4} - \frac{x}{2} \right) \quad \text{in} \quad \frac{kmole_{air}}{kmole_{C_v H_w O_x N_y}} \quad (C.8)$$

and in a specific form:

$$m_{air, min} = \nu_{air, min} \frac{\tilde{m}_{air}}{\tilde{m}_{C_v H_w O_x N_y}} \quad \text{in} \quad \frac{kg_{air}}{kg_{C_v H_w O_x N_y}} \quad (C.9)$$

**Table C.5:** Molecular weight and standard heat of formation of relevant species for the determination of the natural gas properties

Component	Symbol	$\tilde{m}$ kg/kmole	State	$\Delta_f^0 \tilde{h}$ kJ/kmole
Atomic carbon	C	12.01	gas	716'670 <sup>1</sup>
Methane	CH <sub>4</sub>	16.04	gas	-74'873 <sup>1</sup>
Ethane	C <sub>2</sub> H <sub>6</sub>	30.07	gas	-83'850 <sup>2</sup>
Propane	C <sub>3</sub> H <sub>8</sub>	44.10	gas	-104'700 <sup>2</sup>
N-Butane	n-C <sub>4</sub> H <sub>10</sub>	58.12	gas	-127'100 <sup>2</sup>
I-Butane	i-C <sub>4</sub> H <sub>10</sub>	58.12	gas	-134'200 <sup>2</sup>
N-Pentane	n-C <sub>5</sub> H <sub>12</sub>	72.15	gas	-148'460 <sup>2</sup>
I-Pentane	i-C <sub>5</sub> H <sub>12</sub>	72.15	gas	-153'700 <sup>2</sup>
N-Hexane	n-C <sub>6</sub> H <sub>14</sub>	86.18	gas	-167'200 <sup>2</sup>
Carbon dioxide	CO <sub>2</sub>	44.01	gas	-393'522 <sup>1</sup>
Atomic hydrogen	H	1.01	gas	217'999 <sup>1</sup>
Water	H <sub>2</sub> O	18.02	liquid	-285'830 <sup>1</sup>
Water vapour	H <sub>2</sub> O	18.02	gas	-241'826 <sup>1</sup>
Atomic nitrogen	N	14.01	gas	472'680 <sup>1</sup>
Molecular nitrogen	N <sub>2</sub>	28.01	gas	0 <sup>1</sup>
Atomic oxygen	O	16.00	gas	249'170 <sup>1</sup>
Molecular oxygen	O <sub>2</sub>	32.00	gas	0 <sup>1</sup>

1: JANAF Thermochemical Tables [48], 2: NIST Chemistry WebBook [84], most recent values

where the air molar mass is:

$$\tilde{m}_{air} = \tilde{c}_{O_2, air} 2 \tilde{m}_O + \tilde{c}_{N_2, air} 2 \tilde{m}_N = 28.85 \frac{kg}{kmole} \quad (C.10)$$

Under the ideal gas law, the volumetric minimum theoretical air at normal conditions corresponds to the molar value, thus:

$$v_{air, min} = \nu_{air, min} \quad \text{in} \quad \frac{m_{N_{air}}^3}{m_{N^3 C_v H_w O_x N_y}^3} \quad (C.11)$$

The lower and upper heating values at constant pressure are determined on the basis of the heating values of the individual hydrocarbons and their concentration  $\tilde{c}_i$ . The heating values of the individual hydrocarbons are calculated from the standard heat of formation of the reactants (left hand side) and products (right end side) of reaction C.6 (nitrogen is not taken in account, because it does not participate to the ideal combustion process considered). The standard heat of formation corresponds to the energy required to form a component from the elementary species (C, H, N and O) in their most stable state (Graphite, H<sub>2</sub>, N<sub>2</sub> and O<sub>2</sub>) at 1.013 mbar and 298.15 K. The water vapour and liquid water standard heat of formation are used to determine the

lower and upper heating value, respectively. Considering that the molecular oxygen standard heat of formation is zero by definition, the molar lower heating value of the individual hydrocarbons can be expressed as:

$$\begin{aligned} \Delta \tilde{h}_{0,L C_{v_i}H_{w_i}O_{x_i}N_{y_i}} &= \Delta_f^0 \tilde{h}_{C_{v_i}H_{w_i}O_{x_i}N_{y_i}} - v_i \Delta_f^0 \tilde{h}_{CO_2} \\ &- \left(\frac{w_i}{2}\right) \Delta_f^0 \tilde{h}_{H_2O_{vapour}} \quad \text{in} \quad \frac{kJ}{kmole_{C_{v_i}H_{w_i}O_{x_i}N_{y_i}}} \end{aligned} \quad (C.12)$$

where the subscript  $L$  stand for *lower* ( $U$  for *upper*) and the standard heat of formation of the relevant components is given in **table C.5**.

The natural gas lower molar heating value is given by:

$$\Delta \tilde{h}_{0,L C_v H_w O_x N_y} = \sum_{i=1}^n \tilde{c}_i \Delta \tilde{h}_{0,L C_{v_i} H_{w_i} O_{x_i} N_{y_i}} \quad \text{in} \quad \frac{kJ}{kmole_{C_v H_w O_x N_y}} \quad (C.13)$$

and the specific and volumetric values can be derived as follow:

$$\Delta h_{0,L C_v H_w O_x N_y} = \frac{\Delta \tilde{h}_{0,L C_v H_w O_x N_y}}{\tilde{m}_{C_v H_w O_x N_y}} \quad \text{in} \quad \frac{kJ}{kg_{C_v H_w O_x N_y}} \quad (C.14)$$

$$\Delta \check{h}_{0,L C_v H_w O_x N_y} = \frac{\Delta \tilde{h}_{0,L C_v H_w O_x N_y} \rho_{C_v H_w O_x N_y}}{\tilde{m}_{C_v H_w O_x N_y}} \quad \text{in} \quad \frac{kJ}{m_N^3_{C_v H_w O_x N_y}} \quad (C.15)$$

The natural gas upper heating value can be calculated in the same way by replacing in equation C.12 the water vapour standard heat of formation by the liquid water value.

The natural gas molar specific heat at constant pressure is expressed by:

$$\tilde{c}_{p_{C_v H_w O_x N_y}}(T) = \sum_{i=1}^n \tilde{c}_{C_{v_i} H_{w_i} O_{x_i} N_{y_i}} \tilde{c}_{p_{C_{v_i} H_{w_i} O_{x_i} N_{y_i}}}(T) \quad (C.16)$$

where the molar specific heat at constant pressure of each component is calculated with polynomial temperature functions obtained by curve fitting on the data of *JANAF thermochemical tables* [48] for  $CH_4$ ,  $N_2$  and  $CO_2$ , and the *CHEMKIN thermodynamic data base* [85] for  $C_2H_6$  and  $C_3H_8$ . Due to their very low concentration and the difficulty to find suitable data, the molar specific heat at constant pressure of the higher order hydrocarbons ( $C_4^+$ ) have been approximated by the one of  $CH_4$ .

Finally, the specific heat at constant pressure can be obtained by:

$$c_{p_{C_v H_w O_x N_y}} = \frac{\tilde{c}_{p_{C_v H_w O_x N_y}}}{\tilde{m}_{C_v H_w O_x N_y}} \quad (C.17)$$

## C.3 Variable definition

### C.3.1 Steady state variables

The steady state variables are variables which represent mean values of engine operating parameters (temperature, pressure (except in the combustion chamber), mass flow rate or concentration of exhaust emissions). The measuring techniques used do not have a sufficient resolution to capture the variation over the engine cycle.

#### Engine break power output

The engine break power output represents the net mechanical power delivered at the engine crankshaft. In the case of the engine used, this value is determined without integrated cooling water pump (usual in cogeneration application). The engine break power output is given by:

$$\dot{E} = \omega M = 2\pi \frac{n}{60} M \quad (\text{C.18})$$

where  $n$  is the crankshaft rotational speed in  $rpm$  ( $1/min$ ) and  $M$  is the engine torque in  $Nm$ .

and in conventional unit:

$$\dot{E} = \frac{\pi n M}{30 \cdot 10^3} \quad \text{in } kW \quad (\text{C.19})$$

#### Break mean effective pressure

The break mean effective pressure corresponds to the break work produced during an engine cycle per unit of cylinder volume displaced during this cycle. It represents a typical value of comparison between engines and can be expressed:

$$p_{me} = \frac{120 \dot{E}}{n V_s} \quad (\text{C.20})$$

where  $V_s$  is the engine swept volume:

$$V_s = z \frac{\pi B^2}{4} S \quad (\text{C.21})$$

with  $z$ , the number of cylinder,  $B$  and  $S$ , the cylinder bore and piston stroke in  $m$ , respectively.

Considering equations C.18 and C.21, the break mean effective pressure becomes:

$$p_{me} = \frac{16 M}{z B^2 S 10^5} \quad \text{in } bar \quad (\text{C.22})$$

### Fuel conversion efficiency

The fuel conversion efficiency represents the ratio between the net mechanical work delivered at the engine crankshaft per cycle and the chemical energy at the reference conditions ( $p_0$ ,  $T_0$ ) contained in the amount of fuel burnt per cycle. The fuel lower heating value is considered here and is determined for each natural gas blend used in appendix section C.2. The fuel conversion efficiency is expressed by:

$$\eta_f = \frac{\dot{E}}{\dot{m}_{ng} \Delta h_{0,L_{ng}}} \quad (\text{C.23})$$

where  $\dot{m}_{ng}$  and  $\Delta h_{0,L_{ng}}$  are the natural gas mass flow rate and lower heating value at constant pressure, respectively.

Considering equation C.18, the fuel conversion efficiency becomes:

$$\eta_f = \frac{\pi n M}{30 \cdot 10^3 \dot{m}_{ng} \Delta h_{0,L_{ng}}} \quad (\text{C.24})$$

### Exhaust gas emissions

The main exhaust gas emissions are the nitrogen oxides (NO and NO<sub>2</sub> regrouped under the generic NO<sub>x</sub>), the carbon monoxide (CO) and the unburnt hydrocarbons (regrouped under the generic THC). The NO<sub>x</sub> and THC emissions are measured in part per million (*ppm*) concentration in the raw exhaust gas flow, kept at high enough temperature to avoid water vapour condensation, while the CO emissions are measured in the same unit but after preliminary condensation of the water vapour (dew temperature: 5°C). This exhaust gas drying is imposed by the infrared measuring technology used. To enable the comparison with the limits prescribed by the Swiss Federal Clean Air Act (*OPair*) [1], the emissions must be converted in *mg/m<sup>3</sup>* concentration [1, appendix 1, no 22/a] at normal conditions ( $p = 1.013 \text{ bar}$ ,  $T = 273.15 \text{ K}$ ) [1, appendix 1, no 23/§1] and corrected for humidity to 0% *RH* (dry) [1, appendix 1, no 23/§1] and an oxygen (O<sub>2</sub>) residual concentration of 5% *vol.* [1, appendix 1, no 23/§2-3 and appendix 2, no 821]. The sum of the nitrogen monoxide and dioxide emissions (NO<sub>x</sub>) are expressed as nitrogen dioxide (NO<sub>2</sub>) [1, appendix 2, no 824/b].

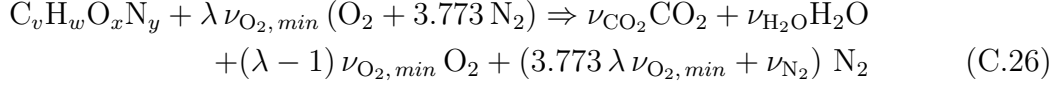
Under the approximation of the ideal gas law, the emissions in *ppm* concentration are converted as follow:

$$\check{c}_i = \dot{c}_i \frac{1.013 \cdot 10^5 \tilde{m}_i}{\mathcal{R} 273.15} \quad \text{in } \text{mg}/\text{m}_N^3 \quad (\text{C.25})$$

where  $\tilde{m}_i$  is the component molar mass and  $\mathcal{R}$  is the universal gas constant, equal to 8'314 *J/(kmole K)*.

Calculated on the basis of the values given in **table C.5**, the NO<sub>2</sub> and CO molar masses are 46.01 and 28.01 *kg/kmole*, respectively. The THC exhaust emissions are not limited by the *OPair*. They are expressed in equivalent methane (CH<sub>4</sub>), which has a molar mass of 16.05 *kg/kmole*.

In order to refer the exhaust emissions to the dry state (0% *RH*), it is necessary to determine the ratio between the number of moles of humid exhaust gas and the number of moles of dry exhaust gas. Considering a complete combustion and that the amount of  $\text{NO}_x$  generated is very small in comparison to the other exhaust gas components, the combustion can be approximated by the following one step chemical reaction:



Where  $\lambda$  is the relative air to fuel ratio:

$$\lambda = \frac{\dot{m}_{\text{air}, \text{dry}}}{\dot{m}_{\text{ng}} m_{\text{air}, \min}} \quad (\text{C.27})$$

Based on dry combustion air, the number of mole of humid exhaust gas per mole of fuel is:

$$n_{\text{eg}, \text{hum}} = \nu_{\text{CO}_2} + \nu_{\text{H}_2\text{O}} + (4.773 \lambda - 1) \nu_{\text{O}_2, \min} + \nu_{\text{N}_2} \quad (\text{C.28})$$

A certain quantity of water is also provided by the moisture of the combustion air. It can be determined as follows:

$$\nu_{\text{H}_2\text{O}, \text{air}} = w \frac{\tilde{m}_{\text{air}} \lambda \nu_{\text{O}_2, \min}}{\tilde{m}_{\text{H}_2\text{O}} \tilde{c}_{\text{O}_2, \text{air}}} \quad (\text{C.29})$$

where  $w$  is the specific water content per unit of dry air and is given by [86]:

$$w = \frac{\tilde{m}_{\text{H}_2\text{O}}}{\tilde{m}_{\text{air}}} \frac{\psi p''_{\text{H}_2\text{O}}}{p_{\text{air}, \text{hum}} - \psi p''_{\text{H}_2\text{O}}} \quad \text{in} \quad \frac{\text{kg}_{\text{H}_2\text{O}}}{\text{kg}_{\text{dry air}}} \quad (\text{C.30})$$

where  $\psi$  is the air relative humidity,  $p''_{\text{H}_2\text{O}}$  is the pressure of saturation at the humid air temperature and  $p_{\text{air}, \text{hum}}$  is the humid air static pressure.

Equation C.28 becomes:

$$n_{\text{eg}, \text{hum}} = \nu_{\text{CO}_2} + \nu_{\text{H}_2\text{O}} + \left[ \left( \frac{w \tilde{m}_{\text{air}}}{\tilde{m}_{\text{H}_2\text{O}} \tilde{c}_{\text{O}_2, \text{air}}} + 4.773 \right) \lambda - 1 \right] \nu_{\text{O}_2, \min} + \nu_{\text{N}_2} \quad (\text{C.31})$$

where

$$\nu_{\text{CO}_2} = v \quad (\text{C.32})$$

$$\nu_{\text{H}_2\text{O}} = \frac{w}{2} \quad (\text{C.33})$$

$$\nu_{\text{N}_2} = \frac{y}{2} \quad (\text{C.34})$$

Introducing these three last equations with equation C.7 in equation C.31 gives:

$$n_{\text{eg}, \text{hum}} = v + \frac{w}{2} + \left[ \left( \frac{w \tilde{m}_{\text{air}}}{\tilde{m}_{\text{H}_2\text{O}} \tilde{c}_{\text{O}_2, \text{air}}} + 4.773 \right) \lambda - 1 \right] \left( v + \frac{w}{4} - \frac{x}{2} \right) + \frac{y}{2} \quad (\text{C.35})$$

The number of moles of dry exhaust gas per mole of fuel can then be derived:

$$n_{\text{eg}, \text{dry}} = v + (4.773 \lambda - 1) \left( v + \frac{w}{4} - \frac{x}{2} \right) + \frac{y}{2} \quad (\text{C.36})$$



The correction factor for humidity is defined by:

$$f_h = \frac{n_{eg, dry}}{n_{eg, hum}} \quad (C.37)$$

and becomes:

$$f_h = \frac{v + (4.773 \lambda - 1) \left( v + \frac{w}{4} - \frac{x}{2} \right) + \frac{y}{2}}{v + \frac{w}{2} + \left[ \left( \frac{w \tilde{m}_{air}}{\tilde{m}_{H_2O} \tilde{c}_{O_2, air}} + 4.773 \right) \lambda - 1 \right] \left( v + \frac{w}{4} - \frac{x}{2} \right) + \frac{y}{2}} \quad (C.38)$$

The objective of the correction for oxygen residual concentration is to convert the emissions to a reference number of moles of exhaust gas per unit of fuel burnt, in order to compensate for the effect of dilution with excess air. The quantity of exhaust gas per mole of fuel burnt can be expressed as follow:

$$n_{eg} = n_{cp} + n_{ea} \quad (C.39)$$

where  $n_{eg}$ ,  $n_{cp}$  and  $n_{ea}$  are the numbers of moles of exhaust gas, combustion products and excess air, respectively.

The number of moles of excess air is given by:

$$n_{ea} = \frac{\tilde{c}_{O_2, eg}}{\tilde{c}_{O_2, air}} n_{eg} \quad (C.40)$$

Introduced in equation C.39, this gives:

$$n_{eg} = n_{cp} \tilde{c}_{O_2, air} \frac{1}{\tilde{c}_{O_2, air} - \tilde{c}_{O_2, eg}} \quad (C.41)$$

The correction factor is the ratio of the number of moles of exhaust gas between the operating and the reference conditions, thus:

$$f_{O_2} = \frac{n_{eg}}{n_{eg, ref}} = \frac{n_{cp}}{n_{cp, ref}} \frac{\tilde{c}_{O_2, air} - \tilde{c}_{O_2, eg, ref}}{\tilde{c}_{O_2, air} - \tilde{c}_{O_2, eg}} \quad (C.42)$$

Assuming complete combustion and that the amount of  $NO_x$  generated is very small in comparison to the quantity of combustion products ( $CO_2$ ,  $H_2O$  and  $N_2$  of the combustion air), it is possible to write:

$$n_{cp} \approx constant \quad \forall \lambda \geq 1.0 \quad (C.43)$$

and then:

$$n_{cp} \approx n_{cp, ref} \quad (C.44)$$

Thus, equation C.42 becomes:

$$f_{O_2} = \frac{\tilde{c}_{O_2, air} - \tilde{c}_{O_2, eg, ref}}{\tilde{c}_{O_2, air} - \tilde{c}_{O_2, eg}} \quad (C.45)$$

Finally, considering an air oxygen concentration of 20.95 % *vol.*, the correction factor for oxygen residual concentration is:

$$\boxed{f_{\text{O}_2} = \frac{0.2095 - 0.05}{0.2095 - \tilde{c}_{\text{O}_2}}} \quad (\text{C.46})$$

Because no specific indication is given in the *OPair* and all exhaust emissions concentrations are referred to the dry state, it is assumed that the reference oxygen concentration is also referred to the dry state. Therefore, the oxygen concentration of the dried exhaust gas is used for the correction.

Finally, the corrected NO<sub>x</sub> and THC exhaust gas emissions are given by:

$$\boxed{\check{c}_i = \dot{c}_i \frac{1.013 \cdot 10^5 \tilde{m}_i}{\mathcal{R} 273.15} \frac{f_{\text{O}_2}}{f_h} \quad \text{in} \quad \frac{\text{mg}}{\text{m}_N^3}} \quad (\text{C.47})$$

In the case of the CO emissions, which are measured on dried exhaust gas, no humidity correction is required and the relation becomes:

$$\boxed{\check{c}_i = \dot{c}_i \frac{1.013 \cdot 10^5 \tilde{m}_i}{\mathcal{R} 273.15} f_{\text{O}_2} \quad \text{in} \quad \frac{\text{mg}}{\text{m}_N^3}} \quad (\text{C.48})$$

Another way to express the exhaust gas emissions is to refer them to the net mechanical work delivered at the engine crankshaft. This represents a more objective means of comparing the emissions-performance ratio of engines operating under different conditions. However, this requires precise information on the fuel composition and characteristics, as well as the preliminary determination of the engine fuel conversion efficiency. If the determination of these parameters is relatively easy to realise on an engine test bed, this is often not the case on operating power plants, which usually are only offering an access to the exhaust gas.

Considering equation C.35, which represents the number of moles of humid exhaust gas per mole of fuel burnt, the emissions per unit of net mechanical work is:

$$\check{c}_i = \tilde{c}_i \tilde{m}_i \frac{n_{eg, hum}}{\tilde{m}_{ng} \Delta h_{0, L_{ng}}} \frac{3.6 \cdot 10^9}{\eta_f} \quad \text{in} \quad \frac{\text{mg}}{\text{kWh}} \quad (\text{C.49})$$

Substituting for the fuel conversion efficiency (equation C.24) and with the emission concentration expressed in *ppm*, it becomes:

$$\boxed{\check{c}_i = \dot{c}_i \tilde{m}_i \frac{n_{eg, hum} \dot{m}_{ng}}{\tilde{m}_{ng}} \frac{1.08 \cdot 10^8}{\pi n M} \quad \text{in} \quad \frac{\text{mg}}{\text{kWh}}} \quad (\text{C.50})$$

This relation holds for the conversion of NO<sub>x</sub> and THC emissions, which are measured on humid exhaust gas. The emissions of CO are measured on dried exhaust gas. Therefore, the number of moles of dried exhaust gas given by equation C.36 has to be considered and the relation becomes:

$$\boxed{\check{c}_i = \dot{c}_i \tilde{m}_i \frac{n_{eg, dry} \dot{m}_{ng}}{\tilde{m}_{ng}} \frac{1.08 \cdot 10^8}{\pi n M} \quad \text{in} \quad \frac{\text{mg}}{\text{kWh}}} \quad (\text{C.51})$$

### Relative air to fuel ratio based on exhaust gas emissions

In parallel to the standard definition based on the air and fuel mass flow rates, given by equation C.27, the relative air to fuel ratio is also calculated on the basis of the exhaust gas composition. This method has been proven to be more accurate than the standard one [87]. In this study, the variations of the relative air to fuel ratio were performed on a small range. This requires a higher accuracy in order to increase the resolution. Therefore, the values indicated in this report were calculated on the basis of the exhaust gas composition.

The approach used assumes that all the  $\text{NO}_x$  and the THC emissions are formed by  $\text{NO}$  and  $\text{CH}_4$ , respectively, and is essentially based on the atomic balance of a fuel-air mixture combustion. In matrix form, this can be written as:

$$\begin{matrix} \text{C} \\ \text{H} \\ \text{O} \\ \text{N} \end{matrix} \begin{bmatrix} \text{O}_2 & \text{CO}_2 & \text{CO} & \text{CH}_4 & \text{NO}_x & \text{H}_2\text{O} & \text{N}_2 \\ 0 & 1 & 1 & 1 & 0 & 0 & 0 \\ 0 & 0 & 0 & 4 & 0 & 2 & 0 \\ 2 & 2 & 1 & 0 & 1 & 1 & 0 \\ 0 & 0 & 0 & 0 & 1 & 0 & 2 \end{bmatrix} \begin{bmatrix} \tilde{c}_{eg, \text{O}_2} \\ \tilde{c}_{eg, \text{CO}_2} \\ \tilde{c}_{eg, \text{CO}} \\ \tilde{c}_{eg, \text{CH}_4} \\ \tilde{c}_{eg, \text{NO}_x} \\ \tilde{c}_{eg, \text{H}_2\text{O}} \\ \tilde{c}_{eg, \text{N}_2} \end{bmatrix} = \\
 f_\nu \begin{bmatrix} \text{O}_2 & \text{H}_2\text{O} & \text{N}_2 & \text{C}_\nu\text{H}_w\text{O}_x\text{N}_y \\ 0 & 0 & 0 & \nu \\ 0 & 2 & 0 & w \\ 2 & 1 & 0 & x \\ 0 & 0 & 2 & y \end{bmatrix} \begin{bmatrix} \tilde{c}_{in, \text{O}_2} \\ \tilde{c}_{in, \text{H}_2\text{O}} \\ \tilde{c}_{in, \text{N}_2} \\ \tilde{c}_{in, \text{C}_\nu\text{H}_w\text{O}_x\text{N}_y} \end{bmatrix} \quad (\text{C.52})$$

where  $\tilde{c}_{in}$  and  $\tilde{c}_{eg}$  are the molar concentrations in the intake and exhaust streams, respectively, and  $f_\nu$  is the ratio of the number of moles in the intake stream to the number of moles in the exhaust stream.

The  $\text{O}_2$ ,  $\text{CO}$  and  $\text{CO}_2$  exhaust gas concentrations are measured on a dried gas sample. The corresponding concentrations based on the wet gas flow are given by the relation:

$$\tilde{c}_{eg} = \tilde{c}_m (1 - \tilde{c}_{eg, \text{H}_2\text{O}}) \quad (\text{C.53})$$

The  $\text{CH}_4$  and  $\text{NO}_x$  exhaust gas concentrations are directly measured on a wet gas sample. Therefore, the wet exhaust concentrations correspond directly to the measured concentrations. In a matrix form, the wet concentrations of the components measured can be written as follows:

$$\begin{bmatrix} \tilde{c}_{eg, \text{O}_2} \\ \tilde{c}_{eg, \text{CO}_2} \\ \tilde{c}_{eg, \text{CO}} \\ \tilde{c}_{eg, \text{CH}_4} \\ \tilde{c}_{eg, \text{NO}_x} \end{bmatrix} = \begin{bmatrix} \tilde{c}_{m, \text{O}_2} \\ \tilde{c}_{m, \text{CO}_2} \\ \tilde{c}_{m, \text{CO}} \\ \tilde{c}_{m, \text{CH}_4} \\ \tilde{c}_{m, \text{NO}_x} \end{bmatrix} - \begin{bmatrix} \tilde{c}_{m, \text{O}_2} \\ \tilde{c}_{m, \text{CO}_2} \\ \tilde{c}_{m, \text{CO}} \\ 0 \\ 0 \end{bmatrix} \tilde{c}_{eg, \text{H}_2\text{O}} \quad (\text{C.54})$$

Rearranging the left hand side of equation C.52 and introducing equation C.54 gives:

$$\mathbf{LHS} = \begin{bmatrix} 0 & 1 & 1 & 1 & 0 \\ 0 & 0 & 0 & 4 & 0 \\ 2 & 2 & 1 & 0 & 1 \\ 0 & 0 & 0 & 0 & 1 \end{bmatrix} \begin{bmatrix} \tilde{c}_{m, O_2} \\ \tilde{c}_{m, CO_2} \\ \tilde{c}_{m, CO} \\ \tilde{c}_{m, CH_4} \\ \tilde{c}_{m, NO_x} \end{bmatrix} + \begin{bmatrix} -\tilde{c}_{m, CO_2} - \tilde{c}_{m, CO} & 0 \\ 2 & 0 \\ 1 - 2\tilde{c}_{m, O_2} - 2\tilde{c}_{m, CO_2} - \tilde{c}_{m, CO} & 0 \\ 0 & 2 \end{bmatrix} \begin{bmatrix} \tilde{c}_{eg, H_2O} \\ \tilde{c}_{eg, N_2} \end{bmatrix} \quad (C.55)$$

where the first term and the matrix of the second term are entirely determined. This equation can be rewritten as:

$$\mathbf{LHS} = \mathbf{A} + \mathbf{B} \begin{bmatrix} \tilde{c}_{eg, H_2O} \\ \tilde{c}_{eg, N_2} \end{bmatrix} \quad (C.56)$$

Now considering the right hand side of equation C.52, the H<sub>2</sub>O and N<sub>2</sub> concentrations in the intake flow can be expressed as function of the O<sub>2</sub> concentration:

$$\tilde{c}_{in, H_2O} = \frac{w \tilde{m}_{air}}{\tilde{m}_{H_2O} \tilde{c}_{O_2, air}} \tilde{c}_{in, O_2} \quad (C.57)$$

$$\tilde{c}_{in, N_2} = \frac{\tilde{c}_{N_2, air}}{\tilde{c}_{O_2, air}} \tilde{c}_{in, O_2} \quad (C.58)$$

where  $w$  is the specific water content per unit of dry air given by equation C.30.

Introducing these two relations and rearranging gives:

$$\mathbf{RHS} = \begin{bmatrix} 0 & v \\ 2 \frac{w \tilde{m}_{air}}{\tilde{m}_{H_2O} \tilde{c}_{O_2, air}} & w \\ 2 + \frac{w \tilde{m}_{air}}{\tilde{m}_{H_2O} \tilde{c}_{O_2, air}} & x \\ 2 \frac{\tilde{c}_{N_2, air}}{\tilde{c}_{O_2, air}} & y \end{bmatrix} \begin{bmatrix} f_\nu \tilde{c}_{in, O_2} \\ f_\nu \tilde{c}_{in, C_\nu H_w O_x N_y} \end{bmatrix} \quad (C.59)$$

The elements of the matrix being known, it can be rewritten as:

$$\mathbf{RHS} = \mathbf{C} \begin{bmatrix} f_\nu \tilde{c}_{in, O_2} \\ f_\nu \tilde{c}_{in, C_\nu H_w O_x N_y} \end{bmatrix} \quad (C.60)$$

Assembling equations C.56 and C.60 gives:

$$\mathbf{A} + \mathbf{B} \begin{bmatrix} \tilde{c}_{eg, H_2O} \\ \tilde{c}_{eg, N_2} \end{bmatrix} = \mathbf{C} \begin{bmatrix} f_\nu \tilde{c}_{in, O_2} \\ f_\nu \tilde{c}_{in, C_\nu H_w O_x N_y} \end{bmatrix} \quad (C.61)$$

and rearranging,

$$[\mathbf{C} \quad -\mathbf{B}] \begin{bmatrix} f_\nu \tilde{c}_{in, O_2} \\ f_\nu \tilde{c}_{in, C_\nu H_w O_x N_y} \\ \tilde{c}_{eg, H_2O} \\ \tilde{c}_{eg, N_2} \end{bmatrix} = \mathbf{A} \quad (C.62)$$

which finally leads to:

$$\begin{bmatrix} f_\nu \tilde{c}_{in, O_2} \\ f_\nu \tilde{c}_{in, C_v H_w O_x N_y} \\ \tilde{c}_{eg, H_2O} \\ \tilde{c}_{eg, N_2} \end{bmatrix} = [\mathbf{C} \quad -\mathbf{B}]^{-1} \mathbf{A} \quad (\text{C.63})$$

The relative air to fuel ratio is given by:

$$\lambda = \frac{\tilde{c}_{in, O_2}}{\tilde{c}_{in, C_v H_w O_x N_y} \nu_{O_2, min}} \quad (\text{C.64})$$

and can directly be calculated with the two first terms of the solution vector because the term  $f_\nu$  simplifies.

Note that the condition that the sum of the exhaust gas concentrations must add up to one is not enforced here. However, the sum of the exhaust gas concentrations is computed during the calculation in order to control the integrity of the emission measurements and evaluate the effect of the assumptions made on the solution obtained.

### Turbocharger operating conditions

The measurement of the flow parameters at the turbocharger inlets and outlets enables the evaluation of its operating performance. This evaluation is based on the total (or stagnation) temperature and pressure, which can be calculated as follow:

The total temperature is derived from the total enthalpy, given by [86]:

$$h_t = h + \frac{v^2}{2} \quad (\text{C.65})$$

where  $v$  represents the local mean flow velocity

Assuming that the gas behave like an ideal gas, thus:

$$dh = c_p(T)dT \quad (\text{C.66})$$

equation C.65 becomes:

$$c_p(T_t) T_t = c_p(T) T + \frac{v^2}{2} \quad (\text{C.67})$$

Considering that  $c_p(T_t) \approx c_p(T)$ , the total temperature can be approximated by:

$$\boxed{T_t = T + \frac{v^2}{2 c_p(T)}} \quad (\text{C.68})$$

with the local mean flow velocity given by:

$$v = \frac{\dot{m}}{\rho A} = \frac{\dot{m} R T}{p A} \quad (\text{C.69})$$

where  $A$  is the local cross sectional area.

The total pressure corresponds to the pressure attained if the gas is isentropically brought to rest. Thus follows the relation:

$$\frac{p_t}{p} = \left( \frac{T_t}{T} \right)^{\frac{\gamma}{\gamma-1}} \quad (\text{C.70})$$

with

$$\gamma = \frac{c_p}{c_v} \quad (\text{C.71})$$

$$R = c_p - c_v \quad (\text{C.72})$$

Considering equation C.68, the total pressure becomes:

$$p_t = p \left( 1 + \frac{v^2}{2 c_p(T) T} \right)^{\frac{c_p(T)}{R}} \quad (\text{C.73})$$

The specific heat at constant pressure is expressed by:

$$c_p(T) = \sum_{i=1}^n c_i c_{p,i}(T) \quad (\text{C.74})$$

with

$$c_i = \frac{\dot{m}_i}{\sum_{i=1}^n \dot{m}_i} \quad (\text{C.75})$$

Where  $i$  are the different gas components. Their individual specific heat at constant pressure is calculated with polynomial temperature functions obtained by curve fitting on the data of *JANAF thermochemical tables* [48] (for natural gas, see appendix section C.2).

The ideal gas constant is given by:

$$R = \mathcal{R} \sum_{i=1}^n \left( \frac{c_i}{\tilde{m}_i} \right) \quad (\text{C.76})$$

The evaluation of the compressor performance is realised by reporting the operating conditions on the performance map. The performance map represents the evolution of the compressor efficiency as a function of the the ratio of total pressure between outlet and inlet and corrected mass flow rate, which are defined by [13]:

$$\pi = \frac{p_{t,out}}{p_{t,in}} \quad (\text{C.77})$$

$$\dot{m}_{corr} = \dot{m} \sqrt{\frac{T_{t,in} p_{ref}}{T_{ref} p_{t,in}}} \quad (\text{C.78})$$

In the case of the compressor used, the corrected mass flow rate is replaced by the corrected volume flow rate, based on the inlet conditions, which is expressed by [34]:

$$\dot{v}_{corr} = \frac{\dot{m} R T_{in}}{p_{in}} \sqrt{\frac{T_{t,in} p_{ref}}{T_{ref} p_{t,in}}} \quad \text{in} \quad \frac{m^3}{s} \quad (\text{C.79})$$

with

$$\dot{m} = \dot{m}_{air,hum} + \dot{m}_{ng} \quad (\text{C.80})$$

where  $\dot{m}_{air,hum}$  and  $\dot{m}_{ng}$  are the measured air and natural gas mass flow rates. The dry air and water vapour mass flow rates necessary to calculate the ideal gas constant can be determined with the specific water content per unit of dry air  $w$  given by equation C.30:

$$\dot{m}_{air,dry} = \dot{m}_{air,hum} \frac{1}{1+w} \quad (\text{C.81})$$

$$\dot{m}_{H_2O} = \dot{m}_{air,hum} \frac{w}{1+w} \quad (\text{C.82})$$

### C.3.2 Dynamic variables

The dynamic variables are variables which change during an engine cycle. In the present project, they are the pressure in the prechamber of cylinder 1, in the main chambers of cylinder 1 and 3, as well as in the intake and exhaust port of cylinder 1. Using a high speed data acquisition system, one hundred consecutive cycles of data were measured at  $0.5^\circ$  crank angle increments. The corresponding crankshaft angular position was measured to enable the analysis and evaluation of the combustion process and the angular position of the piston top dead centre was determined with an inductive transducer.

#### Pressure cycle

The pressure in the pre- and main combustion chambers were measured with piezo-electric transducers. Due to electrical and thermal drift, no external zero calibration can be realised and the signal is *floating*. This means that the measured pressure cycle is shifted from its *true* position and therefore requires a uniform translation over the whole cycle, based on a reference value. This correction is necessary to enable the accurate calculation of the heat release cycle and has been realised with the polytropic method [38]. This method is based on the fact that between  $90$  and  $40^\circ CA_{BTDC}$  the heat transfer to the cylinder wall is approximately constant, resulting in a polytropic compression of constant coefficient and thus:

$$p V^n = constant \quad (\text{C.83})$$

This relation can be rewritten as follow:

$$p_2 = (p_2 - p_1) \frac{V_1^n}{V_1^n - V_2^n} \quad (\text{C.84})$$

where the first term of the right hand side can be evaluated on the basis of the measured pressure cycle (the difference is not affected by the pressure shift), and the cylinder volume as a function of the crank angle is given by the following relation [38]:

$$V(\varphi) = \frac{\pi B^2 S}{4} \left[ \frac{1}{\epsilon - 1} + \frac{1}{2} (1 - \cos \varphi) + \frac{L}{S} \left[ 1 - \sqrt{1 - \left( \frac{S}{2L} \sin \varphi \right)^2} \right] \right] \quad (\text{C.85})$$

with  $\varphi$ , the crank angle ( $0^\circ CA$  at TDC),  $B$ , the cylinder bore,  $S$ , the piston stroke and  $L$ , the connecting rod length.

The pressure correction corresponds to the difference between the measured and the corrected values and is expressed by:

$$\Delta p_{corr} = p_2 - p_{2,corr} = p_2 - (p_2 - p_1) \frac{V_1^n}{V_1^n - V_2^n} \quad (\text{C.86})$$

where the reference crank angles are  $90$  (1) and  $40$  (2)  $^\circ CA_{BTDC}$ , respectively.

Finally the corrected pressure cycle becomes:

$$p_{corr}(\varphi) = p(\varphi) + \Delta p_{corr} \quad (\text{C.87})$$

The polytropic coefficient  $n$  depends on the intensity of the heat transfer to the combustion chamber wall and therefore on the flow motion induced during the intake stroke. Typical values indicated in the literature for a spark ignition engine range from 1.30 [13] to 1.35 [38] and for a diesel engine from 1.36 to 1.38 [38]. Because the tested engine is converted from a diesel engine, the individual pressure cycles were corrected alternatively with polytropic coefficient ranging from 1.30 to 1.38. The mean instantaneous polytropic coefficient was then derived from equation C.83 and determined on the basis of the average pressure cycle as follow:

$$\bar{n}(\varphi_j) = \frac{\ln \overline{p(\varphi_{j+3})} - \ln \overline{p(\varphi_{j-3})}}{\ln \overline{V(\varphi_{j-3})} - \ln \overline{V(\varphi_{j+3})}} \quad (\text{C.88})$$

where

$$\overline{p(\varphi_j)} = \frac{1}{m} \sum_{i=1}^m p_i(\varphi_j) \quad (\text{C.89})$$

with  $m$ , the number of stored pressure cycles.

The determination over a short crank angle interval ( $\varphi_{j-3}$ ,  $\varphi_{j+3}$ ) realises a smoothing of the curve which eases its interpretation. The results corresponding to the two extreme values of polytropic coefficient are represented together with the one selected in **figure C.13**. Due to the much shorter crank angle interval considered, the mean values at  $40^\circ CA_{BTDC}$  no longer correspond to the one used for the correction of the individual pressure cycles. The value of 1.32 gives an approximately constant polytropic coefficient over the crank angle range between  $90$  and  $40^\circ CA_{BTDC}$  and was therefore used for the correction of the pressure cycles in the main combustion chambers of



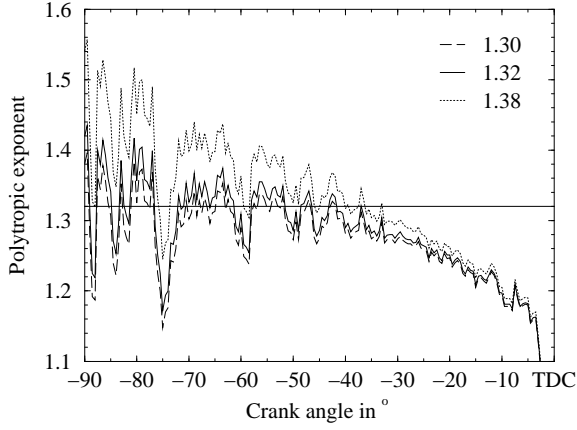


**Figure C.13:** Evolution of the average instantaneous polytropic coefficient after pressure cycle correction with different value of constant polytropic coefficient.

cylinder 1 and 3, as well as for the determination of the corresponding heat release cycles.

The composition of the gas mixture located in the prechamber and the heat transfer to the wall are affected by the flow through the nozzle orifices and thus differ from the main chamber conditions. Consequently, the correction method used in the case of the main chamber cannot be applied for the prechamber. Up to inlet valve closure (IVC), the flow between the main chamber and the prechamber is very weak, generating no significant pressure drop. It is therefore assumed that the pressure at IVC is the same in both chambers and the pressure correction of equation C.87 becomes:

$$\Delta p_{corr} = p_{main}(\varphi_{IVC}) - p_{pre}(\varphi_{IVC}) \quad (\text{C.90})$$

In order to ease the interpretation of the measured pressure cycle, a theoretical compression-expansion cycle, representing an unfired engine cycle, is usually plotted simultaneously. It is calculated as follows:

Up to the spark timing crank angle, the pressure of the unfired cycle is equal to the average measured pressure. Thus,

$$p_{unf}(\varphi_j) = \overline{p(\varphi_j)} \quad \text{if } \varphi_j < \varphi_{st} \quad (\text{C.91})$$

then it is evaluated on the basis of the conditions at the spark timing crank angle, considering a polytropic compression-expansion of constant coefficient expressed by equation C.83:

$$p_{unf}(\varphi_j) = \overline{p(\varphi_{st})} \left( \frac{V(\varphi_{st})}{V(\varphi_j)} \right)^{\overline{n(\varphi_{st})}} \quad \text{if } \varphi_j \geq \varphi_{st} \quad (\text{C.92})$$

The pressure in the intake and exhaust ports of cylinder 1 were measured with piezoresistive transducers. These transducers measure absolute pressure and were calibrated over the engine operating range. Thus, they do not require a pressure correction.

### Indicated mean effective pressure

The indicated mean effective pressure is the work delivered to the piston over the entire four strokes of the cycle, per unit displaced volume:

$$p_{mi} = \frac{4}{\pi B^2 S} \oint p dV \quad (\text{C.93})$$

In the case of a pressure cycle measured at regular intervals, it can be approximated by:

$$p_{mi} = \frac{4}{\pi B^2 S} \sum_{j=1}^k p(\varphi_j) \frac{V(\varphi_{j+1}) - V(\varphi_{j-1})}{2} \quad (\text{C.94})$$

The variation of the indicated mean effective pressure established on a sample of consecutive engine cycles is an adequate means of evaluating the operating stability. This cycle-by-cycle variability is usually expressed in term of the coefficient of variance of the indicated mean effective pressure, which corresponds to standard deviation divided by the mean:

$$COV_{p_{mi}} = \frac{\sigma_{p_{mi}}}{\overline{p_{mi}}} \quad (\text{C.95})$$

where

$$\sigma_{p_{mi}} = \sqrt{\frac{1}{m(m-1)} \left[ m \sum_{i=1}^m p_{mi}^2 - \left( \sum_{i=1}^m p_{mi} \right)^2 \right]} \quad (\text{C.96})$$

and

$$\overline{p_{mi}} = \frac{1}{m} \sum_{i=1}^m p_{mi} \quad (\text{C.97})$$

### Heat release cycle

The heat release cycle represents the way the fuel chemical energy is converted into heat by the combustion process during the engine cycle. It can be determined from the pressure cycle by using an approach based on the first law of thermodynamics. Considering the combustion chamber contents as a single zone, the first law for an open system is [86]:

$$dU = \partial E^+ + \partial Q^+ + \sum_j h_j dm_j^+ \quad (\text{C.98})$$

Based on the simplified combustion chamber model represented in **figure C.14**, the term of the left hand side corresponds to the variation of the internal energy. The first

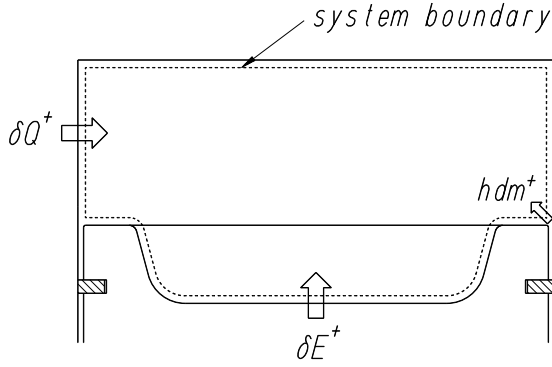


**Figure C.14:** Simplified combustion chamber model for pressure cycle analysis and heat release calculation

term of the right hand side represents the mechanical work through the piston motion, the second term, the heat transferred through the combustion chamber wall and the third term, the enthalpy of the gas exchanged with the piston ring crevices, which is partly transferred to the crankcase (blowby). The superscript “+” indicates that the variable is positive when brought to the system and is negative when delivered from the system.

Considering the gas contained in the combustion chamber as formed by  $n$  components  $i$ , which mass fraction  $c_i$  varies during the combustion process, the internal energy can be written:

$$U = \sum_{i=1}^n m c_i u_i \quad (\text{C.99})$$

with

$$m = \sum_{i=1}^n m_i, \quad c_i = \frac{m_i}{m} \quad (\text{C.100})$$

Differentiating equation C.99 gives:

$$dU = dm \sum_{i=1}^n c_i u_i + m \sum_{i=1}^n c_i du_i + m \sum_{i=1}^n u_i dc_i \quad (\text{C.101})$$

The gas mixture contained in the combustion chamber evolves far away from the saturation curve. It is therefore assumed that it is governed by the ideal gas law:

$$pV = mRT \quad (\text{C.102})$$

thus

$$du_i = c_{v_i} dT \quad (\text{C.103})$$

Equation C.101 becomes:

$$dU = dm \sum_{i=1}^n c_i u_i + m \sum_{i=1}^n c_i c_{v_i} dT + m \sum_{i=1}^n u_i dc_i \quad (\text{C.104})$$

and in a simplified form:

$$dU = u dm + m c_v dT + m \sum_{i=1}^n u_i dc_i \quad (\text{C.105})$$

with

$$u = \sum_{i=1}^n c_i u_i \quad (\text{C.106})$$

$$c_v = \sum_{i=1}^n c_i c_{v_i} \quad (\text{C.107})$$

The three terms on the right hand side of equation C.105 represents the contributions from total mass variation, temperature change due to heat transfer and variation in gas composition due to chemical reactions.

The total differential of the temperature is given by:

$$dT = \frac{1}{m R} \left( V dp + p dV - \frac{pV}{m} dm - \frac{pV}{R} dR \right) \quad (\text{C.108})$$

and becomes, when introducing equation C.102:

$$dT = \frac{1}{m R} (V dp + p dV - RT dm - m T dR) \quad (\text{C.109})$$

where

$$R = \sum_{i=1}^n c_i R_i = \mathcal{R} \sum_{i=1}^n \frac{c_i}{\tilde{m}_i} \quad (\text{C.110})$$

$$dR = \mathcal{R} \sum_{i=1}^n \frac{dc_i}{\tilde{m}_i} \quad (\text{C.111})$$

Introducing equation C.109 into equation C.105 and then into equation C.98 gives:

$$\begin{aligned} u dm + \frac{c_v}{R} (V dp + p dV) - c_v T dm - m c_v T \frac{dR}{R} + m \sum_{i=1}^n u_i dc_i \\ = -p dV + \partial Q^+ + h dm \end{aligned} \quad (\text{C.112})$$

rearranging the equation leads to:

$$\begin{aligned} m c_v T \frac{dR}{R} - m \sum_{i=1}^n u_i dc_i = p dV + \frac{c_v}{R} (V dp + p dV) \\ - \partial Q^+ - (h - u + c_v T) dm \end{aligned} \quad (\text{C.113})$$

The two terms on the left hand side represent the chemical energy converted into heat, which is commonly called combustion *gross heat release*. The first term of the right hand side corresponds to the mechanical work exchanged through the piston. The second term represents the change in sensible energy due to the variation of gas temperature.

The third term corresponds to the heat transferred through the combustion chamber wall and the fourth term represents the energy loss through the crevices gas exchange mechanism and blowby flow.

The heat transferred through the wall can be approximated by the relation:

$$\frac{dQ_{wall}^+}{dt} = A_{wall} k (T_{wall} - T) \quad (C.114)$$

where  $A_{wall}$  is the combustion chamber wall surface,  $k$  is the average heat transfer coefficient and  $T_{wall}$ , the mean wall temperature. The average heat transfer coefficient is a function of the gas temperature and in cylinder flow motion.

The determination of the gross heat release requires the development of sub-models describing the heat transfer coefficient and the mechanism of the crevice gas exchange. A simplified way of evaluating the combustion process consists in determining the *net heat release*, which corresponds to the gross heat release less the heat transferred to the combustion chamber wall and the enthalpy loosed by the blowby. Reorganising equation C.113, the net heat release is expressed by:

$$\begin{aligned} dQ_{hr,n} &= m c_v T \frac{dR}{R} - m \sum_{i=1}^n u_i dc_i + \partial Q^+ + (h - u + c_v T) dm \\ &= p dV + \frac{c_v}{R} (V dp + p dV) \end{aligned} \quad (C.115)$$

Considering Mayer's formula  $R = c_p - c_v$  and the isentropic coefficient  $\gamma = c_p/c_v$ , it becomes:

$$dQ_{hr,n} = \frac{1}{\gamma - 1} (\gamma p dV + V dp) \quad (C.116)$$

The isentropic coefficient depends on the gas composition and is also a function of the temperature. It decreases when the temperature increases. An approximate approach with a constant isentropic coefficient during combustion has been shown to give adequate results [13]. Further, similarly to the method of *Rassweiler* and *Withrow* [88], the use of the polytropic coefficient characterising the compression stroke has also been suggested [75] to partly account for the heat transfer effect. This is the simplified approach used here and the final relation for the heat release becomes:

$$dQ_{hr} = \frac{1}{n - 1} (n p dV + V dp) \quad (C.117)$$

where  $n = 1.32$ , which corresponds to the value used for the pressure cycle correction.

The heat release rate can be established by approximating the derivatives by finite differences and introducing the dependency to the crank angle as follow:

$$\begin{aligned} \frac{dQ_{hr}(\varphi_j)}{d\varphi} &\approx \frac{\Delta Q_{hr}(\varphi_j)}{\Delta\varphi} = \frac{1}{(n - 1) |\varphi_{j+1} - \varphi_{j-1}|} \\ &\left[ n p(\varphi_j) (V(\varphi_{j+1}) - V(\varphi_{j-1})) \right. \\ &\left. + V(\varphi_j) (p(\varphi_{j+1}) - p(\varphi_{j-1})) \right] \end{aligned} \quad (C.118)$$

Related to the piston displacement volume and in suitable units, it becomes:

$$\frac{\Delta Q_{hr}(\varphi_j)}{\Delta\varphi} = \frac{4 \cdot 10^2}{\pi B^2 S (n-1) |\varphi_{j+1} - \varphi_{j-1}|} \left[ n p(\varphi_j) \left( V(\varphi_{j+1}) - V(\varphi_{j-1}) \right) + V(\varphi_j) \left( p(\varphi_{j+1}) - p(\varphi_{j-1}) \right) \right] \text{ in } \frac{kJ}{^\circ CA m^3} \quad (C.119)$$

The heat release integral can then be determined as follows:

$$Q_{hr}(\varphi_j) = \int_{\varphi_{j_s}}^{\varphi_j} dQ_{hr}(\varphi) = \int_{\varphi_{j_s}}^{\varphi_j} \frac{dQ_{hr}(\varphi)}{d\varphi} d\varphi \quad (C.120)$$

and approximated by:

$$Q_{hr}(\varphi_j) \approx \sum_{\varphi_{j_s}}^{\varphi_j} \frac{\Delta Q_{hr}(\varphi)}{\Delta\varphi} \Delta\varphi = \sum_{l=j_s}^j \frac{\Delta Q_{hr}(\varphi_l)}{\Delta\varphi} (\varphi_l - \varphi_{l-1}) \quad (C.121)$$

where  $\varphi_{j_s}$  was chosen equal to  $30^\circ CA_{BTDC}$  because the earliest spark timing was about this value. The upper summation boundary  $\varphi_{j_e}$  was fixed to  $90^\circ CA_{ATDC}$ .

Despite the approximations of the present model, it enables a relatively objective comparison of combustion processes characterising different engine configurations. Further, the development of a more refined model for pressure cycle analysis was outside the scope of this study.

The heat release rate and the integral heat release are determined for each individual pressure cycle measured and the average values used for representation are given by:

$$\frac{\overline{\Delta Q_{hr}(\varphi_j)}}{\Delta\varphi} = \frac{1}{m} \sum_{i=1}^m \frac{\Delta Q_{hr,i}(\varphi_j)}{\Delta\varphi} \quad (C.122)$$

$$\overline{Q_{hr}(\varphi_j)} = \frac{1}{m} \sum_{i=1}^m Q_{hr,i}(\varphi_j) \quad (C.123)$$

## Combustion process characterisation

The combustion process starts directly after the spark triggering with the development of a flame kernel. The flame then propagate rapidly through the unburnt mixture until it quenches when reaching the combustion chamber walls. Finally, the unburnt mixture located in the quenching layer and emerging from the crevices mixes with the burnt gas and oxidises, releasing the remaining chemical energy. The angular positions where the flame kernel development and the rapid flame propagation stages end represent two key combustion process characteristics. They are often considered as effective start and end of the combustion process. The end of the flame kernel development stage is defined here by the crank angle position where 5% of the total heat has been released. The determination of the end of the flame propagation stage is more difficult because the rate of heat release becomes of the same order as the other energy transfer processes. Therefore, the end of the flame propagation stage is defined here by the

crank angle position where 90 % of the total heat has been released. Consequently, the combustion duration is defined by the difference between these two particular angular positions. In the case of the direct spark ignition, the flame development starts almost immediately and there is no effective ignition delay in the sense of the *diesel* principle. However, when the spark ignition is located in a small adjacent prechamber, there is a delay between the spark triggering and the start of the flame propagation in the main chamber. The ignition delay is defined by the difference between the angular positions where 5 % of the total main chamber heat has been released and of the effective spark timing. In order to avoid confusion and because it is not introducing an inconsistency, the term *ignition delay* is also used for the few experiments with direct spark ignition, instead of *flame development duration*, throughout this text.

The effective spark timing is determined on the basis of the discharge current in the high voltage cable between the ignition coil and the spark plug with an inductive transducer coupled to the high speed acquisition system for pressure indication. The acquisition system delivers a voltage square pulse signal. Ignition is defined by the angular position of the pulse leading edge, when the intensity exceeds 25 % of the maximum amplitude.

The start and end of combustion are determined on the integral heat release of the individual pressure cycles and are given by:

$$\varphi_{Q_{5\%}} = \varphi_j \quad \text{when} \quad Q_{hr}(\varphi_j) = 0.05 Q_{hr}(\varphi_{j_e}) \quad (\text{C.124})$$

$$\varphi_{Q_{90\%}} = \varphi_j \quad \text{when} \quad Q_{hr}(\varphi_j) = 0.9 Q_{hr}(\varphi_{j_e}) \quad (\text{C.125})$$

and the average values are:

$$\overline{\varphi_{Q_{5\%}}} = \frac{1}{m} \sum_{i=1}^m \varphi_{Q_{5\%}} \quad (\text{C.126})$$

$$\overline{\varphi_{Q_{90\%}}} = \frac{1}{m} \sum_{i=1}^m \varphi_{Q_{90\%}} \quad (\text{C.127})$$

Finally, the ignition delay and the combustion duration are calculated from the average angular positions of the spark timing and the start and end of combustion as follow:

$$\Delta\varphi_{id} = \overline{\varphi_{Q_{5\%}}} - \overline{\varphi_{st}} \quad (\text{C.128})$$

$$\Delta\varphi_{cd} = \overline{\varphi_{Q_{90\%}}} - \overline{\varphi_{Q_{5\%}}} \quad (\text{C.129})$$

with

$$\overline{\varphi_{st}} = \frac{1}{m} \sum_{i=1}^m \varphi_{st} \quad (\text{C.130})$$

### Temperature cycle

The mean temperature cycle is determined on the basis of the average pressure cycle and considering the ideal gas law as follow:

$$T(\varphi_j) = \frac{\overline{p(\varphi_j)} V(\varphi_j)}{m(\varphi_j) R(\varphi_j)} \quad (\text{C.131})$$

If only the crank angle domain between intake valve closure and exhaust valve opening is considered, while neglecting the blowby, the mass contained in the cylinder is constant. Thus,

$$m(\varphi_j) = m = \frac{120 \dot{m}}{n z} \quad (\text{C.132})$$

The ideal gas constant depends on the gas composition and therefore varies in space and in time during combustion. For consistency with the simplified approach used to compute the heat release cycle and because the engine is operating with a very lean fuel-air mixture, it is here approximated by the value for air:

$$R(\varphi_j) = R_{air} = \frac{\mathcal{R}}{\tilde{m}_{air}} = 287 \frac{J}{kg K} \quad (\text{C.133})$$

Similarly, the temperature of an unfired cycle is calculated as follow:

$$T_{unf}(\varphi_j) = \frac{p_{unf}(\varphi_j) V(\varphi_j)}{m R_{air}} \quad (\text{C.134})$$



## C.4 Influence of specific engine parameters

### C.4.1 Introduction

A complementary study of the influence of specific engine parameters was undertaken in order to evaluate the potential to reduce the relatively high CO emissions of the direct ignition operating mode. The main objective was to reduce the CO emissions under the Swiss limit without catalytic exhaust gas after treatment, to enable the operation on biogas produced by sewage digestion or landfill decomposition. This biogas contains heavy metals, which rapidly deactivate the catalytic coating by permanently occupying the reaction sites. The Swiss Clean Air Act (*OPair*) [1] takes into account this technical limitation through a higher maximum prescribed value for NO<sub>x</sub> emissions of 400 instead of 250 mg/m<sub>N</sub><sup>3</sup>, 5% O<sub>2</sub>. The maximum limit for CO emissions remains unchanged at 650 mg/m<sub>N</sub><sup>3</sup>, 5% O<sub>2</sub>. The principal parameters evaluated were the volumetric compression ratio, the intake and exhaust valves overlap duration and the location of the first piston compression ring. Due to the absence of a biogas source (direct supply or possibility of storage in cylinders) and the high cost of synthetic biogas, natural gas of known composition was used for this study. The data presented is also given in a tabulated form in appendix C.5.

### C.4.2 Volumetric compression ratio

The compression ratio was reduced in a first stage from 12.0 to 9.7 through a deepening of the original piston bowl, while keeping a sufficient bowl wall thickness (**figure C.15, a**). In a second stage, a further reduction of the compression ratio to 9.0 was realised through a new bowl design (**figure C.15, b**). The objective was also to increase the squish surface of the piston crown, in order to compensate somewhat for the combustion slowing down, resulting from the compression ratio reduction. Due to delivery delay, this piston had to be realised out of the piston for diesel operation, thus limiting the potential of increasing the squish effect.

The reduction of the volumetric compression ratio from 12.0 to 9.7 leads to about 30% decrease in CO emissions as well as approximately 45% reduction of THC emissions, for constant NO<sub>x</sub> emissions (**figure C.16, a**). The decrease in pressure at spark timing, associated with the decrease in compression ratio, (**figure C.17, c**) increases the minimum initial flame kernel size required to release enough energy to enable the flame self propagation [58]. This results in an increase of the ignition delay of approximately 5°CA (**figure C.17, a**), which shifts the combustion process into the expansion phase. The rapid decrease of flow turbulence kinetic energy during expansion more than compensates the effect of a higher relative air to fuel ratio and leads to an increase of the combustion duration. The shift and consequent slowing down of the combustion process results in about 2%-point decrease in fuel conversion efficiency, for constant NO<sub>x</sub> emissions (**figure C.16, b**). The decrease in peak combustion temperature resulting from the reduction of peak cylinder pressure (**figure C.17, c**) results in a further reduction of the NO<sub>x</sub> emissions and an increase of the relative air to fuel

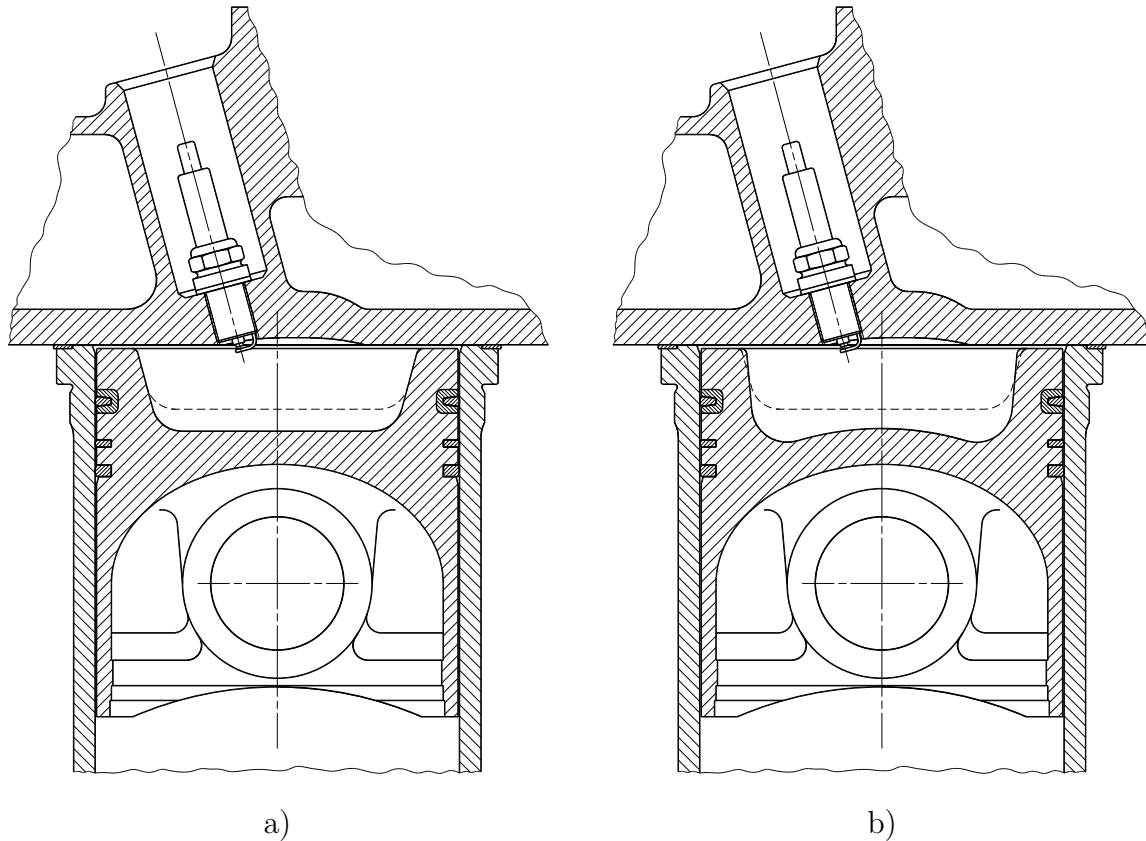


**Figure C.15:** Combustion chambers: a) with piston *C*,  $\epsilon = 9.7$ , b) with piston *D*,  $\epsilon = 9.0$ ; with the dashed outline of piston *A* ( $\epsilon = 12.0$ ).

ratio, which improves the combustion stability; this is expressed by a decrease of the coefficient of variance of the indicated mean effective pressure ( $COV_{pmi}$ ). The much lower cylinder pressure reduces the amount of unburned mixture stored in the combustion chamber crevices at the end of the primary combustion process (through flame propagation) and therefore the quantity of CO emissions generated through hydrocarbon partial secondary oxidation. On the other hand, the slower combustion process results in an increase of the average temperature during expansion (**figure C.17, d**), which promotes a more complete oxidation of the unburnt hydrocarbons emerging from the crevices. These effects both result in a simultaneous and important reduction of CO and THC emissions, able to comply with the Swiss emissions regulation.

A further reduction of the volumetric compression ratio from 9.7 to 9.0 results in an approximately 8% and 4% reduction of CO and THC emissions, respectively, for constant  $NO_x$  emissions (**figure C.16, c**). However, the further increase of the ignition delay and particularly a more pronounced slowing down of the combustion process (**figure C.17, b**) leads to an important complementary decrease in fuel conversion efficiency of about 1.5%-point for constant  $NO_x$  emissions (**figure C.16, d**). The more important THC emissions obtained with piston *C* during the second test serial (C.2), which can be observed when comparing **figure C.16, a** and **figure C.16, c**, originates in the higher methane content of the natural gas blend used.

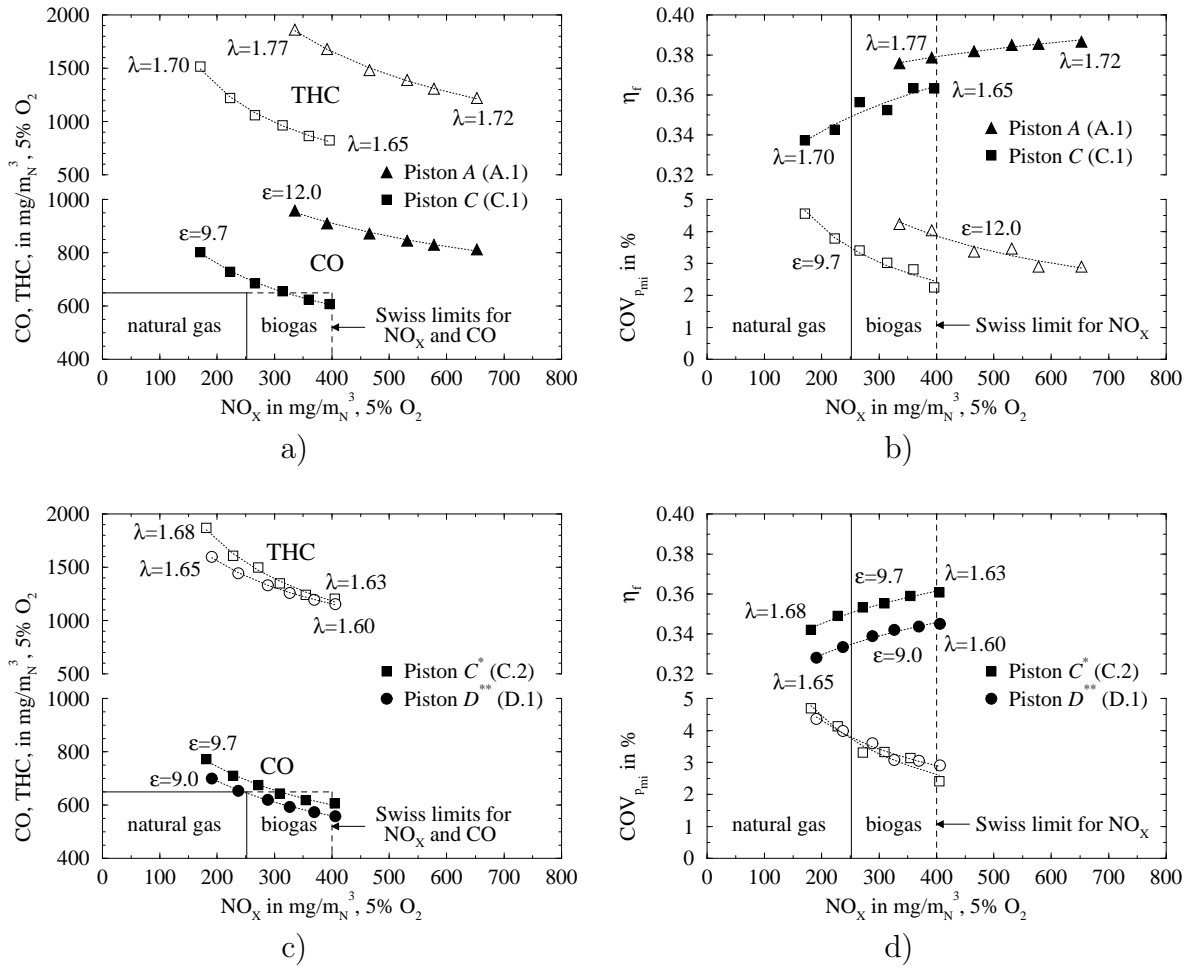


**Figure C.16:** Effect of a volumetric compression ratio reduction from 12.0 to 9.7 on the CO and THC emissions (a) and on the fuel conversion efficiency and coefficient of variance of  $p_{mi}$  (b) (NG2); effect of a complementary reduction from 9.7 to 9.0 on the CO and THC emissions (c) and on the fuel conversion efficiency and coefficient of variance of  $p_{mi}$  (d) (NG3);  $ST = 26.7^\circ\text{C} A_{BTDC}$ ,  $T_{mixt} = 90^\circ\text{C}$ ,  $RH = 45$  (\*50, \*\*30) %.

These tests show the major effect of the compression ratio on the exhaust emissions. A reduction of compression ratio is an effective means of decreasing the CO emissions, but proves also detrimental to the fuel conversion efficiency; the effect on the fuel conversion efficiency being even more pronounced when the reduction of compression ratio is important.

### C.4.3 Valve overlap duration

Appropriate intake and exhaust valve overlap enables the achievement of a more effective combustion chamber scavenging and a reduction of the engine pumping work. For a diesel engine, a limited direct transfer of air from the intake to the exhaust port is beneficial to reduce the amount of residuals trapped in the compression volume. In the case of a gas engine operating on the *Otto* principle, a direct transfer of fuel-air mixture would result in a significant increase in exhaust emissions. Mixed with the

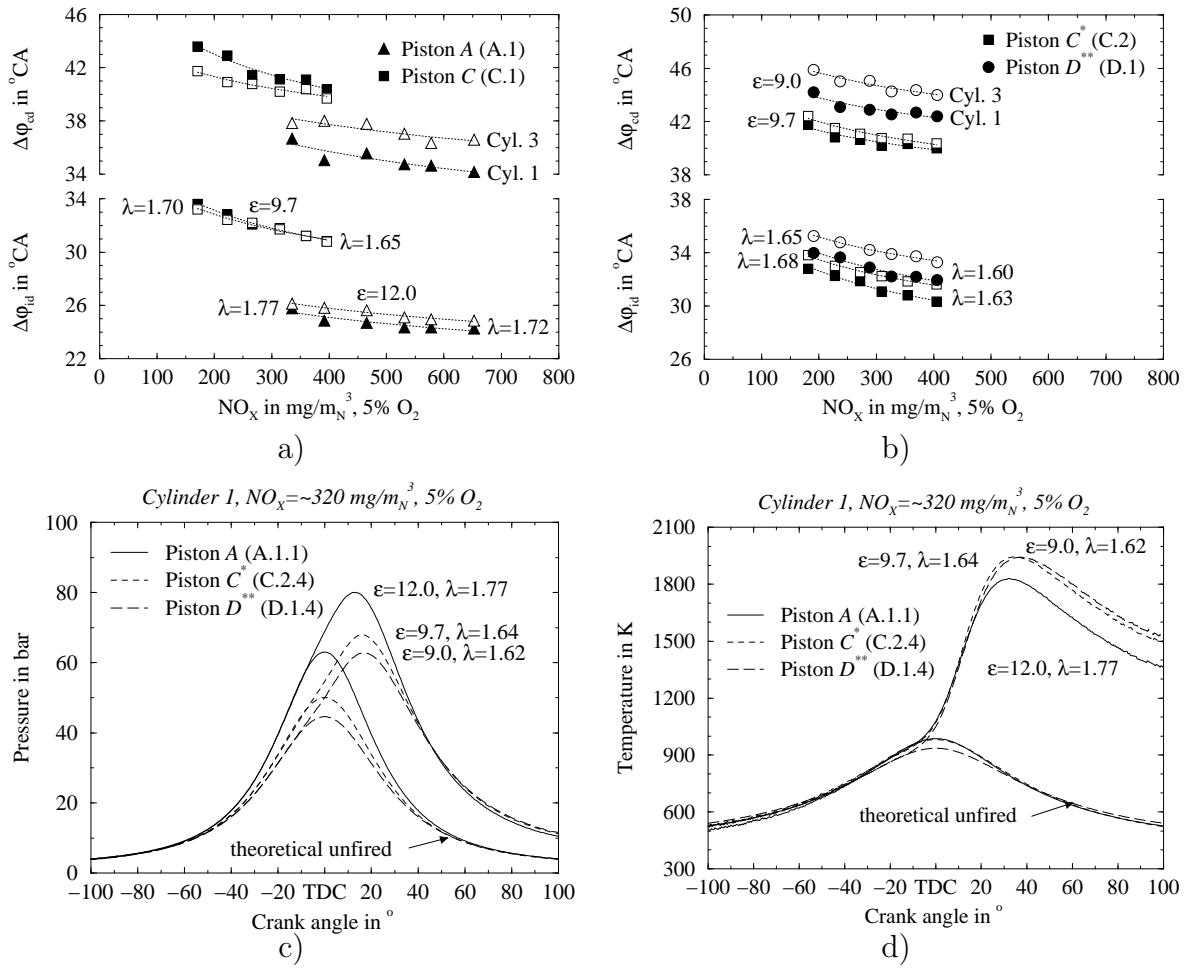


**Figure C.17:** Influence of the volumetric compression ratio on the combustion process: effect of a reduction from 12.0 to 9.7 (a) (NG2) and from 9.7 to 9.0 (b) (NG3) on the ignition delay and combustion duration; effect on the mean pressure (c) and average combustion temperature cycles (d) in cylinder 1, for  $\text{NO}_x$  emissions of  $\approx 320 \text{ mg/m}_N^3$ , 5%  $\text{O}_2$ ;  $ST = 26.7^\circ\text{CA}_{BTDC}$ ,  $T_{\text{mixt}} = 90^\circ\text{C}$ ,  $RH = 45$  (\*50, \*\*30) %.

hot exhaust gas, the unburnt hydrocarbons would partly react to form intermediate products or CO. In order to evaluate the contribution of the direct transfer of unburnt mixture to the exhaust to the global CO and THC emissions, a cam shaft with reduced valve overlap was developed by the engine manufacturer and tested. The theoretical intake and exhaust valve stroke (considering an infinitely rigid valve-gear and no tappet clearance) generated by the original diesel and the modified cam shafts are represented together in **figure C.18, a**. The valve strokes, after deduction of the tappet clearance (0.25 mm for the intake and 0.30 mm for the exhaust), are plotted in **figure C.18, b** to illustrate the effective theoretical valve overlap duration. The use of the modified cam shaft results in a reduction of valve overlap duration from 40 to 16  $^\circ\text{CA}$ .

For constant  $\text{NO}_x$  emissions, the reduction of the valve overlap duration leads to a moderate decrease in THC emissions of about 5% and no significant change in CO emissions (**figure C.19, a**). On the other hand, this results in a reduction of fuel conversion efficiency of approximately 0.5% and a perceptible decrease of engine operating stability (**figure C.19, b**). The reduction of the valve overlap duration has no

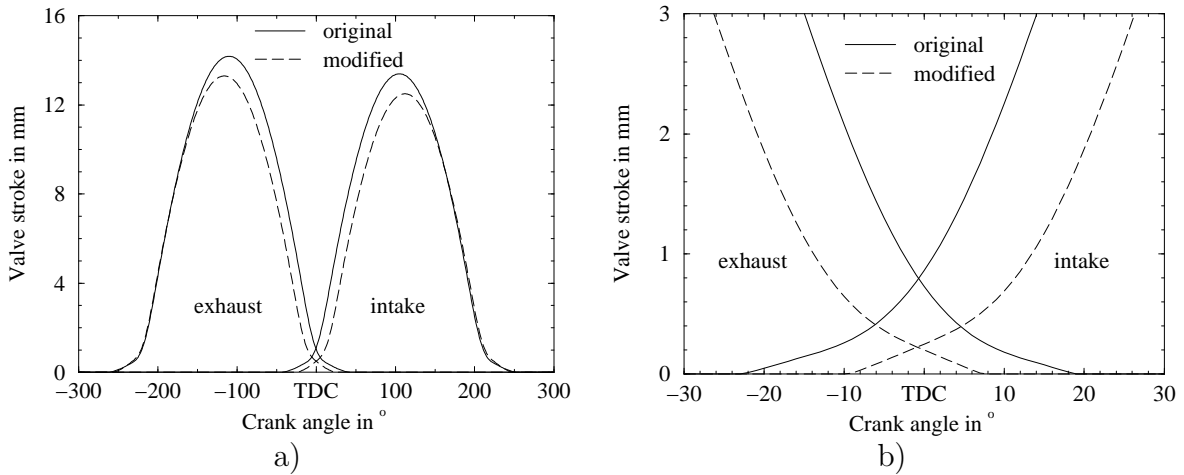


**Figure C.18:** Theoretical intake and exhaust valves stroke generated by the original cam shaft for diesel operation and the modified cam shaft with reduced valves overlap: a) without tappet clearance, b) detail of the valve overlap after deduction of the tappet clearance (0.25 and 0.30 mm for intake and exhaust, respectively).

significant influence on the combustion process in cylinder 1, but causes a perceptible increase of combustion duration in cylinder 3 (**figure C.19, c**). The slowing down of the combustion in cylinder 3 could originate from an increase of unburnt mixture residual concentration in this particular cylinder, due to a change in exhaust port and manifold gas dynamics. Similar changes in other cylinders (without pressure indication) could also explain the notable degradation of the engine operating stability. The less effective cylinder scavenging requires a slightly higher boost pressure to achieve the same filling with fuel-air mixture (**figure C.19, d**). The increase of mass flow rate resulting from the lower fuel conversion efficiency, associated with the higher exhaust gas total temperature, leads to a higher total pressure before turbine. The corresponding increase of energy available to the turbine compensate the greater mechanical power required by the compressor to achieve the higher boost pressure. The increase in exhaust gas temperature (total temperature before turbine) originates mainly in a longer combustion duration in certain cylinders and partly in the somewhat lower dilution with unburnt mixture flowing directly from the intake into the exhaust port. The decrease in fuel conversion efficiency results principally from the increase of engine pumping work, which is expressed by a significant increase of the area delimited by the pumping loop in the indicator diagram (**figure C.20**). The drop in efficiency originates also to some extent from the longer combustion duration in certain cylinders.

Considering the moderate effect of a reduction of valve overlap duration on the exhaust gas emissions (weak on the THC and not significant on the CO) and the significant reduction in fuel conversion efficiency and engine operating stability, the use of a modified cam shaft for gas operation is not justified. Therefore, the original cam shaft for diesel operation has been reinstalled on the engine.

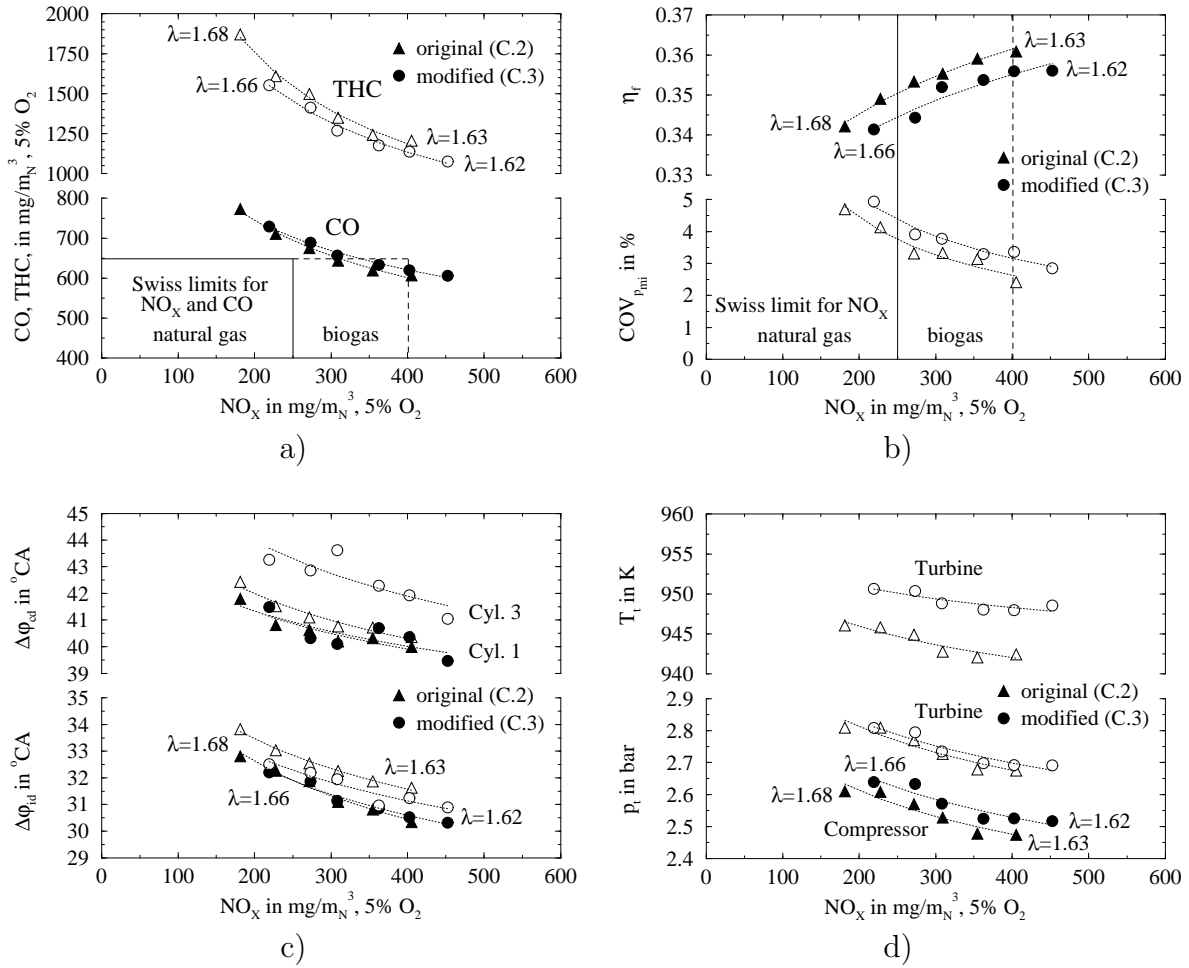


**Figure C.19:** Influence of the intake and exhaust valves overlap on the engine emissions and performance: a) CO and THC emissions, b) fuel conversion efficiency and coefficient of variance of  $p_{mi}$ , c) Ignition delay and combustion duration, d) total boost pressure and total pressure and temperature before turbine; Piston  $C$  ( $\epsilon = 9.7$ ),  $ST = 26.7^\circ\text{C}_{BTDC}$ ,  $T_{mixt} = 90^\circ\text{C}$ ,  $RH = 50\%$ , NG3.

#### C.4.4 Location of the piston first compression ring

The volume located between the piston, the first compression ring and the cylinder liner represents the largest combustion chamber crevice not accessible to the flame front. During compression and combustion, unburnt mixture flows into the combustion chamber crevices until the time when the flame reaches their entrance and quenches. If the cylinder pressure continues to rise, burnt gas will start to flow into the crevices and the amount will depend on the relative location of the spark plug to the crevice entrances. Due to the high surface to volume ratio, the gas in the crevices rapidly cools to close to the local wall temperature, resulting in a relatively important mass stored; the gas density in the crevices is several times higher than the gas density of the bulk gases. Following peak cylinder pressure, the crevice gas flows back into the cylinder and mixes with the hot bulk gases. Brought to high temperature, the emerging unburnt hydrocarbons start to react (secondary oxidation). As the cylinder pressure falls, the bulk gas temperature decreases and the oxidation kinetic reactions

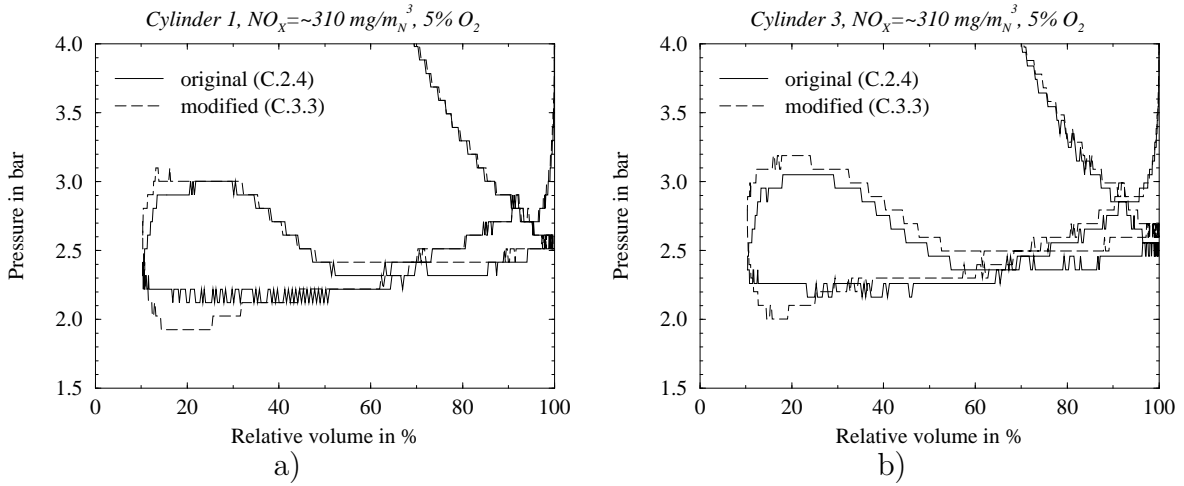


**Figure C.20:** Influence of the intake and exhaust valves overlap on the pumping loop in cylinder 1 (a) and 3 (b) for NO<sub>x</sub> emissions of  $\approx 310 \text{ mg/m}_N^3$ , 5%O<sub>2</sub> ; Piston C ( $\epsilon = 9.7$ ),  $ST = 26.7^\circ\text{C} A_{BTDC}$ ,  $T_{mixt} = 90^\circ\text{C}$ ,  $RH = 50\%$ , NG3.

slow down, leaving unreacted fuel molecules and intermediate combustion products like CO. Depending on their location relative to the exhaust valve, part of these partially burnt products are scavenged and end up in the exhaust gas, forming a substantial part of the emissions. Several studies on spark ignition petrol engines [13, 56, 57] have shown that the piston top land crevice represents one of the principal sources of hydrocarbon exhaust emissions, when operating away from the lean limit. Further, some of them show that a reduction of the piston top land height leads to an important decrease in hydrocarbon emissions [13, 57]. In the case of gas operation, the absence of deposits and liquid fuel effects should increase the relative importance of the crevices mechanism on the THC exhaust emissions. However, a similar reduction on a natural gas spark ignition engine operating at stoichiometric could not be clearly identified [89]. On the other hand, the reduction of the crevice volume located between the cylinder liner, the cylinder head and the cylinder gasket evaluated in a previous study [3, 4] showed an important potential to reduce the THC and CO emissions.

In order to evaluate the effect of a reduction of the piston to land height, an experimental piston (without steel groove insert) with raised first compression ring was designed by the piston manufacturer and tested. The first compression ring was placed as close as possible to the piston face without reducing significantly the piston crown mechanical stability, thus enabling industrial application. The piston top land height is reduced from 16 to 10 mm (**figure C.21**).

At constant NO<sub>x</sub> emissions, the reduction of the piston top land height results in a moderate decrease of about 5% in CO emissions (**figure C.22, a**). Unfortunately, the failure of the FID exhaust gas analyser required its temporary replacement for the test of the piston with reduced top land height and, despite a similar calibration, the use of two different analysers renders very difficult the interpretation of the increase in THC emissions. Because the other engine parameters suggest an opposite trend, these particular results will not be discussed further. The raising of the first compression ring has no perceptible effect on the fuel conversion efficiency, while it increases

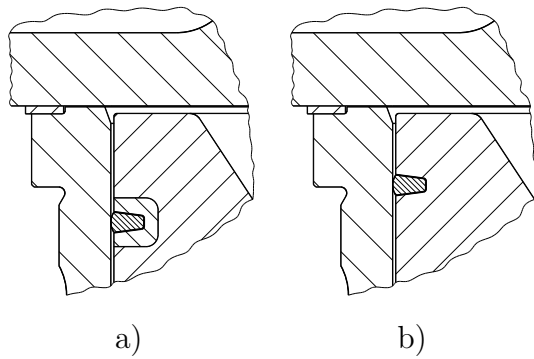


**Figure C.21:** Location of the first piston compression ring: original, 16 mm (a), and reduced, 10 mm (b), piston top land height.

significantly the engine operating stability, particularly when leaning the fuel-air mixture (**figure C.22, b**). The slightly higher volumetric compression ratio increases the cylinder pressure enough to cause a perceptible reduction of the ignition delay (**figure C.22, c**). The increase of the fuel burnt in the primary oxidation process, resulting from the decrease of the mass of unburnt mixture stored in the top land crevice, associated with the reduction of ignition delay, leads to a significant decrease of the combustion duration and an improvement of the combustion stability. A similar behaviour has been established when the crevice volume located between the cylinder liner, the cylinder head and the cylinder gasket was reduced [3, 4]. The decrease in total pressure and temperature before turbine resulting from the reduction of combustion duration is to a large extent compensated by the increase of heat released during the primary oxidation (**figure C.22, d**). The similar combustion behaviour in comparison to the reduction in gasket crevice volume suggests that the decrease in CO emissions originates mainly in the lower amount of unburnt mixture escaping the primary oxidation process. The THC emissions consequently should follow the same trend!

The reduction of the piston top land height induces only a moderate reduction of the CO emissions, which seems not to justify the extra cost associated with the manufacture of a special piston injection mould to accommodate the shift of the steel groove insert; the original piston for gas operation is directly derived from the diesel engine piston, without change in the ring configuration.

### C.4.5 Conclusion

The reduction of the volumetric compression ratio from 12.0 to 9.7 yields approximately 30 % decrease in CO emissions as well as about 45 % reduction of THC emissions, which enables the engine to fulfil the requirement of the OPair for biogas operation (no catalytic exhaust gas after treatment possible). On the other hand, this results in an approximately 2 %-point decrease in fuel conversion efficiency. A further reduction of the volumetric compression ratio from 9.7 to 9.0 causes only a moderate complementary reduction of CO ( $\approx 8\%$ ) and THC ( $\approx 4\%$ ) emissions, but a relatively large decrease in fuel conversion efficiency ( $\approx 1.5\%$ -point). The reduction of the intake and exhaust valve overlap duration from 40 to 16 °CA has no significant effect on



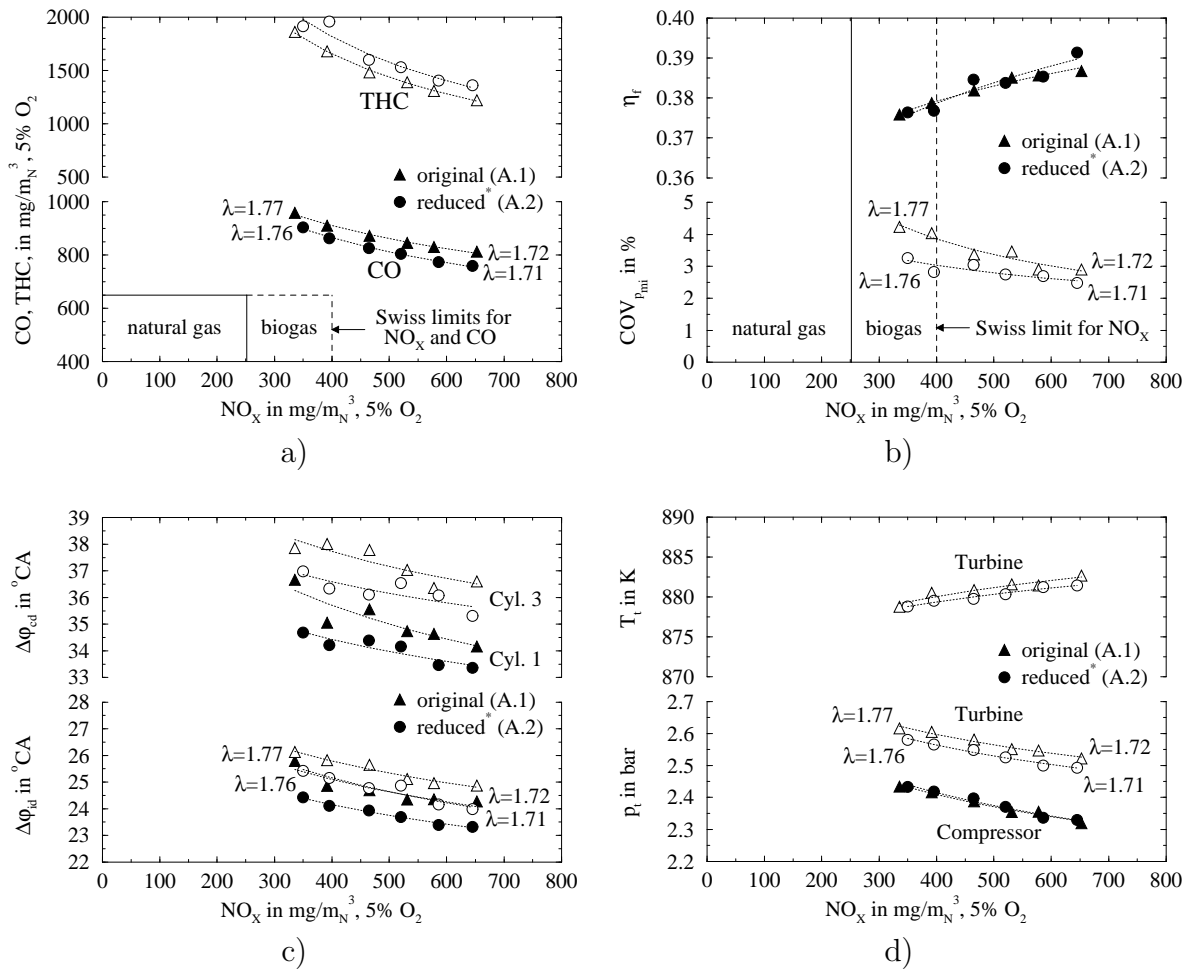


**Figure C.22:** Influence of a reduction of the piston top land height from 16 to 10 mm: a) CO and THC emissions, b) fuel conversion efficiency and coefficient of variance of  $p_{mi}$ , c) Ignition delay and combustion duration, d) total boost pressure and total pressure and temperature before turbine; Piston A ( $\epsilon = 12.0$ ),  $ST = 26.7^\circ\text{CA}_{BTDC}$ ,  $T_{mixt} = 90^\circ\text{C}$ ,  $RH = 45$  (\*50) %, NG2.

the CO emissions but leads to about 5% decrease in THC emissions. On the other hand, the consequent increase of engine pumping work causes an approximately 0.5% reduction of fuel conversion efficiency. Finally, the reduction of the piston top land crevice volume enables a reduction of about 5% in CO emissions, while not affecting the engine performance.

Through a decrease of the peak cylinder pressure and an increase of the bulk combustion gas temperature during expansion, the reduction of the volumetric compression ratio proves to be the more effective mean of reducing both the CO and THC exhaust emissions, however at the cost of a significant reduction in fuel conversion efficiency. On the other hand, the relatively weak effect of a reduction of valves overlap duration and piston top land crevice volume seems not to justify the extra cost associated with the production of special engine parts dedicated for gas operation.

## C.5 Tabulated experimental data

The experimental data given in **table C.6** corresponds to the engine operation with direct spark ignition, represented and discussed in section 4.3 and section C.4. The experimental data given in **table C.7** is related to the engine operation with prechamber spark ignition, analysed in section 4.4. **Table C.8** gives the absolute error on the engine performance and emissions.

**Table C.6:** Tabulated data of the direct ignition experiments

No	fuel <sup>1</sup>	$\epsilon$	ST	$T_{mixt}$	RH	$\lambda$	NO <sub>x</sub>	CO	THC	NO <sub>x</sub>	CO	THC	$\eta_f$	$COV_{pmi}^4$	$\varphi_{Q_{5\%}}^4$	$\varphi_{Q_{90\%}}^4$
		-	<sup>2</sup>	<sup>3</sup>	%	-	$mg/m^3_N, 5\% O_2$			$mg/kWh^3$			%	%	5	5
A.1	NG2	12.0	26.7	50	45	1.773	336	958	1862	981	2801	5444	37.6	4.2	26.0	63.2
						1.760	392	911	1680	1138	2645	4879	37.9	4.0	25.3	61.9
						1.747	465	873	1484	1356	2543	4324	38.2	3.4	25.2	61.8
						1.735	531	846	1391	1531	2439	4010	38.5	3.5	24.7	60.6
						1.730	578	830	1309	1676	2408	3795	38.6	2.9	24.7	60.2
						1.718	653	813	1222	1882	2345	3523	38.7	2.9	24.6	60.0
A.2	NG2	12.0	26.7	90	50	1.756	350	904	1917	1021	2638	5592	37.6	3.3	24.9	60.8
						1.740	395	863	1961	1147	2505	5690	37.7	2.8	24.6	59.9
						1.735	465	826	1601	1345	2391	4635	38.5	3.1	24.4	59.6
						1.724	520	804	1531	1495	2312	4399	38.4	2.8	24.3	59.6
						1.712	586	773	1405	1688	2228	4048	38.5	2.7	23.8	58.6
						1.705	645	760	1363	1849	2178	3908	39.1	2.5	23.6	58.0
B.1	NG1	12.0	26.7	90	30	1.787	128	1265	2524	382	3781	7546	36.6	4.5	27.8	63.0
						1.773	171	1122	2029	507	3323	6012	37.2	3.1	27.2	61.0
						1.762	203	1052	1807	599	3099	5320	37.9	3.1	26.6	59.2
						1.756	233	997	1636	686	2935	4817	38.3	3.1	26.3	58.7
						1.748	265	954	1510	775	2785	4408	38.6	2.5	25.9	57.9
						1.739	301	921	1414	875	2684	4119	38.5	2.2	25.6	56.7
C.1	NG2	9.7	26.7	90	45	1.702	171	802	1518	560	2633	4982	33.7	4.6	33.4	76.1
						1.687	222	729	1222	714	2339	3923	34.3	3.8	32.6	74.5
						1.676	266	685	1059	850	2190	3385	35.6	3.4	32.1	73.3
						1.666	314	656	965	992	2069	3044	35.3	3.0	31.8	72.4
						1.653	360	624	865	1129	1958	2712	36.3	2.8	31.2	72.0
						1.646	396	607	824	1242	1906	2586	36.3	2.3	30.8	70.9
C.2	NG3	9.7	26.7	90	50	1.678	181	773	1870	584	2493	6033	34.2	4.7	33.3	75.4
						1.665	228	711	1609	727	2269	5139	34.9	3.1	32.6	73.8
						1.653	272	675	1498	860	2138	4745	35.3	3.3	32.2	73.1
						1.643	309	644	1349	969	2018	4230	35.5	3.3	31.7	72.2
						1.634	355	619	1242	1104	1929	3867	35.9	2.1	31.3	71.9
						1.627	405	607	1205	1263	1892	3757	36.1	2.4	31.0	71.2
C.3	NG3	9.7	26.7	90	50	1.664	219	729	1553	709	2362	5031	34.1	4.9	32.4	74.7
						1.652	273	689	1413	876	2212	4537	34.4	3.9	32.0	73.6
						1.646	308	657	1270	978	2085	4030	35.2	3.8	31.5	73.4
						1.636	362	634	1177	1145	2004	3722	35.4	3.3	30.9	72.4
						1.633	402	620	1137	1269	1956	3586	35.6	2.4	30.9	72.0
						1.624	452	606	1075	1420	1902	3376	35.6	2.9	30.6	70.9
D.1	NG3	9.0	26.7	90	30	1.654	191	700	1598	646	2373	5418	32.8	4.4	34.6	79.7
						1.642	237	654	1444	788	2178	4806	33.3	4.0	34.2	78.3
						1.629	289	620	1331	955	2052	4405	33.9	3.6	33.6	77.5
						1.617	326	593	1259	1068	1941	4123	34.2	3.1	33.1	76.5
						1.609	369	573	1197	1204	1869	3902	34.4	3.1	33.0	76.5
						1.601	406	559	1156	1318	1815	3752	34.5	2.9	32.6	75.8

1: see table C.4, page 215; 2:  $^{\circ}CA_{BTDC}$ ; 3: referred to the net mechanical work delivered at the crankshaft

4: average value of cylinder 1 and 3; 5:  $^{\circ}CA_{AST}$

**Table C.7:** Tabulated data of the prechamber ignition experiments

No	fuel <sup>1</sup>	$p_{me}$	$A_t$	RH	ST	$\lambda$	NO <sub>x</sub>	CO	THC	NO <sub>x</sub>	CO	THC	$\eta_f$	$COV_{pmi}^4$	$\varphi_{Q_{5\%}}^4$	$\varphi_{Q_{90\%}}^4$
		bar	cm <sup>2</sup>	%	<sup>2</sup>	-	mg/m <sup>3</sup> , 5% O <sub>2</sub>			mg/kWh <sup>3</sup>			%	%	5	5
A.3	NG4	12.0	11	35	26.7	1.778	347	1022	1764	1023	3014	5202	38.4	3.9	25.5	64.1
						1.766	413	969	1569	1221	2865	4638	38.2	3.8	25.1	62.9
						1.754	492	935	1425	1441	2739	4175	39.0	3.4	24.7	61.9
						1.740	588	902	1248	1724	2645	3661	38.9	2.7	24.3	60.6
						1.735	660	887	1192	1926	2587	3476	39.4	2.5	24.0	60.1
A.4	NG4	12.0	11	50	16.8	1.711	313	977	1443	946	2957	4368	37.7	4.4	24.7	60.5
						1.700	365	934	1239	1099	2807	3727	37.8	3.2	23.0	57.7
						1.695	408	911	1122	1219	2723	3354	38.2	3.0	22.5	56.4
						1.689	450	892	1064	1337	2648	3162	38.5	2.5	22.3	56.0
						1.683	488	878	1040	1459	2623	3107	38.4	2.6	21.9	55.7
					1.679	537	869	981	1602	2594	2925	38.7	2.3	21.7	55.1	
					10.8	1.685	187	861	1210	598	2747	3859	36.1	4.1	23.6	57.2
						1.675	231	815	1045	728	2569	3293	36.4	3.8	22.3	55.6
						1.663	283	783	938	885	2448	2935	37.0	3.0	21.5	53.8
						1.653	325	757	851	1003	2332	2624	37.8	2.9	21.1	53.0
1.644	378	733	798	1165		2255	2456	37.8	2.4	20.3	52.2					
A.5	NG4	12.0	11	50	10.8	1.623	822	657	654	2437	1950	1940	38.6	1.9	19.1	44.6
						1.617	882	651	647	2619	1933	1924	38.8	1.6	18.6	44.2
						1.610	992	648	607	2937	1918	1797	39.0	1.4	18.1	43.8
						1.606	1034	642	600	3069	1904	1779	39.1	1.3	17.6	43.1
						1.600	1110	639	590	3286	1893	1749	38.8	1.3	17.8	43.2
A.6	NG4	12.0	11	50	10.8	1.672	317	754	850	971	2307	2603	37.2	3.1	21.3	50.7
						1.662	372	738	810	1133	2248	2466	37.6	2.5	20.3	49.7
						1.654	428	726	776	1301	2207	2357	37.9	2.4	19.8	49.2
						1.647	479	717	741	1446	2162	2237	38.0	2.2	19.3	48.5
						1.642	520	708	718	1577	2145	2176	37.9	2.1	19.1	47.9
A.7	NG4	12.0	11	50	10.8	1.637	347	722	784	1077	2239	2431	36.5	2.6	21.1	54.8
						1.628	405	702	738	1254	2173	2284	37.2	2.5	20.5	53.6
						1.619	457	689	692	1412	2128	2138	37.0	2.3	20.4	53.1
						1.611	519	675	669	1593	2072	2052	37.2	2.1	19.9	52.2
						1.604	591	663	652	1809	2029	1996	37.8	2.1	19.5	51.8
A.8	NG5	12.0	11	50	10.8	1.665	335	742	871	1032	2287	2684	37.4	3.5	21.4	50.8
						1.655	394	734	839	1214	2259	2582	37.2	3.1	20.9	50.5
						1.647	441	726	789	1342	2208	2402	37.8	2.2	20.4	49.5
						1.641	482	723	767	1472	2207	2343	37.4	2.3	20.0	49.1
						1.636	523	718	745	1591	2186	2270	37.9	2.0	19.5	48.4
A.9	NG5	12.0	11	50	10.8	1.648	345	692	784	1060	2124	2406	37.4	2.7	20.6	49.3
						1.638	387	688	759	1186	2111	2326	37.7	2.4	20.0	48.1
						1.631	441	683	714	1349	2088	2183	37.7	2.3	19.5	47.5
						1.625	491	682	688	1498	2082	2099	37.9	2.1	19.2	47.1
						1.621	524	679	682	1597	2069	2078	37.9	2.1	19.2	46.9
					8.3	1.639	260	625	770	831	1997	2462	36.2	3.0	20.7	48.3
						1.633	296	619	687	940	1964	2180	36.4	3.1	20.4	47.6
						1.623	345	618	690	1076	1929	2153	37.0	3.1	19.7	46.6
						1.617	381	613	635	1191	1916	1986	37.3	2.6	19.4	46.4
						1.611	424	612	623	1315	1897	1932	37.3	2.5	18.9	45.6
A.10	NG5	12.0	11	50	10.8	1.648	474	729	792	1429	2199	2388	37.9	2.9	21.0	47.9
						1.642	524	730	754	1570	2187	2259	38.2	2.6	20.5	47.3
						1.639	558	728	743	1677	2190	2233	38.0	2.3	19.8	46.2
						1.635	596	729	733	1786	2184	2198	38.5	2.0	19.4	45.6
						1.632	637	731	721	1916	2199	2168	38.3	2.1	19.4	45.7

continued on next page

**Table C.7:** Tabulated data of the prechamber ignition experiments (continued)

No	fuel <sup>1</sup>	$p_{me}$	$A_t$	RH	ST	$\lambda$	NO <sub>x</sub>	CO	THC	NO <sub>x</sub>	CO	THC	$\eta_f$	$COV_{pmi}^4$	$\varphi_{Q_{5\%}}^4$	$\varphi_{Q_{90\%}}^4$
		bar	cm <sup>2</sup>	%	<sup>2</sup>	-	mg/m <sub>N</sub> <sup>3</sup> , 5% O <sub>2</sub>			mg/kWh <sup>3</sup>			%	%	5	5
A.11	NG5	12.0	11	50	10.8	1.630	326	717	807	1017	2239	2520	36.9	3.2	20.5	52.8
						1.624	372	707	767	1158	2202	2391	37.1	2.7	20.1	52.4
						1.618	425	699	756	1303	2142	2317	37.3	2.8	20.0	51.9
						1.609	478	690	727	1464	2114	2225	37.4	2.4	19.4	51.3
						1.603	527	680	698	1615	2086	2141	37.6	2.2	19.0	50.2
					8.3	1.634	220	674	798	707	2166	2562	35.8	3.5	21.0	53.6
						1.625	256	653	740	817	2082	2357	36.0	3.4	20.7	52.8
						1.616	297	640	717	946	2038	2286	36.1	3.0	20.1	51.4
						1.606	329	629	685	1033	1979	2154	36.7	2.7	19.8	50.9
						1.600	358	620	662	1126	1953	2086	36.3	2.8	19.4	50.2
A.12	NG6	12.0	11	52	8.3	1.639	240	686	798	778	2226	2593	35.4	4.3	23.1	54.6
						1.630	282	666	741	907	2138	2379	36.0	3.6	22.0	53.0
						1.621	322	652	704	1024	2070	2234	36.3	3.2	21.6	51.7
						1.614	352	644	684	1111	2032	2158	36.6	2.9	21.0	51.1
						1.608	398	636	666	1253	2003	2097	36.6	2.7	20.6	50.7
A.13	NG6	12.0	11	49	8.3	1.644	245	622	728	783	1984	2321	35.9	4.4	22.5	49.7
						1.635	282	619	700	898	1970	2228	36.2	3.4	21.6	48.1
						1.626	316	622	678	993	1959	2135	36.5	3.1	21.2	47.4
						1.619	361	625	666	1130	1957	2085	37.0	2.6	20.2	46.1
						1.613	389	629	656	1218	1969	2054	36.7	2.6	20.2	46.0
A.14	NG6	12.0	11	50	8.3	1.667	159	744	1062	523	2440	3481	34.7	3.9	21.4	54.4
						1.655	203	713	901	645	2273	2872	35.6	3.0	20.9	52.3
						1.643	249	692	840	791	2201	2668	35.7	2.4	20.3	51.4
						1.633	291	684	801	915	2147	2516	36.4	2.4	19.8	50.2
						1.623	336	673	766	1053	2108	2398	36.5	2.1	19.2	49.2
A.15	NG6	12.0	11	50	8.3	1.642	165	652	824	554	2196	2775	34.3	4.8	23.6	56.1
						1.630	208	632	742	687	2086	2450	34.8	4.3	22.5	53.9
						1.620	244	617	705	799	2019	2307	35.0	4.1	22.2	52.6
						1.611	289	611	675	936	1979	2186	35.5	3.2	21.5	51.5
						1.600	330	605	656	1064	1952	2118	35.9	2.9	20.8	49.7
A.16	NG7	12.0	11	50	8.3	1.622	276	572	630	887	1840	2023	36.0	3.5	20.7	47.1
						1.609	319	569	610	1013	1809	1937	36.2	3.1	20.3	46.2
						1.602	355	572	592	1122	1804	1866	36.4	2.7	20.0	45.9
						1.595	399	576	581	1257	1813	1828	36.6	2.4	19.6	45.1
						1.589	439	578	571	1383	1821	1799	36.5	2.0	19.1	44.7
B.2	NG7	12.0	11	50	8.3	1.631	327	550	587	1028	1732	1849	36.7	3.1	20.9	44.6
						1.624	362	543	559	1145	1717	1765	36.9	2.9	20.5	43.9
						1.617	397	540	545	1261	1714	1729	36.4	2.5	19.9	42.9
						1.612	434	537	534	1369	1692	1682	36.7	2.2	19.7	42.5
						1.608	466	536	528	1461	1681	1655	37.0	2.1	19.8	42.4
B.3	NG7	12.0	11	49	8.3	1.670	217	595	769	689	1890	2444	35.8	2.3	20.4	44.5
						1.662	253	579	661	801	1835	2097	36.3	2.0	19.9	43.7
						1.654	279	568	639	881	1795	2019	36.7	1.9	19.9	43.3
						1.644	310	561	601	974	1766	1892	36.8	1.7	19.6	42.8
						1.637	349	556	580	1088	1734	1811	37.2	1.5	19.2	41.9
B.4	NG7	12.0	17	47	8.3	1.678	217	616	1168	679	1922	3649	36.7	2.5	20.7	44.9
						1.672	247	599	968	762	1845	2980	37.1	2.0	20.3	43.8
						1.665	280	592	908	867	1836	2815	36.9	1.8	19.9	43.3
						1.656	306	583	860	935	1782	2628	37.6	1.7	19.5	42.5
						1.650	344	580	829	1056	1778	2542	37.3	1.6	19.3	42.0

continued on next page

**Table C.7:** Tabulated data of the prechamber ignition experiments (continued)

No	fuel <sup>1</sup>	$p_{me}$ bar	$A_t$ $cm^2$	RH %	ST 2	$\lambda$ -	NO <sub>x</sub> $mg/m^3_N, 5\% O_2$	CO $mg/m^3_N, 5\% O_2$	THC $mg/m^3_N, 5\% O_2$	NO <sub>x</sub> $mg/kWh^3$	CO $mg/kWh^3$	THC $mg/kWh^3$	$\eta_f$ %	$COV_{pmi}^4$ %	$\varphi_{Q_{5\%}}^4$ 5	$\varphi_{Q_{90\%}}^4$ 5
B.5	NG7	12.0	17	47	8.3	1.665	280	592	908	867	1836	2815	36.9	1.8	19.9	43.3
		10.9				1.648	285	580	877	888	1807	2731	36.7	1.8	19.9	42.8
		9.5				1.636	271	576	881	865	1842	2818	35.6	1.8	20.3	42.8
		8.5				1.621	277	574	884	898	1857	2859	35.3	1.9	20.3	42.4
		7.3				1.595	291	581	852	960	1915	2811	34.5	1.9	20.4	41.8

1: see table C.4, page 215; 2:  $^{\circ}CA_{BTDC}$ ; 3: referred to the net mechanical work delivered at the crankshaft

4: average value of cylinder 1 and 3; 5:  $^{\circ}CA_{AST}$

**Table C.8:** Absolute error on the engine performance and emissions

Variable	Unit	Absolute error <sup>1</sup>
$\eta_f$	%	$\pm 0.6$
NO <sub>x</sub>	$mg/m^3_N, 5\% O_2$	$\pm 15$
CO	$mg/m^3_N, 5\% O_2$	$\pm 20$
THC	$mg/m^3_N, 5\% O_2$	$\pm 40$
$\lambda$	-	$\pm 0.02$

1: averaged over the series of measurements B.3 and B.4 (see table C.7)



# Curriculum vitae

Roger Röthlisberger,

born on the 5<sup>th</sup> of March 1963 in Lausanne, Switzerland,

Swiss citizen.

## Education

- 1990 Diploma of Mechanical Engineering of the *Swiss Federal Institute of Technology of Lausanne (EPFL)*
- 1986 Diploma of Mechanical Engineering ETS of the *School of Engineering of the State of Vaud (EIVD)*
- 1983 Swiss Federal Certificate of Capacity in mechanics at *Bobst S.A.*

## Professional experiences

- 1995- Research assistant at the *Laboratory for Industrial Energy Systems (LENI)* of the *EPFL*, mainly studying the combustion in gas engines for cogeneration applications
- 1994-95 Honorary Research Fellow at the *Department of Mechanical Engineering* of *The University of Auckland, New Zealand*, investigating the ignition of methane-air mixtures through CFD and chemical kinetics simulation
- 1990-93 Calculation engineer at *Motoren- und Turbinen Union (MTU) Friedrichshafen GmbH, Germany*, responsible for the development of a numerical method for the analysis of the diesel engine pressure cycle

## Teaching experiences

- 1998 Introduction to combustion in the frame of *Postgraduate Studies in Energy* at *EPFL*
- 1995- Supervision of student projects and diploma theses